Towards Quantum Simulation of the Sachdev–Ye–Kitaev Model

A dissertation for the degree of
Doctor of Philosophy in Physics
submitted to the
Department of Physics
University of Trento, Italy

by

Philipp Johann Uhrich

from Windhoek, Namibia

Dottorato di Ricerca
XXXV Ciclo
May 2023

Supervisors:
Prof. Dr. Philipp Hauke
Dr. Iacopo Carusotto

Abstract

Analogue quantum simulators have proven to be an extremely versatile tool for the study of strongly-correlated condensed matter systems both near and far from equilibrium. An enticing prospect is the quantum simulation of non-Fermi liquids which lack a quasiparticle description and feature prominently in the study of strange metals, fast scrambling of quantum information, as well as holographic quantum matter. Yet, large-scale laboratory realisations of such systems remain outstanding. In this thesis, we present a proposal for the analogue quantum simulation of one such system, the Sachdev–Ye–Kitaev (SYK) model, using cavity quantum electrodynamics (cQED). We discuss recent experimental advances in this pursuit, and perform analysis of this and related models. Through a combination of analytic calculations and numeric simulations, we show how driving a cloud of fermionic atoms trapped in a multi-mode optical cavity, and subjecting it to a spatially disordered AC-Stark shift, can realise an effective model which retrieves the physics of the SYK model, with random all-to-all interactions and fast scrambling. Working towards the SYK model, we present results from a recent proof-of-principle cQED experiment which implemented the disordered light-shift technique to quantum simulate all-to-all interacting spin models with quenched disorder. In this context, we show analytically how disorder-driven localisation can be extracted from spectroscopic probes employed in cQED experiments, despite their lack of spatially resolved information. Further, we numerically investigate the post-quench dynamics of the SYK model, finding a universal, super-exponential equilibration in the disorder-averaged far-from-equilibrium dynamics. These are reproduced analytically through an effective master equation. Our work demonstrates the increasing capabilities of cQED quantum simulators, highlighting how these may be used to study the fascinating physics of holographic quantum matter and other disorder models in the lab.

Sommario

I simulatori quantistici analogici hanno dimostrato di essere uno strumento estremamente versatile per lo studio di sistemi di materia condensata fortemente correlati sia fuori che in equilibrio. Un'applicazione particolarmente interessante è la simulazione quantistica dei liquidi non di Fermi, che mancano di una descrizione quasi-particellare e hanno un posto di rilievo nello studio sia dei metalli strani, che nel rimescolamento delle informazioni quantistiche, così come nella materia quantistica olografica. Tuttavia, le implementazioni in laboratorio su larga scala di tali sistemi rimangono sporadiche. In questa tesi, presentiamo una proposta analogica per la simulazione quantistica di uno di questi sistemi, il modello di Sachdev–Ye–Kitaev (SYK), utilizzando l'elettrodinamica quantistica in una cavità (cQED). Discuteremo i recenti progressi sperimentali ed eseguiremo l'analisi di questo e dei modelli ad esso collegati. Attraverso una combinazione di calcoli analitici e simulazioni numeriche, mostriamo come, controllando una nuvola di atomi fermionici intrappolati in una cavità ottica multimodale e sottoponendola a uno spostamento AC-Stark spazialmente disordinato, si possa realizzare un modello efficace che riproduce la fisica di il modello SYK, interamente connesso con interazioni casuali e rapida diffusione dell'informazione quantistica. Al fine di ottenere la fisica del modello SYK, presentiamo i risultati di un recente esperimento di cQED, che ha implementato la tecnica di spostamento disordinato della luce per simulare quantisticamente modelli di spin interagenti con disordine indipendente dal tempo. In questo contesto, mostriamo analiticamente come la localizzazione generalizzata dal disordine può essere estratta dalle sonde spettroscopiche impiegate negli esperimenti cQED, nonostante la loro mancanza di informazioni risolte spazialmente. Inoltre, indaghiamo numericamente le dinamiche post-quench del modello SYK, trovando un processo di riequilibrio universale super-esponenziale nelle dinamiche fuori equilibrio mediate dal disordine. Questi sono riprodotti analiticamente attraverso equazione maestra efficace. Il nostro lavoro dimostra le crescenti capacità dei simulatori quantistici cQED, evidenziando come questi possano essere utilizzati per studiare in laboratorio l'affascinante fisica dei modelli disordinati e della materia quantistica olografica.

Acknowledgements

I would like to thank Philipp Hauke for his supervision and guidance afforded to me during the course of my doctoral studies. Thank you for providing a relaxed, yet stimulating, research environment, for the freedom to explore one's own ideas, and for always finding the time for discussions. A big thank you is also due to Soumik Bandyopadhyay, with whom I collaborated closely over the duration of my PhD. Thank you for your patience during our multitudinous discussions, for introducing me to `MPI`, and for sharing your *aloo posto* recipe. More broadly, I would like to thank all of my fellow PhD students, and the Postdocs, of the Hauke research group and of the physics department alike, for creating a pleasant and stimulating research atmosphere. Thank you also for the lighter side of things, including the many hikes, lunch discussions and coffee breaks, the steady supply of paçoca, and the rigorous implementation of "fruit o'clock". I further have many fond memories collaborating with the *Laboratory for Quantum Gases* of Jean-Philippe Brantut. In particular of the countless discussions with Nick Sauerwein, characterised by an inexhaustible enthusiasm for physics and a great sense of humour. I would also like to express my gratitude to Soumik, Andrea Legramandi, Ricardo Costa de Almeida, Nick, and Jan Cillié Louw for helpful discussions during the writing of this thesis. Finally, thank you Jess. For putting up with the challenges of repeatedly moving abroad, for the encouraging notes sprinkled throughout the pages of my diary, for your ceaseless support.

To my parents,
for giving me a foundation.
To Jess,
for helping me build on it.

Contents

1 Introduction

Understanding the equilibrium and dynamic behaviour of quantum many-body systems is of fundamental interest to research in physics. It is a unifying theme and underlies a broad spectrum of research directions. Examples include the quantum chaotic physics of heavy nuclei [1], the description of material properties under the helm of condensed matter physics [2], and the study of intriguing quantum phases of matter such as supersolidity [3] and holographic quantum matter [4]. Whilst the properties of weakly-interacting systems are amenable to analytic calculations via quasiparticle descriptions [5], this framework often fails to capture the properties of strongly-interacting quantum many-body (QMB) systems [4, 6]. Exact numeric simulations are hampered by the exponentially many complex numbers required to describe the wavefunction of QMB systems [7], and approximate algorithms which successfully address this challenge are not universally applicable, for instance due to the sign-problem [8] or the varying entanglement content of QMB states [9, 10].

This has driven rapid advances in the creation and manipulation of synthetic QMB systems engineered to mimic condensed matter physics. In this pursuit, broadly termed "quantum simulation" [7], cold atoms and degenerate quantum gases have taken a prominent role [7, 11, 12]. To quote Lewenstein *et al.* [13], the creation of Bose–Einstein condensates in 1995 marked "the beginning of a new era", in which the manipulation of cold quantum gases offers "unprecedented possibilities for the control of many-body systems". Currently, physicists have at their disposal a diverse range of table-top platforms—with complementary strengths and weaknesses [7, 14]—in which the properties of synthetic quantum systems can be probed in a highly controlled manner. These include ion traps [15, 16], neutral atoms trapped in optical lattices [17, 18], optical tweezer arrays of Rydberg atoms [19, 20], quantum gases trapped in optical resonators (cavity quantum-electrodynamics, cQED) [21, 22], as well as superconducting devices [23, 24].

A useful approach in the study of QMB systems is to construct a simplified many-body Hamiltonian $\hat{H}_{\mathrm{mb}}$, which retains just enough complexity to be able to capture the system properties under study, and to ignore interactions with a possible environment. Such a construction allows one to obtain the equilibrium, low-energy (zero temperature) physics of the isolated QMB system in terms of its ground-state properties, as well as allowing one to study out-of-equilibrium dynamics as generated by $\hat{H}_{\mathrm{mb}}$. Accordingly, research efforts in experimental platforms for synthetic QMB systems have been geared towards engineering effective interactions of the constituent particles so as to reproduce those described by the simplified $\hat{H}_{\mathrm{mb}}$ [7]. Taking, once more, the example of quantum gases, the mastery of optical dipole potentials has allowed for the synthesis of systems with reduced dimensionality, as well as with discrete translational symmetries through confinement in optical lattices with variable geometries. Controlling the strength of these optical potentials offers one route to render the strength of inter-particle interactions, relative to their kinetic energy, an experimentally tunable parameter. This allows for the preparation of the different phases which a given $\hat{H}_{\mathrm{mb}}$ might describe, such as superfluids or Mott insulators [25], and to further tune into critical regimes where the quantum fluctuations due to competing energy scales lead to equilibrium quantum phase transitions [26].

Particularly exciting are the possibilities to monitor quantum many-body dynamics far away from equilibrium in a controlled fashion. One of the fundamental questions in this regard is whether, and if so how, an *isolated* QMB system can thermalise. A fruitful Ansatz has been to study thermalisation on the level of local observables within the framework of the eigenstate thermalisation hypothesis (ETH) [27, 28], and its absence on the level of integrability and the generalised Gibb's ensemble (GGE) [27]. Until quite recently, however, one might have argued that the question of thermalisation in isolated systems is of little practical relevance, with the requisite isolation being absent in Nature (unless one considers the Universe as a whole). Whilst the dynamics of open quantum systems interacting with an environment are no less interesting [29, 30], not least due to their relevance for quantum technologies [31], remarkable experiments probing integrability and the GGE [32, 33], as well as the ETH [34], have demonstrated the ability to prepare QMB systems in far-from equilibrium configurations in near-perfect isolation from their laboratory environments and to study their subsequent closed-system, unitary dynamics.

The generally accepted mechanism underlying the ETH in chaotic QMB systems is subsystem thermalisation [27, 28], the idea that small sub-regions thermalise due to their interaction with the effective environment formed by the remainder of the system. Closely related notions are the spreading (or delocalisation) of quantum information, and entanglement generation, as thermalisation necessarily implies the transport of localised excitations, building-up correlations across the system. Indeed, subsystem thermalisation implies maximisation of the local von Neumann entropy—a measure of bipartite entanglement for pure states [35]—proportional to the subsystem size, in analogy to the thermodynamic entropy [27]. This volume law entanglement generation and its ballistic spread in time was measured in the experiment of Ref. [34], which employed an interference protocol that leveraged the single-site control and measurement resolution offered by state-of-the-art quantum gas microscopes. An alternative, random-measurement protocol, which does not require the generation of identical copies of the system under study, was employed in Ref. [36]. Particularly interesting in this context of thermalisation and entanglement generation, is the competition between quenched disorder (for instance in the form of random potentials) which is known to suppress thermalisation in non-interacting systems [37], and inter-particle interactions, which favour the exchange, and thus delocalisation, of excitations. In QMB systems, these competing phenomena can create many-body localised phases, characterised by the retention of initial configurations and (in contrast to the volume-law entanglement of ETH-obeying states) area-law entanglement which spreads logarithmically with time [38], both of which were experimentally verified by introducing quenched disorder into optical lattices [39–41].

The above mechanisms for delocalisation imply that correlations, encoded in an initial configuration $|\Psi\rangle$ of a QMB system, spread over the entire system under the unitary dynamics generated by $\hat{H}_{\mathrm{mb}}$, and become irretrievable via measurements of local observables. This "locking away" of quantum information in many-body correlations is known as *scrambling*, and can be measured by the decay of mutual information between initially entangled regions [42, 43]. The time at which this mutual information is approximately zero, is referred to as the scrambling time t_*. From the viewpoint of quantum information, the question of thermalisation is thus a question of how quickly $\hat{H}_{\mathrm{mb}}$ can distribute or *scramble* quantum information over its N degrees-of-freedom. Intuitively, the connectivity (hyper)graph of $\hat{H}_{\mathrm{mb}}$ and the presence of disorder should play an important role in determining the size of t_*. Indeed, for local Hamiltonians with short-range interactions $t_* \sim N$, whilst long-ranged interactions decaying as a power-law $r^{-\alpha}$ can lead to enhanced scrambling as α is decreased[1] , with an algebraically suppressed scrambling time $t_* \sim N^{\zeta}$ $(0 < \zeta \leq 1)$. In turn, quenched disorder in local Hamiltonians has been found to suppress scrambling, leading to diffusive behaviour [43].

It has been conjectured that the shortest possible scrambling time t_*, which can be achieved in so-called "fast scrambling" QMB systems, is logarithmic in the system size N [42, 47]. This is motivated by the study of quantum

---

[1] This is in line with Lieb–Robinson bounds which provide universal limits, depending only on the dimensionality d and connectivity of $\hat{H}_{\mathrm{mb}}$, for the rate of information propagation over a distance r in non-relativistic QMB systems [44–46].

information processing of black holes [48], where the exponential temporal decay of out-of-time-order correlators (OTOCs) is typically used to diagnose scrambling [49–51]. Similarly, it was conjectured in Ref. [51] that the OTOC decay rate λ_{L}, the quantum generalisation of the Lyapunov exponent, is subject to a universal bound $\lambda_{\mathrm{L}} \leq 2\pi/\beta$, which is saturated by such "fast scramblers" (here β is the inverse temperature).

In recent years, there has been a flurry of research activity focussed on a particular QMB system, the Sachdev–Ye–Kitaev (SYK) model [52, 53], which dynamically manifests maximal scrambling of quantum information, saturating the above bound for λ_{L}. The model describes N fermions with interactions that are of infinite range, and independently sampled from a Gaussian distribution. The model was originally introduced in the study of strange metals and non-Fermi liquids [54], due to its lack of quasiparticle excitations resulting from an exponentially dense low-energy spectrum. In addition to exhibiting such strongly interacting many-body phenomena, the SYK system provides a toy model for holography [55]: At large-N and strong coupling, the model exhibits a set of properties [56–58] which it shares with two-dimensional Jackiw–Teitelboim gravity [59, 60].

The diversity of intriguing properties, in particular the exciting perspective of performing laboratory experiments on holographic systems, makes it highly desirable to find an experimental realisation of the SYK model. In spite of its connections with strange metals [54], however, no natural material is known that can microscopically realise the particular SYK interaction. Research efforts have thus focused on realising the SYK model in synthetic quantum systems. To date, multiple proposals have been put forward, ranging from solid-state mesoscopic systems [61–63], to cold atoms in optical lattices [64, 65], as well as direct digital quantum simulation [66, 67]. Despite the impressive successes in the synthesis and control of model Hamiltonians in QMB experiments, as outlined above, a large-scale implementation of these proposals remains outstanding. Small-scale, minimal versions of the digital approach have being reported using nuclear magnetic resonance [68] and superconducting qubits [69]. However, the large number of independent couplings, scaling with system size N as $[N(N-1)/2]^2$, as well as their infinite range, remains a formidable challenge for bottom-up approaches. The implementation of Ref. [69] circumvented this by using machine-learning techniques to identify reduced versions of the SYK Hamiltonian which could replicate certain dynamical features. This approach is, however, debated, as it appears to only partially retain the SYK physics [70, 71]. This highlights the need for a concept which is able to realise the dense set of couplings prescribed by the original model, in an experimentally feasible manner.

In this thesis, we address this challenge. We present a proposal for the quantum simulation of the SYK model in the cQED platform, leveraging recent advances such as the realisation of the strong-coupling regime for fermionic quantum gases trapped in optical resonators [72, 73]. Cavity quantum-electrodynamics combines the scalability of quantum gases to mesoscopic and large system sizes N, with the native ability of cavity photons to mediate infinite-range interactions. This makes cQED a promising platform for quantum simulating the SYK model. Theoretical studies have shown that, in addition to engineering *random* all-to-all interactions, quantum simulators of the SYK model must mediate these interactions via multiple bosonic modes whose number scales at least linearly with N [74, 75]. This is a crucial ingredient for synthesising the fast-scrambling dynamics of the SYK model.

In Chapter 3, we will show how advances in multi-mode cQED [76] could be exploited in order to meet this requirement for mesoscopic system sizes, and how spatially disordered AC-Stark shifts can be utilised to randomise the fermionic interactions. Further, we will demonstrate how the number of cavity-modes contributing to the effective interactions can be tuned, and motivate through numeric simulations that the fast scrambling dynamics of the target SYK model can be approached in this way.

In the above endeavour, the randomisation of cavity mediated interactions is an important milestone. Chapter 4 presents results from a recent experimental collaboration which has achieved this in cQED with (fermionic) ^{6}Li atoms in the single-mode regime [77]. By utilising the above idea of a spatially disordered AC-Stark shift, this cQED experiment was able to engineer spin models with quenched disorder. Specifically, the experiment tuned between disordered versions of the Tavis–Cummings and Lipkin–Meshkov–Glick (LMG) models by varying the atom–cavity detuning. We show how the latter model is generated in the far-off-resonant case, yielding a description in terms of a collective spin interaction. We further demonstrate that signatures of disorder-driven localisation can be extracted from the system's dynamic response, despite the lack of spatially resolved measurement protocols. Specifically, we show that the dynamic susceptibility of the simulated system allows one to bound the participation ratio of specific excited states, and we find that our theoretical predictions are in good agreement with the measured data.

In chapter 5, we present a theoretical study of the post-quench dynamics of the SYK model, focussing on the dynamics of the quantum Fisher information (QFI), a witness of multipartite entanglement [78, 79], and moments of local observables. We present numeric evidence for a super-exponential, universal equilibration—in the form of an independence of the dynamics on the initial, pre-quench state—in the SYK model after disorder averaging. We capture these features analytically for generic Hamiltonians by casting the disorder averaged dynamics in the form of a master equation, and demonstrate that in the case of the SYK model this reduces to a purely dissipative evolution, reproducing the numeric findings.

In addition to the above chapters, this thesis is structured as follows: Chapter 2 provides a theoretical background to the SYK model and to quantum simulation with cavity-QED. The discussion there will focus on introducing only the concepts and formalism which are utilised in the remainder of the thesis, but provides references for further reading. Chapters 3–5 contain the main results of this thesis, as outlined above, and are based on the following manuscripts:

1. P. Uhrich, S. Bandyopadhyay, N. Sauerwein, J. Sonner, J.-P. Brantut and P. Hauke, "A cavity quantum electrodynamics implementation of the Sachdev–Ye–Kitaev model", arXiv:2303.11343 [quant-ph] (2023) [80]

2. N. Sauerwein, F. Orsi, P. Uhrich, S. Bandyopadhyay, F. Mattiotti, T. Cantat-Moltrecht, G. Pupillo, P. Hauke and J.-P. Brantut, "Engineering random spin models with atoms in a high-finesse cavity", Nat. Phys. (2023) [77]

3. S. Bandyopadhyay, P. Uhrich, A. Paviglianiti and P. Hauke, "Universal equilibration dynamics of the Sachdev-Ye-Kitaev model", Quantum **7**, 1022 (2023) [81]

4. A. Paviglianiti, S. Bandyopadhyay, P. Uhrich and P. Hauke, "Absence of operator growth for average equal-time observables in charge-conserved sectors of the Sachdev-Ye-Kitaev model", J. High Energ. Phys. **2023**, 126 (2023) [82]

The publication of point 4 is a follow-up work to that of point 3, and the culmination of the Masters thesis of Alessio Paviglianiti [83], in which he provided, amongst other results, an analytic understanding for some of the features observed numerically in our Ref. [81]. This is briefly discussed in Sec. 5.5.

During the course of my PhD, I was co-author of further publications, which however do not form part of this thesis:

5. C. Dağ, Y. Wang, P. Uhrich, X. Na and J. Halimeh, "Critical slowing down in sudden quench dynamics", Phys. Rev. B **107**, L121113 (2023) [84]

6. C. Dağ, P. Uhrich, Y. Wang, I. McCulloch and J. Halimeh, “Detecting quantum phase transitions in the quasistationary regime of Ising chains”, Phys. Rev. B **107**, 094432 (2023) [85]
7. Y. J. Joshi, N. Sauerwein, A. Youssefi, P. Uhrich and T. J. Kippenberg, “Automated wide-ranged finely tunable microwave cavity for narrowband phase noise filtering”, Rev. Sci. Instrum. **92**, 034710 (2021) [86]
8. A. Youssefi, I. Shomroni, Y. J. Joshi, N. R. Bernier, A. Lukashchuk, P. Uhrich, L. Qiu and T. J. Kippenberg, “A cryogenic electro-optic interconnect for superconducting devices”, Nat. Electron. **4**, 326–332 (2021) [87]
9. P. Uhrich, N. Defenu, R. Jafari and J. C. Halimeh, “Out-of-equilibrium phase diagram of long-range superconductors”, Phys. Rev. B **101**, 245148 (2020) [88]

Publications 5, 6 and 9 are concerned with dynamic quantum phase transitions, the experimental investigation of which is hampered by the need to access the full wavefunction in order to determine the return rate of the Lohschmidt echo. The publication of point 9 explores the dynamic phase diagram of the long-range Kitaev chain, establishing a connection between non-analyticities of the return rate and zeros of the string order parameter, a quantity readily accessible in quantum gas microscopes [89, 90]. The publications of points 5 and 6 investigate the use of single-site observables to detect dynamic quantum phase transitions in integrable and non-integrable Ising chains.

Finally, during the time between my MSc and enrolment as a PhD candidate in the 35th cycle of the Università degli studi di Trento, I had the good fortune of completing a pre-doctoral internship in the *Laboratory of Photonics and Quantum Measurement* of Prof. T. J. Kippenberg, during which time I was involved in collaborations which lead to the publications of points 7 and 8. The former documents the design and deployment of a microwave cavity used to reduce room-temperature phase noise in control signals of superconducting circuit experiments. The latter investigates the use of electro-optic phase modulators for the read-out of superconducting circuits at cryogenic temperatures, in an effort to reduce the heat load transferred to the cryogenic environment, as it allows for the replacement of co-axial cables with optical fibres, whose thermal conductivity is two orders of magnitude lower.

2 Theoretical background

In this chapter we provide further context for the Sachdev–Ye–Kitaev (SYK) model (Sec. 2.1), and for quantum simulation with quantum gases trapped in optical resonators (Sec. 2.2). Aside from providing some historic context, we will focus on the formalism which will be utilised in the subsequent chapters. Readers who wish to delve deeper into the material will be pointed to useful references in the introductory part of either section. Note that here, and throughout this thesis, we set $\hbar = 1$.

2.1 The SYK model, Chaos, and Scrambling

The original formulation of the SYK model as a zero dimensional system of $N \gg 1$ Majorana fermions, with random and all-to-all quartic interactions of strength J, was introduced by A. Kitaev as “A simple model of quantum holography” in a pair of talks given at the Kavli Institute for Theoretical Physics in 2015 [53]. Aside from the holographic aspects motivated in his talks, Kitaev noted the similarity, at late times and for strong coupling, between this model and the Sachdev–Ye (SY) model, an SU(M) Heisenberg magnet with random all-to-all interactions [52]. The model introduced by Kitaev has since become known as the Sachdev–Ye–Kitaev (SYK) model, and in recent years its large-N properties have placed it at the intersection of research in condensed matter, quantum information, as well as quantum gravity [54, 91, 92].

The SY model was introduced by its namesakes in 1993 [52] to provide a model which realised the “marginal Fermi-liquid” phase which had been introduced in Ref. [93] on phenomenological grounds in an effort to reproduce the “bad”- and “strange”-metal properties observed in the non-superconducting phase of high-T_c cuprates. The transport properties of these unusual metallic phases cannot be captured by the quasiparticle-based theory of Fermi-liquids. Rather, their description requires an understanding of so-called “non-Fermi-liquids” (nFL), which do not host quasiparticle excitations. Such nFLs typically arise near quantum critical points, but may also appear as stable phases over a range of temperatures for sufficiently strong interactions [54]. The SYK model is an example of the latter, as its low-energy many-body spectrum is exponentially dense in N in the large-N limit , thus precluding a quasiparticle construction [54]. Furthermore, the model is solvable in the large-N limit. For example, fermionic correlation (Green's) functions can be computed analytically in the long-time (infrared, IR) limit $\beta t \gg 1$, under the additional assumption of strong coupling $\beta J \gg 1$, where β is the inverse temperature. Consequently, the SYK model has taken an important place in the study of condensed matter systems exhibiting nFL properties [54].

A further intriguing large-N property of the SYK model is that is an example of a "fast scrambler", redistributing localised excitations over the system's many-body degrees of freedom—a process closely linked to quantum chaos and thermalisation [27, 28], and entanglement generation [42]—at the fastest possible rate [42, 47]. A popular diagnostic of scrambling is the early-time exponential decay of out-of-time-order correlators (OTOCs), governed by the quantum Lyapunov exponent λ_{L}. At strong coupling $\beta J \gg 1$, the SYK model saturates the universal bound $\lambda_{\mathrm{L}} \leq 2\pi/\beta$, conjectured by Maldacena et al. [51] to be the fastest rate at which quantum information can be scrambled [57].

The SYK model shares this fast scrambling property with black holes, hinting at a holographic interpretation of the model. This is substantiated by its effective (disorder-averaged) action. In the IR limit, the effective action is conformally invariant, and reproduces the large-N Schwinger–Dyson equations which lead to the Green's function solutions discussed above. Notably, the explicit form of this Green's function spontaneously breaks the conformal symmetry down to $\mathrm{SL}(2, \mathbb{R})$, and the corrections to the IR effective action are governed by the Schwarzian action [57, 58]. These properties are shared with two-dimensional Jackiw–Teitelboim gravity [59, 60].

The remainder of this section is organised as follows. In Sec. 2.1.1, we present the Hamiltonian of the (Dirac fermion) SYK model, discuss its main features, and mention further variations of the model which appear in the literature. Then, in Secs. 2.1.2 and 2.1.3, we elaborate on, respectively, dynamic manifestations of many-body quantum chaos and scrambling of quantum information in the SYK model.

For an exposition of the SYK model within the condensed matter context, we refer the interested reader to the review of Chowdhury et al. [54]. For an introduction to the gravitational viewpoint, we suggest the review of Trunin [92]. Finally, for an overview of the use of holography as a tool to study strongly-correlated systems without quasiparticles, we suggest the book of Hartnoll et al. [4], as well as the reviews of Liu and Sonner [94, 95].

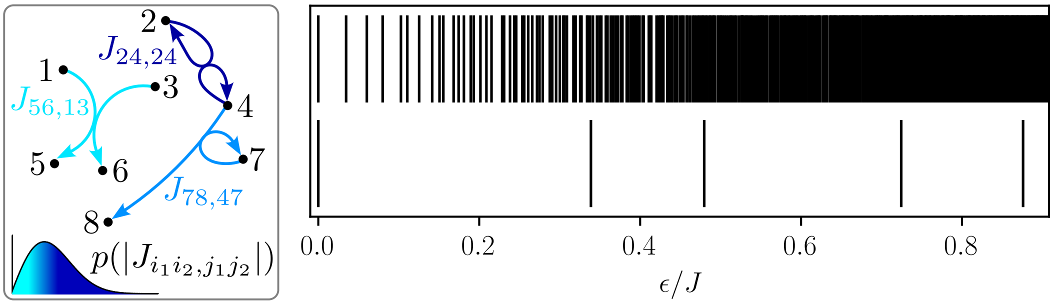

Figure 2.1: SYK model and spectrum. Representation of the SYK model $\hat{H}_{\text{SYK}}$ (left), defined in Eq. (2.1), as a directed hypergraph. Low-energy tail of the many-body spectrum of a single realisation of $\hat{H}_{\text{SYK}}$ (upper vertical lines), versus that of a single realisation of the random hopping model of Eq. (2.5) for $q = 2$ (lower vertical lines), for $N = 14$ and $Q = 1/2$. Both spectra are shown in units of J [see Eq. (2.2)], and have been shifted such that the ground state lies at zero energy. The energy-axis has been truncated so as to show the lowest 25% of the energy window covered by the spectrum of $\hat{H}_{\text{SYK}}$.

2.1.1 Model Hamiltonian

In this thesis we will work with a variation of the SYK model in which the N Majorana fermions modes are replaced by spinless Dirac fermion modes. This variant was introduced shortly after Kitaev's talks by Sachdev in Ref. [55], and its Hamiltonian is given by

$$\hat{H}_{\text{SYK}} = \frac{1}{(2N)^{3/2}} \sum_{i_1,i_2,j_1,j_2=1}^{N} J_{i_1 i_2; j_1 j_2} \hat{c}_{i_1}^{\dagger} \hat{c}_{i_2}^{\dagger} \hat{c}_{j_1} \hat{c}_{j_2}. \tag{2.1}$$

The fermionic operators $\hat{c}_i^{\dagger}, \hat{c}_i$ satisfy the canonical anticommutation relations, and respectively denote the creation and annihilation operator for the ith fermion mode. The Hamiltonian $\hat{H}_{\text{SYK}}$ describes a system of strongly-correlated fermions, with all-to-all two-body interactions as determined by the quartic operators $\hat{c}_{i_1}^{\dagger} \hat{c}_{i_2}^{\dagger} \hat{c}_{j_1} \hat{c}_{j_2}$. The interaction amplitudes $J_{i_1 i_2; j_1 j_2}$ are complex random variables, with real and imaginary parts sampled independently from Gaussian distributions. Their statistics are thus fully determined by their variances, which satisfy

$$\operatorname{var}(\operatorname{Re}[J_{i_1i_2;j_1j_2}]) = \begin{cases} J^2, & \text{for } i_1 = j_1, i_2 = j_2, \\ J^2/2, & \text{otherwise,} \end{cases}$$
$$\operatorname{var}(\operatorname{Im}[J_{i_1i_2;j_1j_2}]) = \begin{cases} 0, & \text{for } i_1 = j_1, i_2 = j_2, \\ J^2/2, & \text{otherwise.} \end{cases} \tag{2.2}$$

Consequently, the only energy scale governing the dynamics of $\hat{H}_{\text{SYK}}$ is $J > 0$. The interaction amplitudes further reflect the fermionic exchange statistics, and hermiticity of $\hat{H}_{\text{SYK}}$,

$$J_{i_1i_2;j_1j_2} = -J_{i_2i_1;j_1j_2} = -J_{i_1i_2;j_2j_1} = J_{i_2i_1;j_2j_1} = J^*_{j_1j_2;i_1i_2}. \tag{2.3}$$

The prefactor in Eq. (2.1) ensures an extensive scaling of the spectral bandwidth.

Physically, the model is zero-dimensional due to its all-to-all connectivity. To visualise the two-body processes described by $\hat{H}_{\text{SYK}}$, one may think of the system as a directed hypergraph on N nodes with $[N(N-1)/2]^2$ hyperedges that have complex weights in $\{J_{i_1i_2;j_1j_2} | i_1 < i_2, j_1 < j_2 \text{ and } i_k, j_k = 1, \ldots, N \text{ for } k = 1, 2\}$, and are oriented from nodes j_1, j_2 to nodes i_1, i_2. This is sketched in Fig. 2.1 (left panel), where we depict representative hyperedges for the possible two-body processes: Density-density interactions ($i_1 = j_1, i_2 = j_2, i_1 \neq i_2$, dark blue), density-assisted hopping (for instance $i_1 = j_2, i_1 \neq i_2 \neq j_1$, sky blue), or pairwise hopping ($i_1 \neq i_2 \neq j_1 \neq j_2$, cyan).

The only symmetry of $\hat{H}_{\text{SYK}}$ is the particle number[1],

$$\hat{Q} = \frac{1}{N} \sum_{i=1}^{N} \hat{c}_i^\dagger \hat{c}_i, \tag{2.4}$$

and the numeric studies presented in Chaps. 3 and 5 were all done at half-filling $Q \equiv \langle \hat{Q} \rangle = 1/2$.

As mentioned in the introductory part of Sec. 2.1, the spectrum of $\hat{H}_{\text{SYK}}$ has been shown analytically in the large-N limit to be exponentially dense in N throughout the entire spectrum, with its many-body density of states scaling as $\exp(NS_0)$ near the edges of the spectrum [54]. Despite our numeric (exact diagonalisation) constraints to small system sizes, the dense low-energy spectrum of $\hat{H}_{\text{SYK}}$ can already be appreciated away from the large-N limit

---

[1] Note that $\hat{H}_{\text{SYK}}$ as defined here is not particle-hole symmetric, but requires additional correction terms to enforce this [96, 97]. In this thesis, we do not consider these correction terms.

(see also Fig. A.2 for a scaling analysis for $N = 8, 10, 12, 14$), for instance by comparison to the spectrum of an (integrable) random-hopping Hamiltonian [Eq. (2.5) for $q = 2$], for which the low energy many-body density of states is much sparser (scaling as $1/N$ in the large-N limit [54]). As an example, and to give an intuition for the larger density of the low-energy tail of $\hat{H}_{\text{SYK}}$, we give such a comparison in Figure 2.1 which shows a realisation of the spectrum of $\hat{H}_{\text{SYK}}$ (upper vertical lines) and of the random-hopping Hamiltonian (lower vertical lines). Both spectra are for $N = 14$ at half filling, and have been shifted such that the ground-state lies at zero energy. The energies are shown in units of J [the standard deviation of the Gaussian-distributed interaction amplitudes of either Hamiltonian, see Eq. (2.2)], and the energy-axis has been truncated so as to show the lowest 25% of the energy window covered by the $\hat{H}_{\text{SYK}}$ spectrum. The exponentially dense low-energy spectrum of $\hat{H}_{\text{SYK}}$ at $N \gg 1$ prohibits a quasiparticle description [54], and further yields a non-vanishing zero-temperature entropy density $S_0 \equiv \lim_{T\to 0} S(T) > 0$ [55, 57, 98].

To end this sub-section, we note that the SYK model as defined by Eq. (2.1) falls within a broader class of two-body random ensembles and embedded Gaussian unitary matrices, which have long been studied in the context of many-body quantum chaos and nuclear shell models [99]. Several variations of the SYK model have been studied, with some examples being: Brownian SYK models, with time-dependent random couplings $J_{i_1 i_2; j_1 j_2}(t)$ [100]; Generalisations to arbitrary $q/2$-body interactions [for integers $q/2 \geq 1$, see also Eqs. (C.1)–(C.3)] [57, 101], given by,

$$\hat{H}_q = \frac{\sqrt{[(q/2)!(q/2-1)!]/N^{q-1}}}{[(q/2)!]^2} \sum_{\substack{i_1,\ldots,i_{q/2}=1\\ j_1,\ldots,j_{q/2}=1}}^{N} J_{i_1\ldots i_{q/2};j_1\ldots j_{q/2}} \hat{c}^\dagger_{i_1}\ldots\hat{c}^\dagger_{i_{q/2}}\hat{c}_{j_1}\ldots\hat{c}_{j_{q/2}}; \tag{2.5}$$

as well as combinations of various SYK-q Hamiltonians $\hat{H}_q$ [102]. Sparse variants, in which the all-to-all connectivity is broken by randomly removing interactions from $\hat{H}_{\text{SYK}}$, as well as variants with non-Gaussian disorder have been found to retain the fast-scrambling dynamics [103–106]. Coupled SYK models have been proposed in the context of heavy fermions [107], and as holographic duals to wormholes [108, 109].

2.1.2 Spectral probes of quantum chaos

The SYK model, as defined in Eq. (2.1), is quantum chaotic in the sense of the Bohigas–Giannoni–Schmit conjecture [110]. That is, given the energy levels ϵ_n of $\hat{H}_{\text{SYK}}$ (where $n = 1, \ldots, D$, and D is the Hilbert space dimension),

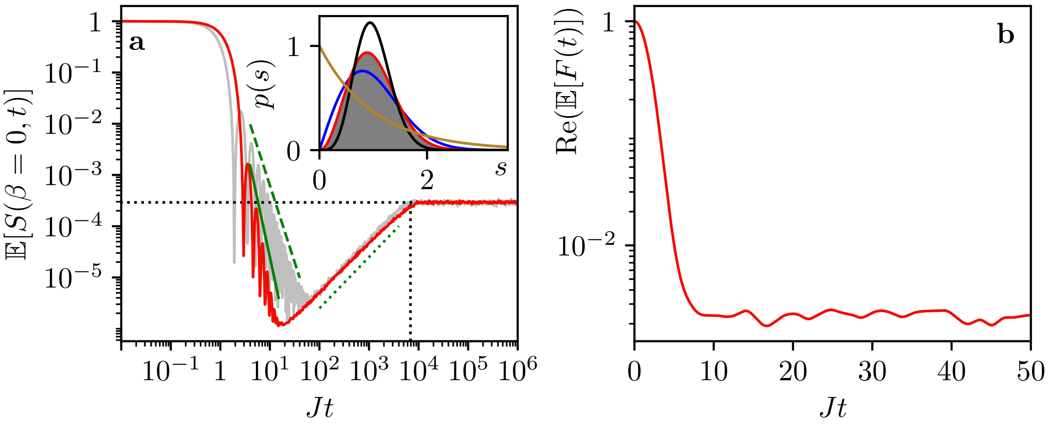

Figure 2.2: Examples of SFF and OTOC for $\hat{H}_{\mathrm{SYK}}$. (a) Long- and short-range spectral correlations of the SYK model (red curve) as probed, respectively, by the SFF (main) and level-spacing distribution (grey histogram, inset). Curves in the inset show the Wigner–Dyson distribution of Eq. (2.6) for $\boldsymbol{\beta} = 1$ (blue), $\boldsymbol{\beta} = 2$ (red), and $\boldsymbol{\beta} = 4$ (black), as well as the exponentially decaying distribution typical of integrable systems (brown). A comparison to the SFF of the GUE ensemble is given in the main panel by the gray curve. Vertical and horizontal black-dotted lines in the main panel indicate, respectively, the RMT predictions for the Heisenberg time $2D$ and the plateau value $1/D$ for $\beta = 0$. Green dashed, solid, and dotted lines indicate power laws t^{-3}, $t^{-4.5}$, and t respectively (see main text for details), and are included to guide the eye. (b) Scrambling in the SYK model, as diagnosed by the OTOC $\mathrm{Re}[F(t)]$ of Eq. (2.13) for $\hat{W} = 2\hat{c}_i^\dagger \hat{c}_i - 1$, $\hat{V} = 2\hat{c}_j^\dagger \hat{c}_j - 1$, with indices $i = 0$ and $j = 1$, at $\beta = 0$. Both panels depict data averaged over an ensemble of 1000 independent realisations of $\hat{H}_{\mathrm{SYK}}$, with $N = 14$ and $N = 10$ for the SFF and OTOC, respectively (both at half-filling). For the GUE SFF data, the matrix dimension was chosen to match the Hilbert space dimension of $\hat{H}_{\mathrm{SYK}}$ for $N = 14$ at half filling, $D = 3432$. For $p(s)$, spectral unfolding has been performed for 1000 independent realisations of $\hat{H}_{\mathrm{SYK}}$ for $N = 14$.

their nearest-neighbour spacings $s_n = \epsilon_{n+1} - \epsilon_n$ for $n = 1, \ldots, D - 1$ follow a probability distribution $p(s)$ which agrees well with the Wigner-surmise for random matrices. In particular, $p(s)$ of $\hat{H}_{\mathrm{SYK}}$ displays level repulsion $p(s = 0) = 0$ [see the inset of Fig. 2.2(a)], an accepted signature of quantum chaotic systems [111].

The BGS conjecture proposes that the quantised form $\hat{H}$ of any classically chaotic system exhibits short-range spectral correlations, captured by $p(s)$, which follow those of random matrix ensembles, consistent with its symmetries [112]. Within this random matrix theory (RMT), $p(s)$ is then given by the

Wigner-surmise (or Wigner–Dyson distribution) [111]

$$p(s) = A_{\boldsymbol{\beta}} s^{\boldsymbol{\beta}} \mathrm{e}^{-B_{\boldsymbol{\beta}} s^2} \tag{2.6}$$

where[2] $\boldsymbol{\beta} \in \{1, 2, 4\}$ parameterises the symmetry of $\hat{H}$, according to the three Gaussian universality classes of RMT: The time-reversal symmetric Gaussian Orthogonal Ensemble ($\boldsymbol{\beta} = 1, A_{\boldsymbol{\beta}} = \pi/2, B_{\boldsymbol{\beta}} = \pi/4$), the Gaussian Unitary Ensemble ($\boldsymbol{\beta} = 2, A_{\boldsymbol{\beta}} = 32/\pi^2, B_{\boldsymbol{\beta}} = 4/\pi$) which breaks time-reversal symmetry, and the Gaussian Symplectic Ensemble [$\boldsymbol{\beta} = 4, A_{\boldsymbol{\beta}} = 2^{18}/(3^6\pi^3), B_{\boldsymbol{\beta}} = 64/(9\pi)$] which additionally breaks a rotational symmetry. The complementary Berry–Tabor conjecture [113] states that for integrable quantum systems, the energy levels will be independent and thus follow a Poissonian distribution, yielding an exponentially decaying level-spacing distribution $p(s) = \mathrm{e}^{-s/\mu}/\mu$ (for mean level-spacing μ). As such, $p(s)$ distinguishes between integrable, versus chaotic ETH obeying Hamiltonians. Unsurprisingly, the SYK Hamiltonian of Eq. (2.1) satisfies the ETH [114].

Note that in analysing the chaotic properties of a Hamiltonian's spectrum, care must be taken to account for all symmetries of the system (see Ref. [111], also for details on the necessary spectral unfolding). This is because energies of different symmetry sectors are essentially independent, and so will cause a spurious level attraction when mixed. For $\hat{H}_{\mathrm{SYK}}$ of Eq. (2.1), the only symmetry is the particle number (or charge) defined in Eq. (2.4), and it is within a given charge sector that $\hat{H}_{\mathrm{SYK}}$ agrees with the distribution of Eq. (2.6). Interestingly, the exact symmetry class of $\hat{H}_{\mathrm{SYK}}$, as determined by $\boldsymbol{\beta}$, depends on the parity of $N (\mathrm{mod}\ 4)$ [97].

Whilst short-range (nearest-neighbour) level repulsion in $p(s)$ is a useful diagnostic of quantum chaos, its dynamic manifestation is, by definition, limited to fluctuations of observables at late-times on the order of $1/s$. To diagnose quantum chaos over a broader range of times, one should study correlations of a Hamiltonian's eigenenergies beyond nearest-neighbours. In particular, quantum chaotic Hamiltonians exhibit spectral rigidity, which arises due to long-range (with respect to the mean level-spacing) level-repulsion competing with the finite spectral bandwidth. A useful tool for studying this spectral rigidity is the spectral form-factor (SFF), where it manifests as an early-time dip-ramp behaviour, the so-called correlation hole [98, 111, 115].

We will work with the following definition of the SFF,

$$S(\beta, t) = \left| \frac{Z(\beta + it)}{Z(\beta)} \right|^2, \tag{2.7}$$

---

[2] We use a boldface $\boldsymbol{\beta}$ for the Wigner–Dyson index to distinguish it from the inverse temperature β.

where $Z(\beta + it) = \mathrm{tr}(\exp(-(\beta + it)\hat{H}))$ is the analytically continued partition function, and the denominator is included for normalisation at $t = 0$. To gain an intuition on $S(\beta, t)$, note that when averaged ($\mathbb{E}[\ldots]$) over an ensemble of disorder realisations of $\hat{H}$ at $\beta = 0$, the numerator of Eq. (2.7) reduces (up to some constants and prefactors) to the Fourier transform of the two-point spectral correlator $\rho^{(2)}(\epsilon_1, \epsilon_2)$ as $\mathbb{E}\big[|Z(\beta + it)|^2\big] \sim \int \mathrm{d}\epsilon_1 \int \mathrm{d}\epsilon_2 \rho^{(2)}(\epsilon_1, \epsilon_2) \exp(i(\epsilon_1 - \epsilon_2)t)$ [98, 115]. The SFF is thus sensitive to pair-wise spectral correlations[3] over the entire spectral bandwidth.

The dynamics of the SYK model's SFF has been found to agree well with the predictions of RMT [98, 112, 114, 117–120], exhibiting three distinct features, as shown in Fig. 2.2(a): For early times, $\mathbb{E}[S(\beta, t)]$ displays oscillations decaying with a power-law envelope. The RMT prediction for the power-law envelope is t^{-3}, which has been shown analytically to be present also in the SFF of the Majorana variant of the SYK model in the large-N limit [98]. In contrast, for the Dirac variant studied in this thesis, numeric evidence—from exact diagonalisation and thus limited to small system sizes—has been found for a $t^{-\alpha}$ decay with $\alpha \approx 4.5$ [114, 121]. This early-time decay is followed at intermediate times $t \sim \mathcal{O}(\sqrt{D})$ by a linear in t ramp, which flattens out into a plateau of height $1/D$ around the Heisenberg time[4] $2D$, where D is the Hilbert-space dimension. The early-time oscillations, most pronounced at infinite temperature $\beta = 0$, are determined by the edges of the density of states [115, 122], and contribute to the disconnected part of Eq. (2.7). The connected part is given by the ramp and plateau, which are, respectively, the dynamic manifestation of long-range and nearest-neighbour level repulsion.

In Chap. 3, we will study the spectral statistics of $\hat{H}_{\text{eff}}$, realised in our proposed cQED simulation of the SYK model. There we will see that the sensitivity of the SFF to correlations throughout the entire many-body spectrum is necessary in order to study how $\hat{H}_{\text{eff}}$ approximates $\hat{H}_{\text{SYK}}$ as a function of experimental control parameters.

2.1.3 Scrambling and OTOCs

Consider a QMB system $\mathcal{S}$ with a large number of degrees of freedom N, prepared in some initial state $|\Psi\rangle$, and subjected at time $t = 0$ to a local[5]

---

[3] Ref. [116] showed that a “partial” SFF, constructed from partition functions of local subregions of the system under study, is furthermore sensitive to eigenstate statistics, and thus able to probe eigenstate thermalisation.

[4] The Heisenberg time is set by the mean level-spacing $\sim 1/D$ [98].

[5] Local in the sense of having a small support, $\mathrm{supp}(V) \ll N$, or being a linear combination of operators with small supports.

perturbation represented by the operator $\hat{V}$. For a chaotic system with Hamiltonian $\hat{H}$ (and assuming $[\hat{H}, \hat{V}] \neq 0$), the unitary evolution given by $\exp(-i\hat{H}t)$ will spread this localised perturbation over $\mathcal{O}(N)$ degrees of freedom, such that it becomes inaccessible to measurements of other local observables $\hat{W}$ at later times $t > 0$. This delocalisation of quantum information over the entire system is referred to as scrambling [123]. By definition, it is state-dependent, and is closely tied to (sub-system) thermalisation and entanglement growth in isolated quantum systems. Indeed, an accepted definition of a scrambled state $|\Psi\rangle$ is one in which the reduced state ρ_A of any subsystem $A \subset \mathcal{S}$ covering less than half the system's degrees of freedom is close to maximally mixed—and thus also the entanglement entropy $S(\rho_A) = -\mathrm{tr}(\rho_A \log(\rho_A))$ is near-maximal [47, 123]. As an example, a state $|\Psi\rangle$ of an N qubit system, is scrambled if $S(\rho_A) \lesssim n_A$ for any subsystem A containing $n_A < N/2$ qubits (here we have used $\log_2$ in the entanglement entropy). This is known as Page scrambling [47, 123]. The stronger notion of Haar scrambling (which implies Page scrambling [124]) defines a state $|\Phi\rangle$ to be scrambled if it has been randomised with respect to the Haar measure, i.e., $|\Phi\rangle = U|\Psi\rangle$ where U is drawn from the unitary group according to the Haar measure, and is thus typically highly non-local [47].

Within this quantum information theoretic picture, scrambling of initially localised quantum information in the time-evolved state $\exp(-i\hat{H}t)|\Psi\rangle$ of a system $\mathcal{S}$ is diagnosed by the decay of the mutual information $I(A:B) = S(\rho_A) + S(\rho_B) - S(\rho_{AB})$ between disjoint local (in the sense that A and B cover $\ll N$ degrees of freedom) subsystems A and B with $\mathcal{S} \setminus (A \cup B) \equiv C \neq \emptyset$, and local Hilbert space dimensions d_A, respectively, d_B: If subsystems A and B are maximally entangled at $t = 0$, then $I(A:B) = 2\min(d_A, d_B)$. This entanglement will propagate to the remainder of the system C under the action of $\exp(-i\hat{H}t)$, causing a decay of $I(A:B)$. The time t_* at which $I(A:B) \approx 0$ is referred to as the scrambling time [43, 49, 92, 123]. Note the importance of the adjective *local*: If either subsystem covers more than $N/2$ degrees of freedom, $I(A:B)$ will remain near its maximum value of $2\min(d_A, d_B)$ [43].

In this thesis we will utilise a closely related, operational diagnostic of scrambling, the out-of-time-order correlators (OTOCs). For two initially commuting operators $\hat{V}$ and $\hat{W}$, the OTOC is typically[6] defined with respect to the thermal ensemble $\hat{\rho}_\beta = \mathrm{e}^{-\beta\hat{H}}/\mathrm{tr}(\mathrm{e}^{-\beta\hat{H}})$ as

$$F(t) = \mathrm{tr}(\hat{\rho}_\beta \hat{W}^\dagger(t) \hat{V}^\dagger \hat{W}(t) \hat{V}), \tag{2.8}$$

where $\hat{W}(t) = \mathrm{e}^{i\hat{H}t}\hat{W}\mathrm{e}^{-i\hat{H}t}$. Correlators of this form appear naturally in lower

---

[6] For a discussion of regularised versus non-regularised OTOCs see, for instance, Refs. [51, 92, 125, 126].

bounds to $I(A:B)$ [43], and so their decay can be taken as a diagnostic of scrambling[7].

Furthermore, OTOCs contribute to the dynamics of squared-commutators as

$$\begin{aligned} C(t) \equiv& \mathrm{tr}(\hat{\rho}_\beta[\hat{W}(t),\hat{V}]^\dagger[\hat{W}(t),\hat{V}]) \qquad (2.9)\\ =& \mathrm{tr}(\hat{\rho}_\beta \hat{W}^\dagger(t)\hat{V}^\dagger\hat{V}\hat{W}(t)) + \mathrm{tr}(\hat{\rho}_\beta\hat{V}^\dagger\hat{W}^\dagger(t)\hat{W}(t)\hat{V})\\ &- 2\mathrm{Re}[F(t)]. \qquad (2.10)\end{aligned}$$

Under the correspondence principle, the commutators $[\hat{W}(t),\hat{V}]$ are related to Poisson brackets in the classical limit. The norm of the latter exhibits an exponential temporal growth $\exp(\lambda t)$ for classical chaotic systems, leading to the classical definition of the Lyapunov exponent λ as quantifying the exponential (phase-space) sensitivity of a chaotic system to perturbations [128]. An exponential growth period of $C(t)$ thus lends itself to the definition of a quantum Lyapunov exponent λ_L.

For initially commuting operators $[\hat{W}(0),\hat{V}] = 0$, $C(0) = 0$. The subsequent dynamics of $C(t)$ for $t > 0$ are governed by two timescales in chaotic systems with a large number of local degrees-of-freedom strongly interacting via few-body couplings (such as the SYK model) [51, 92, 127]: The first is the dissipation time $t_\mathrm{d} \sim \beta$, over which thermal two-point correlators decay as $\exp(-t/t_\mathrm{d})$. For $t < t_\mathrm{d}$, all terms of $C(t)$ factorise as $\mathrm{tr}(\hat{\rho}_\beta\hat{W}\hat{W}^\dagger)\mathrm{tr}(\hat{\rho}_\beta\hat{V}\hat{V}^\dagger) + \mathcal{O}(\mathrm{e}^{-t/t_\mathrm{d}})$, and thus cancel, such that $C(t)$ remains small. Subsequently, for $t_\mathrm{d} < t < t_*$, the OTOC contribution decays exponentially[8] as

$$F(t) \sim \mathrm{tr}(\hat{\rho}_\beta\hat{W}\hat{W}^\dagger)\mathrm{tr}(\hat{\rho}_\beta\hat{V}\hat{V}^\dagger) - \frac{c}{N}\mathrm{e}^{\lambda_\mathrm{L}(t-t_*)}, \qquad (2.11)$$

saturating at the scrambling time t_* (here c is some numerical prefactor), thus causing an equivalent exponential growth and saturation of $C(t)$. For so-called "fast-scramblers", t_* is on the order of $\beta\log(N)$ [47, 92]. In fact, it was shown in Ref. [51], that the rate λ_L of the exponential dynamics of $F(t)$ is subject to

---

[7] Similarly, Ref. [127] identified OTOCs as probes of unitary k-designs (in the above case for $k = 2$), and showed that their operator average is proportional to order $k = 2$ frame potentials. The latter measures the Frobenius distance of a $k = 2$-fold unitary channel from the Haar channel. The decay of OTOCs thus indicates that the dynamics of a given system become indistinguishable from Haar random dynamics, i.e., it indicates Haar scrambling.

[8] In systems with small local Hilbert spaces, such as qubit models, or where the local degrees-of-freedom have an all-to-all (instead of few-body) coupling, the scrambling time t_* is $\mathcal{O}(1)$ in units of the system's natural timescale, and it is no longer possible to identify a well defined exponential decay of $F(t)$ [95].

a universal (independent of the choice of operators $\hat{W}$ and $\hat{V}$) bound

$$\lambda_{\mathrm{L}} \leq \frac{2\pi}{\beta}. \tag{2.12}$$

The SYK model is a fast scrambler, and further saturates this bound in the strong coupling regime $\beta J \gg 1$ (see the review of Ref. [92], and references therein). This fastest possible decay of OTOCs can thus be used to benchmark proposed quantum simulations of the SYK model, and we will make use of this property in Sec. 3.5.

For unitary operators $\hat{W}\hat{W}^\dagger = \mathbb{1}, \hat{V}\hat{V}^\dagger = \mathbb{1}$, the time-ordered contributions of $C(t)$ [first line of Eq. (2.10)] yield a t-independent contribution of 2, such that Eq. (2.10) can be written as

$$\mathrm{Re}[F(t)] = 1 - \frac{C(t)}{2}. \tag{2.13}$$

We will make use of this relation in Sec. 3.5.1 to determine the OTOC from $C(t)$, as the latter is cheaper to calculate numerically, and thus allows one to study larger system sizes. An example for $\hat{H}_{\mathrm{SYK}}$ is shown in Fig. 2.2(b).

Finally, we note the exponential decay of OTOCs should not be conflated with quantum chaos in the sense of the BGS conjecture, since exponentially decaying OTOCs have been found in integrable systems [129], as well non-decaying OTOCs in quantised versions of classically chaotic systems [130] (see also the discussion of Ref. [92]). Rather, the (early time) "scrambling chaos" diagnosed by OTOCs is complementary to the (late time) "spectral chaos" diagnosed by level-spacing distributions and spectral form factors [95].

2.2 Cold atoms & Cavity QED

In this section, we provide a brief account of the study of quantum gases trapped within the mode-volume of an optical Fabry–Pérot resonator. This platform, typically referred to as cavity-QED (cQED), has played host to many exciting developments in the synthesis of bosonic, fermionic, and magnetic QMB Hamiltonians with long-range interactions [22].

Quantum gases on their own, particularly when confined to optical lattices, have become an established platform for the realisation of condensed matter models of strongly-correlated systems, largely due to their versatility in tuning, for instance, dimensionality, geometry, and interaction strength [11, 13]. Integrating quantum gases into optical cavities—electromagnetic cavities whose resonant modes lie in the optical frequency range—further augments physicist's capabilities in the quantum simulation of condensed-matter models with (ultra)cold atomic gases. This is due to the enhanced light–matter interactions in high-quality optical cavities, allowing for the formation of hybridised light–matter states, as well as due to the native ability of cavity photons to mediate long-range interatomic interactions. A striking demonstration of the application of cQED to the quantum simulation of QMB systems, was the observation of superradiance, as predicted by the Dicke model [131], and the concomitant self-organisation transition in a transversely driven Bose–Einstein condensate (BEC), reported in Ref. [132]. As discussed by Mivehvar et al. [22], it was soon realised that the associated ordered phase is a candidate for a *lattice* supersolid, a phase predicted to exist for the long-range Bose–Hubbard model, and for which subsequent cQED experiments provided further evidence [133]. Extensions of this work to crossed cavities, demonstrated the capability to realise also the supersolid phase with *continuous* translational symmetry breaking in cQED [134].

Whilst these pioneering works with ultracold gases in optical cavities were done with BECs (^{87}Rb), very recently the realisation of the strong coupling regime for Fermi gases in high-finesse optical cavities has been achieved using ^{6}Li [72, 73]. These advances have opened the door to experimentally studying the competition of short- and long-range interactions also in fermionic cQED systems [22], which may, for instance, be utilised to experimentally probe the numerically predicted MBL transition of the long-range Fermi–Hubbard model [135], to realise proposals for quantum charge glasses [136], or, as we show in Chap. 3, to realise the fast-scrambling dynamics of the SYK model. In general, the expansion of experimental capabilities in simulating fermionic QMB systems is crucial, as numerical studies of such systems are often hampered by the sign-problem [8, 13].

The derivations presented below will focus on the single cavity-mode regime. However, as we show in Chap. 3, to quantum simulate the SYK model using cQED it is crucial to operate in the multi-mode regime, where the atoms couple to multiple cavity-modes. This regime has been achieved, for example, with BECs in confocal cavities (where transverse cavity-modes form degenerate families according to the parity of the sum of their transverse mode indices) [76], expanding the cQED toolkit to tunable-range interactions [137], compliant optical lattices capable of simulating phonon modes [138], and models of associative memory [139], to name a few. Multi-mode coupling for fermionic quantum gases was achieved in the above work of Ref. [72]. The formal extension of the following derivations to the multi-mode case require one to generalise to a set $\{\hat{a}_m\}$ of cavity-mode operators, where each mode is labelled by a unique index m. As an example, the atom–cavity interactions presented in Eq. (2.14) must then be extended to a sum over all possible interactions of the atom with the various cavity modes $(\sum_m \Omega_m \hat{a}_m g_m(\boldsymbol{r}) + \text{H.c.})(\hat{\sigma}^+ + \hat{\sigma}^-)$. This will be treated further in Sec. 3.2.2.

We begin in Secs. 2.2.1 and 2.2.2 with a brief recapitulation of the canonical scenario of a two-level atom interacting with a single quantised eigenmode of an optical cavity. This serves to introduce the basic formalism, and to discuss the approximations typically made in the treatment of cQED. Then, in Sec. 2.2.3, we generalise to the many-body case of a quantum gas in an optical cavity. We will show in Sec. 2.2.4 how a description in terms of a spin-polarised gas can be achieved in the dispersive regime, and finally, in Sec. 2.2.5, we will show how the virtual exchange of cavity photons between atoms at arbitrary locations generates long-range atom–atom interactions. The formalism of Secs. 2.2.3–2.2.5 will be utilised in Chaps. 3 and 4, and follows in part that of the review by Mivehvar et al. [22], but with some modifications to the notation in order to conform to that used in Chapter 3.

For detailed discussions on the history, capabilities and recent developments in cQED with ultracold gases, we refer the interested reader to the reviews by H. Ritsch, P. Domokos, F. Brennecke and T. Esslinger, "Cold atoms in cavity-generated dynamical optical potentials", Rev. Mod. Phys. **85**, 553–601 (2013) [21], and F. Mivehvar, F. Piazza, T. Donner and H. Ritsch, "Cavity QED with quantum gases: new paradigms in many-body physics", Adv. Phys. **70**, 1–153 (2021) [22]. Here, instead, we will focus on those details necessary for the discussions and derivations of subsequent chapters. For an overview of the related field of cavity quantum materials and micro-cavities, see for instance the review of Schlawin et al. [140].

2.2.1 A single atom in an electromagnetic cavity—The quantum Rabi model

In general, an electromagnetic cavity supports several quantised electromagnetic modes, whose shape and frequency are determined by the boundary conditions as set by the cavity [141]. Let us focus on a single such mode, and denote its frequency and coordinate-space mode-volume, respectively, as ω_c and V_c. Let $\hat{a}^\dagger$ and $\hat{a}$, respectively, denote the operators that create and annihilate a photon in this cavity mode, so that its total energy is given by $\hat{H}_\text{c} = \omega_\text{c}\hat{a}^\dagger\hat{a}$. We will consider a linear optical cavity, as is assumed in Chapter 3, and was employed for the experiment reported on in Chapter 4. For an overview of the different types of optical cavities in use, we refer the reader to Sec. 2.8.1 of Mivehvar et al. [22].

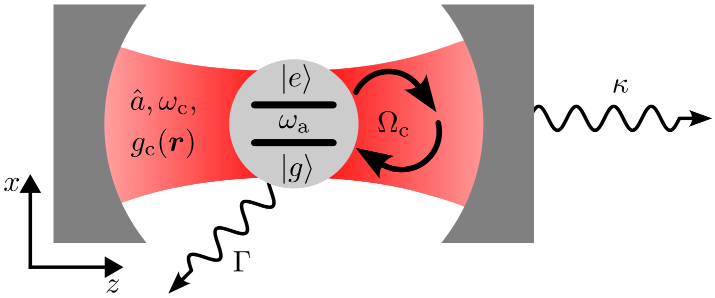

Figure 2.3: Two-level atom in a cavity. Representation of a two-level atom (TLA), composed of a ground $|g\rangle$ and excited $|e\rangle$ state, in a single mode $\hat{a}$ of an optical cavity. Their respective resonance frequencies are ω_a and ω_c. Excitations are exchanged coherently at a rate Ω_c, and can be lost from the TLA via spontaneous emission at a rate Γ, or from the cavity mode at a rate κ. The cavity-mode's profile $g_c(\boldsymbol{r})$ is depicted schematically in red.

Consider now an atom with a single valence electron—such as an alkali atom—that can occupy two states which are separated in energy by an amount ω_a. It is common practice to refer to these states as the ground state $|g\rangle$, and the excited state $|e\rangle$. Taking the ground state's energy as our reference, the energy of this two-level atom (TLA) is given by $\hat{H}_a = \omega_a \hat{\sigma}^+ \hat{\sigma}^-$, where $\hat{\sigma}^+ = (\hat{\sigma}^-)^\dagger = |e\rangle\langle g|$. Suppose now that the TLA is placed at a fixed location $\boldsymbol{r}$ within the mode-volume V_c, such that it can interact with the photons sustained by the cavity mode. This scenario is described by the Hamiltonian

$$\hat{H}_R = \hat{H}_c + \hat{H}_a + \hat{H}_{ac}, \text{ where } \hat{H}_{ac} = \Omega_c(\hat{a} g_c(\boldsymbol{r}) + \hat{a}^\dagger g_c^*(\boldsymbol{r}))(\hat{\sigma}^+ + \hat{\sigma}^-), \quad (2.14)$$

which is known as the quantum Rabi model [142].

The interaction term $\hat{H}_{ac}$ describes the minimal-coupling atom–light interaction in the dipole-approximation (see, for instance, Secs. 5.1, 6.1–6.2 of the book by Scully and Zubairy [141]). Within this approximation, the strength of the atom–cavity interaction is given by the single-photon Rabi frequency $\Omega_c = \sqrt{d^2 \omega_c / (2\epsilon_0 V_c)}$, where d is the atomic dipole moment, and ϵ_0 the vacuum permittivity constant. The dipole approximation is based on the assumption that the variation of the electromagnetic mode over the spatial extent of the TLA is negligible (long-wavelength approximation). This is certainly the case for an atom in an optical cavity, since optical frequencies have wavelengths of several hundred nm, whilst atomic radii, being on the order of the Bohr radius, are on the order of ångström. The function $g_c(\boldsymbol{r})$ is the dimensionless cavity-mode amplitude (profile), which satisfies $\int \mathrm{d}\boldsymbol{r} g_c(\boldsymbol{r}) g_c^*(\boldsymbol{r}) = V_c$.

The above scenario is sketched in Fig. 2.3. There we also depict the possible loss processes, either from the atom via spontaneous emission at a rate Γ, or from the cavity mode via leakage through the cavity mirror at a rate κ. The rate of coherent atom–cavity interactions relative to these loss processes is quantified by the "single-atom cooperativity" $C = \Omega_\mathrm{c}^2/(2\kappa\Gamma)$. This parameter allows one to delineate different physical regimes, depending on the properties of the atomic species (via d and Γ), and of the cavity (via V_c and κ) [140, 143]: Weak coupling refers to the low-cooperativity regime $C \ll 1$, where losses dominate the dynamics $\Omega_\mathrm{c} \ll \kappa, \Gamma$. The strong coupling regime is achieved when $C \gtrsim 1$. Here, the coherent coupling either becomes comparable to both loss processes $\Omega_\mathrm{c} \gtrsim \kappa, \Gamma$, or dominant over one of them (for instance $\Gamma > \Omega_\mathrm{c} \gg \kappa$ as in Chap. 4), allowing for the formation of hybridised light–matter states (cavity polaritons). If $\Omega_\mathrm{c} \lesssim \omega_\mathrm{c}$, one reaches the ultra-strong coupling regime, which is, however, more applicable in the regime of micro-cavities whose mode volumes are significantly smaller (larger Ω_c), and in *circuit*-QED where resonances are on the order of GHz (compared to hundreds of THz for optical cavities). Cavity-QED experiments fundamentally realise driven–dissipative systems, the dynamics of which can be captured in a master equation description, as discussed, for instance, in Sec. II of Ref. [21]. We will continue to focus on the unitary dynamics here, but will return to the role of loss processes in Sec. 4.2.3 and App. A.5.

2.2.2 Rotating-wave approximation—The Jaynes–Cummings model

Within the weak- and strong-coupling regime, the Hamiltonian of Eq. (2.14) can be simplified further by making the rotating-wave approximation (RWA) [144], which entails dropping the operators $\hat{a}^\dagger\hat{\sigma}^+$, $\hat{a}\hat{\sigma}^-$ and their Hermitian conjugates: Within the interaction picture representation of Eq. (2.14)—where $\hat{H}_0 = \hat{H}_\mathrm{c} + \hat{H}_\mathrm{a}$ and $\hat{V} = \hat{H}_\mathrm{ac}$—one has

$$\hat{V}_\mathrm{I}(t) = \Omega_\mathrm{c}\left(\hat{a}^\dagger\hat{\sigma}^+ \mathrm{e}^{i\bar{\omega}t} g_\mathrm{c}^*(\boldsymbol{r}) + \hat{a}^\dagger\hat{\sigma}^- \mathrm{e}^{i\Delta_\mathrm{ca}t} g_\mathrm{c}^*(\boldsymbol{r}) + \mathrm{H.c.}\right), \tag{2.15}$$

where $\bar{\omega} \equiv \omega_\mathrm{c} + \omega_\mathrm{a}$, $\Delta_\mathrm{ca} \equiv \omega_\mathrm{c} - \omega_\mathrm{a}$, and H.c. denotes the Hermitian conjugate. Assuming that ω_c and ω_a are of the same order such that $\omega_\mathrm{c}, \omega_\mathrm{a} \gg \left|\Delta_\mathrm{ca}\right|, \left|\Omega_\mathrm{c}\right|$, the physical intuition is then that the rapidly oscillating terms $\mathrm{e}^{\pm i\bar{\omega}t}$ average out over the dynamics of the remaining processes, which evolve on much slower timescales given by $1/\left|\Delta_\mathrm{ca}\right|$ and $1/\left|\Omega_\mathrm{c}\right|$. More formally (see also Secs. 4.2–4.3 of the book by Gerry and Knight [145]), the time-evolution operator generated in the interaction picture by $\hat{V}_\mathrm{I}(t)$, permits a series expansion in $\Omega_\mathrm{c}/\omega_\mathrm{c}, \Omega_\mathrm{c}/\omega_\mathrm{a}$ and $\Omega_\mathrm{c}/\Delta_\mathrm{da}$. Dropping all orders of $\Omega_\mathrm{c}/\omega_\mathrm{c}, \Omega_\mathrm{c}/\omega_\mathrm{a}$ in line with the above hierarchy of energy-scales then yields a time-evolution operator generated by only the slowly rotating terms $\Omega_\mathrm{c}\left(\hat{a}^\dagger\hat{\sigma}^- \mathrm{e}^{i\Delta_\mathrm{ca}t} g_\mathrm{c}^*(\boldsymbol{r}) + \mathrm{H.c.}\right)$. In the regime of ultra-strong coupling $\Omega_\mathrm{c} \lesssim \omega_\mathrm{c}$, this approximation is, by definition, not valid, and all terms of Eq. (2.15) contribute to the dynamics.

Applying the RWA to Eq. (2.14), we obtain the Hamiltonian for what is known as the Jaynes–Cummings model [146],

$$H_\mathrm{JC} = \omega_\mathrm{c}\hat{a}^\dagger\hat{a} + \omega_\mathrm{a}\hat{\sigma}^+\hat{\sigma}^- + \Omega_\mathrm{c}(\hat{a}\hat{\sigma}^+ g_\mathrm{c}(\boldsymbol{r}) + \mathrm{H.c.}). \tag{2.16}$$

This Hamiltonian conserves the total number of excitations (in contrast to $\hat{H}_\mathrm{R}$, which conserves only the parity of excitations), and is exactly solvable [147].

The many-body extension of H_JC, with $N > 1$ TLAs (or two-level emitters) in a cavity, is known as the Tavis–Cummings (TC) model [148], which we will encounter in Chapter 4. In the many-body case, the single-photon Rabi frequency is enhanced as $\sqrt{N}$ [21], which has allowed for quantum simulation of the ultra-strong coupling regime in optical cavities: The collective enhancement, as well as coupling to motional instead of electronic degrees of freedom, was used in Ref. [132] to quantum simulate the superradiance phase transition of the Dicke model [131], the many-body version of $\hat{H}_\mathrm{R}$.

2.2.3 A quantum gas in an optical cavity

We now generalise the scenario of a single TLA in an optical cavity, as sketched in Fig. 2.3, to the many-body case of an (ultra)cold gas of atoms trapped in an optical cavity.

As before, the Hamiltonian for the QMB system will include the energy of photons in the quantised cavity mode $\hat{H}_\mathrm{c}$, the internal electronic structure of the atoms $\hat{H}_\mathrm{a}$, and the interaction of atoms with the quantised cavity field $\hat{H}_\mathrm{ac}$. In contrast to the treatment of Eqs. (2.14), (2.16), however, we do not assume the atoms to be located at fixed positions in the cavity's mode volume. Rather, we consider the general situation in which the atoms are free to move within the confines of an external trapping potential, and possess an amount of kinetic energy in accordance with their temperature. We will denote this energy of the atoms' motional degrees of freedom by $\hat{H}_\mathrm{kt}$. Further, since the atoms are mobile, they can scatter off of one-another, and we denote the interactions due to this interatomic scattering as $\hat{H}_\mathrm{int}$. Finally, we will denote by $\hat{H}_\mathrm{d}$ a coherent drive field which may couple directly to the electronic levels of the atoms when impinging onto the quantum gas transversely to the cavity axis, or may couple to the cavity mode when the cavity is pumped on-axis. The total many-body Hamiltonian is thus given by

$$\hat{H}_\mathrm{mb} = \hat{H}_\mathrm{c} + \hat{H}_\mathrm{a} + \hat{H}_\mathrm{kt} + \hat{H}_\mathrm{int} + \hat{H}_\mathrm{ac} + \hat{H}_\mathrm{d}, \tag{2.17}$$

and the explicit expressions for each contribution are discussed further below.

Remaining in the TLA approximation, an atom at location $\boldsymbol{r}$ is represented in second-quantised form by the field operators $\hat{\psi}_{\mathrm{s}}(\boldsymbol{r})$ and $\hat{\psi}^{\dagger}_{\mathrm{s}}(\boldsymbol{r})$, which respectively annihilate and create an excitation in the atomic ground ($\mathrm{s} = \mathrm{g}$) or excited state ($\mathrm{s} = \mathrm{e}$). For (fermionic)bosonic atoms, the field operators satisfy the canonical (anti)commutation rules

$$
\begin{aligned}
&[\hat{\psi}_{\mathrm{s}}(\boldsymbol{r}), \hat{\psi}_{\mathrm{s}}(\boldsymbol{r}')]_{\pm} = [\hat{\psi}_{\mathrm{g}}(\boldsymbol{r}), \hat{\psi}_{\mathrm{e}}(\boldsymbol{r}')]_{\pm} = [\hat{\psi}_{\mathrm{g}}(\boldsymbol{r}), \hat{\psi}^{\dagger}_{\mathrm{e}}(\boldsymbol{r}')]_{\pm} = 0, \\
&[\hat{\psi}_{\mathrm{s}}(\boldsymbol{r}), \hat{\psi}^{\dagger}_{\mathrm{s}}(\boldsymbol{r}')]_{\pm} = \delta(\boldsymbol{r} - \boldsymbol{r}'),
\end{aligned}
\tag{2.18}
$$

where, for instance $[\hat{\psi}_{\mathrm{g}}(\boldsymbol{r}), \hat{\psi}^{\dagger}_{\mathrm{e}}(\boldsymbol{r}')]_{\pm} = \hat{\psi}_{\mathrm{g}}(\boldsymbol{r})\hat{\psi}^{\dagger}_{\mathrm{e}}(\boldsymbol{r}') \pm \hat{\psi}^{\dagger}_{\mathrm{e}}(\boldsymbol{r}')\hat{\psi}_{\mathrm{g}}(\boldsymbol{r})$, and the (upper)lower sign is applied when dealing with (fermionic)bosonic field operators. We will follow this convention throughout this thesis, unless stated otherwise.

Within the frame rotating at the drive frequency ω_{d}, the various terms of $\hat{H}_{\mathrm{mb}}$ are given by

$$\hat{H}_{\mathrm{c}} = \Delta_{\mathrm{cd}} \hat{a}^{\dagger}\hat{a}, \tag{2.19}$$

$$\hat{H}_{\mathrm{a}} = -\int \mathrm{d}\boldsymbol{r} \Delta_{\mathrm{da}} \hat{\psi}^{\dagger}_{\mathrm{e}}(\boldsymbol{r})\hat{\psi}_{\mathrm{e}}(\boldsymbol{r}), \tag{2.20}$$

$$\hat{H}_{\mathrm{kt}} = \sum_{\mathrm{s=e,g}} \int \mathrm{d}\boldsymbol{r} \hat{\psi}^{\dagger}_{\mathrm{s}}(\boldsymbol{r}) \left(\frac{-\boldsymbol{\nabla}^2}{2m_{\mathrm{at}}} + V_{\mathrm{t}}(\boldsymbol{r}) \right) \hat{\psi}_{\mathrm{s}}(\boldsymbol{r}), \tag{2.21}$$

$$\hat{H}_{\mathrm{int}} = \sum_{\mathrm{s=e,g}} \frac{1 \mp 1}{4} g_{\mathrm{ss}} \int \mathrm{d}\boldsymbol{r} \hat{\psi}^{\dagger}_{\mathrm{s}}(\boldsymbol{r})\hat{\psi}^{\dagger}_{\mathrm{s}}(\boldsymbol{r})\hat{\psi}_{\mathrm{s}}(\boldsymbol{r})\hat{\psi}_{\mathrm{s}}(\boldsymbol{r}) + g_{\mathrm{eg}} \int \mathrm{d}\boldsymbol{r} \hat{\psi}^{\dagger}_{\mathrm{e}}(\boldsymbol{r})\hat{\psi}^{\dagger}_{\mathrm{g}}(\boldsymbol{r})\hat{\psi}_{\mathrm{g}}(\boldsymbol{r})\hat{\psi}_{\mathrm{e}}(\boldsymbol{r}), \tag{2.22}$$

$$\hat{H}_{\mathrm{ac}} = \frac{1}{2} \int \mathrm{d}\boldsymbol{r} \left(\Omega_{\mathrm{c}} g_{\mathrm{c}}(\boldsymbol{r}) \hat{a} \hat{\psi}^{\dagger}_{\mathrm{e}}(\boldsymbol{r})\hat{\psi}_{\mathrm{g}}(\boldsymbol{r}) + \mathrm{H.c.} \right), \tag{2.23}$$

$$\hat{H}_{\mathrm{d}} = \eta \hat{a}^{\dagger} + \int \mathrm{d}\boldsymbol{r} \Omega_{\mathrm{d}} g_{\mathrm{d}}(\boldsymbol{r}) \hat{\psi}^{\dagger}_{\mathrm{e}}(\boldsymbol{r})\hat{\psi}_{\mathrm{g}}(\boldsymbol{r}) + \mathrm{H.c.}, \tag{2.24}$$

where the parameters and functions are, in order of appearance, the cavity–drive detuning $\Delta_{\mathrm{cd}} \equiv \omega_{\mathrm{c}} - \omega_{\mathrm{d}}$; the drive–atom detuning $\Delta_{\mathrm{da}} \equiv \omega_{\mathrm{d}} - \omega_{\mathrm{a}}$; the Laplace operator $\boldsymbol{\nabla}^2$, the atomic mass m_{at}, and the external trapping potential $V_{\mathrm{t}}(\boldsymbol{r})$; the contact-interaction strengths g_{gg}, g_{ee} and $g_{\mathrm{eg}} = g_{\mathrm{ge}}$; the atom–cavity coupling strength (single-photon Rabi frequency, see Sec. 2.2.1) Ω_{c}, and the dimensionless cavity-mode profile $g_{\mathrm{c}}(\boldsymbol{r})$. The last contribution $\hat{H}_{\mathrm{d}}$ is written in a general form to describe both an on-axis drive coupling to the cavity mode with strength η, and a transverse drive which impinges directly on the atomic cloud. In the latter case, the drive's coupling to the internal states of an atom at location $\boldsymbol{r}$ depends on the drive's Rabi frequency $\Omega_{\mathrm{d}} = d\sqrt{I}$ (where I is the intensity of the drive field), as well as the local drive amplitude $g_{\mathrm{d}}(\boldsymbol{r})$. For the remainder of this Chapter, we will focus on the transverse scenario $\eta = 0$, $\Omega_{\mathrm{d}} \neq 0$, but we will come back to the longitudinal configuration $\eta \neq 0$, $\Omega_{\mathrm{d}} = 0$ in Sec. 3.6.3 and in Chap. 4.

The term $\hat{H}_{\mathrm{int}}$ describes mutual scattering of the atoms. In the ultracold regime, their kinetic energy is so low that interatomic scattering occurs predominantly between atoms occupying the lowest orbital angular momentum states $l = 0$. This so called s-wave scattering is described by the contact-interaction pseudo-potential of $\hat{H}_{\mathrm{int}}$. There, the $\mp$ term reflects the fact that the fundamental anti-symmetry of fermionic wavefunctions prevents s-wave scattering between fermionic atoms occupying the same spin state. Hence, for fermions, only the inter-species scattering g_{eg} contributes to $\hat{H}_{\mathrm{int}}$. For a detailed overview of $\hat{H}_{\mathrm{int}}$, we refer the interested reader to the introductory section of the review by Bloch et al. [11].

We note that, as in Sec. 2.2.1, the atom–light interactions of $\hat{H}_{\mathrm{ac}}$ and $\hat{H}_{\mathrm{d}}$ assume a two-level atom, as well as the validity of the dipole approximation and the RWA.

2.2.4 Dispersive regime

The many-body Hamiltonian $\hat{H}_{\mathrm{mb}}$ presented in the previous section describes a gas of spin-full atoms. Here we will discuss a canonical situation, where the quantum gas is driven in the dispersive regime, in which the effective many-body dynamics can be projected onto the collective ground-state manifold of the atoms. This will be an essential ingredient of our proposal in Chap. 3, which requires effective dynamics of *spinless* fermions.

Within the Heisenberg picture, the cavity and field operators are dynamical degrees of freedom $\hat{a} = \hat{a}(t)$, $\hat{\psi}_{\mathrm{s}}(\boldsymbol{r}) = \hat{\psi}_{\mathrm{s}}(\boldsymbol{r}, t)$, whose time-evolution is governed by $\hat{H}_{\mathrm{mb}}$ [Eqs. (2.17)–(2.24)] as well as loss processes. Following Ref. [22], we focus here on the Hamiltonian evolution. Thus, the operators evolve according to the Heisenberg equation of motion as follows[9] (for notational convenience, we will suppress the time-dependence of the cavity and field operators throughout

---

[9] For the derivation of the kinetic contribution, see App. A.4.

this thesis),

$$\begin{aligned}\frac{\mathrm{d}\hat{a}}{\mathrm{d}t} =& - i\Delta_{\mathrm{cd}}\hat{a} - i\frac{1}{2}\int \mathrm{d}\boldsymbol{r}(\Omega_{\mathrm{c}}g_{\mathrm{c}}(\boldsymbol{r}))^{*}\hat{\psi}^{\dagger}_{\mathrm{g}}(\boldsymbol{r})\hat{\psi}_{\mathrm{e}}(\boldsymbol{r}), \qquad (2.25)\\ \frac{\mathrm{d}\hat{\psi}_{\mathrm{g}}(\boldsymbol{r})}{\mathrm{d}t} =& - i\left(\frac{-\boldsymbol{\nabla}^2}{2m_{\mathrm{at}}} + V_{\mathrm{t}}(\boldsymbol{r}) + \frac{1\mp 1}{2}g_{\mathrm{gg}}\hat{\psi}^{\dagger}_{\mathrm{g}}(\boldsymbol{r})\hat{\psi}_{\mathrm{g}}(\boldsymbol{r}) + g_{\mathrm{eg}}\hat{\psi}^{\dagger}_{\mathrm{e}}(\boldsymbol{r})\hat{\psi}_{\mathrm{e}}(\boldsymbol{r})\right)\hat{\psi}_{\mathrm{g}}(\boldsymbol{r})\\ & - i\hat{\Phi}^{\dagger}(\boldsymbol{r})\hat{\psi}_{\mathrm{e}}(\boldsymbol{r}), \qquad (2.26)\\ \frac{\mathrm{d}\hat{\psi}_{\mathrm{e}}(\boldsymbol{r})}{\mathrm{d}t} =& - i\left(\frac{-\boldsymbol{\nabla}^2}{2m_{\mathrm{at}}} + V_{\mathrm{t}}(\boldsymbol{r}) - \Delta_{\mathrm{da}} + \frac{1\mp 1}{2}g_{\mathrm{ee}}\hat{\psi}^{\dagger}_{\mathrm{e}}(\boldsymbol{r})\hat{\psi}_{\mathrm{e}}(\boldsymbol{r}) + g_{\mathrm{eg}}\hat{\psi}^{\dagger}_{\mathrm{g}}(\boldsymbol{r})\hat{\psi}_{\mathrm{g}}(\boldsymbol{r})\right)\\ & \times\hat{\psi}_{\mathrm{e}}(\boldsymbol{r}) - i\hat{\Phi}(\boldsymbol{r})\hat{\psi}_{\mathrm{g}}(\boldsymbol{r}), \qquad (2.27)\end{aligned}$$

where we have defined $\hat{\Phi}(\boldsymbol{r}) \equiv \Omega_{\mathrm{c}}g_{\mathrm{c}}(\boldsymbol{r})\hat{a}/2 + \Omega_{\mathrm{d}}g_{\mathrm{d}}(\boldsymbol{r})$, similar to Ref. [149].

Consider now the scenario where the drive–atom detuning Δ_{da} is the dominant energy scale in $\hat{H}_{\mathrm{mb}}$. This is known as the dispersive regime, since the drive is far off-resonant with the atomic transition. Consequently, the probability to excite atoms is suppressed, and most atoms remain in their ground state—the so-called low-saturation limit [150]. Then, the field operator for the excited state can be “adiabatically eliminated”, the intuitive picture being that the operators $\hat{\psi}_{\mathrm{e}}(\boldsymbol{r})$ evolve so rapidly that they adapt to the dynamics of the ground state field operators $\hat{\psi}_{\mathrm{g}}(\boldsymbol{r})$ essentially instantaneously. More formally, taking the Laplace transform—defined as $\mathcal{L}[f(t)] \equiv \int_0^\infty \mathrm{d}t e^{-st}f(t)$ for a function $f(t)$ of time t—of Eq. (2.27), expanding to zeroth order in s/Δ_{da}, and taking the inverse Laplace transform, one obtains

$$\hat{\psi}_{\mathrm{e}}(\boldsymbol{r}) = \frac{1}{\Delta_{\mathrm{da}}}\hat{\Phi}(\boldsymbol{r})\hat{\psi}_{\mathrm{g}}(\boldsymbol{r}), \qquad (2.28)$$

which is valid for times $t \gg |\Delta_{\mathrm{da}}|^{-1}$. Here we have assumed, following Refs. [22, 151], that $|\langle\hat{H}_{\mathrm{kt}}\rangle|, |g_{\mathrm{ee}}|, |g_{\mathrm{eg}}| \ll |\Delta_{\mathrm{da}}|$, such that the contributions from $\hat{H}_{\mathrm{kt}}$ and $\hat{H}_{\mathrm{int}}$ can be dropped.

Inserting Eq. (2.28) into the remaining evolution Eqs. (2.25) and (2.26), one obtains effective equations of motion for the time regime $t \gg |\Delta_{\mathrm{da}}|^{-1}$, from which one can deduce the corresponding effective Hamiltonian to be

$$\begin{aligned}\hat{H}_{\mathrm{eff},\mp} =& \hat{H}_{\mathrm{c}} + \hat{H}_{\mathrm{kt}} + \frac{1\mp 1}{2}g_{\mathrm{gg}}\int \mathrm{d}\boldsymbol{r}\hat{\psi}^{\dagger}_{\mathrm{g}}(\boldsymbol{r})\hat{\psi}^{\dagger}_{\mathrm{g}}(\boldsymbol{r})\hat{\psi}_{\mathrm{g}}(\boldsymbol{r})\hat{\psi}_{\mathrm{g}}(\boldsymbol{r})\\ & + \frac{1}{\Delta_{\mathrm{da}}}\int \mathrm{d}\boldsymbol{r}\hat{\Phi}^{\dagger}(\boldsymbol{r})\hat{\Phi}(\boldsymbol{r})\hat{\psi}^{\dagger}_{\mathrm{g}}(\boldsymbol{r})\hat{\psi}_{\mathrm{g}}(\boldsymbol{r}) + \mathcal{O}(\Delta_{\mathrm{da}}^{-2}),\end{aligned} \qquad (2.29)$$

where now $\hat{H}_{\mathrm{kt}} = \int \mathrm{d}\boldsymbol{r}\hat{\psi}^{\dagger}_{\mathrm{g}}(\boldsymbol{r})\left(\frac{-\boldsymbol{\nabla}^2}{2m_{\mathrm{at}}} + V_{\mathrm{t}}(\boldsymbol{r})\right)\hat{\psi}_{\mathrm{g}}(\boldsymbol{r})$.

Expanding the product $\hat{\Phi}^\dagger(\boldsymbol{r})\hat{\Phi}(\boldsymbol{r})$ in the last term of Eq. (2.29), one obtains an atomic-density-dependent dispersive shift of the cavity resonance $\hat{a}^\dagger\hat{a}\int \mathrm{d}\boldsymbol{r}\,|\Omega_\mathrm{c}g_\mathrm{c}(\boldsymbol{r})|^2\,\hat{\psi}_\mathrm{g}^\dagger(\boldsymbol{r})\hat{\psi}_\mathrm{g}(\boldsymbol{r})/(4\Delta_\mathrm{da})$, a dipole potential due to the drive $\int \mathrm{d}\boldsymbol{r}\,|\Omega_\mathrm{d}g_\mathrm{d}(\boldsymbol{r})|^2\,\hat{\psi}_\mathrm{g}^\dagger(\boldsymbol{r})\hat{\psi}_\mathrm{g}(\boldsymbol{r})/\Delta_\mathrm{da}$, as well as an interference[10] term between the cavity and drive fields $\int \mathrm{d}\boldsymbol{r}\Omega_\mathrm{d}g_\mathrm{d}(\boldsymbol{r})(\Omega_\mathrm{c}g_\mathrm{c}(\boldsymbol{r})\hat{a})^\dagger\hat{\psi}_\mathrm{g}^\dagger(\boldsymbol{r})\hat{\psi}_\mathrm{g}(\boldsymbol{r})/(2\Delta_\mathrm{da}) + \mathrm{H.c.}$. The strength of this interference term is given by the two-photon Rabi frequency $\eta_0 = |\Omega_\mathrm{d}\Omega_\mathrm{c}/\Delta_\mathrm{da}|$.

In this thesis, we will focus on cQED with fermionic atoms. Thus, from this point onwards we will work with the effective Hamiltonian (up to and including order $1/\Delta_\mathrm{da}$)

$$\hat{H}_{\mathrm{eff},-} = \hat{H}_\mathrm{c} + \hat{H}_\mathrm{kt} + \frac{1}{\Delta_\mathrm{da}}\int \mathrm{d}\boldsymbol{r}\hat{\Phi}^\dagger(\boldsymbol{r})\hat{\Phi}(\boldsymbol{r})\hat{\psi}^\dagger(\boldsymbol{r})\hat{\psi}(\boldsymbol{r}), \tag{2.30}$$

where, from now on, we will use $\hat{\psi}(\boldsymbol{r}) \equiv \hat{\psi}_\mathrm{g}(\boldsymbol{r})$.

2.2.5 Cavity-mediated long-range interactions

We have seen in Sec. 2.1 that the SYK Hamiltonian of Eq. (2.1) is characterised by all-to-all two-body interactions, with random complex amplitudes, between spinless fermions. In this section we will demonstrate the native ability of the cQED platform to mediate such infinite-range interactions.

Our starting point is the fermionic many-body Hamiltonian $\hat{H}_{\mathrm{eff},-}$, as given by Eq. (2.30). Having adiabatically eliminated the excited state, the spin degree-of-freedom is frozen out, such that the Hamiltonian describes a system of spinless fermions. Long-range interactions between fermion pairs at arbitrary locations $\boldsymbol{r}$ and $\boldsymbol{r}'$, can then be engineered via the virtual exchange of cavity photons. The intuitive picture is that, in the dispersive regime, a drive photon is scattered into the cavity mode by an atom at location $\boldsymbol{r}$. Assuming that also the cavity–atom detuning Δ_ca is large, this cavity photon subsequently scatters from another atom at $\boldsymbol{r}'$ without exciting it. In the strong coupling regime, photons can be scattered repeatedly in this way, before being dissipated, leading to an effective atom–atom interaction.

In the regime of large Δ_ca, the cavity photons can be "integrated out", and one obtains effective interactions of the form $\int \mathrm{d}\boldsymbol{r}\int \mathrm{d}\boldsymbol{r}' D(\boldsymbol{r},\boldsymbol{r}')\hat{\psi}^\dagger(\boldsymbol{r})\hat{\psi}(\boldsymbol{r})\hat{\psi}^\dagger(\boldsymbol{r}')\hat{\psi}(\boldsymbol{r}')$, where $D(\boldsymbol{r},\boldsymbol{r}')$ is a product of cavity and drive mode-functions. To show this

---

[10] In the case of a standing-wave transverse drive with $g_\mathrm{d}(\boldsymbol{r}) \propto \cos(k_\mathrm{d}x)$, it is this interference term which, above a critical drive strength, dynamically forms a chequerboard lattice allowing for the self-organisation transition, discussed in the introductory part of this section, to occur.

formally, one can take various approaches. The photon operators $\hat{a}$ can be adiabatically eliminated on the level of the Heisenberg equations of motion (as in Ref. [22]), similar to the procedure which we followed for $\hat{\psi}_{\mathrm{e}}(\boldsymbol{r})$ in Sec. 2.2.4. As before, this procedure is motivated by a separation of timescales. For $\Delta_{\mathrm{ca}} = \Delta_{\mathrm{da}} + \Delta_{\mathrm{cd}}$ comparable to Δ_{da}, such that it is larger than the remaining energy scales of $\hat{H}_{\mathrm{eff},-}$, $\hat{a}$ evolves on timescales much shorter than the rest of the system, so that its dynamics average out. This can be made explicit also on the Hamiltonian level: Going into the rotating frame generated by $\Delta_{\mathrm{ca}}\hat{a}^\dagger\hat{a}$, the photonic operators explicitly acquire rapidly oscillating phases $\exp(\pm i\Delta_{\mathrm{ca}}t)$, which can then be leveraged to perform an expansion in powers of $1/\Delta_{\mathrm{ca}}$. This high-frequency expansion is known as a Floquet–Magnus expansion [152, 153], and is suitable for time-dependent periodic Hamiltonians.

In anticipation of Chap. 3, we will, instead, use an alternative technique known as the Schrieffer–Wolff transformation (SWT) [154, 155]. The basic idea is that for a Hamiltonian $\hat{H} = \hat{H}_0 + \hat{V}$—where $(\hat{H}_0)\hat{V}$ is the (non)interacting part—, one performs a unitary transformation

$$\mathrm{e}^{\hat{S}}\hat{H}\mathrm{e}^{-\hat{S}} = \hat{H}_0 + \left(\hat{V} + [\hat{S}, \hat{H}_0]\right) + [\hat{S}, \hat{V}] + \frac{1}{2}[\hat{S}, [\hat{S}, \hat{H}_0 + \hat{V}]] + \dots, \tag{2.31}$$

generated by an ant-hermitian operator $\hat{S}$ which is chosen such that $\hat{V} + [\hat{S}, \hat{H}_0] = 0$. In this way, one rotates $\hat{H}$ into a frame where, to lowest order, the interactions described by $\hat{V}$ are removed.

For $\hat{H}_{\mathrm{eff},-}$ as in Eq. (2.30) we have

$$\hat{H}_0 = \hat{H}_{\mathrm{c}} + \hat{H}_{\mathrm{kt}} + \int \mathrm{d}\boldsymbol{r} \frac{|\Omega_{\mathrm{c}} g_{\mathrm{c}}(\boldsymbol{r})|^2}{4\Delta_{\mathrm{da}}} \hat{a}^\dagger\hat{a}\hat{\psi}^\dagger(\boldsymbol{r})\hat{\psi}(\boldsymbol{r}) + \int \mathrm{d}\boldsymbol{r} \frac{|\Omega_{\mathrm{d}} g_{\mathrm{d}}(\boldsymbol{r})|^2}{\Delta_{\mathrm{da}}} \hat{\psi}^\dagger(\boldsymbol{r})\hat{\psi}(\boldsymbol{r}), \tag{2.32}$$

$$\hat{V} = \frac{1}{2\Delta_{\mathrm{da}}} \int \mathrm{d}\boldsymbol{r} (\Omega_{\mathrm{c}} g_{\mathrm{c}}(\boldsymbol{r}))^* \Omega_{\mathrm{d}} g_{\mathrm{d}}(\boldsymbol{r}) \hat{a}^\dagger \hat{\psi}^\dagger(\boldsymbol{r})\hat{\psi}(\boldsymbol{r}) + \mathrm{H.c.}\,. \tag{2.33}$$

The condition $\hat{V} + [\hat{S}, \hat{H}_0] = 0$ is then fulfilled[11] by the generator

$$\hat{S} = \frac{1}{2\Delta_{\mathrm{da}}\Delta_{\mathrm{cd}}} \int \mathrm{d}\boldsymbol{r} \left[(\Omega_{\mathrm{c}} g_{\mathrm{c}}(\boldsymbol{r}))^* \Omega_{\mathrm{d}} g_{\mathrm{d}}(\boldsymbol{r}) \hat{a}^\dagger - \mathrm{H.c.}\right] \hat{\psi}^\dagger(\boldsymbol{r})\hat{\psi}(\boldsymbol{r}). \tag{2.34}$$

---

[11] In evaluating the commutator, we drop a term of relative order $1/(\Delta_{\mathrm{da}}\Delta_{\mathrm{cd}})$, stemming from the third term of $\hat{H}_0$. A similar approach is taken in Ref. [22] when performing the adiabatic elimination on the level of the Heisenberg equations of motion. If $\Omega_{\mathrm{c}} \ll \Omega_{\mathrm{d}}$, one could also already neglect this term in $\hat{H}_0$. Alternatively, one can include the third term of $\hat{H}_0$ in the coupling term V. This adds to $\hat{H}_{\mathrm{eff}}$ terms which are linear in $\hat{a}$ and thus vanish when projecting onto a subspace of constant photon number.

This yields a series expansion for $\mathrm{e}^{\hat{S}}\hat{H}\mathrm{e}^{-\hat{S}}$ in powers of $|\Omega_{\mathrm{c}}\Omega_{\mathrm{d}}/(\Delta_{\mathrm{da}}\Delta_{\mathrm{cd}})|$, which yields, to linear order, the effective Hamiltonian

$$\hat{H}_{\text{eff}} = \hat{H}_0 + \int \mathrm{d}\boldsymbol{r} \int \mathrm{d}\boldsymbol{r}' D(\boldsymbol{r},\boldsymbol{r}')\hat{\psi}^\dagger(\boldsymbol{r})\hat{\psi}(\boldsymbol{r})\hat{\psi}^\dagger(\boldsymbol{r}')\hat{\psi}(\boldsymbol{r}'), \tag{2.35}$$

where $D(\boldsymbol{r},\boldsymbol{r}') = (\Omega_{\mathrm{c}}g_{\mathrm{c}}(\boldsymbol{r}))^*\Omega_{\mathrm{d}}g_{\mathrm{d}}(\boldsymbol{r})\Omega_{\mathrm{c}}g_{\mathrm{c}}(\boldsymbol{r}')(\Omega_{\mathrm{d}}g_{\mathrm{d}}(\boldsymbol{r}'))^*/(4\Delta_{\mathrm{da}}^2\Delta_{\mathrm{cd}})$ describes the fermion–fermion interaction amplitude, with magnitude $\eta_0^2/4\Delta_{\mathrm{cd}}$. Note that the effective two-body interaction of the above equation is separable, in the sense that it can be factorised into a product $\operatorname{sgn}(\Delta_{\mathrm{cd}})\hat{I}\hat{I}^\dagger$, with

$$\hat{I} = \int \mathrm{d}\boldsymbol{r} \frac{\Omega_{\mathrm{d}}g_{\mathrm{d}}(\boldsymbol{r})(\Omega_{\mathrm{c}}g_{\mathrm{c}}(\boldsymbol{r}))^*}{2\Delta_{\mathrm{da}}\sqrt{|\Delta_{\mathrm{cd}}|}}\hat{\psi}^\dagger(\boldsymbol{r})\hat{\psi}(\boldsymbol{r}). \tag{2.36}$$

We will see in Sec. 3.3 that this separability is lifted by including multiple cavity-modes in the calculation. Finally, note that the long-range interactions of Eq. (2.35) need not be uniformly all-to-all: The interaction amplitude between a pair of atoms at locations $\boldsymbol{r}$ and $\boldsymbol{r}'$ depends on the overlap of their mode function with that of the cavity mode, as is evident from Eqs. (2.35) and (2.36). If an atom is localised at a node of $g_{\mathrm{c}}(\boldsymbol{r})$, it will interact only negligibly, as compared to atoms located at antinodes of $g_{\mathrm{c}}(\boldsymbol{r})$. We will see in Chap. 4 how position-independent (uniform) long-range interactions can be generated by trapping atoms at positions commensurate with the antinodes (along the cavity axis) of $g_{\mathrm{c}}(\boldsymbol{r})$.

3 A cavity quantum electrodynamics implementation of the Sachdev–Ye–Kitaev model

This chapter is based on the manuscript P. Uhrich, S. Bandyopadhyay, N. Sauerwein, J. Sonner, J.-P. Brantut and P. Hauke, “A cavity quantum electrodynamics implementation of the Sachdev–Ye–Kitaev model”, arXiv:2303.11343 [quant-ph] (2023) [80]. As such, most of the derivations and discussion presented in this chapter are adapted from there, with some additional unpublished results included. My main contributions to this work include the derivation of the effective model $\hat{H}_{\text{eff}}$, the numeric calculation of its interaction amplitudes $\mathcal{J}_{i_1 i_2; j_1 j_2}$, and the analysis of the effective model’s dynamics as a function of the control parameters $\widetilde{\delta\omega}$ and ζ. These are discussed in Secs. 3.2–3.5. I further performed the supplementary calculations reported in App. A, as well as for the alternative on-axis drive configuration discussed in the outlook Sec. 3.6.3.

In this chapter, we present the details of Ref. [80], in which we propose an experimentally feasible quantum simulation of the Sachdev–Ye–Kitaev (SYK) model, leveraging on recent advances in cavity quantum electrodynamics (cQED) architectures. This platform natively realises long-range all-to-all interactions, mediated by the virtual exchange of cavity photons [22] (see also the derivations of the introductory Sec. 2.2.5). This capability has been used in proposals for the study of, for instance, glassy physics [136, 156, 157]. More recently, it has been used to implement hyperbolic interaction geometries, relevant to the study of holographic quantum matter[158]. Furthermore, controlled disorder in the light-matter coupling [77, 159] (as discussed further in Chap. 4), as well as the strong-coupling regime for quantum degenerate Fermi gases [72, 73], are now available in the cQED framework.

Here we will see that this combination, together with the multimode nature of optical cavities, allows for the realisation of the long-range, all-to-all and random SYK interaction in existing state-of-the-art experimental systems with up to hundreds of particles. Starting from a complete model of trapped Fermions in a high-finesse cavity in Sec. 3.2, we identify in Sec. 3.3 two key physical parameters allowing for the dynamics of the effective model to replicate that of the SYK model:

(i) The effective number of modes participating in the light-matter interactions, parameterised by $\widetilde{\delta\omega} \equiv \delta\omega/\Delta_{\mathrm{cd}}$—the frequency spacing $\delta\omega$ of the cavity modes, relative to the drive–cavity detuning Δ_{cd}—which can be varied so as to tune the effective model into the chaotic regime [74, 75].

(ii) The transverse size $\zeta \equiv x_0/(w_0/\sqrt{2})$ of the atomic cloud—given by the harmonic length of the dipole trap x_0, relative to the cavity mode waist w_0—controlling the mechanical coupling between atoms and cavity photons.

In Sec. 3.4, we numerically calculate the interaction amplitudes of the effective model over a broad, experimentally available, range of these parameters. There, we uncover a feature common to existing proposals [63, 65], which was, however, not reported on; namely that the statistical distribution of the interaction amplitudes is not Gaussian, but interpolates between a Gaussian and a Cauchy distribution. Despite this deviation from the original SYK prescription, the dynamics generated by these interaction show good agreement with those of the ideal SYK model, as we demonstrate for the effective model in Sec. 3.5, and for the variant of the ideal model with Cauchy-distributed interactions in App. A.6. In particular, we numerically exactly simulate out-of-time-order correlators and the spectral form factor of the effective model over a range of system parameters, showing that both quantities approach their SYK counterparts as the effective number of cavity modes is increased by varying $\widetilde{\delta\omega}$.

3.1 Target model

Our target is the SYK model whose Hamiltonian $\hat{H}_{\mathrm{SYK}}$ was defined in the introductory Sec. 2.1.1. For convenience, we briefly recapitulate its properties here: The Hamiltonian,

$$\hat{H}_{\mathrm{SYK}} = \frac{1}{(2N)^{3/2}} \sum_{i_1,i_2,j_1,j_2=1}^{N} J_{i_1 i_2; j_1 j_2} \hat{c}^{\dagger}_{i_1} \hat{c}^{\dagger}_{i_2} \hat{c}_{j_1} \hat{c}_{j_2}, \tag{3.1}$$

describes complex two-body interactions among N spinless Dirac fermions [55]. The interaction amplitudes $J_{i_1 i_2; j_1 j_2} = J^{*}_{j_1 j_2; i_1 i_2}$ are complex random variables, with real and imaginary parts sampled independently and identically from normal distributions with zero mean, and variances parameterised by the interaction strength $J \geq 0$, as defined in Eq. (2.2). The interactions are all-to-all, rendering the model fully connected and zero-dimensional, as shown schematically in Fig. 2.1.

Realizing these all-to-all interactions in a random and uncorrelated way is a formidable experimental challenge. In spite of its connections with strange metals in condensed-matter physics [54], no natural material is known that can microscopically realise the particular SYK interaction. The search has therefore focused on artificial systems in solid-state mesoscopic systems [61–63, 160], cold atoms in optical lattices [64, 65], or on direct digital quantum simulation [66, 67]. The work of Ref. [63], for instance, suggests to make use of electronic states in the lowest Landau level of graphene flakes, immersed in an external magnetic field, whose irregular boundaries randomise the spatial profiles of the fermionic modes. Together with the native Coulomb repulsion, this yields long-range, random interactions, as required for the complex(Dirac) fermion version of the SYK model. In Ref. [62], it is suggested that the Majorana SYK model could be realised by coupling N superconducting wires hosting Majorana zero-modes to a two-dimensional quantum dot. The idea is that the Majorana edge-states delocalise over the quantum dot, whose intrinsic disorder then randomises the all-to-all interactions resulting from the spatial overlap of the Majorana modes within the dot. A disadvantage of such solid-state schemes is that the disorder is intrinsic to the system, and can thus not be tuned and is not reproducible between different set-ups. The optical-lattice proposal of Ref. [65] addresses this issue, by suggesting to utilise spinless itinerant fermions in an optical Kagome lattice to engineer all-to-all interactions amongst momentum states forming a flat band. The disorder is introduced via local impurity potentials, distributed randomly over the lattice sites and with tunable strength. The proposal of Ref. [64] instead considers fermionic atoms localised in deep optical lattices, where each potential well can host N localised atomic states. The idea in this case is that these can interact virtually via molecular states, through a photo-association process. A practical limitation here is that simulating a system of N SYK modes would require $N(N-1)/2$ photo-association lasers. Small-scale, minimal versions of the digital approach have been reported using nuclear magnetic resonance [68] and superconducting qubits [69]. However, the $[N(N-1)/2]^2$ scaling of the number of independent couplings and their infinite range nature represents a formidable challenge for such bottom-up approaches. Sparse variants of the SYK model, where the number of couplings is reduced, and the conditions under which they retain the chaotic and holographic properties of the original model have been studied theoretically in for instance Refs. [104–106, 161]. Within this context, the experiment of Ref. [69] above, performed a digital

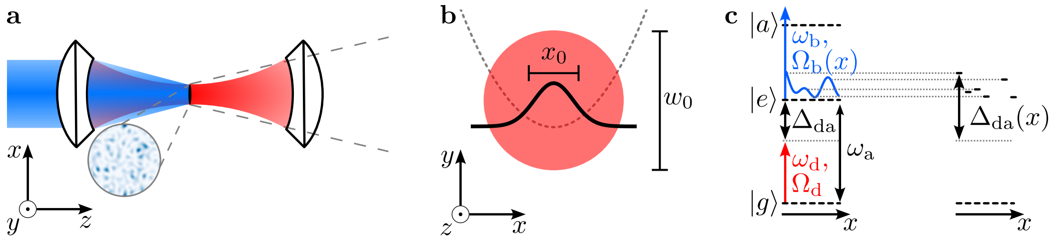

Figure 3.1: Cavity-QED setup and atomic level structure. (a) A quasi-two-dimensional cloud of fermionic atoms (black ellipse) is trapped at an antinode of a longitudinal mode (red) of a multi-mode optical cavity. A random phase-mask is imprinted on a light-shift beam (blue) which is focused into the atomic cloud via a lens attached to the cavity mirror, and thus creates a disordered intensity distribution (speckle, lower circle). (b) Cross section, transverse to cavity axis, showing lowest cavity mode (red circle) with waist w_0. Together with the zero-point fluctuation $x_0 = 1/\sqrt{m_\mathrm{at}\omega_\mathrm{t}}$ of the harmonic trapping potential $V_\mathrm{t}(\boldsymbol{r}) = m_\mathrm{at}\omega_\mathrm{t}^2/\boldsymbol{r}^2$ (grey-dotted curve), this determines the relative transverse size $\zeta = x_0/(w_0/\sqrt{2})$ of the atomic cloud. (c) The required atomic level structure (left) consists of a ground $|g\rangle$, excited $|e\rangle$, and auxiliary $|a\rangle$ electronic state for an atom at position x (horizontal black arrow). The drive beam (red arrow) is far red detuned by $|\Delta_\mathrm{da}|$ from the g–e transition at frequency ω_a, allowing for adiabatic elimination of state $|e\rangle$. The light-shift beam (blue), with speckled intensity $\Omega_\mathrm{b}(x)$, off-resonantly couples states $|a\rangle$ and $|e\rangle$, thereby inducing a position-dependent AC-Stark shift of the excited state energy (right).

quantum simulation a highly sparsified Majorana SYK model, whose reduced connectivity graph was identified by training a machine-learning algorithm to reproduce the dynamics of selected correlators. Especially the gravitational interpretations of this experiment are, however, vigorously debated as they appear to only partially retain the SYK physics [70, 71]. The experimental realisation of the SYK model, specifically in the large-N limit, thus remains an exciting challenge.

3.2 Experimental approach for cQED

We describe the general approach in what follows, and defer specific experimental numbers, in particular for the platform using ^{6}Li atoms of Ref. [77], upon which we report in Chap. 4, to the discussion of Sec. 3.6.1.

The envisaged cQED setup is sketched in Fig. 3.1(a). It consists of a Fermi gas trapped in a two-dimensional (pancake) geometry at the antinode of a longitudinal cavity mode, of a linear optical cavity. This can be achieved, for instance, with an intra-cavity standing-wave optical dipole trap, such as that used in Ref. [77]. We consider the trapping potential $V_{\mathrm{t}}(\boldsymbol{r})$ to be harmonic, as sketched in Fig. 3.1(b), and use the motional eigenstates in the xy-plane to represent the modes of $\hat{H}_{\mathrm{SYK}}$. The mechanical coupling between an atom and a cavity photon is parameterised by the ratio $\zeta \equiv x_0/(w_0/\sqrt{2})$, where x_0 is the oscillator length associated to $V_{\mathrm{t}}(\boldsymbol{r})$, and w_0 is the waist of the fundamental cavity mode.

A pump laser, with Rabi(angular) frequency $\Omega_{\mathrm{d}}(\omega_{\mathrm{d}})$ drives a transition between a ground, $|g\rangle$, and excited, $|e\rangle$, electronic level, see Fig. 3.1(c, left), either from the side or along the cavity axis. We denote the associated transition frequency as ω_{a}, and the detuning of the drive therefrom as $\Delta_{\mathrm{da}} \equiv \omega_{\mathrm{d}} - \omega_{\mathrm{a}}$. For sufficiently large $|\Delta_{\mathrm{da}}|$, the excited state can be adiabatically eliminated, such that the N atoms encode N complex, spinless fermions. The relevant derivation will be presented in Sec. 3.3.2, which generalises the calculation of the introductory Sec. 2.2.4 to the multi-mode scenario. We make a long-wavelength approximation for the amplitude of the drive beam $g_{\mathrm{d}}(\boldsymbol{r}) = 1$ over the spatial extent of the atomic cloud, which supposes either on-axis pumping or a very-low angle from the side (we will discuss these alternatives in the outlook of Sec. 3.6.3). Simulations illustrating the qualitative differences for drive amplitudes with non-uniform phases are reported in Fig. A.7.

3.2.1 Spatially disordered light shift

We have seen in Sec. 2.2.5 that the above cQED setup naturally mediates long-ranged fermion–fermion interactions $\mathcal{J}_{i_1 i_2; j_1 j_2}$ via the virtual exchange of photons between atoms at arbitrary positions $\boldsymbol{r}$ within the pancake, yielding a fully connected, zero dimensional geometry. Approaching the SYK model of Eq. (3.1) requires to render these interactions random and independent between different fermion mode four-tuples (i_1, i_2, j_1, j_2).

To randomise the two-body interaction amplitudes $\mathcal{J}_{i_1 i_2; j_1 j_2}$, we propose to dress the excited state $|e\rangle$ with light near-resonant with a transition to a higher excited state, as sketched in the right half of Fig. 3.1(c). Using a random intensity distribution such as a speckle pattern [lower circle of Fig. 3.1(a)] for the dressing produces a random light shift, proportional to the local intensity: Consider the scenario where a light-shifting beam with Rabi frequency $\Omega_{\mathrm{b}}(\boldsymbol{r})$ is off-resonant with the e–a transition by an amount $|\Delta_{\mathrm{b}}|$. The excited-state is then shifted in energy[1] (AC-Stark shift) by an amount $|\Omega_{\mathrm{b}}(\boldsymbol{r})|^2/(4\Delta_{\mathrm{b}})$, where

---

[1] An explicit calculation is given in App. A.1.

$\Delta_{\mathrm{b}} > 0$ for blue detuning, and $\Delta_{\mathrm{b}} < 0$ for red detuning,

$$\begin{aligned}\Delta_{\mathrm{da}}(\boldsymbol{r}) \equiv& \omega_{\mathrm{d}} - \omega_{\mathrm{a}}(\boldsymbol{r}) \\ =& (\omega_{\mathrm{d}} - \omega_{\mathrm{a}}) - \frac{|\Omega_{\mathrm{b}}(\boldsymbol{r})|^2}{4\Delta_{\mathrm{b}}} = \begin{cases} -\left(|\Delta_{\mathrm{da}}| + \frac{|\Omega_{\mathrm{b}}(\boldsymbol{r})|^2}{4|\Delta_{\mathrm{b}}|}\right) & \text{for } \Delta_{\mathrm{b}} > 0, \\ -\left(|\Delta_{\mathrm{da}}| - \frac{|\Omega_{\mathrm{b}}(\boldsymbol{r})|^2}{4|\Delta_{\mathrm{b}}|}\right) & \text{for } \Delta_{\mathrm{b}} < 0. \end{cases}\end{aligned} \tag{3.2}$$

Here we have used that $\Delta_{\mathrm{da}} < 0$, i.e. that the drive frequency ω_{d} is red detuned from the ground-to-excited state transition. We choose the light-shifting beam to be blue detuned, such that the light shift increases the magnitude of $\Delta_{\mathrm{da}}(\boldsymbol{r})$. The above shows that a spatial disorder of $\Delta_{\mathrm{da}}(\boldsymbol{r})$ can be engineered via a spatial disorder of the light-shifting beam's intensity $I_{\mathrm{b}}(\boldsymbol{r}) \propto |\Omega_{\mathrm{b}}(\boldsymbol{r})|^2$. We will see below that this translates into an effective model with random two-body interactions $\mathcal{J}_{i_1 i_2; j_1 j_2}$ by randomising the spatial integral of Eq. (3.24).

To produce such a random intensity distribution, we propose to utilise an optical speckle (see for instance Ref. [162] or the thesis [163]). This can, for instance, be achieved by letting the beam pass through a diffuser or, in a more reproducible manner, by utilizing a spatial-light-modulator, and then focusing the beam into the atomic cloud with a lens [77]. The speckle pattern is characterised by grains of high intensity, randomly distributed in space, whose correlation length across the lens' focal plane is set by the wavelength of the light-shift beam, and the numerical aperture of the lens (Rayleigh criterium). The distribution of the light intensity I of the speckle pattern follows an exponential probability distribution $P(I) = \exp(-I/\langle I\rangle)/\langle I\rangle$ with $\langle I\rangle$ being the mean intensity (proportional to that of the light-shift beam) and a measure of the strength of the disorder. Tuning the laser's intensity thus allows one to tune between weak and strong disorder.

3.2.2 Multimode cQED and microscopic Hamiltonian

Within the single-mode regime of cQED, the above scheme only leads to a separable (low-rank) SYK-type model, where the effective interactions $\mathcal{J}_{i_1 i_2; j_1 j_2}$ factorise, as was discussed in the context of Eq. (2.36). Intuitively, this yields a product of two correlated SYK-$q = 2$ Hamiltonians [see Eq. (2.5)]. It was shown in Ref. [75] that coupling to a number of modes which is (super)extensive in the system size N reduces these correlations and allows for the manifestation of SYK physics, such as maximal scrambling. As we show in the next sections, the multimode structure of optical Fabry–Pérot cavities can be exploited to achieve this (examples of multimode cQED experiments were given in the introductory part of Sec. 2.2), even in cases where the cavity modes are not exactly degenerate [137].

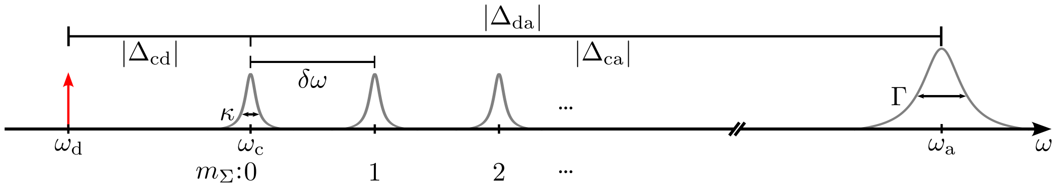

Figure 3.2: Frequency-space sketch of degenerate mode-families relative to the atomic resonance. Location in frequency space (horizontal axis, not to scale) of the atomic (ω_{a}) and cavity resonance (ω_{c}), with respective line-widths Γ and κ. The multi-mode cavity has mode-families, labelled by m_Σ, at intervals $m_\Sigma \delta\omega$ above the fundamental cavity resonance (ω_{c}). The drive beam (red arrow) is red-detuned by $|\Delta_{\mathrm{cd}}|$ from the fundamental cavity mode, which is in turn red-detuned from the atomic resonance by $|\Delta_{\mathrm{ca}}|$. The drive–atom detuning Δ_{da} is thus of magnitude $|\Delta_{\mathrm{da}}| = |\Delta_{\mathrm{ca}}| + |\Delta_{\mathrm{cd}}|$.

Concretely, we will consider multiple transverse cavity modes (TCMs), whose amplitudes $g_m(\boldsymbol{r})$ over the plane of the atomic cloud are given by two-dimensional Hermite–Gauss modes [22]. These are labelled by integer transverse-mode indices $n_x, n_y \geq 0$, and have frequency $\omega_{\mathrm{c}} + (n_x + n_y)\delta\omega$, where ω_{c} is the frequency of the lowest cavity mode, and $\delta\omega$ is the transverse-mode spacing[2]. We use Cantor's pairing function[3] to assign a unique integer label $m \geq 0$ to each TCM,

$$m = \mathrm{CP}(n_x, n_y) \equiv (n_x + n_y)(n_x + n_y + 1)/2 + n_y. \tag{3.3}$$

Introducing the notation

$$m_\Sigma \equiv n_x + n_y, \tag{3.4}$$

we write the frequencies of the TCMs as

$$\omega_m = \omega_{\mathrm{c}} + m_\Sigma \delta\omega. \tag{3.5}$$

---

[2] Note that the exact frequency arrangement of the transverse modes depends on the configuration of the linear cavity, for example whether it is a planar, confocal or concentric cavity [22]. The above assumption, that modes appear in families defined by the sum of their transverse mode indices, is taken for convenience, and the subsequent derivations can be adapted for a given cavity by adapting the definition of index m to possibly include the longitudinal mode-index, and adapting the expressions for the mode-frequencies and mode-profiles accordingly.

[3] Note that Cantor's pairing function is invertible [164]: Given an integer $m \geq 0$, let $\alpha = (-1 + \sqrt{1 + 8m})/2$. Then, the integers $n_x, n_y \geq 0$ which satisfy $m = \mathrm{CP}(n_x, n_y)$ are given by $n_y = m - \lfloor \alpha \rfloor (\lfloor \alpha \rfloor + 1)/2$ and $n_x = \lfloor \alpha \rfloor - n_y$, where $\lfloor \alpha \rfloor$ is the largest integer smaller or equal to α, i.e., $\lfloor \dots \rfloor$ denotes the floor function.

The TCMs are thus arranged in degenerate families, labelled as $m_\Sigma = 0, 1, 2, \ldots$, situated at frequency $\omega_\mathrm{c} + m_\Sigma \delta\omega$ and of degeneracy $m_\Sigma + 1$, see also Fig. 3.2.

Incorporating this multimode structure, the many-body Hamiltonian for the setup described in the previous section, is given by,

$$\hat{H}_\mathrm{mb}(t) = \hat{H}_\mathrm{c} + \hat{H}_\mathrm{a} + \hat{H}_\mathrm{kt} + \hat{H}_\mathrm{ac} + \hat{H}_\mathrm{ad}(t)\,. \tag{3.6}$$

As in Sec. 2.2.3, $\hat{H}_\mathrm{kt}$ governs the dynamics of the atomic centre-of-mass (external) degrees of freedom, subject to the harmonic trapping potential $V_\mathrm{t}(\boldsymbol{r})$ discussed above. In contrast to Eq. (2.17), in Eq. (3.6) we have already neglected the contact interaction term $\hat{H}_\mathrm{int}$, since we will eliminate the excited state in Sec. 3.3.2 below[4]. The remaining terms are similar to those of Eqs. (2.17)–(2.24), but generalised to the multi-mode case, and with the spatial integrals $\int \mathrm{d}\boldsymbol{r}$ running over the plane of the atomic cloud,

$$\hat{H}_\mathrm{c} = \sum_m \omega_m \hat{a}_m^\dagger \hat{a}_m, \tag{3.7}$$

$$\hat{H}_\mathrm{a} = \int \mathrm{d}\boldsymbol{r} \omega_\mathrm{a}(\boldsymbol{r}) \hat{\psi}_\mathrm{e}^\dagger(\boldsymbol{r}) \hat{\psi}_\mathrm{e}(\boldsymbol{r}), \tag{3.8}$$

$$\hat{H}_\mathrm{ac} = \frac{1}{2} \sum_m \int \mathrm{d}\boldsymbol{r} \left(\Omega_m g_m(\boldsymbol{r}) \hat{a}_m \hat{\psi}_\mathrm{e}^\dagger(\boldsymbol{r}) \hat{\psi}_\mathrm{g}(\boldsymbol{r}) + \mathrm{H.c.} \right), \tag{3.9}$$

$$\hat{H}_\mathrm{ad}(t) = \Omega_\mathrm{d} \int \mathrm{d}\boldsymbol{r} \left(g_\mathrm{d}(\boldsymbol{r}) \mathrm{e}^{-i\omega_\mathrm{d} t} \hat{\psi}_\mathrm{e}^\dagger(\boldsymbol{r}) \hat{\psi}_\mathrm{g}(\boldsymbol{r}) + \mathrm{H.c.} \right). \tag{3.10}$$

We have incorporated the random spatial modulation of the atomic resonance in the second line. We will see in the subsequent sections that this spatial disorder propagates into the two-body interactions of our effective model, thereby randomizing them. The summations $\sum_m$ run over the set of resonator modes of the multi-mode cavity, at angular frequencies ω_m as defined in Eq. (3.5). The corresponding photonic creation and annihilation operators are, respectively, $\hat{a}_m^\dagger$ and $\hat{a}_m$. The dimensionless mode-profiles are denoted by $g_m(\boldsymbol{r})$, and the coupling-rate of the atoms to the mth mode is given by the corresponding single-photon Rabi frequency Ω_m.

For the atom–drive interaction $\hat{H}_\mathrm{ad}(t)$ in Eq. (3.10), we have assumed that the drive beam, of amplitude $g_\mathrm{d}(\boldsymbol{r})$, propagates transverse to the cavity(z)-axis, and directly interacts with the fermionic atoms [comparing to Eq. (2.24), $\eta = 0$ and $\Omega_\mathrm{d} \neq 0$]. The long wavelength approximation—utilised in the numeric

---

[4] The resulting Hamiltonian is similar to that of Eq. (2.29), where Pauli's exclusion principle prevents s-wave scattering between spin-polarised fermions. See also Ref. [165], for instance.

calculations presented below in Secs. 3.4–3.5—may thus not be valid, depending on the transverse size ζ of the atomic cloud [see also the sketch of Fig. 3.1(b)]. In such a case one may consider reducing the angle between the drive's wave-vector and the cavity axis, in order to increase the effective (projected) wavelength over the cloud. This scenario is captured by the subsequent derivations, as it simply amounts to modifying $g_{\mathrm{d}}(\boldsymbol{r})$. However, this approach is limited by the cavity geometry, which may prohibit a sufficient enhancement of the effective wavelength. As an alternative, one may consider an on-axis drive [$\eta \neq 0$, $\Omega_{\mathrm{d}} = 0$, in Eq. (2.24)], for which the derivation proceeds analogously to the transverse case, and is summarised in the outlook Sec. 3.6.3 below.

With the above, we have all the ingredients necessary to derive an effective Hamiltonian $\hat{H}_{\mathrm{eff}}$ describing SYK-type physics, as we now show.

3.3 Derivation of the effective Hamiltonian

Here, we present the details for the derivation of the effective Hamiltonian whose SYK physics we investigate numerically in Secs. 3.4–3.5.

Motivated by a discussion of the hierarchy of energy scales present in Eq. (3.12) below, we will adiabatically eliminate the excited atomic state, and subsequently perform a Schrieffer–Wolff transformation to arrive at $\hat{H}_{\mathrm{eff}}$ in Eqs. (3.21)–(3.23). For convenience, we will drop the contribution of the motional degrees-of-freedom $\hat{H}_{\mathrm{kt}}$, as they pass through the various transformations unaffected, and can thus be re-introduced at the end of the derivation of $\hat{H}_{\mathrm{eff}}$. The interested reader may refer to App. A.4, where this is shown explicitly.

We start by going into a frame rotating at the drive's angular frequency ω_{d}, generated by

$$\hat{H}_{\mathrm{RF}} = \omega_{\mathrm{d}} \int \mathrm{d}\boldsymbol{r} \hat{\psi}_{\mathrm{e}}^{\dagger}(\boldsymbol{r}) \hat{\psi}_{\mathrm{e}}(\boldsymbol{r}) + \omega_{\mathrm{d}} \sum_{m} \hat{a}_{m}^{\dagger} \hat{a}_{m}, \tag{3.11}$$

so that the Hamiltonian of Eq. (3.6) becomes time-independent,

$$\begin{aligned} \hat{H}_{\mathrm{mb}} = & \sum_{m} \Delta_{m} \hat{a}_{m}^{\dagger} \hat{a}_{m} - \int \mathrm{d}\boldsymbol{r} \Delta_{\mathrm{da}}(\boldsymbol{r}) \hat{\psi}_{\mathrm{e}}^{\dagger}(\boldsymbol{r}) \hat{\psi}_{\mathrm{e}}(\boldsymbol{r}) \\ & + \int \mathrm{d}\boldsymbol{r} \left(\hat{\Phi}(\boldsymbol{r}) \hat{\psi}_{\mathrm{e}}^{\dagger}(\boldsymbol{r}) \hat{\psi}_{\mathrm{g}}(\boldsymbol{r}) + \mathrm{H.c.} \right). \end{aligned} \tag{3.12}$$

where

$$\hat{\Phi}(\boldsymbol{r}) = \Omega_{\mathrm{d}} g_{\mathrm{d}}(\boldsymbol{r}) + \frac{1}{2} \sum_{m} \Omega_{m} g_{m}(\boldsymbol{r}) \hat{a}_{m}. \tag{3.13}$$

Here, $\Delta_{\mathrm{da}}(\boldsymbol{r}) \equiv \omega_{\mathrm{d}} - \omega_{\mathrm{a}}(\boldsymbol{r})$ denotes the drive's detuning from the disordered atomic resonance $\omega_{\mathrm{a}}(\boldsymbol{r})$, and the cavity-drive detunings are denoted as $\Delta_m \equiv \omega_m - \omega_{\mathrm{d}}$.

3.3.1 Energy scales

We envision the scenario depicted in Fig. 3.2, where the drive beam is detuned by an amount $\Delta_{\mathrm{cd}} \equiv \Delta_{m=0} = \omega_{\mathrm{c}} - \omega_{\mathrm{d}}$ from the fundamental (TEM$_{00}$) mode of the cavity at frequency $\omega_{\mathrm{c}} \equiv \omega_{m=0}$, which in turn is far detuned from the bare atomic frequency ω_{a}, by an amount $\Delta_{\mathrm{ca}} \equiv \omega_{\mathrm{c}} - \omega_{\mathrm{a}}$. The drive–atom detuning is thus $\Delta_{\mathrm{da}} = \Delta_{\mathrm{ca}} - \Delta_{\mathrm{cd}}$. We assume red detunings, i.e., that $\omega_{\mathrm{d}} < \omega_{\mathrm{c}} < \omega_{\mathrm{a}}$, such that $|\Delta_{\mathrm{da}}| = |\Delta_{\mathrm{ca}}| + |\Delta_{\mathrm{cd}}|$. The cavity loss rate is parameterised by κ, and the light–matter coupling of the mth cavity mode $\Omega_m \propto \sqrt{\omega_{\mathrm{c}} + (n_x + n_y)\delta\omega}$ can be approximated as $\Omega_m \approx \Omega_{m=0}$: Whilst $\delta\omega/2\pi$ depends on the cavity's deviation from confocality [22], for optical cavities $\omega_{\mathrm{c}}/2\pi$ is on the order of hundreds of THz, such that one can reasonably assume $\delta\omega/\omega_{\mathrm{c}} \ll 1$ [77, 137]: Considering, for instance, the parameters of Ref. [77] (the experiment discussed in Chap. 4) the corrections would be of order $\delta\omega/\omega_{\mathrm{c}} \sim 10^{-6}$ since there, $\delta\omega \sim 100\,\mathrm{MHz}$ whilst $\omega_{\mathrm{c}} \sim 100\,\mathrm{THz}$.

The frequency of the harmonic trap along the cavity axis is assumed to be large enough to produce a quasi-two-dimensional fermionic cloud, extended radially, i.e., transverse to the cavity axis. The relevant trapping frequency is thus that along the radial direction, which we denote as ω_{t}.

The loss rate due to spontaneous emission of the atoms is parameterised by Γ. In the subsequent derivations, we will work in the dispersive regime $|\Gamma/\Delta_{\mathrm{da}}| \ll 1$, to allow for the adiabatic elimination of the excited internal atomic state, similar to the single-mode derivation of Sec. 2.2.4. This is achieved by far-detuning the cavity from the bare atomic transition such that Δ_{ca} is large, and consequently $|\Delta_{\mathrm{da}}| > |\Delta_{\mathrm{ca}}|$ is the dominant energy scale in the system. In so doing, care must be taken to account for the non-zero TMS, which imposes a lower bound on Δ_{ca}, depending on the number of TCMs mediating the atom–atom interactions.

A reasonable hierarchy of the above parameters in cQED platforms [72, 73, 77, 137, 166] is given by

$$\Delta_{\mathrm{ca}} \gg \Delta_{\mathrm{cd}}, \delta\omega \gg \Gamma > \Omega_m > \kappa \gg \omega_{\mathrm{t}}, \tag{3.14}$$

where the Rabi frequency of the drive Ω_{d} can be tuned across this hierarchy, with feasible strengths ranging from 0 to the order of several GHz.

We will neglect atomic and cavity losses throughout our derivation, as they can be treated as subdominant in the dispersive regime: already for

$\Delta_{\mathrm{da}}/2\pi \sim 1\,\mathrm{GHz}$, photonic and atomic losses such as those reported in [77] occur at timescales suppressed by $|\kappa/\Delta_{\mathrm{da}}| \sim 10^{-4}$, $|\Gamma/\Delta_{\mathrm{da}}| \sim 10^{-3}$. Eventually, like for all methods based on cavity QED, the finite cooperativity of the cavity will limit the total duration available for the coherent evolution [21].

3.3.2 Adiabatic elimination of the excited electronic state

With $|\Delta_{\mathrm{da}}(\boldsymbol{r})|$ being the dominant energy scale at all positions $\boldsymbol{r}$, the system is in the dispersive regime, and $\hat{\psi}_{\mathrm{e}}(\boldsymbol{r})$ adiabatically follows $\hat{\psi}_{\mathrm{g}}(\boldsymbol{r})$ according to (see App. A.4.2),

$$\hat{\psi}_{\mathrm{e}}(\boldsymbol{r}) = \frac{\hat{\Phi}(\boldsymbol{r})\hat{\psi}_{\mathrm{g}}(\boldsymbol{r})}{\Delta_{\mathrm{da}}(\boldsymbol{r})}. \tag{3.15}$$

As in the single-mode case of Sec. 2.2.4, by inserting Eq. (3.15) into the Heisenberg equations of motion [generated by $\hat{H}_{\mathrm{mb}}$ of Eq. (3.12)] for $\hat{a}_m$ and $\hat{\psi}_{\mathrm{g}}(\boldsymbol{r})$, one can determine the corresponding Hamiltonian to be

$$\hat{H} = \sum_m \Delta_m \hat{a}_m^\dagger \hat{a}_m + \int \mathrm{d}\boldsymbol{r} \frac{\hat{\Phi}^\dagger(\boldsymbol{r})\hat{\Phi}(\boldsymbol{r})\hat{\psi}_{\mathrm{g}}^\dagger(\boldsymbol{r})\hat{\psi}_{\mathrm{g}}(\boldsymbol{r})}{\Delta_{\mathrm{da}}(\boldsymbol{r})}. \tag{3.16}$$

In what follows, we simplify our notation by denoting the remaining field operator $\hat{\psi}_{\mathrm{g}}(\boldsymbol{r})$ as $\hat{\psi}(\boldsymbol{r})$.

3.3.3 Schrieffer–Wolff transformation

We now integrate out all of the cavity modes, generalising the Schrieffer–Wolff transformation (SWT) introduced in Sec. 2.2.5 to the multi-mode case. This will finally yield our desired effective Hamiltonian with all-to-all, random interactions.

To begin, we group the Hamiltonian of Eq. (3.16) as $\hat{H} = \hat{H}_0 + \hat{V}$, where

$$\hat{H}_0 = \sum_m \Delta_m \hat{a}_m^\dagger \hat{a}_m + \int \mathrm{d}\boldsymbol{r} \frac{|\Omega_{\mathrm{d}} g_{\mathrm{d}}(\boldsymbol{r})|^2}{\Delta_{\mathrm{da}}(\boldsymbol{r})} \hat{\psi}^\dagger(\boldsymbol{r})\hat{\psi}(\boldsymbol{r}), \tag{3.17}$$

$$\begin{aligned}\hat{V} &= \int \mathrm{d}\boldsymbol{r} \frac{1}{4\Delta_{\mathrm{da}}(\boldsymbol{r})} \sum_{m,n} \left(\Omega_m^* g_m^*(\boldsymbol{r}) \Omega_n g_n(\boldsymbol{r}) \hat{a}_m^\dagger a_n\right) \hat{\psi}^\dagger(\boldsymbol{r})\hat{\psi}(\boldsymbol{r}) \\ &\quad + \sum_m (\hat{a}_m \hat{\Theta}_m + \mathrm{H.c.}), \text{ with} \end{aligned} \tag{3.18}$$

$$\hat{\Theta}_m = \frac{1}{2} \int \mathrm{d}\boldsymbol{r} \frac{\Omega_{\mathrm{d}}^* g_{\mathrm{d}}^*(\boldsymbol{r}) \Omega_m g_m(\boldsymbol{r})}{\Delta_{\mathrm{da}}(\boldsymbol{r})} \hat{\psi}^\dagger(\boldsymbol{r})\hat{\psi}(\boldsymbol{r}). \tag{3.19}$$

The effective two-body interactions of Eq. (3.32) below are obtained by decoupling the atom–light interactions contained in $\hat{V}$. We do so through the SWT $\hat{H}_{\mathrm{eff}} = \mathrm{e}^{\hat{S}} \hat{H} \mathrm{e}^{-\hat{S}}$, as defined in Eq. (2.31).

The transformation is simplified by using that $|\Omega_m| \ll |\Omega_{\mathrm{d}}|$, $\forall m$ (see Sec. 3.3.1 above). Within this hierarchy of scales, $\hat{V}$ can be approximated as $\hat{V} \simeq \sum_m (\hat{a}_m \hat{\Theta}_m + \mathrm{H.c.})$ [we will return to this simplification below Eq. (3.21)]. The decoupling is then achieved by choosing the generator

$$\hat{S} = -\sum_m \left(\frac{1}{\Delta_m} \hat{a}_m \hat{\Theta}_m - \mathrm{H.c.} \right), \tag{3.20}$$

which is of order $|\Omega_{\mathrm{d}} \Omega_m| \,/\, |\Delta_{\mathrm{da}} \Delta_{\mathrm{cd}}|$. Truncating $\hat{H}_{\mathrm{eff}}$ at $\mathcal{O}(S)$ (which requires $|\Omega_{\mathrm{d}} \Omega_m| \,/\, |\Delta_{\mathrm{da}} \Delta_{\mathrm{cd}}| \ll 1$), then yields

$$\hat{H}_{\mathrm{eff}} = \hat{H}_0 + \frac{1}{2} [\hat{S}, \hat{V}] = \hat{H}_0 - \sum_m \frac{\hat{\Theta}_m^\dagger \hat{\Theta}_m}{\Delta_m}. \tag{3.21}$$

The last term is the effective two-body interaction, mediated by the exchange of virtual photons between pairs of atoms located at arbitrary positions, see Fig. 3.3. The remaining photonic contribution within $\hat{H}_0$ [see Eq. (3.17)] is eliminated by projecting onto a subspace with a fixed number of cavity photons.

We briefly return to the first term of $\hat{V}$ in Eq. (3.18), which we denote as $\hat{V}'$: If the assumption $|\Omega_m| \ll |\Omega_{\mathrm{d}}|$, $\forall m$ is not met, then [using the same generator $\hat{S}$ of Eq. (3.20), and again truncating at $\mathcal{O}(S)$] one would obtain the additional terms $\hat{V}' + [\hat{S}, \hat{V}']$ in Eq. (3.21). Projection onto a subspace of fixed photon number would then remove the commutator (as it is linear in photonic operators, $[\hat{S}, \hat{V}'] \propto [\hat{a}_k, \hat{a}_m^\dagger \hat{a}_n] = \delta_{km} \hat{a}_n$), and the remaining term would simply modify $\hat{H}_0$. In what follows, we thus continue to neglect $\hat{V}'$.

3.3.4 Effective Hamiltonian and interactions

The above procedure, namely adiabatic elimination of $\hat{\psi}_{\mathrm{e}}(\boldsymbol{r})$ followed by the SWT to integrate out the cavity photons $\hat{a}_m$, yields long-range all-to-all two-body interactions via a fourth order process, as shown diagrammatically in Fig. 3.3.

In more detail, the remaining one-body part of $\hat{H}_{\mathrm{eff}}$ in Eq. (3.21) is given by

$$\hat{H}_0 = \hat{H}_{\mathrm{kt}} + \int \mathrm{d}\boldsymbol{r} \frac{|\Omega_{\mathrm{d}} g_{\mathrm{d}}(\boldsymbol{r})|^2}{\Delta_{\mathrm{da}}(\boldsymbol{r})} \hat{\psi}^\dagger(\boldsymbol{r}) \hat{\psi}(\boldsymbol{r}), \tag{3.22}$$

where we have added the kinetic and external trap terms back in, which just pass through the various transformations done from Eq. (3.12) up to this point (see

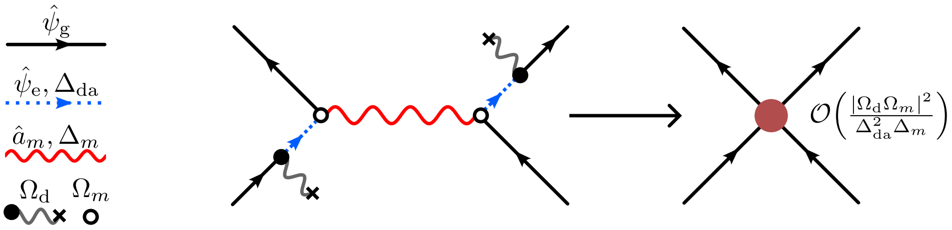

Figure 3.3: Diagrammatic representation of the effective two-body interaction. Feynman diagram for the fourth-order process (left diagram) which yields the long-ranged all-to-all interactions $\mathcal{J}_{i_1 i_2; j_1 j_2} \sim \mathcal{O}(|\Omega_\mathrm{d}\Omega_m|^2 / \Delta_\mathrm{da}^2 \Delta_m)$ of the effective model $\hat{H}_\mathrm{eff}$ (right diagram, large greyish-red vertex) after adiabatic elimination of the excited-state (blue dashed edges), and integrating-out the cavity modes (red wavy edge). On the left, grey wavy edges ending in a cross represent the classical drive field, and solid(empty) vertices indicate drive–atom(cavity–atom) interactions.

App. A.4). This can be diagonalised, as it is a quadratic fermion Hamiltonian [167]. Formally, we denote the corresponding eigenmodes as $\phi_{i_1}(\boldsymbol{r})$, and use these to expand the field operators in Eq. (3.21) as $\hat{\psi}(\boldsymbol{r}) = \sum_{i_1} \phi_{i_1}(\boldsymbol{r})\hat{c}_{i_1}$. In this way, we formally obtain an effective Hamiltonian in terms of spinless, complex fermions, as required by the target Hamiltonian $\hat{H}_\mathrm{SYK}$ in Eq. (3.1),

$$\hat{H}_\mathrm{eff} = \sum_{i_1} \epsilon_{i_1} \hat{c}_{i_1}^\dagger \hat{c}_{i_1} + \mathcal{E} \sum_m \frac{\Delta_\mathrm{cd}}{\Delta_m} \left(\sum_{i_1, j_1} I_{i_1 j_1, m} \hat{c}_{i_1}^\dagger \hat{c}_{j_1} \right) \left(\sum_{i_2, j_2} I_{j_2 i_2, m} \hat{c}_{j_2}^\dagger \hat{c}_{i_2} \right)^\dagger . \tag{3.23}$$

The two-body interactions are randomised via the spatially disordered drive–atom detuning $\Delta_\mathrm{da}(\boldsymbol{r})$ appearing in the dimensionless interaction integrals

$$I_{i_1 j_1, m} = \frac{1}{2} \int \mathrm{d}\boldsymbol{r} \frac{g_\mathrm{d}(\boldsymbol{r}) g_m(\boldsymbol{r})^* \phi_{i_1}^*(\boldsymbol{r}) \phi_{j_1}(\boldsymbol{r})}{\Delta_\mathrm{da}(\boldsymbol{r}) / \Delta_\mathrm{da}} . \tag{3.24}$$

In Eq. (3.23), we have extracted the two-body interactions' energy scale

$$\mathcal{E} = \frac{\eta_0^2}{\Delta_\mathrm{cd}}, \tag{3.25}$$

with $\eta_0 = |\Omega_\mathrm{d}\Omega_{m=0}/\Delta_\mathrm{da}|$ being the two-photon Rabi frequency [see also below Eq. (2.29)], and $\Delta_\mathrm{cd} = \Delta_{m=0}$ (as defined in Sec. 3.3.1 above). In defining $\mathcal{E}$, we have set $\Omega_m = \Omega_{m=0}$, since m-dependent corrections to Ω_m are of order $\delta\omega/\omega_\mathrm{c}$, and can thus be assumed to be negligible (see the discussion of Sec. 3.3.1 for an example).

For the two-body interactions of $\hat{H}_{\text{eff}}$ above to formally match those of the target SYK Hamiltonian $\hat{H}_{\text{SYK}}$ in Eq. (3.1), the second term of Eq. (3.23) needs to be normal ordered. This yields additional one-body terms, also of order $\mathcal{E}$, which are however suppressed as $1/N^2$ due to combinatorics. We thus neglect these terms, such that Eq. (3.23) becomes

$$\hat{H}_{\text{eff}} = \sum_{i_1} \epsilon_{i_1} \hat{c}_{i_1}^{\dagger} \hat{c}_{i_1} + \hat{H}_{\text{eff}}^{(4)} \tag{3.26}$$

with the two-body interactions given by the (quartic fermion operator) normal-ordered term

$$\hat{H}_{\text{eff}}^{(4)} = \sum_{i_1,i_2,j_1,j_2} \mathcal{J}_{i_1 i_2; j_1 j_2} \hat{c}_{i_1}^{\dagger} \hat{c}_{i_2}^{\dagger} \hat{c}_{j_1} \hat{c}_{j_2}, \tag{3.27}$$

where

$$\mathcal{J}_{i_1 i_2; j_1 j_2} = \mathcal{E} \sum_{m} \frac{I_{i_1 j_1, m} I_{j_2 i_2, m}^{*}}{1 + m_{\Sigma} \frac{\delta\omega}{\Delta_{\text{cd}}}} = \mathcal{J}_{j_2 j_1; i_2 i_1}^{*}, \tag{3.28}$$

and the integers m and m_{Σ} are, respectively, defined in Eqs. (3.3) and (3.4).

The remaining one-body part $\sum_{i_1} \epsilon_{i_1} \hat{c}_{i_1}^{\dagger} \hat{c}_{i_1}$ of $\hat{H}_{\text{eff}}$ in Eq. (3.26) consists of $\hat{H}_{\text{kt}}$, and an effective dipole potential of order $|\Omega_{\text{d}}^2/\Delta_{\text{da}}|$, as given in Eq. (3.22). SYK models with one-body perturbations as in $\hat{H}_{\text{eff}}$ have been studied in, for instance, Ref. [102, 168], which showed that the chaoticity of the model is maintained for sufficiently weak one-body perturbations. In our case, the contribution from the effective dipole potential can be compensated by introducing an additional dipole potential of equal magnitude and opposite sign at all $\boldsymbol{r}$ (for an example using an additional laser driving directly the $|g\rangle$ to $|a\rangle$ transition, see App. A.2). Further, by increasing the drive power, $\mathcal{E}$ is enhanced as $|\Omega_{\text{d}}|^2$, permitting one to render $\hat{H}_{\text{kt}}$ sufficiently weak relative to $\mathcal{J}_{i_1 i_2; j_1 j_2}$. In what follows, we will therefore compare only the two-body term $\hat{H}_{\text{eff}}^{(4)}$ to the full target Hamiltonian $\hat{H}_{\text{SYK}}$.

3.3.5 Tuning the number of cavity modes mediating the effective interactions

We will see in the comparison of $\hat{H}_{\text{eff}}^{(4)}$ and $\hat{H}_{\text{SYK}}$, presented in Sec. 3.5, that a crucial feature of our proposal is the ability to tune the number of cavity modes mediating the effective interactions $\mathcal{J}_{i_1 i_2; j_1 j_2}$. As the expression of Eq. (3.28) shows, the contributions of the various cavity modes are suppressed with increasing mode index m as

$$\frac{1}{1 + m_{\Sigma} \tilde{\delta\omega}}, \quad \text{where } \tilde{\delta\omega} \equiv \delta\omega/\Delta_{\text{cd}}. \tag{3.29}$$

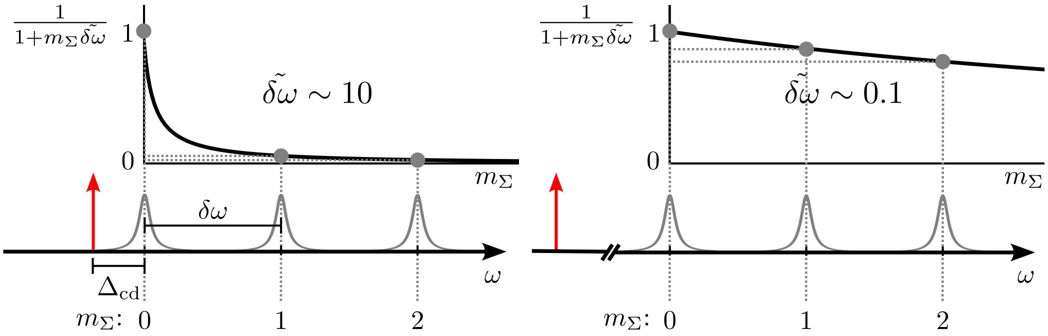

Figure 3.4: Tuning the number of cavity modes via $\widetilde{\delta\omega}$. Plots of Eq. (3.29) versus m_Σ (top row) for $\widetilde{\delta\omega}\sim 10$ (left) and $\widetilde{\delta\omega}\sim 0.1$ (right). For a given cavity, with mode-families $m_\Sigma \geq 0$ and mode-spacing $\delta\omega$, the value of $\widetilde{\delta\omega}$ can be varied by detuning the drive (red arrow) relative to the lowest mode-family $m_\Sigma = 0$. The near- and far-detuned cases are sketched qualitatively in the lower-left, respectively, lower-right. For small cavity–drive detuning $\Delta_{\mathrm{cd}} \ll \delta\omega$ (left), mode-families with $m_\Sigma > 0$ contribute to $\mathcal{J}_{i_1 i_2; j_1 j_2}$ with a negligibly small weight (grey circles). In contrast, for $\Delta_{\mathrm{cd}} \gg \delta\omega$ (right), many mode-families contribute significantly.

The weight of a given mode m can thus be controlled by tuning the ratio $\widetilde{\delta\omega} = \delta\omega/\Delta_{\mathrm{cd}}$ of the transverse-mode spacing $\delta\omega$, to the cavity–drive detuning Δ_{cd}. Two limiting cases are sketched in Fig. 3.4: In the limit of large ratio $\widetilde{\delta\omega} = \delta\omega/\Delta_{\mathrm{cd}}$ (left), only the single mode $m = 0$ contributes significantly to the dynamics, resulting in an approximate product form of the amplitudes $\mathcal{J}_{i_1 i_2; j_1 j_2} \simeq \mathcal{E} I_{i_1 j_1, m=0} I^*_{j_2 i_2, m=0}$. However, decreasing $\widetilde{\delta\omega}$ by increasing the cavity–drive detuning (right), increases the effective number of cavity modes mediating the two-body interactions, thus generating dynamics that approach those of the SYK model, as we probe numerically in Sec. 3.5.

We note that this is in accordance with the study of Ref. [75]. There it was found that low (matrix) rank variants of the SYK model can realise a maximally scrambling model, nearly indistinguishable from the target SYK model of Eq. (3.1), when their rank scales extensively with the number of modes N. These low-rank variants are defined as a sum over products of fermion bilinear operators, such that the desired rank-4 interaction tensor is decomposed as a sum over products of rank-2 tensors. In our proposal, the two-body part of Eq. (3.23) is of this low-rank form, with the rank-2 tensors given by $I_{i_1 j_1, m}$ as defined in Eq. (3.24). Following Ref. [75], the matrix form of the rank-4 interaction tensor is then

$$M_{i_1 j_1, j_2 i_2} = \sum_m \frac{1}{1 + m_\Sigma \widetilde{\delta\omega}} I_{i_1 j_1, m} I^*_{j_2 i_2, m}. \tag{3.30}$$

Note that whilst the right-hand sides of Eqs. (3.28) and (3.30) differ only in the factor $\mathcal{E}$, the composite indices on the left-hand side of either equation differ. Essentially, the two matrices are reshuffled (or reshaped, to use the language of tensor networks) versions of one-another[5]. This new assignment of matrix elements is done in order to match the definition of the "low-rank" coupling-constant matrix of Ref. [75], in which the composite row index consists of one "creation" index i_1 and one "annihilation" index j_1 (similarly for the column index, with i_2 and j_2), in contrast to the usual definition of the SYK interaction tensor $J_{i_1 i_2;j_1 j_2}$, in which both creation indices form the composite row index, and both annihilation indices form the composite column index. Importantly, the rank of M depends via $\sum_m$ on the number of TCMs mediating the interaction, which can be tuned via $\widetilde{\delta\omega}$, as explained above.

In Fig. 3.5(a, b), we numerically investigate the dependence of $r = \operatorname{rank}(M)$ as a function of $\widetilde{\delta\omega}$, over a range of transverse sizes ζ of the atomic cloud. To avoid complications with numeric determination of r, we utilise two alternative measures of the matrix rank: The first is an entropic measure r_e, akin to a participation ratio (see Sec. 4.3.1), defined in terms of the Shannon entropy $H(\boldsymbol{p}) = -\sum_i p_i \log(p_i)$, where the elements of the probability vector $\boldsymbol{p}$ are given by $p_i = \sigma_i / \sum_i |\sigma_i|$ and σ_i are the singular values of M [169]. The second is a lower bound $r_\mathrm{lb} \leq r$ for the rank r of square matrices M [170]. The two measures are given by,

$$r_\mathrm{e} = \exp(H(\boldsymbol{p})), \text{ and } r_\mathrm{lb} = \frac{|\operatorname{tr}(M)|^2}{\operatorname{tr}(MM^\dagger)}. \tag{3.31}$$

Note that also the effective rank satisfies $r_\mathrm{e} \leq r$ [169]. Figure 3.5 shows that either measure increases systematically as $\widetilde{\delta\omega}$ is reduced, in line with the intuition garnered from the discussion related to the sketches of Fig. 3.4. Interestingly, for a given value of $\widetilde{\delta\omega}$, we find that reducing the transverse size of the atomic cloud ζ (black to light grey markers) leads to a reduction of both r_e and r_lb. Whilst this is not definitive proof that the matrix rank r also reduces, it is a first indication of the crucial role played by the size of the atomic cloud when aiming to approximate SYK physics with multimode cQED, in addition to $\widetilde{\delta\omega}$.

---

[5] In more detail, for the matrix construction, a given pair of fermionic mode indices $k, l \in \{0, \ldots, N-1\}$, is mapped to a "composite index" via the function $f(k,l) = k + Nl$. Let the composite row and column indices of matrix M be denoted as r_M and c_M, respectively. Similarly for matrix $\mathcal{J}$ and $r_\mathcal{J}$ and $c_\mathcal{J}$. Then, looking at the subscripts of $M_{i_1 j_1, j_2 i_2}$, we have $r_M = f(i_1, j_1)$ and $c_M = f(j_2, i_2)$, whilst for $\mathcal{J}_{i_1 i_2; j_1 j_2}$ we have $r_\mathcal{J} = f(i_1, i_2)$ and $c_\mathcal{J} = f(j_1, j_2)$. Clearly, $(r_M, c_M) \neq (r_\mathcal{J}, c_\mathcal{J})$, and so the term $\sum_m \frac{I_{i_1 j_1, m} I^*_{j_2 i_2, m}}{1 + m_\Sigma \frac{\delta\omega}{\Delta_\mathrm{cd}}}$ is assigned to different matrix elements of M and $\mathcal{J}$.

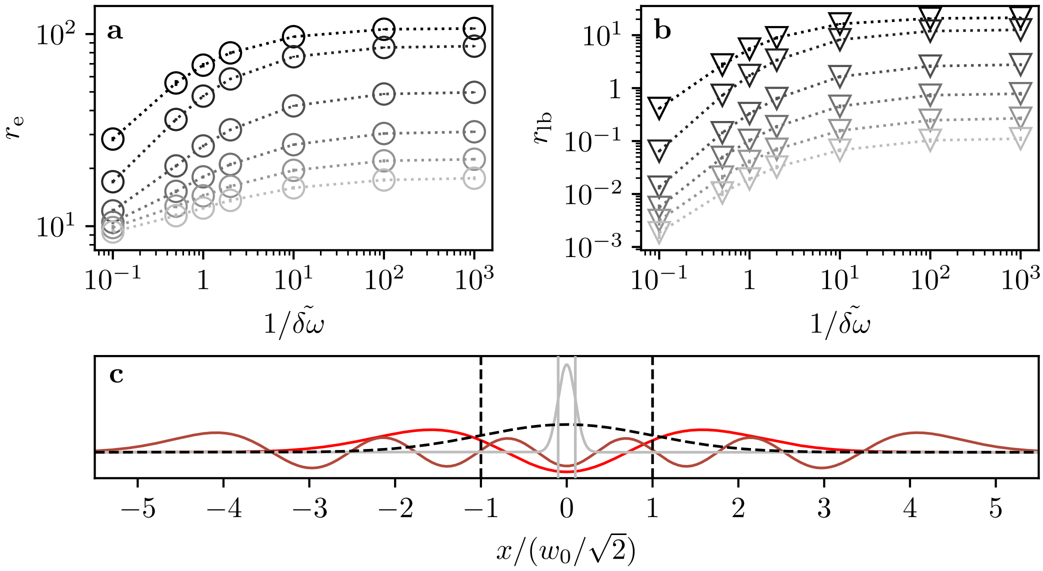

Figure 3.5: Qualitative dependence of interaction rank on $\tilde{\delta\omega}$ and ζ. Effective rank r_e (a), and rank lower bound r_lb (b), versus $\tilde{\delta\omega}$, for the matrix M defined in Eq. (3.30), constructed for $\hat{H}^{(4)}_\mathrm{eff}$ with $N = 14$ at half filling. Shading, from black to light-grey, indicates decreasing transverse size $\zeta = 1, 1/2, 1/4, 1/6, 1/8, 1/10$ of the atomic cloud. Markers indicate mean values, averaged over 100 independent realisations of M (each generated by an independent realisation of $\Delta_\mathrm{da}(\boldsymbol{r})$). Error bars indicating the standard deviation are barely visible and lie within the markers. Dotted lines included to guide the eye. (c) Cavity-mode profiles, as defined above Eq. (A.13), for $(m_x, m_y) = (2, 0)$ (bright red) and $(m_x, m_y) = (10, 0)$ (dark red), relative to the lowest harmonic oscillator fermion mode of a small (grey-solid, $\zeta = 1/10$), and large (black-dashed, $\zeta = 1$) atomic cloud. Vertical grey-solid and black-dashed lines indicate $\pm x_0 = \zeta(w_0/\sqrt{2})$ for $\zeta = 1/10$ and $\zeta = 1$, respectively.

That ζ should play an important role in our proposal, can be understood intuitively at the hand of Fig. 3.5(c). There we show cross-sections of the lowest (Gaussian) eigenmode of the one-body part of $\hat{H}_\mathrm{eff}$ in Eq. (3.26) for two different sizes $\zeta = 1$ (black-dashed curve) and $\zeta = 1/10$ (grey-solid curve), relative to the profiles of two distinct cavity modes $m \neq m'$. The characteristic length scale $\pm x_0$ for either size are indicated by the vertical lines. It is clear that for the smaller cloud, the two cavity modes look near-identical, leading to an effective degeneracy of different cavity modes, despite their large separation in frequency space. Only for sufficiently large ζ can the distinct profiles of the different cavity-modes be resolved by the fermionic modes.

3.4 Distribution of random two-body interactions

We now investigate the distribution of the effective interaction amplitudes $\mathcal{J}_{i_1i_2;j_1j_2}$ of $\hat{H}^{(4)}_{\text{eff}}$, defined in Eqs. (3.27) and (3.28). In the literature, it is often assumed that for sufficiently many cavity modes the interaction amplitudes $\mathcal{J}_{i_1i_2;j_1j_2}$ will follow a Gaussian distribution, due to the central limit theorem [64, 136, 157]. Here, instead, we numerically calculate the interactions $\mathcal{J}_{i_1i_2;j_1j_2}$ from first principles.

To this end, we note that, as in the target model $\hat{H}_{\text{SYK}}$ of Eq. (3.1), only the antisymmetric part of $\mathcal{J}_{i_1i_2;j_1j_2}$ contributes to $\hat{H}^{(4)}_{\text{eff}}$. We thus redefine $\mathcal{J}_{i_1i_2;j_1j_2}$ as the antisymmetric part of Eq. (3.28),

$$\begin{aligned}\mathcal{J}_{i_1i_2;j_1j_2} =& \frac{\mathcal{E}}{4}\sum_m \frac{I_{i_1j_1,m}I^*_{j_2i_2,m} - I_{i_2j_1,m}I^*_{j_2i_1,m} - I_{i_1j_2,m}I^*_{j_1i_2,m} + I_{i_2j_2,m}I^*_{j_1i_1,m}}{1+m_\Sigma\tilde{\delta\omega}} \\ =& \frac{\mathcal{E}}{8}\sum_m \frac{1}{1+m_\Sigma\tilde{\delta\omega}}\int \mathrm{d}\boldsymbol{r}\int \mathrm{d}\boldsymbol{r}'\frac{\operatorname{Re}\left[g_{\text{d}}(\boldsymbol{r})g_m(\boldsymbol{r})^* g_{\text{d}}(\boldsymbol{r}')^* g_m(\boldsymbol{r}')\right]}{(\Delta_{\text{da}}(\boldsymbol{r})/\Delta_{\text{da}})(\Delta_{\text{da}}(\boldsymbol{r}')/\Delta_{\text{da}})} \\ & \times\left(\phi_{i_1}(\boldsymbol{r})\phi_{i_2}(\boldsymbol{r}') - \phi_{i_2}(\boldsymbol{r})\phi_{i_1}(\boldsymbol{r}')\right)^* \phi_{j_1}(\boldsymbol{r})\phi_{j_2}(\boldsymbol{r}')\end{aligned} \tag{3.32}$$

where the factor 1/4 in the first line stems from the antisymmetrisation of Eq. (3.28).

The second line in Eq. (3.32) clarifies that $\mathcal{J}_{i_1i_2;j_1j_2} \in \mathbb{R}$ if $\phi_k(\boldsymbol{r}) \in \mathbb{R}$ for $k = i_1, i_2, j_1, j_2$. This is indeed the case, since $\hat{H}_0$, which is formally diagonalised by $\hat{\psi}(\boldsymbol{r}) = \sum_{i_1}\phi_{i_1}(\boldsymbol{r})\hat{c}_{i_1}$, is itself real [time-reversal symmetric, see Eq. (3.22)]. Whilst the target model $\hat{H}_{\text{SYK}}$ has complex amplitudes $J_{i_1i_2;j_1j_2} \in \mathbb{C}$, variants with $J_{i_1i_2;j_1j_2} \in \mathbb{R}$ have been studied in the literature, and found to agree with the complex version in the thermodynamic limit [64, 104]. In our numeric comparison of the dynamics of $\hat{H}^{(4)}_{\text{eff}}$ and $\hat{H}_{\text{SYK}}$, we will thus focus on the target model with $J_{i_1i_2;j_1j_2} \in \mathbb{R}$.

Given that $\hat{H}^{(4)}_{\text{eff}}$ and $\hat{H}_{\text{SYK}}$ are disordered Hamiltonians, we average over multiple disorder realisations of $\mathcal{J}_{i_1i_2;j_1j_2}$ [i.e., over multiple realisations of $\Delta_{\text{da}}(\boldsymbol{r})$], respectively, of $J_{i_1i_2;j_1j_2}$. With $\mathcal{J}_{i_1i_2;j_1j_2} \in \mathbb{R}$, their ensemble variance is given by $J^2 = \mathbb{E}\left[\mathcal{J}^2_{i_1i_2;j_1j_2}\right] - \mathbb{E}\left[\mathcal{J}_{i_1i_2;j_1j_2}\right]^2$, where $\mathbb{E}[\ldots]$ denotes averaging over an ensemble of disorder realisations $\Delta_{\text{da}}(\boldsymbol{r})$. For the numerics presented in this, and the subsequent sections, we will normalise the interaction amplitudes of either model such that their ensemble variance is $J^2 = 1$.

Figure 3.6(a) shows the distribution for a single, representative, realisation of $\hat{H}^{(4)}_{\text{eff}}/J$ (details on the numeric calculation of the speckle pattern and interaction amplitudes are given in App. A.3). The distribution deviates from a Gaussian probability density, and is better approximated by a Cauchy distribution: For

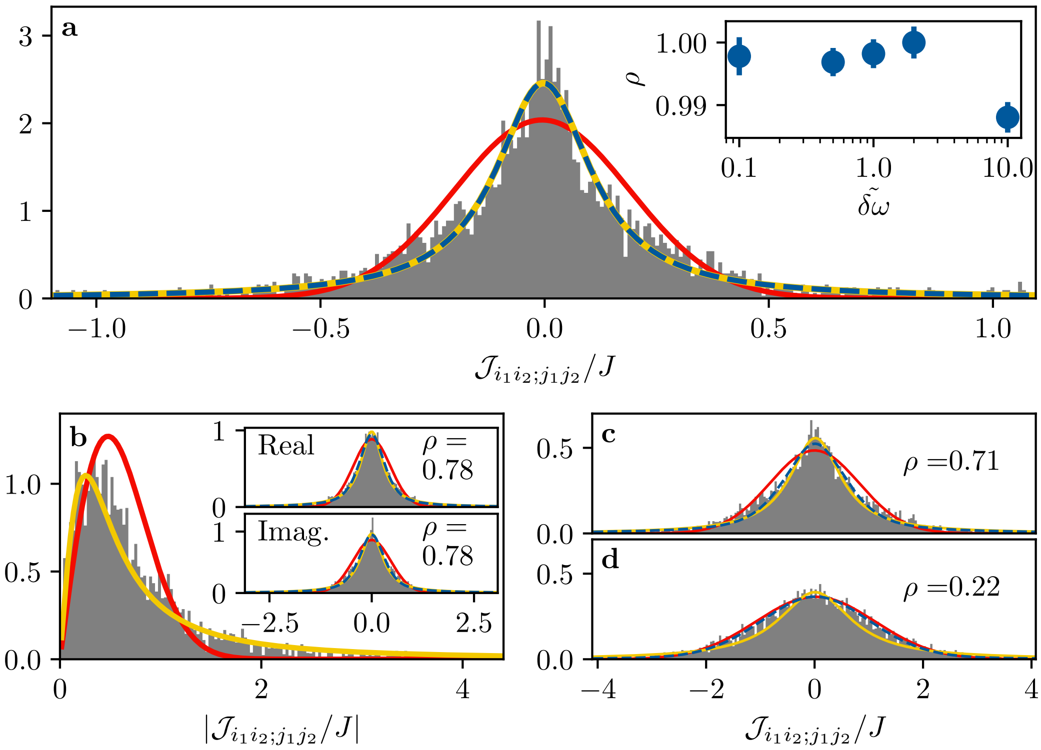

Figure 3.6: Distribution of two-body interaction amplitudes. (a) Representative distribution of $\mathcal{J}_{i_1 i_2; j_1 j_2}$ from numeric calculation of Eq. (3.32), for $N = 14$ fermionic modes, $\tilde{\delta\omega} = 10^{-1}$, and $\zeta = 1$. Fitting the distribution by a (pseudo)Voigt profile [171] [blue dashed line, Eq. (3.33)], which interpolates with a parameter ρ between a Gaussian ($\rho = 0$, red line) and a Cauchy ($\rho = 1$, yellow line) probability density, quantifies the deviation from Gaussian statistics. The interactions are more Cauchy than Gaussian for all $\tilde{\delta\omega}$ considered, as indicated by the inset, which shows the mean value (circles) and standard deviation (error-bars) of ρ over 100 independent disorder realisations. Numerical data of previous proposals shows similar features: (b) Data provided by the authors of a graphene-based proposal Ref. [63], is more Cauchy than Gaussian. (c), (d) Data provided by the authors of Ref. [65], show that depending on the hopping phase ϕ of their optical lattice proposal, the two-body interactions follow more closely a Cauchy [(c), $\phi = 0$] or Gaussian distribution [(d), $\phi = \pi$]. All fitted curves represent the best least-squares fit.

a given realization of the set of $[N(N-1)/2]^2$ antisymmetrised interactions $\{\tilde{\mathcal{J}}_{i_1 i_2;j_1 j_2} | i_1 < i_2, j_1 < j_2\}$ of $\hat{H}_{\text{eff}}$, we quantify the deviation from a Gaussian probability distribution by fitting a (pseudo)Voigt profile [171] to the realised distribution. The (pseudo)Voigt profile is given by a superposition of a Cauchy and a Gaussian probability density, both centred at $\bar{x} \in \mathbb{R}$, and sharing the same full-width-at-half-max $2\sqrt{2\ln(2)}\sigma$,

$$\begin{aligned} f(x) =& \rho \left[\frac{2\sqrt{2\ln(2)}\sigma}{2\pi} \frac{1}{(x-\bar{x})^2 + (2\sqrt{2\ln(2)}\sigma/2)^2} \right] \\ &+ (1-\rho) \left[\frac{1}{\sqrt{2\pi\sigma^2}} \exp\left(-\frac{(x-\bar{x})^2}{2\sigma^2}\right) \right], \end{aligned} \tag{3.33}$$

with $\sigma \geq 0$. The interpolation parameter $\rho \in [0,1]$ can thus be used to quantify the extent to which the set of two-body interaction amplitudes of a given realisation of $\hat{H}_{\text{eff}}$ deviates from the targeted Gaussian ($\rho = 0$), towards a Cauchy ($\rho = 1$) distribution. The inset of Fig. 3.6(a) shows that, in our effective model, $\mathcal{J}_{i_1 i_2;j_1 j_2}$ closely follows a Cauchy distribution for all considered values of $\widetilde{\delta\omega}$. Interestingly, this feature is not unique to the setup considered here: Fig. 3.6(b–d) shows the distributions reported in the proposals of Refs. [63, 65], which also numerically calculated the effective interactions according to the microscopic description of their respective proposals. Whilst these works did not report the non-Gaussian character of their distributions, it is clearly visible. A possible reason for the failure of the CLT may be the presence of correlations within each realisation of $\hat{H}_{\text{eff}}^{(4)}$, which could arise, for instance, between distinct interaction amplitudes that have one or more fermion modes in common and thus sample the spatial disorder in a similar way (see Fig. A.5 for a plot of the covariances within $\{\mathcal{J}_{i_1 i_2;j_1 j_2}\}$). Similarly, and as noted in Sec. 2.2.5, the magnitude of a given effective interaction $\mathcal{J}_{i_1 i_2;j_1 j_2}$ will depend on the precise manner in which the underlying fermionic modes $\phi_i(\boldsymbol{r})$ overlap spatially with the cavity modes $g_m(\boldsymbol{r})$, as determined by the overlap integrals of Eq. (3.24). This could also affect the distribution of interaction amplitudes, with the magnitude of the interaction depending on the combination of modes i_1, i_2, j_1, j_2. A possible approach to investigate such an effect in future works, could be, for instance, to identify in our numerics whether a specific subset of fermionic modes is systematically contributing to the tails of the observed Cauchy distributions.

In light of the above, the important question then arises in how far the deviating probability distribution modifies the physics of the SYK model. We address this in the subsequent section, where we numerically compare the dynamics of $\hat{H}_{\text{eff}}^{(4)}$ to those of the target Hamiltonian $\hat{H}_{\text{SYK}}$. Note also, that the dynamics of the target SYK model are currently actively researched also for other probability distributions, including variations where the interactions are randomly sampled from a set of discrete values, or randomly removed so as to create sparse connectivity graphs [104–106, 172]. In App. A.6, we compare the dynamics of $\hat{H}_{\mathrm{SYK}}$ with Cauchy distributed interactions to its Gaussian counterpart, finding that they are qualitatively the same.

3.5 Comparison of effective and target model

In this section, we numerically probe the chaoticity of the dynamics generated by $\hat{H}^{(4)}_{\mathrm{eff}}$, and compare them to the dynamics of the target model $\hat{H}_{\mathrm{SYK}}$ with $J_{i_1 i_2; j_1 j_2} \in \mathbb{R}$. To this end, we simulate out-of-time-order correlators (OTOCs), and the spectral form factor (SFF) as probes of, respectively, early-time scrambling and late-time chaos [51, 53, 98, 115, 173] (as introduced in Secs. 2.1.2–2.1.3). We employ exact diagonalisation methods, limiting our study to small system sizes N. Given that the maximal scrambling rate of the SYK model is a large-N property, this approach prevents one from observing the saturation of the bound on the quantum Lyapunov exponent [Eq. (2.12)] in the decay of the OTOCs [96]. Thus, our goal is rather to use the dynamics of $\hat{H}_{\mathrm{SYK}}$ for a given accessible N as a benchmark to which we can compare the dynamics of $\hat{H}^{(4)}_{\mathrm{eff}}$, and to show how the parameters entering $\hat{H}^{(4)}_{\mathrm{eff}}$ can be tuned such that its dynamics approach those of $\hat{H}_{\mathrm{SYK}}$.

Our simulations start by numerically calculating the interaction amplitudes $\mathcal{J}_{i_1 i_2; j_1 j_2}$ as defined by Eq. (3.32), with $m = 0, 1, \ldots, M$ (all data shown here is converged with respect to the cut-off M, see Fig. A.3), for multiple independent disorder realisations. For a given realisation, we use the normalised amplitudes $\mathcal{J}_{i_1 i_2; j_1 j_2}/J$ to construct $\hat{H}^{(4)}_{\mathrm{eff}}/J$, whose dynamics are then solved via exact diagonalisation (see App. A.3 for an elaboration of the numerics). The simulated time t is thus in units of J.

3.5.1 Out-of-time-order correlators

Figure 3.7(a) shows the real part of the OTOC $F(t) = \mathrm{tr}(\hat{\rho}_\beta \hat{W}^\dagger(t) \hat{V}^\dagger \hat{W}(t) \hat{V})$, calculated according to Eq. (2.13) with respect to the infinite temperature state $\hat{\rho}_{\beta=0} = \mathbb{1}/D$ ($\mathbb{1}$ is the identity operator, and D is the Hilbert-space dimension of the half-filling sector, $D = N!/[(N/2)!]^2$), for a large atomic cloud $\zeta = 1$, and unitary operators $\hat{W} = 2\hat{c}_i^\dagger \hat{c}_i - 1$, $\hat{V} = 2\hat{c}_j^\dagger \hat{c}_j - 1$, with indices $i = 0$ and $j = 1$. The blue curves correspond to disorder averaged dynamics for $\tilde{\delta\omega} \in [0.1, 10]$. As $\tilde{\delta\omega}$ is decreased [effective number of involved cavity modes is

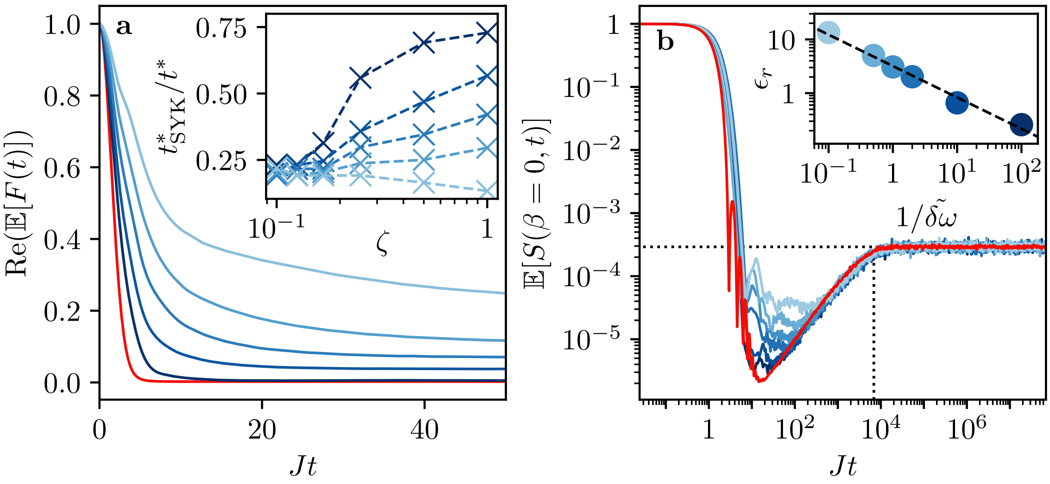

Figure 3.7: OTOCs and SFF of effective and target model. $\mathrm{Re}(\mathbb{E}[F(t)])$ (a) and $\mathbb{E}[S(\beta = 0, t)]$ (b) at $\beta = 0$, generated by $\hat{H}^{(4)}_{\mathrm{eff}}$ with $\zeta = 1$ (blue curves), and $\hat{H}_{\mathrm{SYK}}$ with $J_{i_1 i_2; j_1 j_2} \in \mathbb{R}$ (red curve). (a) Curves represent ensemble averages over 250(1000) disorder realisations of $\hat{H}^{(4)}_{\mathrm{eff}}(\hat{H}_{\mathrm{SYK}})$ for $N = 10$ fermionic modes at half filling. Shades of blue, from light to dark, correspond to $\tilde{\delta\omega} = 10, 2, 1, 1/2, 1/10$. (inset) The inverse times $1/t^*$, relative to that of the target model $1/t^*_{\mathrm{SYK}}$, at which $\mathrm{Re}(\mathbb{E}[F(t^*)]) = 1/e$, for each value of $\tilde{\delta\omega}$, as a function of the transverse size ζ of the atomic cloud (dashed lines to guide the eye). With decreasing $\tilde{\delta\omega}$ and increasing ζ, the OTOCs approach the fast dynamics of the SYK model. (b) Curves represent ensemble averages over 100(1000) disorder realisations of $\hat{H}^{(4)}_{\mathrm{eff}}(\hat{H}_{\mathrm{SYK}})$ for $N = 14$ fermionic modes at half filling. Vertical(Horizontal) black dotted line indicate the Heisenberg time $t_{\mathrm{H}} = 2D$(plateau height $1/D$), showing good agreement with the SFF of $\hat{H}_{\mathrm{SYK}}$. Shades of blue, from light to dark, correspond to $\tilde{\delta\omega} = 10, 2, 1, 1/2, 1/10, 1/100$. The time axes for the SFFs of $\hat{H}^{(4)}_{\mathrm{eff}}$ have been rescaled in order to match the Heisenberg time of $\hat{H}_{\mathrm{SYK}}$ (see Methods, Sec. A.3). (upper inset) The deviation ϵ_r (see text) of the ramp time t_{r} decreases as a power law $\tilde{\delta\omega}^{-\alpha}$ with $\alpha = 0.58 \pm 0.03$, as extracted from a least-squares fit (black dashed line).

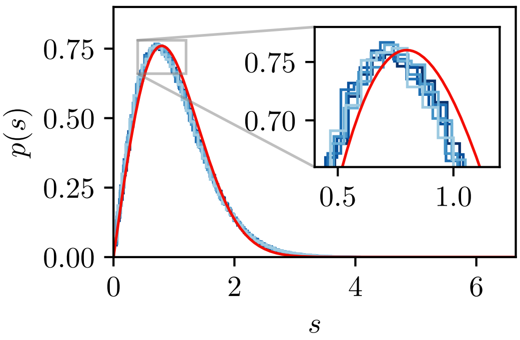

Figure 3.8: Level-spacing distribution. The unfolded level-spacing distribution $p(s)$ of $\hat{H}_{\text{eff}}^{(4)}$ (blue histograms) for the same disorder realisations of the SFF curves in Fig. 3.7(b), compared to the GOE Wigner–Dyson distribution (red) of Eq. (2.6) with Wigner–Dyson index $\boldsymbol{\beta} = 1$. There is no qualitative change with varying $\tilde{\delta\omega}$.

increased, as discussed previously in Sec. 3.3.5] the OTOCs decay faster, and finally approach those of the SYK model (red curve). This speed-up is more prominent for large transverse sizes ζ of the atomic cloud, as shown by the inset. There, we use $1/t^*$—defined via $\text{Re}(\mathbb{E}[F(t^*)]) = 1/e$, with e being Euler's constant—as a proxy for the decay rate, and find the speed-up with decreasing $\tilde{\delta\omega}$ to be ζ dependent. This dependence is due to the shape of the cavity mode functions, as discussed in Sec. 3.3.5 with reference to Fig. 3.5(c): Since the cavity modes feature a length scale (the cavity waist w_0), all interactions mediated by different transverse cavity modes become linearly dependent for small sizes, leading to a reduction of the effective number of modes mediating interactions in $\hat{H}_{\text{eff}}^{(4)}$. As a consequence, the convergence to the SYK model is slower. This indicates that the effective model resembles the SYK model at a length scale comparable to the cavity waist, $\zeta = 1$.

3.5.2 Spectral form factor

As was discussed in Sec. 2.1.2, a typical diagnostic of quantum chaos is the distribution $p(s)$ of the spacings s of nearest-neighbour energy-levels, with integrable models displaying Poisson statistics and chaotic models following the Wigner surmise of Eq. (2.6) [99]. Indeed, the SYK model's distribution $p(s)$ is known to follow the Wigner surmise [97] [see also the inset of Fig. 2.2(a)], and we find that also for $\hat{H}_{\text{eff}}^{(4)}$, $p(s)$ matches the Wigner surmise well for all considered values of $\tilde{\delta\omega}$, as shown in Fig. 3.8. The figure shows that, in contrast to the OTOCs, we do not find a qualitative change of $p(s)$ as a function of $\tilde{\delta\omega}$ in our numerics. However, since $p(s)$ is a measure of short range (nearest-neighbour) spectral correlations, it is only able to identify the presence of chaotic behaviour at long timescales, on the order of $1/s$.

To study the many-body chaotic properties of our effective model in more detail, we thus turn to the SFF, which is sensitive also to long-range spectral correlations, and thus able to diagnose chaotic behaviour already at short to intermediate times. Fig. 3.7(b) shows the SFF [Eq. (2.7)] of $\hat{H}_{\text{eff}}^{(4)}$ for $\zeta = 1$, as compared to that of $\hat{H}_{\text{SYK}}$, at inverse temperature $\beta = 0$. The SFF of $\hat{H}_{\text{SYK}}$ (red curve) exhibits the characteristic random matrix theory (RMT) features discussed in the introductory Sec. 2.1.2. For all values of $\tilde{\delta\omega}$ considered, the SFF of $\hat{H}_{\text{eff}}^{(4)}$ (blue curves) shows signatures of the dip and ramp and, similar to the OTOCs, the depth of the dip and the temporal range of the ramp approach that of the SYK model as $\tilde{\delta\omega}$ is decreased (light to dark blue).

For a quantitative comparison of the effective and target model's SFF, one would ideally want to compare their Thouless time. This is the time at which the connected part of the SFF starts to match the RMT predictions. This, however, is generically masked by the early-time slope, which stems from the disconnected part, making it very challenging to determine numerically even for the target model [106, 115]. Instead, we focus on comparing the time t_{r} at which the ramp of the SFF starts. To extract this time, we follow the procedure of Ref. [115] by defining t_{r} as the earliest time at which the deviation of the SFF from a linear fit to the ramp falls below a chosen threshold (see Fig. A.6 for an example of the fitting procedure). The upper inset to Fig. 3.7(b) shows that the deviation $\epsilon_r = \left| t_{\text{r}}(\tilde{\delta\omega}) - t_{\text{r,SYK}} \right| / t_{\text{r,SYK}}$ scales as $\tilde{\delta\omega}^{-\alpha}$, with $\alpha \approx 0.58$. In contrast to the nearest-neighbour level statistics $p(s)$, the SFF reveals that our effective model approaches the SYK model as $\tilde{\delta\omega}$ is reduced and more cavity-modes mediate the all-to-all interactions.

3.6 Discussion

The numeric results of the previous section highlight the key requirements for $\hat{H}_{\text{eff}}$ to faithfully approximate the dynamics of $\hat{H}_{\text{SYK}}$. In particular, we have seen the importance of the microscopic parameters $\tilde{\delta\omega}$ and ζ: By controlling these parameters, the interactions of Eq. (3.32) can be tuned into a regime (small $\tilde{\delta\omega}$, large ζ) in which the early-time fast scrambling dynamics (OTOCs) and long-range spectral correlations (SFF) of the SYK model are well approximated.

3.6.1 Experimental implementation

Here we motivate that the above requirements can be met using existing experimental capabilities.

The need for a large ζ suggests the use of a light atomic species. ^{6}Li is a natural choice of Fermionic atom: considering a trap with transverse frequencies of 25 Hz, such as that produced by the magnetic field curvatures in Ref. [166], yields $x_0 = 5.8\,\mu\mathrm{m}$. Quantum degenerate Fermi gases of ^{6}Li are now routinely produced in high finesse cavities [72, 73]. To produce mesoscopic samples of ten to hundreds of atoms, the methods of Ref. [174] could be adapted to the context of cavity QED. While the target model is amenable to direct numerical studies for small N, and becomes analytically tractable when perturbing around the $N \to \infty$ limit, this mesoscopic regime remains inaccessible by these methods. At the same time this regime harbours highly interesting quantum effects both from the many-body and the holographic perspective, sensitive to non-perturbative effects caused by the presence of a finite level spacing.

The lowest possible cavity waists, together with low mode spacing $\delta\omega$, are achieved through the use of close-to-concentric cavities. For instance, Ref. [77]—the basis of Chap. 4—operates with ^{6}Li in a cavity with a waist of $13.2\,\mu\mathrm{m}$, and mode waists as low as $2.4\,\mu\mathrm{m}$ have been demonstrated close to the concentric limit [175]. The coupling of atoms to a very large number of modes has been achieved in confocal cavities [137]. In close-to-concentric cavities, transverse modes are not degenerate even close to the stability limit, but as long as the transverse mode spacing is much lower than the free-spectral range, it is possible to emulate multimode driving using a comb of pump frequencies, each tuned close to one transverse mode family [176]. While scaling-up the number of cavity modes together with atom number is challenging in this context, the high degeneracy of high-order cavity modes alleviates the experimental overheads, so that reaching up to several hundreds of atoms seems realistic.

An intrinsic limitation of cavity-QED platforms is the occurrence of dissipation channels in the form of spontaneous photon scattering by the atoms, and photon leakage through the cavity mirrors. The corresponding irreversible dynamics are described by jump operators in the Lindblad equation formulation. These jump operators inherit the random structure of the light-matter coupling, formally reproducing a dissipative SYK model similar to that studied recently in Ref. [177] (see App. A.5). The finite cooperativity of the cavity will yield a timescale below which the dynamics will be faithfully described by the Hamiltonian of Eq. (3.26). Since the central feature of the SYK model is the onset of chaos at logarithmically short time, we expect the study of this process not to be strongly hindered by dissipative effects.

3.6.2 Summary

We have shown that state-of-the-art cQED experiments—with ultracold fermionic atoms coupled to a multi-mode optical cavity, and subjected to a spatially disordered AC-Stark shift—are able to realise an effective model $\hat{H}_{\mathrm{eff}}$ with dominant random all-to-all two-body interactions $\mathcal{J}_{i_1 i_2; j_1 j_2}$, as given by

Eq. (3.32).

Numeric calculations from first principles reveal an underlying Cauchy distribution, rather than the Gaussian distribution of the ideal target model $\hat{H}_{\mathrm{SYK}}$ in Eq. (3.1), and we have shown this feature to be present also in previous proposals based on solid-state and optical-lattice architectures. Nevertheless, our exact simulations show good agreement between the considered OTOCs and the SFF of the effective model and the target $\hat{H}_{\mathrm{SYK}}$. We identify how one can tune into the relevant parameter regime by tuning the transverse size ζ of the atomic cloud, as well as increasing the number of cavity-modes mediating $\mathcal{J}_{i_1 i_2;j_1 j_2}$, by decreasing the ratio of the mode-spacing to the cavity–drive detuning $\widetilde{\delta\omega} = \delta\omega/\Delta_{\mathrm{cd}}$.

Our work shows that the SYK model is within the reach of cQED-based experiments, and it sheds further light on the robustness of SYK physics against experimentally motivated imperfections. Even more, it offers exciting prospects for further exploration. An immediate extension is to vary the disordered light shift in time, thereby generating random time-dependent interactions $\mathcal{J}_{i_1 i_2;j_1 j_2}(t)$ as required for so-called Brownian SYK models [100]. The setup also permits for controlled deformations of the model, opening a platform on which to test the robustness of SYK-type physics, a question that is attracting increased interest lately [102, 104–106, 172, 178]. An interesting direction for future work is to investigate whether the real interaction amplitudes $\mathcal{J}_{i_1 i_2;j_1 j_2}$ could be made complex by breaking time-reversal symmetry through the synthesis of an artificial magnetic field, for instance via spin–orbit coupling [179]. Finally, whilst we have considered a single atomic cloud, multiple quasi-two-dimensional clouds can be trapped within the same cavity, and could be subjected to identical disorder using spatial light modulators. Such an extension of our work may offer the exciting prospect of realizing coupled SYK systems such as described by the Maldacena–Qi model [108], and studied in the context of traversable wormholes [69, 70, 109].

3.6.3 Alternative approaches and outlook

Speckle correlation length. We have seen the importance of finite size effects, as captured by ζ, in realising SYK physics. A further important length scale in the above protocol is the correlation length ξ of the speckle pattern employed to realise the disordered AC-Stark shift. In our numerics, we have considered the ratio of speckle correlation length ξ to oscillator length x_0 to be fixed (see App. A.3 for details). Intuitively, however, there should also be an optimal value for the relative size of the speckle grains ξ/x_0: For $\xi \gg x_0$, the whole atomic cloud is covered by a single speckle grain, and there is no disorder. For $\xi \ll x_0$,

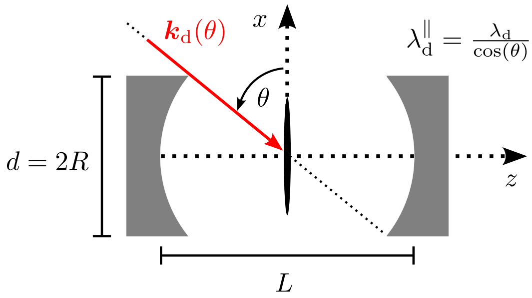

Figure 3.9: Drive beam at an angle. To increase the drive's wavelength $\lambda_{\mathrm{d}}^{\parallel}$ over the two-dimensional atomic cloud (black ellipse), one could let the drive beam propagate at an angle θ relative to the x-axis, instead of transversely to the cavity(z)-axis. The enhancement of the wavelength is then limited by the cavity geometry, as given by the diameter d of the mirrors, and their separation L.

in contrast, the disorder may be averaged out in the spatial integrals of $\mathcal{J}_{i_1 i_2; j_1 j_2}$ [see, e.g., Eq. (3.32)]. Tuning also ξ/x_0, for instance via the wavelength of the light-shifting beam, or the numerical aperture of the focussing lens [162], may offer the capability to further optimise the chaotic and scrambling properties of $\hat{H}_{\mathrm{eff}}$.

Details of the cavity modes. For our derivations, we have taken a simplified scenario, in which the transverse cavity modes appear in degenerate families at frequencies $\omega_{\mathrm{c}} + m_{\Sigma}\delta\omega$, where m_{Σ} was the sum of the transverse mode indices. The precise frequency arrangement, however, will depend on which type of cavity is used, and the above general derivations may need to be adapted to a given cQED setup accordingly. Similarly, we have neglected Gouy phase shifts which depend on the longitudinal cavity coordinate z. For the scenario assumed above, where a single quasi two-dimensional cloud is tightly confined along the cavity(z)-axis and extends radially, the Gouy phase should be negligible when trapping the cloud at $z = 0$. Especially for extensions to coupled SYK models, possibly simulated by multiple quasi two-dimensional clouds trapped along the cavity axis, this phase will need to be taken into account. The role of an additional phase off-set, imposed by the boundary conditions of the cavity mirrors and scaling as m_{Σ}, provides a further avenue for future refinements [22].

On-axis drive As motivated in Sec. 3.2, one could increase the wavelength of the drive λ_{d} over the atomic cloud by letting it impinge at an angle, instead of transverse to the cavity axis, as sketched in Fig. 3.9. This yields an effective wavelength $\lambda_{\mathrm{d}}^{\parallel}$ over the atomic cloud (black ellipse), enhanced by a geometric prefactor $\lambda_{\mathrm{d}}^{\parallel} = \lambda_{\mathrm{d}}/\cos(\theta)$. For simplicity, assume the mirrors to be identical and suppose that their diameter d is equal to twice their radius of curvature R. For a planar cavity ($L \gg R$), one could achieve $\lambda_{\mathrm{d}}^{\parallel} \gg \lambda_{\mathrm{d}}$. However, the diverging mode-volume of the eigenmodes of planar cavities would lead to an undesirable decrease in the light–matter coupling Ω_m (single-photon Rabi frequency, see Sec. 2.2.1). In contrast, for confocal ($L = R$) or concentric ($L = 2R$) cavities, one could achieve only minor enhancements of $\lambda_{\mathrm{d}}^{\parallel} = (\sqrt{5}/2)\lambda_{\mathrm{d}}$, respectively, $\lambda_{\mathrm{d}}^{\parallel} = \sqrt{2}\lambda_{\mathrm{d}}$.

As an alternative to this geometric enhancement, one may consider an on-axis drive beam ($\theta = \pi/2$), which couples to the cavity modes instead of the atoms, in order to satisfy the long-wavelength approximation. Here, we show that this approach formally yields the same effective model as in Sec. 3.3, only with $g_{\mathrm{d}}(\boldsymbol{r})$ replaced by a superposition of cavity modes, as will be defined in Eq. (3.43) below.

Changing from a transverse to an on-axis drive, the many-body Hamiltonian of Eq. (3.6) is modified accordingly as [see also Eq. (2.24)]

$$\begin{aligned}\hat{H}_{\mathrm{mb}} =& \sum_m \Delta_m \hat{a}_m^{\dagger}\hat{a}_m - \int \mathrm{d}\boldsymbol{r} \Delta_{\mathrm{da}}(\boldsymbol{r})\hat{\psi}_{\mathrm{e}}^{\dagger}(\boldsymbol{r})\hat{\psi}_{\mathrm{e}}(\boldsymbol{r}) \\ &+ \frac{1}{2}\sum_m \int \mathrm{d}\boldsymbol{r} \left(\Omega_m g_m(\boldsymbol{r})\hat{a}_m \hat{\psi}_{\mathrm{e}}^{\dagger}(\boldsymbol{r})\hat{\psi}_{\mathrm{g}}(\boldsymbol{r}) + \mathrm{H.c.}\right) + \sum_m (\Omega_{\mathrm{d}}^{*} c_m \hat{a}_m + \mathrm{H.c.}),\end{aligned} \tag{3.34}$$

where now the last term represents the coupling of the on-axis drive to the transverse cavity modes, with coefficients c_m quantifying the strength of this coupling to the mth cavity mode. As for the case of transverse drive, we neglect the kinetic and external trap terms $\hat{H}_{\mathrm{kt}}$ here and in what follows. Note further that we have already moved into the frame rotating at the drive frequency ω_{d}.

Since the cavity modes are now driven, we decompose $\hat{a}_m$ into a sum of quantum fluctuations $\delta\hat{a}_m$ around a classical contribution $\alpha_m = \mathrm{tr}(\rho\hat{a}_m)$, $\hat{a}_m = \alpha_m + \delta\hat{a}_m$, similar to Ref. [180]. The equation of motion for $\hat{a}_m$, including cavity losses κ, is

$$i\partial_t \hat{a}_m = (\Delta_m - i\kappa/2)\hat{a}_m + \Omega_d c_m^{*} + \frac{1}{2}\int \mathrm{d}\boldsymbol{r}\, (\Omega_m g_m(r))^{*}\, \hat{\psi}_{\mathrm{g}}^{\dagger}(\boldsymbol{r})\hat{\psi}_{\mathrm{e}}(\boldsymbol{r}). \tag{3.35}$$

Taking the trace and equating zero order terms we obtain,

$$i\partial_t \alpha_m = (\Delta_m - i\kappa/2)\alpha_m + \Omega_d c_m^{*}, \tag{3.36}$$

which is solved by $\alpha_m(t) = \alpha_m(0)\exp(-(i\Delta_m + \kappa/2)t) - \Omega_{\mathrm{d}} c_m^{*}/(\Delta_m - i\kappa/2)$. Assuming $|\Delta_m| \gg \kappa$, we find $\langle \alpha_m \rangle_T \equiv (1/T)\int_0^T \mathrm{d}t\alpha_m(t) \simeq -\Omega_{\mathrm{d}} c_m^{*}/\Delta_m$, where we have additionally assumed that the time interval satisfies $T \gg 2\,|\alpha_m(0)/\Delta_m|$, which is valid for sufficiently large cavity–drive detuning Δ_m. Substituting $\hat{a}_m$ by $\langle\alpha_m\rangle_T + \hat{a}_m$ in Eq. (3.34), we obtain

$$\begin{aligned}\hat{H} =& \sum_m \left(\Delta_m \hat{a}_m^\dagger \hat{a}_m - \frac{|\Omega_\mathrm{d} c_m|^2}{\Delta_m}\right) - \int \mathrm{d}\boldsymbol{r} \Delta_\mathrm{da}(\boldsymbol{r}) \hat{\psi}_\mathrm{e}^\dagger(\boldsymbol{r}) \hat{\psi}_\mathrm{e}(\boldsymbol{r}) \\ &+ \int \mathrm{d}\boldsymbol{r} \left(\hat{\tilde{\Phi}}(\boldsymbol{r}) \hat{\psi}_\mathrm{e}^\dagger(\boldsymbol{r}) \hat{\psi}_\mathrm{g}(\boldsymbol{r}) + \mathrm{H.c.}\right),\end{aligned} \tag{3.37}$$

where now $\hat{\tilde{\Phi}}(\boldsymbol{r}) = \frac{1}{2}\sum_m \left(-\frac{\Omega_\mathrm{d} c_m^*}{\Delta_m} + \hat{a}_m\right) \Omega_m g_m(\boldsymbol{r})$. Comparing this with $\hat{\Phi}(\boldsymbol{r})$ of Eq. (3.13) already indicates how the transverse drive profile $g_\mathrm{d}(\boldsymbol{r})$ of Sec. (3.3) is replaced here by a superposition of the cavity mode profiles, governed by the drive strength Ω_d and the coupling coefficients c_m. In what follows, we drop the constant contained in the first term of $\hat{H}$ above.

Equation (3.37) is formally similar to Eq. (3.12), and thus adiabatic elimination of $\hat{\psi}_\mathrm{e}(\boldsymbol{r})$ and integration of the cavity photons $\hat{a}_m$ via the SWT proceed analogously to the derivation of Eq. (3.21). Formally, we obtain the same result, only with modified terms,

$$\hat{H}_0 = \hat{H}_\mathrm{kt} + \sum_m \Delta_m \hat{a}_m^\dagger \hat{a}_m \tag{3.38}$$

$$+ \frac{|\Omega_\mathrm{d}|^2}{4} \int \mathrm{d}\boldsymbol{r} \frac{1}{\Delta_\mathrm{da}(\boldsymbol{r})} \sum_{m,n} \frac{(c_m^* \Omega_m g_m(\boldsymbol{r}))^* c_n^* \Omega_n g_n(\boldsymbol{r})}{\Delta_m \Delta_n} \hat{\psi}^\dagger(\boldsymbol{r}) \hat{\psi}(\boldsymbol{r}), \tag{3.39}$$

$$\hat{\Theta}_m = -\frac{1}{4} \int \mathrm{d}\boldsymbol{r} \Omega_\mathrm{d}^* \Omega_m g_m(\boldsymbol{r}) \left(\sum_n \frac{c_n^* \Omega_n g_n(\boldsymbol{r})}{\Delta_n}\right)^* \frac{\hat{\psi}^\dagger(\boldsymbol{r}) \hat{\psi}(\boldsymbol{r})}{\Delta_\mathrm{da}(\boldsymbol{r})}. \tag{3.40}$$

The interactions

$$\mathcal{J}_{i_1 i_2; j_1 j_2} = \sum_m \frac{I_{i_1 j_1, m} I^*_{j_2 i_2, m}}{\Delta_m} = \mathcal{J}^*_{j_2 j_1; i_2 i_1}, \tag{3.41}$$

of the effective model with on-axis drive are thus formally equivalent to those of Eq. (3.28) with transverse drive, but with the interaction integrals of Eq. (3.24) modified to

$$I_{i_1 j_1, m} = \int \mathrm{d}\boldsymbol{r} \frac{\Omega_\mathrm{d} \left(\Omega_m g_m(\boldsymbol{r})\right)^* \mu(\boldsymbol{r}) \phi_{i_1}^*(\boldsymbol{r}) \phi_{j_1}(\boldsymbol{r})}{4\Delta_\mathrm{da}(\boldsymbol{r})}, \tag{3.42}$$

where

$$\mu(\boldsymbol{r}) = \sum_n \frac{c_n^* \Omega_n g_n(\boldsymbol{r})}{\Delta_n}, \tag{3.43}$$

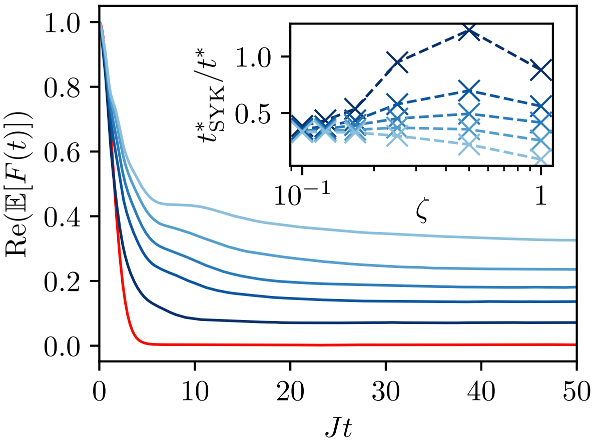

Figure 3.10: OTOCs for effective model with on-axis drive. Dynamics of $\mathrm{Re}(\mathbb{E}[F(t)])$ for $\zeta = 1$, similar to Fig. 3.7(a), but for the on-axis drive configuration coupling to only the lowest cavity mode $[c_{n=0} = 1, c_{n>0} = 0$ in Eq. (3.43)$]$. Data are for $N = 8$ fermionic modes at half filling, and represent ensemble averages over 5000(2500) disorder realisations of $\hat{H}^{(4)}_{\mathrm{eff}}(\hat{H}_{\mathrm{SYK}})$. Shades of blue, and inset are as for Fig. 3.7(a).

is a superposition of those cavity modes to which the on-axis drive has non-zero coupling. The coupling coefficients may be varied so as to achieve a desired profile $\mu(r)$. For instance, one may engineer the on-axis drive so as to couple only to the lowest (Gaussian) cavity mode, $c_m = 0$ for $m > 0$, such that the drive profile $g_{\mathrm{d}}(\boldsymbol{r})$ in Eq. (3.24) is replaced by the Gaussian cavity mode.

This scenario is investigated in Fig. 3.10, for the same OTOCs studied in Fig. 3.7(a) for the transverse-drive configuration. This preliminary data shows that the dependence of the OTOC decay on $\tilde{\delta\omega}$ and ζ is qualitatively similar to the behaviour observed for the transverse-drive configuration: For a given ζ, decreasing $\tilde{\delta\omega}$ yields an increased decay rate. In contrast to the data of Fig. 3.7(a), here we do not see a monotonic increase of the decay rate when varying ζ for a given $\tilde{\delta\omega}$, which is likely due to numerics finite-size effects of the smaller system size ($N = 8$) studied here. The data however indicate that also the on-axis configuration could be employed to approximate the SYK dynamics, and merit further investigation for larger system sizes, or different sets of couplings c_n in Eq. (3.43).

4 Engineering random spin models with atoms in a high-finesse cavity

This chapter is based on the publication N. Sauerwein, F. Orsi, P. Uhrich, S. Bandyopadhyay, F. Mattiotti, T. Cantat-Moltrecht, G. Pupillo, P. Hauke and J.-P. Brantut, "Engineering random spin models with atoms in a high-finesse cavity", Nat. Phys. (2023) [77]. As such, the derivations and discussion presented in this chapter are adapted from there. The publication reports on the realisation of spin models with quenched disorder realised in a single-mode cQED experiment with ^{6}Li atoms. My main contributions to this work are the calculations, and analysis of experimental and numeric data, presented in Secs. 4.2–4.3, related to the off-resonant regime of the experiment in which a random Lipkin–Meshkov–Glick (LMG) is realised.

The unavoidable presence of impurities and inhomogeneities in most real-world physical systems has given a strong motivation to the study of disordered models. Several quantum simulation platforms, such as trapped ions [15], ultracold atoms [18] and Rydberg atoms [181–183], have demonstrated the capability to implement controlled disorder into otherwise clean many-body systems. Those allowed for the investigation of non-equilibrium dynamics, revealing some of the most intriguing phenomena of random systems, such as Anderson [184–188] and many-body localisation [39, 41, 189].

As discussed in Sec. 2.2, cavity quantum electrodynamics (cQED) has emerged as a new platform for quantum simulation in recent years. By harnessing photons to tailor novel types of interactions beyond the native van der Waals and dipolar interactions between atoms, cavity QED unites the scalability of atom devices with tunable long-range interactions [22]. In Sec. 4.1, we discuss the implementation of random spin models in a cQED platform, as reported in Ref. [77], which studied their low-lying excitations. We show how the light shift technique introduced in Sec. 3.2.1 was used to realise a quasi-random longitudinal field with controlled strength, which competes with an all-to-all flip-flop interaction mediated by the exchange of cavity photons.

By varying the detuning of the cavity from the clean atomic resonance, the setup is able to realise a central-mode model (near-resonant regime) and a Lipkin–Meshkov–Glick (LMG) model (far off-resonant regime) with an all-to-all spin-exchange interaction. Tuning the disorder strength allowed for the observation of disorder-driven crossovers in either regime, namely a disorder-induced dressing of otherwise dark anti-symmetric states with cavity photons in the central-mode model, and the breaking of ferromagnetic order in the LMG model. We briefly review the experimental protocol—which utilised the open nature of the cavity to observe the frequency-resolved response in the cavity field and atomic polarisation channels—as well as results for the near-resonant regime in Sec. 4.1, before turning to the analyses of the LMG model in Sec. 4.2. We further show theoretically and experimentally in Sec. 4.3, that the frequency-resolved susceptibilities measured in the experiment are sensitive to the detailed structure of excitations, providing insights in particular about their localisation properties.

4.1 Experimental details

Here, we cover the basic details of the employed cQED setup and the implementation of pseudo-random AC-Stark shifts which yields a disordered version of the Tavis–Cummings (TC) model (the many-body generalisation of the Jaynes–Cummings model introduced in Sec. 2.2.2) in the near-resonant regime. We briefly review the general measurement protocol and its results for the TC model, before moving on to the realisation of the LMG model in the off-resonant regime in Sec. 4.2. For further details on the experimental apparatus, atoms preparation, and interrogation, we refer the interested reader to the Methods of Ref. [77].

4.1.1 Setup and Model

For the proposal of the previous chapter, the ensemble of cold atoms was considered to be trapped in a single cloud at an antinode of the longitudinal cavity mode. In this experiment, instead, the atoms are trapped across multiple antinodes, forming a one-dimensional chain. This is achieved via a cavity enhanced optical dipole trap, created by pumping the cavity on-axis with a laser beam whose wavelength is $2\lambda_{\text{cavity}}$. This choice of wavelength ensures that the optical lattice's potential minima are commensurate with the antinodes of the longitudinal cavity mode, as sketched in the lower panel of Fig. 4.1(b). This

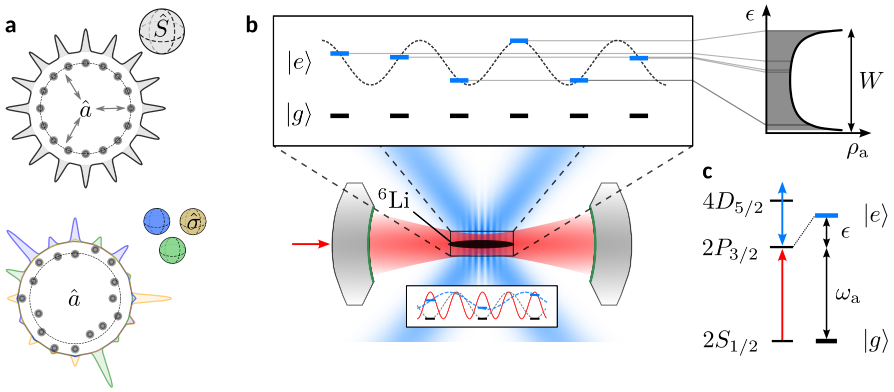

Figure 4.1: Concept of the experiment. (a) Fragmentation of collective light–matter eigenstates with increasing disorder. Top: Disorder-free system with all spins (spheres) identically coupled to the central mode $\hat{a}$ provided by the cavity field, forming a symmetric collective Dicke state. Bottom: With disorder, the collective state fragments into few- or single-spin ensembles whose constituents are located at arbitrarily large distances, exchanging excitations through the cavity, sketched here for three excitation modes. (b) Experimental realisation: Atoms are trapped in an optical resonator, forming an atom array commensurate with the cavity mode, ensuring identical atom–light coupling. Two crossed light-shifting beams (blue) illuminate the atoms with an incommensurate standing-wave inference pattern, leading to a quasi-random intensity distribution ρ_a over the atoms (right). The inset below illustrates the positions of the atoms (black bars) with respect to the cavity field intensity (red wave), the optical dipole trapping potential (grey wave) and the intensity of the light shifting lattice (blue wave). (c) Simplified level-diagram of the ^{6}Li atoms. The light-shifting laser (blue arrow) off-resonantly couples the $2P_{3/2}$ manifold with the higher-lying $4D_{5/2}$ manifold, yielding a dressed state $|e\rangle$ (blue), with an energy shift proportional to the laser intensity.

ensures a site-independent light–matter coupling g. Together with mapping the internal atomic states to spin-1/2 degrees-of-freedom, this yields a model of N Ising spins identically coupled to the central, bosonic photon mode of the cavity. By formally exposing the ith spin to a random energy shift ϵ_i, the model is described by the disordered Tavis–Cummings-type Hamiltonian

$$\hat{H}_\mathrm{TC} = \Delta_\mathrm{ca}\hat{a}^\dagger\hat{a} + g\sqrt{N}\left(\hat{S}^+\hat{a} + \hat{S}^-\hat{a}^\dagger\right) + \sum_{i=1}^{N}\epsilon_i\,\frac{\hat{\sigma}_i^z}{2}. \tag{4.1}$$

Here, $\hat{a}^\dagger$ and $\hat{a}$ are the creation and annihilation operators of photons in the cavity, $\hat{\sigma}_i^r$ are the r-Pauli operators acting on the Ising (pseudo-)spin-1/2 of

Table 4.1: Parameters of cQED setup. Spontaneous emission rate Γ of the D2 line of ^{6}Li, and measured values of the cavity loss rate κ and the single-photon Rabi frequency g, yielding the single-atom, single-photon cooperativity η. The thermal motion of the atoms, as set by the cloud's temperature T, yields an average atom–cavity coupling $\bar{g}$.

$\Gamma/2\pi$	$\kappa/2\pi$	$g/2\pi$	$\eta = (4g^2)/(\kappa\Gamma)$	T	$\bar{g}/2\pi$
5.8 MHz	0.45 MHz	2.05 MHz	6.4	200 μK	1.23 MHz

the i^{th} atom, $\hat{S}^{+(-)} = \sum_{i=1}^{N} \hat{\sigma}_i^{+(-)}/\sqrt{N}$ are the collective spin-raising (lowering) operators, and Δ_{ca} is the detuning between the cavity and the bare atomic resonance.

Experimentally, the Hamiltonian in Eq. 4.1 is realised by an array of $N = 90$ to 800 thermal ^{6}Li atoms confined in about 160 trapping sites, positioned at the anti-nodes of the resonant cavity field. The spins are encoded in the $2S_{1/2}^{F=1/2}$ ($|g\rangle$) and $2P_{3/2}$ ($|e\rangle$) states of the ^{6}Li atoms [Fig. 4.1(b,c)]. The cavity resonance is tuned close to the $2S_{1/2}$–$2P_{3/2}$ transition at 671 nm, with the detuning given by Δ_{ca}. The cavity is close to concentric, and the parameters relevant to the analyses presented in this chapter are summarised in Table 4.1.

The Hamiltonian of Eq. (4.1) conserves the total excitation number $\hat{a}\hat{a}^\dagger + \sum_{i=1}^{N} \hat{\sigma}_i^+\hat{\sigma}_i^-$, and we will work in the single-excitation regime. This is motivated by the fact that the experiment operates in the linear response regime, where the probe beam, with Rabi frequency Ω_{p}, is weak as compared to the rate of spontaneous emission Γ of the atomic excited state, as well as compared to the cavity loss rate κ, $|\Omega_{\text{p}}| \ll \Gamma, \kappa$. In the disorder-free instance of $\hat{H}_{\text{TC}}$ [Fig. 4.1(a), top], the single-excitation manifold is composed of (i) two bright states (polaritons) $(1/\sqrt{2})(\hat{S}^+ \pm \hat{a}^\dagger)|G\rangle|0\rangle$ at energies $\Delta_{\text{ca}}/2 \pm g\sqrt{N}$, and described by a single collective spin coupled to the cavity mode, and (ii) $N-1$ degenerate zero-energy dark states which are decoupled from the cavity field, and can be written as $(1/\sqrt{j(j+1)})(\sum_{i=1}^{j} \hat{\sigma}_i^+ - j\hat{\sigma}_{j+1}^+)|G\rangle|0\rangle$ for $j = 1, \dots, N-1$ [190]. Here, $|G\rangle \equiv \bigotimes_{i=1}^{N} |g\rangle_i$ is the global atomic ground state, and $|G\rangle|0\rangle$ denotes the product state with zero excitations in the joint atom–photon Hilbert space.

The collective spin description is broken by disorder, as illustrated in Fig. 4.1(a), bottom. This leads to a fragmentation of the dark state manifold into an ensemble of 'grey eigenstates' that are hybridisations of the delocalised photon field and of a few localised spins with similar energies [191]. Because the coupling to the cavity extends over the entire system, energy resonances between spins can occur at arbitrarily large distances in the presence of disorder. As a result, grey eigenstates have wave functions that are neither localised nor

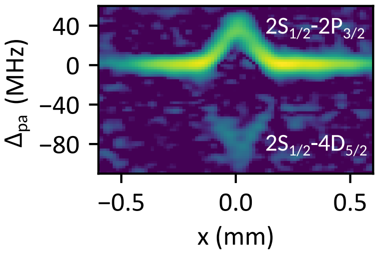

Figure 4.2: Example of spatially varying light-shift. Spatially resolved absorption spectroscopy of the D2 transition in the presence of a single light-shifting beam (Gaussian, centred at $x = 0\,\mathrm{mm}$ with a waist of $120\,\mu\mathrm{m}$), blue detuned from the $2P_{3/2}$–$4D_{5/2}$ transition by 50 MHz. The vertical axis indicates the detuning of the probe light from the bare atomic resonance. Both resonances of the Autler–Townes doublet are visible, the strong light-shifted single photon transition (top) and the faint two-photon transition (bottom).

delocalised, but *semi-localised* over multiple, arbitrarily distant spins [192, 193]. It has been demonstrated theoretically that for any strength of light–matter coupling this results in a *multi-fractal* structure of the eigenstates, similar to that found at the critical points of localisation–delocalisation transitions [194].

4.1.2 Implementation of disorder

Disorder was implemented by means of a spatially-varying AC-Stark shift, similar to the procedure proposed in Sec. 3.2.1.

Instead of a speckled light-shift beam, however, in this case the disorder is created by two laser beams that intersect at the position of the atoms, with frequency slightly detuned from the $2P_{3/2}$–$4D_{5/2}$ transition at 460 nm. These intersecting beams form a light-shifting lattice with a period of $1.04\,\mu\mathrm{m}$ that is incommensurate[1] with the trapping lattice, which has a period of 671 nm. This produces a quasi-random pattern of strong light-shifts of the $2P_{3/2}$ state, with negligible effect on atoms in the ground state, as illustrated in Fig. 4.1(b,c). These light-shifts result in quasi-disordered energy shifts ϵ_i, that translate into the spin language as random local longitudinal fields sampled from the distribution

$$\rho_{\mathrm{a}}(\epsilon) = \frac{1}{\pi\sqrt{\epsilon(W-\epsilon)}}, \tag{4.2}$$

where W is proportional to the intensity of the control laser (see App. B.1). For a given disorder strength W, the mean atomic resonance frequency is thus $\omega_{\mathrm{a}} + W/2$, as depicted in Fig. 4.1(b).

---

[1] The period of the light-shifting lattice was chosen such that the ratio to the period of the trapping lattice, $1.04\,\mu\mathrm{m}/671\,\mathrm{nm} \simeq 1.5499\ldots$, was near the golden ratio.

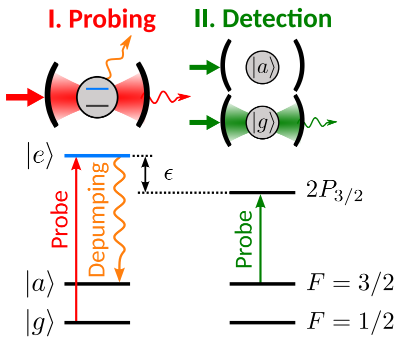

Figure 4.3: Measurement scheme. When probing the disordered system (I), photons entering the cavity from the probe (red arrow) have two decay channels: Either they leak out of the cavity (red wiggled arrow) and are detected by a single photon counter, or they are lost by free-space spontaneous emission of an atomic excitation (orange wiggled line). The latter can depump the atom into the $|a\rangle$ state, as the $|g\rangle$ to $|e\rangle$ transition is not closed. (II) These depumped atoms can be detected by measuring the cavity transmission: If the cavity is on resonance with the $|a\rangle$–$|e\rangle$ transition and only a single atom is in state $|a\rangle$, the transmission is strongly suppressed.

A demonstration of the spatially-varying light shift is given in Fig. 4.2, which shows an absorption image taken during the calibration of the excited-state's light shift, for a single Gaussian beam impinging on the atomic cloud.

4.1.3 Measurement protocol

By leveraging the open nature of the cavity, the cQED setup described above allows for the frequency-resolved measurement of both the optical and atomic response of the system. After preparing all atoms in the (ground, $|g\rangle$) state $2S_{1/2}^{F=1/2}$, the system is interrogated by weakly driving the cavity on-axis with a probe beam for a chosen interrogation time t_{meas}, as depicted in Fig. 4.3(I). During this time, a single-photon counter is used to measure the cavity's photon transmission signal, proportional to $\langle \hat{a}^\dagger \hat{a} \rangle$.

To measure the atomic excitations, the experiment exploited the fact that the transition between the $2S_{1/2}^{F=1/2}$ ($|g\rangle$) and $2P_{3/2}$ ($|e\rangle$) states of ^{6}Liis not closed: A ^{6}Li atom in the $2P_{3/2}$ state can spontaneously decay both back into the $2S_{1/2}^{F=1/2}$ state, or into the $2S_{1/2}^{F=3/2}$ state, which we denote as the auxiliary state $|a\rangle$. The large hyperfine splitting of 228 MHz between these two $2S_{1/2}^{F}$ states ensures that the auxiliary state $|a\rangle$ is not coupled to the cavity mode[2]. Consequently, measuring the total atomic population P_A in $|a\rangle$ after the interrogation has ended, allows one to extract information on the atomic

---

[2] The detuning of the cavity from the average light-shifted $2S_{1/2}^{F=3/2}$–$2P_{3/2}$ (a–e) transition is $\Delta_{c\bar{a}} + 228\,\text{MHz}$, so the a–e transition can become resonant only in the red-detuned case $\Delta_{c\bar{a}} < 0$. For the experiment in the near-resonant regime (Sec. 4.1.4), $\Delta_{c\bar{a}}$ was on

excitations $\langle \hat{S}^z \rangle = \langle \sum_{i=1}^{N} \hat{\sigma}_i^z \rangle/(2N)$. In the experiment, $P_A(t_{\mathrm{meas}})$ was measured subsequent to the above interrogation by shifting the cavity on-resonance with the a–e transition, and then performing another transmission spectroscopy measurement of the cavity, as depicted in Fig. 4.3(II). In this configuration, the cavity transmission is suppressed by $1/(\eta + 1)$ [195] in the presence of a single atom in the $F = 3/2$ state, yielding a single-atom level sensitivity for the detection of the atomic response.

For a weak probe beam, the measurement scheme can be treated within linear response, in which case the measured optical and atomic signals can be related to the absorptive part of the system's dynamic susceptibility [196]. This will be elaborated upon in Secs. 4.2.2–4.2.3. Repeating the above procedure over a range of probe frequencies thus provides the frequency-dependent photonic and atomic (spin) susceptibilities, χ_{p} and χ_{a}. In what follows we will mainly focus on the case where the cavity is far-detuned from the atomic resonance. In this regime, the cavity mode can be integrated out, such that the atomic susceptibility χ_{a} is the relevant observable.

4.1.4 Near-resonant regime and grey states

We briefly review the experimental results for the regime at small $\Delta_{\mathrm{c\bar{a}}}$ where the cavity resonance is close to the mean atomic resonances, $\Delta_{\mathrm{c\bar{a}}} = \Delta_{\mathrm{ca}} - W/2$ [see Fig. 4.4(a)].

In this regime, the system's dynamics are described by the TC Hamiltonian of Eq. (4.1), and the data for χ_{a} in Fig. 4.4(b) shows the expected normal-mode splitting of width $2g\sqrt{N}/2\pi = 22\,\mathrm{MHz}$ at zero disorder, $W = 0$. As a result of this splitting, a Rabi gap forms at $\Delta_{\mathrm{c\bar{a}}} = 0$, and direct atomic excitations at the bare resonance frequency are suppressed [see centre of Fig. 4.4(b)]. Although there are $N - 1$ eigenstates of the Hamiltonian lying within the gap, these are purely atomic, and the symmetry of the all-to-all atom–cavity coupling prevents their excitation, rendering them completely dark. Upon introducing disorder, we observe the onset of a non-zero response around zero detuning, a manifestation of the increase of photon weight of the originally dark purely atomic states. A representative spectrum of χ_{a} for $W/(2\pi) = 26\,\mathrm{MHz}$ is presented in Fig. 4.4(c). We observe that the fading out of the Rabi splitting occurs via a redistribution of the spectral weight from the polaritons to a wide spectrum of mid-gap states.

To further understand the evolution of the spectrum with disorder strength,

---

the order of ±30 MHz, for which the a–e transition remains far off-resonant. For the experiment in the large-detuning regime (Sec. 4.2), $\Delta_{\mathrm{c\bar{a}}} > 0$, i.e., blue-detuned.

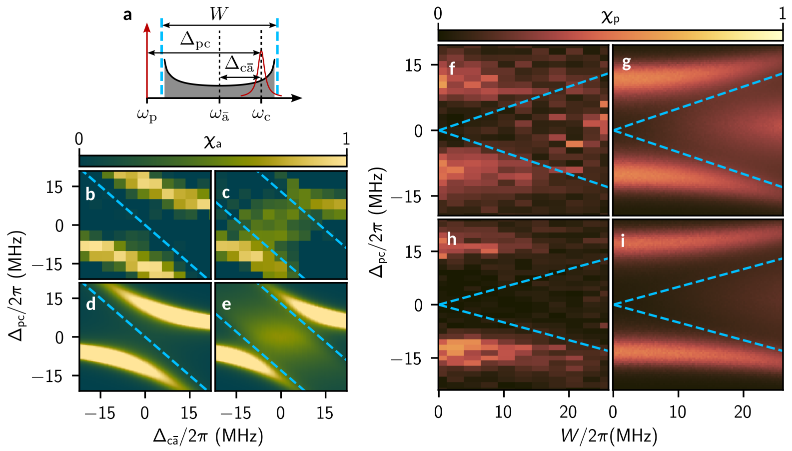

Figure 4.4: Response of the system in the central-mode regime. (a) Frequency diagram illustrating the relative detunings between the atoms with average frequency $\omega_{\bar{a}}$ in a range W, the cavity at frequency ω_c, and the probe at ω_p. The light-blue dashed lines indicate the edges of the atomic frequency distribution. In all other panels, the atomic states lie between the two light-blue lines. (b–e) Measured (b, c) and simulated (d, e, see Methods of Ref. [77], with $N = 100$ atoms) atomic susceptibility maps as a function of atom–cavity and pump–cavity detunings (x- and y-axis, respectively), for the clean system (b, d) and at maximal disorder $W/2\pi = 26\,\mathrm{MHz}$ (c, e). (f–i) Measured (f, h) and simulated (g, i) photonic susceptibility as a function of disorder strength W for different atom numbers; $N = 74$ (f, g) and $N = 145$ (h, i).

we probe the photonic susceptibility χ_p at $\Delta_{c\bar{a}} = 0$ as a function of disorder strength W, and detuning Δ_{pc}. The results are presented in Fig. 4.4(f,h) for different mean atom numbers N. For weak disorder, the photonic susceptibility χ_p confirms the presence of the two bright polaritons, and a manifold of degenerate dark states at the centre of the Rabi gap. As the disorder becomes comparable with the collective atom–cavity coupling, $W \sim g\sqrt{N}$, we observe a smooth increase of χ_p around $\Delta_{pc} = 0$, signalling the onset of a finite coupling of a grey state manifold emerging from the originally dark states. Simultaneously, the polaritons' response weakens and fades away for the largest disorder, where the spectrum consists of a resonance centred at $\Delta_{pc} = 0$ strongly broadened by the disorder.

The evolution of the spectrum with disorder is driven by the fragmentation of the eigenstates, from fully delocalised bright and dark states without disorder, to randomly distributed, isolated resonances for the largest disorder. This interpretation was confirmed by comparison of the data [Fig. 4.4(b,c,f,h)] with theoretical calculations [Fig. 4.4(d,e,g,i)] of the cavity transmission based on Green function techniques (see the Methods of Ref. [77]).

4.2 Large-detuning regime and Lipkin–Meshkov–Glick model

In the central mode model investigated so far, an essential role is played by the finite admixture of the spin excitations to the delocalised photon field. For large detuning $\Delta_{\mathrm{ca}} \gg g\sqrt{N}$, the cavity field is only virtually populated, giving rise to an all-to-all interaction between the spins, thereby realising an effective Lipkin–Meshkov–Glick (LMG) model [180, 197, 198], as we now show.

4.2.1 Derivation of the LMG model

Our starting point is the disordered Tavis–Cummings Hamiltonian $\hat{H}_{\mathrm{TC}}$, which is expressed in Eq. (4.1) relative to the rotating frame (RF) of the *bare* atomic resonance frequency ω_{a}. Within this RF, the probe beam is described by

$$\hat{V}(t) = \Omega_{\mathrm{p}} \mathrm{e}^{-i(\omega_{\mathrm{p}}-\omega_{\mathrm{a}})t} \hat{a}^{\dagger} + \mathrm{H.c.}, \tag{4.3}$$

with probe-laser and Rabi frequency ω_{p} and Ω_{p}, respectively.

The total Hamiltonian is thus $\hat{H}_{\mathrm{TC}} + \hat{V}(t)$. Modelling the cavity losses at rate κ through a dissipator superoperator $\mathcal{D}\bullet = \kappa(\hat{a} \bullet \hat{a}^{\dagger} - \left\{\bullet, \hat{a}^{\dagger}\hat{a}\right\}/2)$ in a Lindblad master equation [199], the equation of motion for the (Heisenberg picture) photonic operator $\hat{a}(t)$ is

$$\partial_t \hat{a}(t) = -i\left[\hat{a}(t), \hat{H}_{\mathrm{TC}} + \hat{V}(t)\right] - (\kappa/2)\hat{a}(t). \tag{4.4}$$

Using that cavity losses are sub-dominant, i.e., $\Delta_{\mathrm{ca}} \gg \kappa$ (see Table 4.1), the cavity mode adiabatically follows the evolution of the spin degrees of freedom as

$$\hat{a}(t) = -\frac{g\sqrt{N}\hat{S}^{-} + \Omega_{\mathrm{p}} \mathrm{e}^{-i(\omega_{\mathrm{p}}-\omega_{\mathrm{a}})t}}{\Delta_{\mathrm{ca}}}. \tag{4.5}$$

Substituting this expression into $\hat{H}_{\mathrm{TC}} + \hat{V}(t)$ eliminates the cavity mode, and one obtains (up to an irrelevant constant term $-\left|\Omega_{\mathrm{p}}\right|^2/\Delta_{\mathrm{ca}}$) the effective spin

Hamiltonian

$$\hat{H}(t) = \hat{H}_{\mathrm{LMG}} - \hat{\mathcal{V}}(t)\,, \text{ where} \tag{4.6}$$

$$\hat{H}_{\mathrm{LMG}} = \sum_{i=1}^{N} \epsilon_i \frac{\hat{\sigma}_i^z}{2} - JN\hat{S}^+\hat{S}^-, \tag{4.7}$$

$$\hat{\mathcal{V}}(t) = \frac{g\sqrt{N}}{\Delta_{\mathrm{ca}}}\left(\Omega_{\mathrm{p}} \mathrm{e}^{-i\Delta_{\mathrm{pa}}t}\hat{S}^+ + \mathrm{H.c.}\right), \tag{4.8}$$

with $\Delta_{\mathrm{pa}} \equiv \omega_{\mathrm{p}} - (\omega_{\mathrm{a}} + 2g^2/\Delta_{\mathrm{ca}})$. We note that Eqs. (4.6)–(4.8) are obtained after performing an additional RF transformation, which serves only to remove an otherwise constant contribution $(2g^2N/\Delta_{\mathrm{ca}})\hat{S}^z$—which is simply the dispersive shift of the collective spin—to Eq. (4.7). This yields the contribution $2g^2/\Delta_{\mathrm{ca}}$ in Δ_{pa} above.

Eliminating the cavity mode thus yields (all-to-all) spin-exchange interactions of strength $J = g^2/\Delta_{\mathrm{ca}}$, and the quenched disorder of Eq. (4.1) has propagated into the diagonal part of Eq. (4.7) as a random longitudinal field. Similar to $\hat{H}_{\mathrm{TC}}$, $\hat{H}_{\mathrm{LMG}}$ conserves the total number of excitations $\sum_{i=1}^{N} \hat{\sigma}_i^+\hat{\sigma}_i^-$. The level structure of $\hat{H}_{\mathrm{LMG}}$ thus consists of $N+1$ manifolds, with the nth manifold composed of $\binom{N}{n}$ states containing $n = 0, 1, \ldots, N$ excitations. In what follows, we will focus on the dynamics within the two lowest manifolds, $n = 0, 1$.

We note that Eq. (4.7) can be mapped to a pairing Hamiltonian [200, 201], central to the Bardeen–Cooper–Schrieffer (BCS) theory of superconductivity [202], and more generally is a particular case of the class of exactly solvable Richardson–Gaudin models [203–205].

4.2.2 Dynamic susceptibility

Having obtained the effective long-range interacting model of Eqs. (4.6)–(4.8), we now derive the form of the atomic susceptibility $\chi_{\mathrm{a}}(\Delta_{\mathrm{pa}})$ in the dispersive regime. In particular, $\chi_{\mathrm{a}}(\Delta_{\mathrm{pa}})$ is obtained from the absorptive part $\chi''(\Delta_{\mathrm{pa}})$ of the dynamic susceptibility of the effective model $\hat{H}_{\mathrm{LMG}}$ of Eq. (4.7), when the latter is initialised in its ground state $|G\rangle \equiv \bigotimes_{i=1}^{N} |g\rangle_i$, and subsequently subjected to the probe via the interaction $\hat{\mathcal{V}}(t)$ of Eq. (4.8).

Studying the dynamic susceptibility is motivated by the fact that the probe beam is weak $|\Omega_{\mathrm{p}}| \ll \Gamma$, so that one may treat $\hat{\mathcal{V}}(t)$ as a perturbation within the regime of linear response [196]. That it is the absorptive part which is relevant follows from the fact that the probe beam is driving, and thus depositing energy into, the system for the duration of the interrogation phase [Fig. 4.3(I)]. In particular, $|\Omega_{\mathrm{p}}| \ll \Gamma$ implies that atomic excitations decay much faster than the rate at which they are introduced into the system, so that one may study the limit in which there is at most a single excitation $n = 0, 1$ present in the system. That is, one need only consider the eigenstates $|G\rangle$ and $\{|m\rangle\}_{m=1}^{N}$, where the latter set of states forms the single-excitation manifold (SEM) of $\hat{H}_{\text{LMG}}$. These SEM states are superpositions of the single-excitation basis $|i\rangle = \hat{\sigma}_i^+|G\rangle$,

$$|m\rangle = \sum_{i=1}^{N} c_{mi}\hat{\sigma}_i^+|G\rangle, \tag{4.9}$$

where the expansion coefficients c_{mi} depend on the particular disorder realisation for $W > 0$. We denote the ground and SEM eigenenergies as $\mathcal{E}_G, \mathcal{E}_m$, and the spectral gaps as $E_{mG} \equiv \mathcal{E}_m - \mathcal{E}_G$, for $m = 1, \ldots, N$.

With respect to the set of states $\{|G\rangle, \{|m\rangle\}_{m=1}^{N}\}$, we then have (see App. B.3 for the derivation)

$$\chi''(\Delta_{\text{pa}}) = \pi \sum_{m\in\text{SEM}} \left| \langle m| \frac{g\sqrt{N}\Omega_{\text{p}}}{\Delta_{\text{ca}}} \hat{S}^+|G\rangle \right|^2 \delta(\Delta_{\text{pa}} - E_{mG}). \tag{4.10}$$

In what follows, we approximate the Dirac-delta functions in Eq. (4.10) as Lorentzian responses

$$\delta_\gamma(\omega) \equiv \frac{\gamma/\pi}{\gamma^2 + \omega^2}, \text{ such that } \delta(\omega) = \lim_{\gamma\to 0} \delta_\gamma(\omega). \tag{4.11}$$

Here, γ is the line-width of the (normalised) resonance, which according to the Wiener–Khintchine theorem [206, 207] corresponds to a finite experimental measurement time $1/\gamma$.

Inserting Eq. (4.11) into Eq. (4.10), and extracting the energy scales, we define the dimensionless atomic susceptibility $\chi_{\text{a}}(\Delta_{\text{pa}})$, as

$$\begin{aligned} \chi_{\text{a}}(\Delta_{\text{pa}}) =& \gamma \left| \frac{\Delta_{\text{ca}}}{g\Omega_{\text{p}}} \right|^2 \chi''(\Delta_{\text{pa}}) \\ =& \sum_{m\in\text{SEM}} N \left| \langle m|\hat{S}^+|G\rangle \right|^2 \frac{\gamma^2}{\gamma^2 + (\Delta_{\text{pa}} - E_{mG})^2} \\ \equiv& \sum_{m\in\text{SEM}} \chi_{\text{a},m}(\Delta_{\text{pa}}). \end{aligned} \tag{4.12}$$

At zero disorder, $W = 0$, the SEM basis can be determined analytically to be

$$|m\rangle = \begin{cases} \hat{S}^+|G\rangle, & m = 1 \\ \sum_{j\neq i^*} c_{mj}(|i^*\rangle - |j\rangle), & m = 2, \ldots, N, \end{cases} \tag{4.13}$$

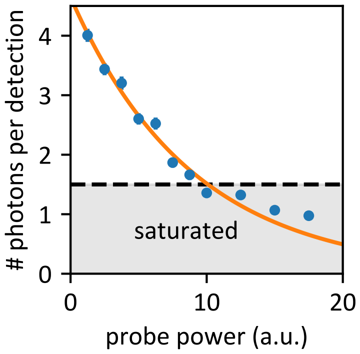

Figure 4.5: Saturation of depumping signal. Data taken during the calibration of the depumping scheme of Fig. 4.3(II). The mean number of transmitted photons during the depumping detection is plotted against the power of the probe used during the interrogation of the disordered system. Error bars represent statistical fluctuations. The exponential decay of the signal with probe power is made evident by the orange line, which shows a fit of $P_\mathrm{A}(t_\mathrm{meas})$ as given by Eq. (4.19).

where the choice of $i^* \in \{1, \ldots, N\}$ is arbitrary due to the translational symmetry of $\hat{H}_\mathrm{LMG}$ at $W = 0$. The corresponding energies [3] are

$$\begin{aligned}\mathcal{E}_m =& \begin{cases} -NJ, & m = 1 \\ 0, & m = 2, \ldots, N, \end{cases} \\ \mathcal{E}_G =& 0. \end{aligned} \tag{4.14}$$

Inserting Eq. (4.13) into Eq. (4.12), one finds that for $W = 0$, only the first excited state $|m = 1\rangle$ contributes to $\chi_\mathrm{a}(\Delta_\mathrm{pa})$, such that on resonance $\chi_\mathrm{a}(\Delta_\mathrm{pa} = E_{1G}) = \chi_{\mathrm{a},1}(E_{1G}) = N$ (see Fig. 4.7 and inset).

4.2.3 Modelling the measurement protocol via a Lindblad master equation

We now show that the atomic susceptibility $\chi_\mathrm{a}(\Delta_\mathrm{pa})$ of Eq. (4.12) can be extracted from measurements of the atomic population $P_\mathrm{A}(t)$ of the auxiliary state $|a\rangle$ at a given point in time t.

Intuitively, it is plausible that $\chi_\mathrm{a}(\Delta_\mathrm{pa})$ and $P_\mathrm{A}(t)$ should be connected: On the one hand, $\chi_\mathrm{a}(\Delta_\mathrm{pa})$ is simply a rescaling of the absorptive part of the dynamic susceptibility $\chi''(\Delta_\mathrm{pa})$ [see Eq. (4.10)–(4.12)] of the effective model described by Eq. (4.6), and thus quantifies the time-averaged energy absorbed by this system when subjected to a perturbation at frequency Δ_pa. On the other hand, the system can absorb energy from the probe beam *only* via coherent excitations of the atomic population from state $|g\rangle$ ($2S_{1/2}^{F=1/2}$) to $|e\rangle$ ($2P_{3/2}$). The population

---

[3] The degeneracy of the global ground state $|G\rangle$ with the $N-1$ states $|m > 1\rangle$ is a result of the first term of Eq. (4.7) vanishing as $W \to 0$. If instead, $\epsilon_i \to h > 0$ as $W \to 0$, then the energies would be shifted to $\mathcal{E}_G = -Nh/2$, $\mathcal{E}_{m=1} = -(N-2)h/2 - NJ$ and $\mathcal{E}_{m>1} = -(N-2)h/2$. Assuming $h > NJ$ then explains the choice of nomenclature for $|G\rangle$ and $|m = 1\rangle$ being the ground, respectively, first-excited state.

of state $|a\rangle$ ($2S_{1/2}^{F=3/2}$) can then change *only* via spontaneous decay from state $|e\rangle$ at a rate Γ_{a}. Therefore, detecting $P_{\mathrm{A}}(t) > 0$ implies that the system has absorbed energy via atomic excitations. Furthermore, the probability to excite the system into a collective state containing an atomic excitation upon probing, is maximised when the probe frequency Δ_{pa} [see Eq. (4.8)] is resonant with transitions from the system's collective ground state $|G\rangle$. It follows that the total atomic population $P_{\mathrm{A}}(t_{\mathrm{meas}})$ found in state $|a\rangle$ after the interrogation time is a measure of how *susceptible* the system was to excitations introduced by the probe at frequency Δ_{pa}.

We give the above intuition an analytic foundation by modelling the measurement protocol of Sec. 4.1.3 via a Lindblad master equation. Detailed calculations are given in App. B.2, and we discuss only the pertinent steps here.

We work in a rotating frame generated by $N\Delta_{\mathrm{pa}}\hat{S}^z$, such that the Hamiltonian of Eq. (4.6) is time-independent, i.e., $\hat{\mathcal{V}}(t) \to \hat{\mathcal{V}} = \hat{\mathcal{V}}(0)$. The Lindblad equation is then given by

$$\partial_t\hat{\rho}(t) = -i\left[\hat{H}_{\mathrm{LMG}} - N\Delta_{\mathrm{pa}}\hat{S}^z + \hat{\mathcal{V}}, \hat{\rho}(t)\right] + \left(\mathcal{D}[\Gamma_{\mathrm{g}}; \{\hat{\sigma}_i^-\}] + \mathcal{D}[\Gamma_{\mathrm{a}}; \{|a\rangle\langle e|_i\}]\right)\hat{\rho}(t), \tag{4.15}$$

where $\hat{\rho}(t)$ denotes the system's density matrix, and the superoperators

$$\mathcal{D}[\gamma'; \{\hat{L}_i\}]\hat{\rho}(t) \equiv \gamma' \sum_{i=1}^{N} \left(\hat{L}_i\hat{\rho}(t)\hat{L}_i^\dagger - \left\{\hat{L}_i^\dagger\hat{L}_i, \hat{\rho}(t)\right\}/2\right), \tag{4.16}$$

describe dissipation at a rate γ', due to jump processes generated by $\{\hat{L}_i\}$. Specifically, the superoperators with rates Γ_{g} and Γ_{a} describe spontaneous decay of atoms from $|e\rangle$ to $|g\rangle$ and $|a\rangle$, respectively. The decay rates $\Gamma_{\mathrm{g}}, \Gamma_{\mathrm{a}}$ are branching ratios of the natural linewidth $\Gamma = 5.8 \times 2\pi\,\mathrm{MHz}$ of the D2 line of ^{6}Li, i.e., $\Gamma_{\mathrm{g}} + \Gamma_{\mathrm{a}} = \Gamma$. Spontaneous emission from $|a\rangle$ to $|g\rangle$ can be neglected on the timescales of the experiment, as for ^{6}Li it is forbidden by selection rules.

In the derivations of App. B.2, we make the simplifying assumption that there is a single excitation in the system. This is motivated physically by the fact that the probe beam's amplitude Ω_{p} is much weaker than the natural linewidth Γ of ^{6}Li. Consequently, atomic excitations decay at a rate much faster than the rate at which they are introduced by the probe beam, $|\Omega_{\mathrm{p}}| \ll \Gamma$. For long probing times, or strong probes, however, multiple excitations can, in principle, accumulate in the auxiliary state manifold. However, the presence of a single atom in state $|a\rangle$ drastically suppresses the transmission signal, due to the cavity's high cooperativity [195]. To avoid saturation of the transmission signal, the experiment was thus operated in a regime where at most one atom was in state $|a\rangle$. We therefore project the dynamics of Eq. (4.15) onto the Hilbert subspace with at most one excitation and at most one atom in the auxiliary state $|a\rangle$.

We then utilise a separation of scales to derive the equation of motion for $P_\mathrm{A}(t) \equiv \sum_{i=1}^{N} \langle a_i|\hat{\rho}(t)|a_i\rangle$, where $|a_i\rangle \equiv |a\rangle\langle g|_i|G\rangle$ are single-excitation states in the auxiliary-state manifold: Within the time domain $t \gg (\Gamma/2)^{-1}$, all coherences as well as the SEM populations can be adiabatically eliminated from the rate equations of the remaining populations $p_G(t)$ and $\{\langle a_i|\hat{\rho}(t)|a_i\rangle\}_{i=1}^{N}$. Doing so, one finds that

$$\partial_t p_G(t) = -\partial_t P_\mathrm{A}(t), \tag{4.17}$$

and to lowest order in $(\Gamma/2)^{-1}$,

$$\begin{aligned} \partial_t p_G(t) &= -\Gamma_\mathrm{a} \sum_{m\in\mathrm{SEM}} \frac{|\mathcal{V}_{mG}|^2}{(\Gamma/2)^2 + (E_{mG} - \Delta_\mathrm{pa})^2} p_G(t) \\ &= -\frac{\Gamma_\mathrm{a}}{(\Gamma/2)^2} \left|\frac{g\Omega_\mathrm{p}}{\Delta_\mathrm{ca}}\right|^2 \chi_\mathrm{a}(\Delta_\mathrm{pa}) p_G(t). \end{aligned} \tag{4.18}$$

In the last line, we have identified the Lorentzian response of Eq. (4.11), with linewidth $\gamma = \Gamma/2$. Further, using that (within the rotating frame of $N\Delta_\mathrm{pa}\hat{S}^z$) the matrix elements $\mathcal{V}_{mG}$ follow from Eq. (4.8) as $\mathcal{V}_{mG} = \frac{g\sqrt{N}\Omega_\mathrm{p}}{\Delta_\mathrm{ca}}\langle m|\hat{S}^+|G\rangle$, we have identified the relation to $\chi_\mathrm{a}(\Delta_\mathrm{pa})$, as defined by Eq. (4.12).

Integrating Eq. (4.18) over a measurement time t_meas, with initial conditions $p_G(0) = 1, P_\mathrm{A}(0) = 0$, and making use of the conservation of atomic population as given by Eq. (4.17), we find

$$P_\mathrm{A}(t_\mathrm{meas}) = 1 - \exp\left(-\frac{\Gamma_\mathrm{a}}{(\Gamma/2)^2}\left|\frac{g\Omega_\mathrm{p}}{\Delta_\mathrm{ca}}\right|^2 \chi_\mathrm{a}(\Delta_\mathrm{pa}) t_\mathrm{meas}\right). \tag{4.19}$$

This result confirms the monotonic relation between $P_\mathrm{A}(t)$ and $\chi_\mathrm{a}(\Delta_\mathrm{pa})$. It is obtained with respect to the experiment's initial conditions $p_G(0) = 1, P_\mathrm{A}(0) = 0$, and is valid for times $t \gg (\Gamma/2)^{-1}$.

The saturation of $P_\mathrm{A}(t_\mathrm{meas})$ as a function of the probe power $|\Omega_\mathrm{p}|^2$, as illustrated by the data of Fig. 4.5, is captured by Eq. (4.19). Further, for a given probe power, the saturation rate is maximal at those probe frequencies Δ_pa at which $\chi_\mathrm{a}(\Delta_\mathrm{pa})$ is largest: Since population transfer from $|G\rangle$ to a state $|m\rangle$ of the SEM is maximised when the probe frequency is resonant with the transition frequency E_{mG} [i.e., resonant with a frequency at which the system is most *susceptible* to perturbations, as quantified by $\chi_\mathrm{a}(\Delta_\mathrm{pa})$], the concomitant

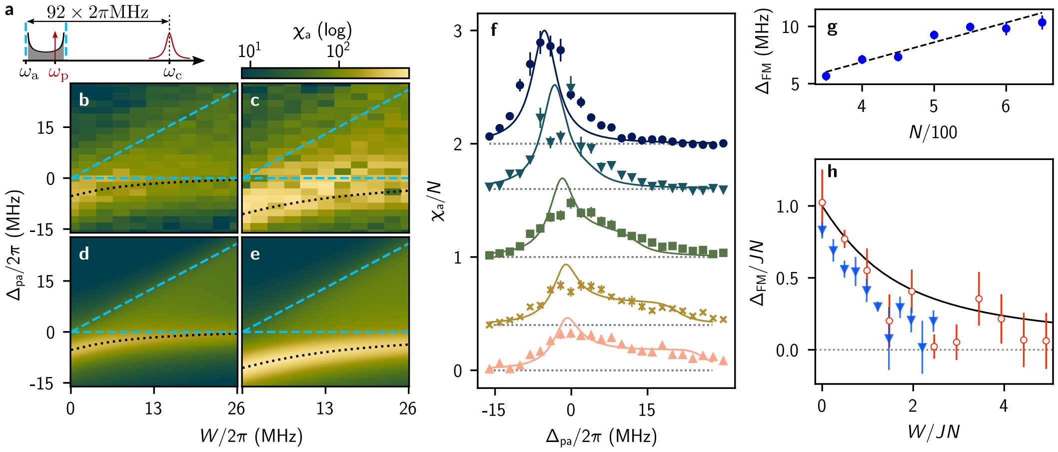

Figure 4.6: Response of the random LMG model. (a) Frequency diagram depicting the detuning between the atomic disorder, the cavity and the weak cavity probe. (b–e) Measured (b, c) and simulated (d, e) atomic susceptibility for $N = 303$ (b, d), and $N = 610$ (c, e) atoms. (f) Cuts through b and d, illustrating the quantitative agreement between experiment (markers) and theory (solid lines). Cuts show data for different disorder strengths $W/2\pi = 0.0, 5.2, 13.0, 20.8, 26.0$ (MHz) (top to bottom), and are offset from one another according to $(26 - W/2\pi)/13$. (g) Scaling of the collective ferromagnetic gap $\Delta_{\text{FM}} = JN$ at zero disorder $W = 0$ with mean atom number N. (h) Behaviour of Δ_{FM} as a function of disorder strength W for $N = 303$ (empty red circles) and $N = 610$ (blue triangles) atoms. To illustrate the scale invariance of the system, the axes are rescaled by the zero-disorder ferromagnetic gap size JN. Markers represent the experimental data with statistical error bars, and the lines show the theoretical results obtained by exact diagonalisation (see App. B.5).

accumulation of population in the auxiliary state is also maximised. Conversely, for a fixed measurement time t_{meas}, saturation of the signal $P_{\text{A}}(t_{\text{meas}})$ can be suppressed by reducing the probe's power. This is crucial for the precision of the experimental data presented in Fig. 4.6, which consists of multiple datasets taken for different probe powers in the (Δ_{pa}, W) parameter space.

4.2.4 Comparison to experimental results

Similar to the central mode model, in the absence of disorder ($W = 0$), Eq. (4.7) describes the dynamics of a collective spin within the Hilbert subspace of symmetric states. The non-linearity inherited from the spin–cavity coupling favours a ferromagnetic ground state, protected by a finite gap of size $\Delta_{\text{FM}} = JN$ [see Eq. (4.14) and the related footnote]. A striking manifestation of ferromagnetism is the strong suppression of the zero–frequency magnetic response.

To realise the model of Eq. (4.7), the cavity was blue-detuned from the atomic transition by $\Delta_{\mathrm{ca}}/2\pi = 92\,\mathrm{MHz}$, and subsequently probed at a frequency ω_{p} in the vicinity of the bare atomic resonance ω_{a} [see Fig. 4.6(a)]. In this regime, the transmission of the cavity is negligible such that $\chi_{\mathrm{p}} \sim 0$, and the atomic signal $\chi_{\mathrm{a}}(\Delta_{\mathrm{pa}})$ of Eq. (4.12) directly measures the transverse spin susceptibility of the system at frequency $\Delta_{\mathrm{pa}} = \omega_{\mathrm{p}} - (\omega_{\mathrm{a}} + 2g^2/\Delta_{\mathrm{ca}})$ [as defined below Eq. (4.8)]. As shown in Fig. 4.6(b,c), in the absence of disorder, the frequency dependence of χ_{a} reveals the finite ferromagnetic gap, of magnitude Δ_{FM}, as well as the reduced zero–frequency susceptibility at $\Delta_{\mathrm{pa}} = 0$. The signal is broadened by the finite decay rate of the excited atomic states, which reduces to a convolution of the response with the linewidth of the atomic transition, as shown in the derivation of $P_A(t_{\mathrm{meas}})$ in Eqs. (4.18)–(4.19).

We now investigate this model in the presence of disorder. Similar to the central mode model, this breaks the description in terms of a collective spin, restoring the system's ability to explore the full Hilbert space. For a given disorder strength W, the susceptibility [see Fig. 4.6(f)] shows an asymmetric peak, corresponding to a collectively enhanced response superimposed with a weak and broad background whose width traces the disorder strength [dashed blue line in Fig. 4.6(b–e)]. This is a manifestation of the gradual fragmentation of the collective spin, as disorder renders the individual spins off-resonant with each other. The peak is located at $-\Delta_{\mathrm{FM}}$, and we denote its amplitude by $\chi_{\mathrm{a}}^{\mathrm{FM}}$. Tracking the location of this peak provides a measurement of the ferromagnetic gap as a function of W. Without disorder, this gap increases linearly with atom number, as shown in Fig. 4.6(g). With increasing disorder, it decreases smoothly towards zero, as shown in Fig. 4.6(h), where, for low enough atom numbers, the gap is zero within the error bars. This demonstrates the competition between the infinite-range cavity-mediated interaction J and spectral disorder W for the dynamics of the effective model $\hat{H}_{\mathrm{LMG}}$.

The experiment's results are in very good agreement with numeric simulations of the response χ_{a} of $\hat{H}_{\mathrm{LMG}}$ (detailed in App. B.5), over the entire parameter regime [see Fig. 4.6(b–f)]: The simulated system sizes were set as the mean atom numbers N realised across all experimental runs, and the effect of the atoms' thermal motion on the atom–cavity coupling g, quoted in Table. 4.1, has been taken into account. The decrease of the ferromagnetic gap [Fig. 4.6(h)] indicates a drastic change of the system properties as disorder increases. However, in the thermodynamic limit the system is always ferromagnetic and no paramagnetic phase transition should occur. Indeed, intuitively for any fixed disorder strength, increasing the number of atoms will always lead to an infinite number of close-to-resonance spins, enforcing ferromagnetism in the thermodynamic limit for an arbitrarily large disorder strength. However, for any finite number of atoms, there exists a disorder strength large enough to bring the ferromagnetic gap close to zero, by rendering each spin essentially spectrally isolated from all the others, thus crossing the system over into a paramagnet.

More precisely, our simulations show that finite systems display a minimal gap at a disorder strength $W^\star$ suggestive of critical behaviour; however, the value of $W^\star$ diverges with increasing atom number (see App. B.6 and Fig. B.1).

4.3 Localisation of excitations

The existence and distribution of energy resonances in disordered systems is the essence of Anderson localisation. In the cQED experiment described above, excitations can hop at arbitrarily large distances provided the spins are closely resonant. Disorder thus decimates the spins available for resonance by offsetting most spins from each other, but does not prevent long-distance propagation [192, 194]. In this way, increasing the disorder strength should induce localisation, in the sense that collective spin excitations become localised over fewer and fewer (albeit arbitrarily separated in space) sites.

A typical measure to probe localisation is the participation ratio, which quantifies the extent to which a given state is (de)localised over a basis of interest. In our context, we wish to study the (de)localisation of a SEM eigenstate $|m\rangle$ [as defined in Eq. (4.9)] of $\hat{H}_{\mathrm{LMG}}$ over the spins i of the system. This is quantified by the participation ratio

$$\mathrm{PR}_m = \left(\sum_{i=1}^{N} |c_{mi}|^4 \right)^{-1} \in [1, N], \tag{4.20}$$

of which the limiting values 1 and N are respectively obtained at $c_{mi} = \delta_{i,i^*}$ (full localisation at some site i^*, achieved at $W \to \infty$), and $c_{mi} = 1/\sqrt{N}$, $\forall\, i$ (full delocalisation over all N sites, achieved at $W \to 0$).

The spectroscopic probe employed in the above experiment, however, does not yield information which is spatially-resolved over the sites i. Nevertheless, the frequency-resolved information contained in the measured atomic susceptibility χ_{a} does carry relevant insights about the localisation of excitations. In particular, the participation ratio PR_1 of the first excited state obeys

$$\chi_{\mathrm{a},1} \geq \mathrm{PR}_1, \tag{4.21}$$

at any $W \geq 0$, where $\chi_{\mathrm{a},1} = \chi_{\mathrm{a},1}(E_{1G})$ is the contribution of the first excited state to the atomic susceptibility when the system is probed on resonance with the transition to this state, from the global ground state.

We now prove this relation, before discussing the experimental results.

4.3.1 Participation ratio and its relation to the susceptibility

Our proof of Inequality (4.21) relies on the identification of PR_1 and $\chi_{\mathrm{a},1}(E_{1G})$ [Eqs. (4.20) and (4.12)] as monotonic functions of different Rényi entropies,

$$H_\alpha(\boldsymbol{p}) = \frac{1}{1-\alpha}\log\left(\sum_i p_i^\alpha\right), \tag{4.22}$$

over a probability distribution $\boldsymbol{p} = (p_1, p_2, \ldots)$, and then exploiting the hierarchy [208],

$$H_{\alpha_1}(\boldsymbol{p}) \geq H_{\alpha_2}(\boldsymbol{p}), \text{ for any real numbers } \alpha_2 \geq \alpha_1 \geq 0. \tag{4.23}$$

To this end we note that:

(i) On resonance $\Delta_{\mathrm{pa}} = E_{mG}$, the mth summand of the atomic susceptibility defined in Eq. (4.12) reduces to

$$\chi_{\mathrm{a},m}(E_{mG}) = \left|\sum_{i=1}^N c_{mi}\right|^2 \in [1, N], \tag{4.24}$$

whose limiting values are obtained with the same distributions of c_{mi} as for PR_m [see Eq. (4.20) and text thereafter].

(ii) Using Perron–Frobenius theory [209], one can show that for any disorder strength $W \geq 0$, the lowest SEM eigenstate $|m=1\rangle$ of $\hat{H}_{\mathrm{LMG}}$ [as defined in Eq. (4.7)] satisfies $c_{1i} \geq 0, \forall i = 1, \ldots, N$. Hence, one has that $c_{1i} = +\sqrt{p_{1i}}$, where $p_{mi} \equiv |c_{mi}|^2$ are the probabilities associated to the amplitudes c_{mi}. A proof is provided in App. B.4.

Now, for the identification with Rényi entropies, we expand both sides of Inequality (4.21) and employ point (ii). This yields

$$\chi_{\mathrm{a},1}(E_{1G}) = \left|\sum_{i=1}^N c_{1i}\right|^2 = \left(\sum_i p_{1i}^{\alpha_1}\right)^{\frac{1}{1-\alpha_1}} = \exp(H_{\alpha_1}(\boldsymbol{p}_1)), \tag{4.25}$$

$$\mathrm{PR}_1 = \left(\sum_{i=1}^N |c_{1i}|^4\right)^{-1} = \left(\sum_i p_{1i}^{\alpha_2}\right)^{\frac{1}{1-\alpha_2}} = \exp(H_{\alpha_2}(\boldsymbol{p}_1)), \tag{4.26}$$

where $\alpha_1 = 1/2$, $\alpha_2 = 2$, and $\boldsymbol{p}_1 \equiv (p_{11}, p_{12}, \ldots, p_{1N})$. Since $\exp(x)$ is monotonic, the hierarchy of Rényi entropies in Eq. (4.23) is preserved, and thus

$$\exp(H_{\alpha_1}(\boldsymbol{p}_1)) \geq \exp(H_{\alpha_2}(\boldsymbol{p}_1)) \text{ for } \alpha_1 = 1/2 \text{ and } \alpha_2 = 2. \tag{4.27}$$

This concludes the proof.[4]

We note that Inequality (4.21) [as well as its looser form in terms of the full $\chi_{\mathrm{a}}(E_{1G})$, see Inequality (4.28) below] becomes an equality in both limits of $|m = 1\rangle$ being fully (de)localised. This too follows from the above expression in terms of Rényi entropies: For any $\alpha \geq 0$, $H_\alpha(\boldsymbol{p}) = \log(N)$ if $p_i = 1/N$, $\forall i = 1, \ldots, N$ (maximal uncertainty), and $H_\alpha(\boldsymbol{p}) = 0$ if $p_i = \delta_{i,i^*}$ for some $i^* = 1, \ldots, N$ (maximal certainty).

4.3.2 Comparison to experimental results

We have seen above that a system's magnetic response may be used to bound the participation ratio of the excitations, i.e., the number of spins contributing to the wave function.

However, the bound of the participation ratio, as defined by Inequality (4.21), is not directly accessible from the measured data presented in Fig. 4.6: Due to the finite atomic linewidth [see Eq. (4.19) and the derivation thereof], extracting *only* the $m =$ 1st summand of the atomic susceptibility is not feasible, as nearby

---

[4] The relation of Eq. (4.26) exemplifies that the participation ratio is an entropic measure, quantifying the degree of (un)certainty [(de)localisation]—obtained from some state's expansion coefficients—as to its spread over a chosen set of degrees of freedom (basis). In this context, the generalised *inverse* participation ratio $\mathrm{IPR}_q(|\psi\rangle) = \sum_{i=1}^{N} |\langle i|\psi\rangle|^{2q}$ is used to study the behaviour of all moments $q \geq 0$ of a state's probability distribution $\boldsymbol{p} = (|\langle i = 1|\psi\rangle|^2, \ldots, |\langle i = N|\psi\rangle|^2)$, and thus study a state's localisation properties in more detail. In particular, states with a non-trivial, q-dependent, system-size scaling $\mathrm{IPR}_q(|\psi\rangle) \propto N^{-\tau_q}$ for all $q \geq 0$ are termed to be "multifractal" [210]. In this context, it is convenient to define the multifractal dimension $D_q = d\frac{\tau_q}{q-1}$ (d is the physical dimension of the system), which is identically zero in insulating states, whilst metallic states exhibit $D_q = d$ for all $q \geq 0$. At critical points, in contrast, D_q is a non-trivial function of q, indicating multifractality. It was shown in Refs. [77, 194] that the semi-localised grey eigenstates of the TC model studied in Sec. 4.1.4 are multifractal. As alluded to in [194], $\mathrm{IPR}_q(|\psi\rangle)$ can be viewed as an analogue of the Rényi entropy, being most sensitive to the tails(largest components) of the probability distribution $\boldsymbol{p}$ for small(large) q. Using our derivations above, we can formalise this analogy as follows: Combining the expressions for $\mathrm{IPR}_q(|\psi\rangle)$ and D_q, one has $D_q = \frac{d}{1-q}\frac{\log(\mathrm{IPR}_q(|\psi\rangle))}{\log(N)}$, which can be expressed in terms of Rényi entropies as $D_q = d\frac{H_{\alpha=q}(\boldsymbol{p})}{\log(N)}$. This relation exemplifies the intimate link between entropy and quantifiers of a state's (de)localisation properties, and has as an immediate consequence that D_q decays monotonically with $q \geq 0$.

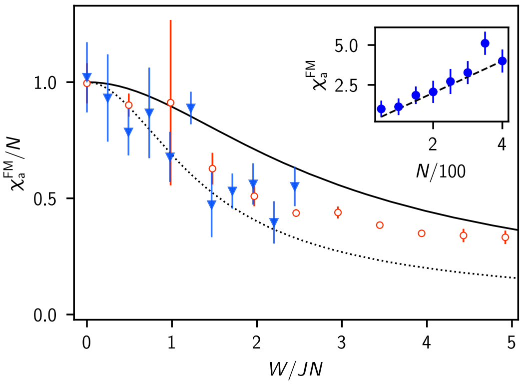

Figure 4.7: Participation ratio bound from atomic susceptibility. Normalised atomic susceptibility χ_a^{FM}, an upper bound to the participation ratio PR_1 of the first excited state, for $N = 303$ (empty red circles) and $N = 610$ (blue triangles) as a function of normalised disorder strength W/JN. The solid black line shows the corresponding simulation results for $\chi_{a,1}$ of Eq. (4.21). The black dotted line is the directly simulated participation ratio of the first excited state, PR_1. Inset: Maximum value of the zero-disorder atomic susceptibility as a function of atom number, showing linear scaling expected from the definition of χ_a in Eq. (4.12).

resonances add to the measured signal. What can be feasibly extracted is the on-resonance amplitude χ_a^{FM} of the full susceptibility of Eq. (4.12), which satisfies

$$\chi_a^{FM} \equiv \chi_a(E_{1G}) \geq \chi_{a,1}(E_{1G}), \tag{4.28}$$

by definition.

The frequency resolved measurements of Sec. 4.2.4 thus allow one to verify the fragmentation of the system's collective excitations into ever-more localised wave-functions, consistent with the expectations for eigenstates of the central mode model of Sec. 4.1.4 [192, 194, 211]. The bounds of Inequalities (4.21) and (4.28) are saturated for $W = 0$, where $PR_1 = N$ corresponds to a wavefunction uniformly distributed over all spins, as well as in the limit $W \to \infty$ in which the excitation becomes localised on a single spin ($PR_1 \to 1$).

Figure 4.7 shows the bound to the participation ratio extracted from the measured data of Fig. 4.6(b,c) via Inequality (4.28). The data shows a decrease by more than a factor of two as the disorder strength reaches the largest values. Upon normalisation of PR_1 by the mean atom number N, and of W by the corresponding zero-disorder ferromagnetic gap JN, all the data collapse onto each other and agree with simulations. The figure shows also the theoretically predicted value of PR_1 (simulated numerically as in App. B.5), which obeys the bound given by the data. Similar to the ferromagnetic gap, suggestive as these findings are, they do not herald a transition from delocalised to localised. For a fixed disorder strength, increasing the number of atoms leads to an infinite number of close-to-resonance spins at arbitrary distances, preventing full localisation but leading to a semi-localised regime similar to the critical regime of the Anderson transition [192].

4.4 Discussion

The ability to introduce controlled disorder in cQED offers exciting prospects for further investigations. For example, the relation of $\hat{H}_{\mathrm{LMG}}$ to the pairing Hamiltonian of BCS theory offers the prospect of experimentally studying the role of disorder in superconductivity, as proposed in Refs. [212, 213]. In this case, the atomic susceptibility measurements, in particular of $\chi_{\mathrm{a},1}(\Delta_{\mathrm{pa}} = E_{1G}) = \sum_{i,j=1}^{N} c_{1i}^{*} c_{1j}$, would directly map to the pairing gap, defined in Ref. [212] as $\sqrt{\langle m = 1|\hat{S}^{+}\hat{S}^{-}|m = 1\rangle} = \sum_{i,j=1}^{N} c_{1i}^{*} c_{1j}/N$. More broadly, Eq. (4.7) allows the direct simulation of Richardson–Gaudin models that are relevant to a variety of many-body systems, from superconductivity in ultrasmall grains to quark physics and neutron stars [205]. The combination of disorder with cavity-mediated interactions could further be used to study glassy phases of matter [214].

Within the context of Chap. 3, the realisation of controlled disorder in a fermionic cQED system, using a disordered light-shift as discussed in Secs. 3.2.1 and 4.1.2, marks the achievement of an important milestone on the path to quantum simulating the Sachdev–Ye–Kitaev model in the cQED platform. Whilst the light-shifting technique was employed in the above experiments to generate pseudo-random disorder in the on-site energies of spin systems, adding an off-resonant drive and eliminating the excited state will allow for the generation of effective models of spinless fermions with random interaction amplitudes as required for the Sachdev–Ye–Kitaev model.

5 Universal equilibration dynamics of the Sachdev–Ye–Kitaev model

This chapter is based on the publication S. Bandyopadhyay, P. Uhrich, A. Paviglianiti and P. Hauke, “Universal equilibration dynamics of the Sachdev-Ye-Kitaev model”, Quantum **7**, 1022 (2023). As such, most of the derivations and discussion presented in this chapter are adapted from there. My main contributions are the development of the effective master equation framework of Secs. 5.3–5.4, as well as to the interpretation of the numeric results of Sec. 5.2. Corrections to the theory developed in Sec. 5.3 are discussed in Sec. 5.5, which provides a brief summary of the follow-up work A. Paviglianiti, S. Bandyopadhyay, P. Uhrich and P. Hauke, “Absence of operator growth for average equal-time observables in charge-conserved sectors of the Sachdev-Ye-Kitaev model”, J. High Energ. Phys. **2023**, 126 (2023), which formed part of the Masters thesis [83] of A. Paviglianiti.

Equilibrium quantum many-body systems in the vicinity of phase transitions generically manifest universality [26]. In contrast, limited knowledge has been gained on possible universal characteristics in the non-equilibrium evolution of systems in quantum critical phases. In this chapter, we present such a universal feature in the equilibration dynamics of the SYK Hamiltonian, which, as we saw in Chap. 2, lends itself to a phenomenological description of quantum critical regions due to its lack of quasiparticles.

Far-from equilibrium, universality is generically attributed to the insensitivity of observables to the microscopic system parameters and initial conditions. However, a main obstacle for arriving at a unified theoretical understanding of out-of-equilibrium quantum dynamics is the absence of a universal principle that would be as general as the minimisation of free energy for equilibrium phase transitions [26, 215]. Nevertheless, powerful frameworks, as introduced in Chap. 1 and 2, such as the ETH, quantum chaos, the concept of subsystem thermalisation, as well as the spread and scrambling of quantum information, have been developed to understand the thermalisation of isolated quantum systems.

A central role in bridging the different paradigms of scrambling and chaotic dynamics has been taken by the SYK model, as elaborated in Sec. 2.1. Despite the recent progresses in understanding the dynamics of this intriguing model and of quantum many-body systems in general, it remains an outstanding challenge to extract universal quantum out-of-equilibrium behaviour [216–223]. For slow near-adiabatic sweeps across a critical region, the Kibble-Zurek mechanism [224, 225] has provided deep insights, including universal scaling laws [225, 226].

Here, however, we are interested in violent quenches, as will be introduced in Sec. 5.1, where a significant amount of energy is instantaneously injected into the system. Excepting few situations, such as non-thermal fixed points [227–233], much less is known about universality in such far-from-equilibrium situations.

In Sec. 5.2, we identify a universal equilibration in the quench dynamics of the SYK model $\hat{H}_{\mathrm{SYK}}$, as defined in Eq. (2.1), revealed through numerical calculations for the exact dynamics: For a variety of few-body observables, including multipartite entanglement as given by the quantum Fisher information (QFI), the disorder-averaged evolution collapses onto a single curve after a simple amplitude rescaling, independent of (generic) initial states. Over vast stretches of the dynamical evolution, this universal curve is well approximated by a Gaussian, with a fast decay on the order of the time-scales of leading-order processes.

In Sec. 5.3, we substantiate our numerical findings by devising a Lindblad master equation (ME), based on the Novikov–Furutsu theorem, that describes the Hamiltonian disorder average as an effective non-unitary time evolution. In this formalism, the unitary, isolated-system dynamics generated by a general disordered Hamiltonian $\hat{H}(t)$, is mapped to the dynamics of a clean, but dissipative system, governed by a Liouvillian superoperator $\mathcal{L}$. Applied to the SYK model, these effective dynamics reproduce the Gaussian equilibration curve. In Sec. 5.4, we use a spectral decomposition of $\mathcal{L}$ to study the observed dynamical universality on a formal level, showing that the initial-state independence is due to the population of only specific, highly degenerate eigenspaces of $\mathcal{L}$. This is verified through numeric diagonalisation of the Liouvillian superoperator describing the ensemble-averaged dynamics of $\hat{H}_{\mathrm{SYK}}$. The degenerate eigenspace structure was studied in detail in our follow-up work Ref. [82], which further builds upon the master equation formalism presented here, by developing a cumulant expansion for the Liouvillian evolution. We provide a brief summary of this work in Sec. 5.5.

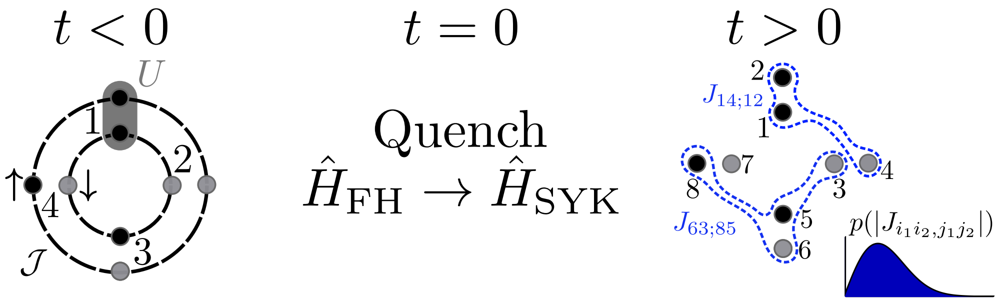

Figure 5.1: Illustration of the quench protocol. Initial states are chosen as ground states of the Fermi–Hubbard Hamiltonian (left) for different values of $U/\mathcal{J}$. The black and grey circles respectively represent occupied and empty fermionic modes. Dashed lines illustrate hopping of fermions between nearest-neighbour sites. The system is evolved under the SYK Hamiltonian (right), where spinless fermions (black circles) can hop to any empty fermionic mode (light grey circles).

5.1 Quench protocol

We are interested in the disorder-averaged out-of-equilibrium dynamics generated by $\hat{H}_{\rm SYK}$, following the quench protocol sketched in Fig. 5.1. As in previous chapters, we will denote the disorder average over multiple realisations of $\hat{H}_{\rm SYK}$ by $\mathbb{E}[\ldots]$.

For the initial states $|\psi(0)\rangle$, prepared at time $t<0$, we consider ground states of the one-dimensional spinful Fermi–Hubbard (FH) model [234, 235] given by the Hamiltonian

$$\hat{H}_{\rm FH} = -\mathcal{J}\sum_{\ell=1}^{N/2}\sum_{\sigma=\uparrow,\downarrow}\left(\hat{c}^{\dagger}_{\ell,\sigma}\hat{c}_{\ell+1,\sigma} + \text{H.c.}\right) + U\sum_{\ell=1}^{N/2}\hat{n}_{\ell,\uparrow}\hat{n}_{\ell,\downarrow}. \tag{5.1}$$

In the FH model, physical modes are given by $N/2$ spatial lattice sites, $\ell = 1,\ldots,N/2$, and additional spin degrees of freedom $\sigma =\uparrow,\downarrow$ which are not present in the SYK model. Since the interactions of the latter are site-independent (random amplitudes) and all-to-all, the mapping of FH modes to the SYK modes is arbitrary. For our quench protocol, we choose $\{\ell,\uparrow\} \leftrightarrow i = 2\ell$ and $\{\ell,\downarrow\} \leftrightarrow i = 2\ell-1$. The numeric simulations presented below focus on the case of half-filling, $Q = N/2$, and zero magnetisation, where there are $N/4$ fermions in each spin sector. The above choice of the initial Hamiltonian is only for convenience of preparing initial states that cover a range of parameters in a strongly-correlated system.

Once the system is prepared in the initial state $|\psi(0)\rangle$, we perform a global quench at $t=0$ to the SYK model and track the state's subsequent unitary time evolution

$$|\psi(t)\rangle = \mathrm{e}^{-i\hat{H}_{\mathrm{SYK}}t}|\psi(0)\rangle, \tag{5.2}$$

which is simulated numerically using exact diagonalisation techniques, the details of which are summarised in Ref. [81]. We average the time series over multiple realisations of $\hat{H}_{\mathrm{SYK}}$ in order to filter out the salient, realisation-independent features of the equilibration dynamics.

5.2 Universal super-exponential equilibration dynamics

Here, we study the post-quench dynamics of the quantum Fisher information (QFI) as well as moments of local operators.

We find that the disorder-averaged evolution of the considered few-body observables shows universality under the rescaling

$$\mathcal{G}\left(f(t)\right) \equiv \frac{f(t) - \overline{f(t)}}{f(0) - \overline{f(t)}}, \tag{5.3}$$

where $\overline{f(t)}$ represents the long-time average of a function $f(t)$ computed over a time window starting at t_0 and with duration T,

$$\overline{f(t)} = \frac{1}{T}\int_{t_0}^{t_0+T} \mathrm{d}t f(t). \tag{5.4}$$

For all the numeric simulations presented in what follows, we will use $Jt_0 = 50$ and $J(t_0 + T) = 100$.

We have seen in Sec. 2.1.1, particularly in Eq. (2.2), that the SYK model is only parameterised by the variance $\propto J^2$ of the random all-to-all interaction strengths $J_{i_1 i_2; j_1 j_2}$. Therefore, the universality in the evolution of observables can be probed as the insensitivity to the initial conditions, which becomes evident under the rescaling in Eq. (5.3), as is discussed throughout this chapter.

5.2.1 Dynamics of the quantum Fisher information

To illustrate the universal equilibration dynamics, we present here results for the QFI evolved under $\hat{H}_{\mathrm{SYK}}$. The QFI is an observable of central relevance in quantum sensing [236–238], which can witness multipartite entanglement in quantum many-body systems at zero and finite temperatures [78, 79, 239–241]. Interestingly, like the out-of-time-order correlators discussed in Sec. 2.1.3, this

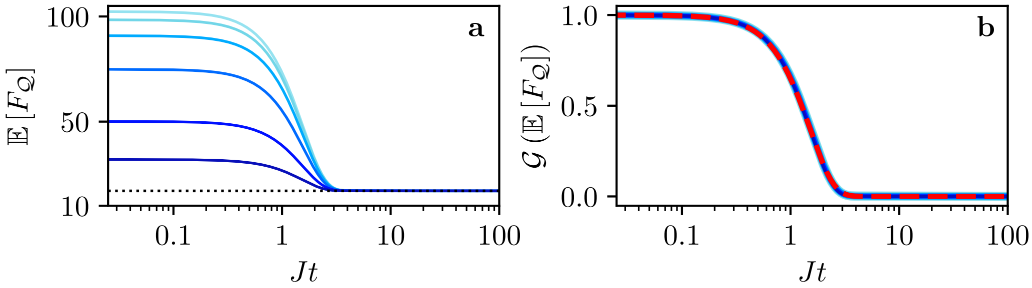

Figure 5.2: Universal super-exponential equilibration dynamics of the QFI F_Q, under $\hat{H}_{\mathrm{SYK}}$. (a) QFI averaged over 400 disorder realisations, $\mathbb{E}\,[F_Q]$, computed with respect to the operator $\hat{R}$ defined in Eq. (5.6). Initial states from darker to lighter shade of blue are for $U/\mathcal{J} = 0, 2, 4, 6, 8$, and 10. The system rapidly equilibrates to the expectation value of the Gibbs infinite temperature state (dotted black line). (b) Rescaling the dynamical curves according to Eq. (5.3) reveals a universal (initial-state independent) equilibration, which further agrees very well with a Gaussian fit, $\exp\left[-(Jt/\tau)^2\right]$, with a fast decay constant of $\tau = 1.52$ (dashed red curve). Data is for $Q = 8$ fermions occupying $N = 16$ fermionic modes.

quantum information theoretic measure can distinguish a pure eigenstate of an ETH-obeying Hamiltonian from the corresponding Gibbs thermal state [242–244].

In the present context of pure states, the QFI with respect to an observable $\hat{O}$ is simply proportional to its variance

$$F_Q[\hat{O}](t) = 4\left(\langle\psi(t)|\hat{O}^2|\psi(t)\rangle - \langle\psi(t)|\hat{O}|\psi(t)\rangle^2\right). \tag{5.5}$$

In this chapter, we consider the staggered magnetisation, which in the FH model is defined as $\hat{O}_{\mathrm{SM}} = \sum_{\ell=1}^{N/2}(-1)^{\ell}(\hat{n}_{\ell\downarrow} - \hat{n}_{\ell\uparrow})$, and which in the SYK model translates to [see below Eq. (5.1) for the mapping]

$$\hat{R} = \sum_{i=1}^{N/2}(-1)^i\hat{\kappa}_i = \sum_{i=1}^{N/2}(-1)^i(\hat{n}_{2i-1} - \hat{n}_{2i}). \tag{5.6}$$

The $\hat{\kappa}_i$ denote 2-local operators which we use to construct the 4-local operators discussed in App. C.3.4, where we also consider a non-diagonal generator for the QFI.

The time evolution of the disorder-averaged QFI, $\mathbb{E}\,[F_Q]$, computed with respect to the operator $\hat{R}$, is shown in Fig. 5.2(a). The considered initial states are the symmetry unbroken ground states of the FH model for a non-interacting initial system with $U/\mathcal{J} = 0$, as well as strongly interacting systems at larger values of $U/\mathcal{J} = 2, 4, 6, 8, 10$. As a result, the initial states are characterised by a varying amount of multipartite entanglement that is witnessed by the QFI.[1] At short times, the system still retains memory of the initial state. However, the completely disordered all-to-all interactions of the SYK model lead to a quick loss of this memory, and already at a time of about $Jt \approx 4$ the QFI equilibrates to a steady state value that is independent of the initial state. This rapid equilibration is reminiscent of the fast scrambling characteristic of the model, discussed in Sec. 2.1.3, and also bears similarities to the relaxation curves derived in Ref. [245] for the out-of-equilibrium dynamics of isolated quantum many-body systems. There it is shown that rapid, non-exponential equilibration is expected for, in a random matrix sense, typical Hamiltonians and observables.

The attained steady state value matches with the one obtained from the infinite temperature Gibbs state [horizontal dotted black line in Fig. 5.2(a)]

$$\hat{\rho}_\infty = \left.\frac{\mathrm{e}^{-\beta \hat{H}}}{Z}\right|_{\beta=0} = \frac{\mathbb{1}}{D}, \tag{5.7}$$

where $\mathbb{1}$ is the identity operator, Z is the partition function and $D = N!/[(N-Q)!Q!]$ is the Hilbert space dimension [Q is the filling fraction, see Eq. (2.4) and below]. This finding suggests that the overlaps between a generic initial state and the energy eigenstates of $\hat{H}_{\text{SYK}}$ are uniformly distributed over the spectrum. This can be substantiated by, for instance, computing the Kullback–Leibler divergence $D_{\text{KL}}(P(E)\|Q(E))$ between the uniform distribution $Q(E) = 1/D$, and the initial states' amplitude distribution $P(E) = |\langle\psi(0)|E\rangle|^2$ with respect to the energy basis $\{|E\rangle\}$ (see Figs. C.1–C.2).[2]

Even though the steady state $\hat{\rho}_\infty$ has vanishing QFI (see for instance Ref. [236]), it is nevertheless an interesting question of how the system reaches that point, starting from initial states with different amounts of quantum correlations. Indeed, by applying the rescaling $\mathbb{E}\,[F_Q]$ of Eq. (5.3), we find that the equilibration dynamics are universal within numerical precision. As shown in Fig. 5.2(b), all curves collapse throughout the dynamics, independent of the

---

[1] Note that the scaling of the QFI with system size N depends on the amount of multipartite entanglement of the state [238]: For separable states states, $F_Q \leq N$, whilst for genuinely N-partite entangled states $F_Q \leq N^2$.

[2] For 4000, respectively, 2000 independent realisations of $\hat{H}_{\text{SYK}}$ for system sizes $N = 8$ and $N = 12$, we find $\mathbb{E}\,[D_{\text{KL}}] = 0.0997 \pm 0.0154$ and 0.0627 ± 0.0028. This indicates that the initial states are almost uniformly distributed, and the uniformity of $P(E)$ improves with increasing N. The quoted values are for the FH initial state $U/\mathcal{J} = 10$, and are representative of all considered initial states.

initial state. In addition, the universal curve can be well approximated by a Gaussian (red-dashed curve), with a fast decay constant of $\tau = 1.52$. Thus, under the Hamiltonian evolution of the SYK model, the disorder-averaged QFI exhibits universal and super-exponential equilibration dynamics.

Note that a Gaussian temporal evolution is not unique to SYK dynamics. In the context of random matrix theory it is well known that it can occur in the survival probability, for instance during the quench dynamics generated by Wigner random banded matrices and two-body random ensembles (see for instance Refs. [246, 247]), where the latter is a specific case of embedded random matrix ensembles [248]. The same behaviour has also been studied for a generic disordered interacting spin model [249]. In these cases, the survival probability initially decays as a Gaussian, followed by a regime in which it shows oscillations with a power-law envelope [249].

5.2.2 Dynamics of operator moments

We now generalise the above study to the quench dynamics of the kth moment,

$$M_k(t) = \langle \psi(t) | \hat{O}^k | \psi(t) \rangle, \tag{5.8}$$

of the operator $\hat{O} = \hat{R}$ defined in Eq. (5.6). This is motivated by the fact that we consider initial pure states, for which the QFI is composed of operator moments as given in Eq. (5.5). In Appendix C.3.4, we report analogous results for 4-local operators and QFI computed with respect to a non-diagonal operator $\hat{T}$, defined in Eqs. (C.17) and (C.18), respectively.

With respect to the symmetry unbroken FH ground states, the ensemble averaged expectation values of all the odd moments of the staggered magnetisation operator $\hat{R}$ show negligibly small fluctuations around zero during their entire time evolution under the SYK Hamiltonian.[3] In contrast, the even moments exhibit the same super-exponential universal equilibration behaviour as the QFI. This is illustrated in Fig. 5.3 for $k = 2, 4, 6$ (similar results for $k = 8, 10, 12$ are presented in App. C.3.3, where we also study the survival probability as an

---

[3] For a formal proof that odd moments of $\hat{R}$ vanish, see the thesis [83]. The main idea is as follows: The considered initial states, having zero magnetisation, have spin-flip symmetry. In contrast, the staggered magnetisation operator is odd under such a transformation. Regarding the SYK Hamiltonian, spin-flip (i.e., $2i \leftrightarrow 2i-1$) turns one disorder realisation into a different one with the same probability of occurring. As a consequence, given an instance of the SYK Hamiltonian that produces a certain dynamics of $\hat{R}^k$, with k odd, there will always exist another realisation that generates dynamics of equal amplitude, but opposite sign, leading to a vanishing ensemble average.

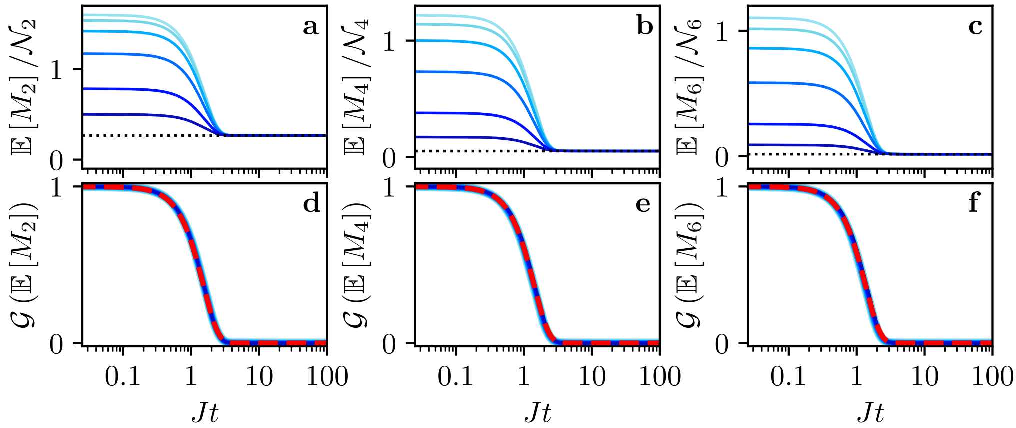

Figure 5.3: Equilibration dynamics of operator moments M_k, under $\hat{H}_{\mathrm{SYK}}$. (a–c) Disorder-averaged dynamics of moments M_2, M_4, and M_6 of the operator $\hat{R}$, averaged over 400 disorder realisations, after normalisation to values $\leq \mathcal{O}(1)$ by an empirical factor $\mathcal{N}_k = N^{\left(\frac{3k}{4}-\frac{1}{2}\right)}$ for visualisation purposes. The moments rapidly equilibrate to their expectation value with respect to the Gibbs infinite temperature state (dotted black lines). (d–f) After rescaling by the function $\mathcal{G}$ of Eq. (5.3), the dynamics collapse onto a universal curve, which agrees very well with a Gaussian fit (dashed-red curves) $\exp\left[-(Jt/\tau)^2\right]$, with $\tau = 1.52, 1.42, 1.35$, for $k = 2, 4, 6$, respectively. Data is for $Q = 8$ fermions occupying $N = 16$ modes.

example of a truly non-local observable). The super-exponential approach to equilibrium is clearly visible in this data.

As is evident from Fig. 5.3(d–f), the rescaling defined in Eq. (5.3) collapses the even moments evolved from different initial states onto a single curve. During most of the evolution, this collapsed curve can be well approximated by a Gaussian, similar to the QFI dynamics in Sec. 5.2. In the transient regime, curves corresponding to different initial states for even $k \geq 4$ do show small deviations, an effect that becomes more prominent for larger N (see App. C.3.5 for a finite-size study). In other words, while the universality found for $k = 2$ is very robust, for larger k it becomes approximate in an intermediate time window. This finding also suggests that universality is more precise for few-body operators, as is further corroborated by comparison with the global many-body observable of the survival probability, see Fig. C.4. However, we do not exclude the possibility of a suitably constructed, highly non-local observable exhibiting universality with respect to Eq. (5.3).

An interesting feature of the different moments is that their respective curves shift towards earlier times with increasing order k. This is evident from

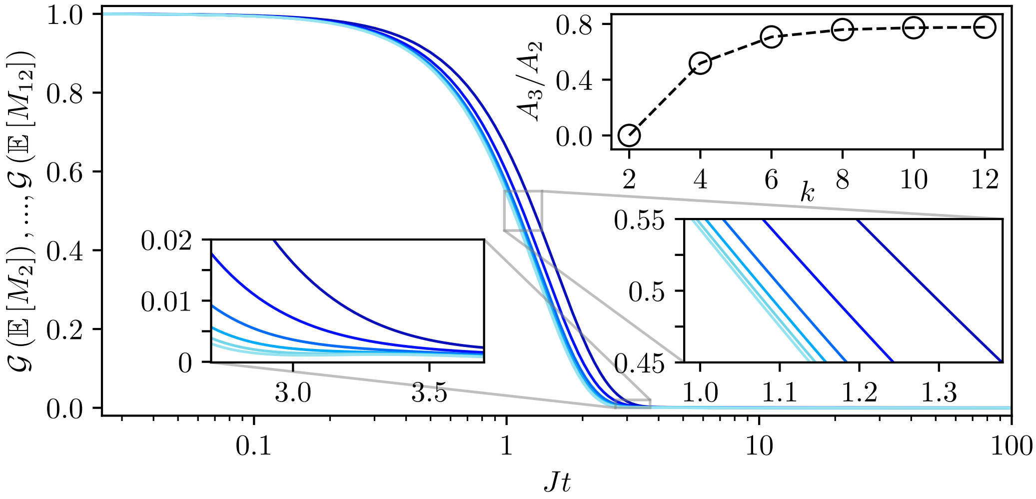

Figure 5.4: Rescaled dynamics of the disorder-averaged moments. $\mathcal{G}(\mathbb{E}[M_k])$, of operator $\hat{R}$, averaged over 400 realisations of $\hat{H}_{\text{SYK}}$ with $N = 16$ modes at half-filling. For all curves the initial state is $U/\mathcal{J} = 10$, and dark to light shading corresponds to different moment orders $k = 2, 4, 6, 8, 10$ and 12, respectively. The shift to earlier times with increasing k is highlighted by the two lower insets, which also indicate a convergence with increasing k. This is quantified in the top inset (see Sec. 5.4), which shows the ratio A_3/A_2 of the effective amplitudes of the kth moments in accordance with Eq. (5.28). The monotonic increase, and indication of saturation, with increasing k shows that the faster time-scale $|\lambda_3|$ is favoured with increasing moment k.

Gaussian fits to the universal curves for $k = 2, 4, 6$ in Fig. 5.3, which yield the decreasing decay times $\tau = 1.52, 1.42, 1.35$, respectively. To illustrate this effect further, we show the rescaled curves for $k = 2, 4, ..., 12$ in Fig. 5.4, where it appears that the curves converge with sufficiently high order.

In the next section, we will develop an analytical framework which reproduces the salient features observed in the above numerics by mapping the disorder averaged, closed-system dynamics to an effective master equation describing dissipation. Applied to the SYK model, this yields a Liouvillian superoperator, whose dynamics reproduce the Gaussian decay, as well as the initial state independence. Furthermore, a spectral analysis of this Liouvillian, presented in Sec. 5.4, will shed light on the origin of the approximate universality for moments M_k of order $k > 2$, their increasing decay rate, as well as the apparent convergence thereof, with increasing k.

5.3 Dissipative ensemble dynamics

In this section, we develop an open-system formalism for general disordered Hamiltonians, which we use to understand the main features observed in the average dynamics of the unitary ensemble discussed in the previous section.

A detailed prescription for Hamiltonian disorder averaging, based on a matrix formalism, has been introduced in Refs. [250–252]. Here, we present an alternative route to Gaussian disorder averaging based on the Novikov–Furutsu theorem. In earlier works, this theorem has been applied in the context of averaging noise with finite correlation times in, for instance, quantum walks subjected to pure dephasing noise [253, 254], stochastic Schrödinger equations [255], or proposals for simulating dissipation via noisy unitary dynamics [256–259]. We exploit that framework by formally promoting the quenched disorder to noise with infinite correlation time, permitting a fruitful application to a generic system with Gaussian disorder, of the form given in Eq. (5.9) below. This approach has the advantage of treating quenched disorder and temporally fluctuating noise on equal footing, enabling an application to a large variety of settings. The interested reader may find further details on the derivation, and the explicit derivation for static processes in App. C.2.

5.3.1 Effective master equation for general disordered Hamiltonians

Our aim is to directly study the dynamics of the ensemble's density matrix $\tilde{\rho}(t) \equiv \mathbb{E}\left[\hat{\rho}(t)\right]$ via the ensemble averaged von Neumann equation, where the time-evolution of each state $\hat{\rho}(t)$ is generated by a realisation of the general closed system Hamiltonian

$$\hat{H}(t) = \hat{H}_0(t) + \sum_{\alpha} \hat{H}_\alpha(t). \tag{5.9}$$

Here, $\hat{H}_0(t)$ is a disorder-free contribution, which in general can be time dependent, whereas the terms

$$\hat{H}_\alpha(t) = \sum_{l_\alpha} \xi_{l_\alpha}^{(\alpha)}(t) \hat{h}_{l_\alpha}^{(\alpha)}, \tag{5.10}$$

capture the dynamics due to disorder or noise, encoded in the functions $\xi_{l_\alpha}^{(\alpha)}(t)$. The index α is used to distinguish different subsets of Hermitian operators

$\hat{h}_{l_\alpha}^{(\alpha)}$, and the operators within a subset are labelled by the (multi-)index l_α.[4] In particular, upon rewriting the SYK Hamiltonian in the generic form of Eq. (5.10), we identify three operator subsets, as will be shown in the next section below.

We assume the functions $\xi_{l_\alpha}^{(\alpha)}(t)$ to describe a Gaussian process possessing—without loss of generality—vanishing cross-correlations, $\mathbb{E}\left[\xi_{l_\alpha}^{(\alpha)}(t)\xi_{l_\beta}^{(\beta)}(t')\right] = 0$ for $\alpha \neq \beta$, so that their correlation tensor is given by

$$F_{l_\alpha,k_\alpha}^{(\alpha)}(t,t') \equiv \mathbb{E}\left[\xi_{l_\alpha}^{(\alpha)}(t)\xi_{k_\alpha}^{(\alpha)}(t')\right]. \tag{5.11}$$

Formally, the SYK Hamiltonian defined in Eq. (2.1) corresponds to setting $\hat{H}_0(t) = 0$ and taking all $\xi_{l_\alpha}^{(\alpha)}(t)$ to be time independent, in which case $F_{l_\alpha,k_\alpha}^{(\alpha)}(t,t')$ is constant with respect to time. To keep the formalism general, we will specialise to this case only further below.

Consider now the ensemble averaged von Neumann equation generated by averaging over multiple realisations of the Hamiltonian in Eq. (5.9),

$$\partial_t\tilde{\rho}(t) = -i\left[\hat{H}_0(t),\tilde{\rho}(t)\right] - i\sum_{\alpha,l_\alpha}\left[\hat{h}_{l_\alpha}^{(\alpha)},\mathbb{E}\left[\xi_{l_\alpha}^{(\alpha)}(t)\hat{\rho}(t)\right]\right]. \tag{5.12}$$

The correlations $\mathbb{E}\left[\xi_{l_\alpha}^{(\alpha)}(t)\hat{\rho}(t)\right]$ are non-trivial since the density matrix is—by virtue of the von Neumann equation—a functional $\hat{\rho}[\xi,t]$ of the Gaussian processes $\xi_{l_\alpha}^{(\alpha)}(t)$. Our framework rests upon the Novikov–Furutsu theorem [260–263], which provides an exact expression of these correlations in terms of $F_{l_\alpha,k_\alpha}^{(\alpha)}(t,t')$ as

$$\mathbb{E}\left[\xi_{l_\alpha}^{(\alpha)}(t)\hat{\rho}[\xi,t]\right] = \sum_{k_\alpha}\int_0^\infty \mathrm{d}t' F_{l_\alpha,k_\alpha}^{(\alpha)}(t,t')\mathbb{E}\left[\frac{\delta\hat{\rho}[\xi,t]}{\delta\xi_{k_\alpha}^{(\alpha)}(t')}\right], \tag{5.13}$$

where the last term on the right-hand side contains the functional derivative of $\hat{\rho}[\xi,t]$ with respect to $\xi_{k_\alpha}^{(\alpha)}(t')$. An explicit expression for this can be obtained from the integrated von Neumann equation. Formally, this yields an infinite series in which the nth term ($n \geq 1$) contains $n-1$ time integrals over n nested commutators [see Eq. (C.6)]. The role of the higher order terms will

---

[4] Whilst the distinction via index α is not strictly necessary for our derivation, it does facilitate translation of our general results to specific models in which such a distinction may naturally arise. For example, in a system of spins arranged on a lattice, $\alpha = 1$ could refer to a disordered external potential and $\alpha = 2$ to a noisy drive. For either, the operator label l_α would refer to the site index of the spins.

be discussed in Sec. 5.5, which summarises the study of our follow-up work Ref. [82]. Here, we retain only the lowest order contribution ($n = 1$), which reads

$$\frac{\delta \hat{\rho}[\xi, t]}{\delta \xi^{(\alpha)}_{k_\alpha}(t')} \simeq -i \left[\hat{h}^{(\alpha)}_{k_\alpha}, \hat{\rho}[\xi, t'] \right] \Theta(t - t'), \tag{5.14}$$

where the step-function Θ arises from causality. Substituting Eqs. (5.13) and (5.14) into Eq. (5.12), we obtain the evolution equation

$$\partial_t \tilde{\rho}(t) = -i \left[\hat{H}_0(t), \tilde{\rho}(t) \right] - \sum_{\alpha, l_\alpha, k_\alpha} \left[\hat{h}^{(\alpha)}_{l_\alpha}, \left[\hat{h}^{(\alpha)}_{k_\alpha}, \int_0^t \mathrm{d}t' F^{(\alpha)}_{l_\alpha, k_\alpha}(t, t') \tilde{\rho}(t') \right] \right]. \tag{5.15}$$

This evolution equation is not exact, due to our use of the approximate functional derivative given by Eq. (5.14). Such a leading order truncation amounts to the well-known decorrelation assumption typically made in the analysis of stochastic evolution equations [264, 265] (see also App. C.2.1). The remaining time integral in Eq. (5.15) is known as a Bourret integral [266, 267]. While the decorrelation assumption becomes exact in the limit of white noise, for non-Markovian noise it corresponds to an expansion controlled by the noise correlation time [268]. One may then wonder what justifies this approximation for $\hat{H}_{\text{SYK}}$ (see also Fig. 5.5), whose quenched disorder has an infinite correlation time. The reason could be attributed to the chaoticity of the SYK model: Each term of the Hamiltonian in Eq. (5.10) can be thought of as an independent noise process governing the evolution of the density operator. Then, in the presence of a *large* number of such processes, as in $\hat{H}_{\text{SYK}}$, one may expect the correlations between the density operator and any individual process to be strongly suppressed. Viewed differently, the decorrelation assumption can be seen as a linear-response approximation [269, 270], i.e., the response of the state $\hat{\rho}$ at time t towards a perturbation with $\xi^{(\alpha)}_{l_\alpha} \hat{h}^{(\alpha)}_{l_\alpha}$ at an earlier time t_1 is taken into account only to linear order. In the context of Kubo's linear response theory [271], it is well known that averaging effects due to chaos lead to a superb success much beyond the regime of applicability predicted by naïve estimates [269, 272–275]. In the present context, the success of the linear approximation, observed in Sec. 5.3.3 below, can be seen as a manifestation of the strong effects of quantum chaos in the SYK model.

The master equation as given by Eq. (5.15) is still rather unwieldy, since it is not local in time. We thus perform a Markov approximation $\tilde{\rho}(t') \approx \tilde{\rho}(t)$, leading us to a Lindblad master equation in non-diagonal form [199] governed by a time-dependent Liouvillian superoperator

$$\mathcal{L}(t) \tilde{\rho}(t) = -i \left[\hat{H}_0(t), \tilde{\rho}(t) \right] + \sum_\alpha \mathcal{D}^{(\alpha)}(t) \tilde{\rho}(t), \tag{5.16}$$

with Hermitian dissipator

$$\mathcal{D}^{(\alpha)}(t)\tilde{\rho}(t) = \sum_{l_\alpha,k_\alpha} 2f^{(\alpha)}_{l_\alpha,k_\alpha}(t) \left(\hat{h}^{(\alpha)}_{l_\alpha} \tilde{\rho}(t) \hat{h}^{(\alpha)}_{k_\alpha} - \frac{1}{2} \left\{ \hat{h}^{(\alpha)}_{k_\alpha} \hat{h}^{(\alpha)}_{l_\alpha}, \tilde{\rho}(t) \right\} \right), \tag{5.17}$$

in which we have defined

$$f^{(\alpha)}_{l_\alpha,k_\alpha}(t) = \int_0^t \mathrm{d}t' F^{(\alpha)}_{l_\alpha,k_\alpha}(t,t'). \tag{5.18}$$

Equations (5.16)–(5.18) form the final evolution equations of this section. They are valid under a Bourret–Markov approximation for the generic Hamiltonians of Eq. (5.9) with disorder and/or noise contributions. The master equation is a result of averaging over an ensemble of disorder realisations, yielding an effective evolution equation which does not require the presence of noise (see Sec. C.2.3). Whilst each individual disorder realisation evolves unitarily, the ensemble evolves like an open system, with a dynamics that is approximately generated by the Liouvillian $\mathcal{L}(t)$. The coherent and dissipative processes that constitute $\mathcal{L}(t)$ can be read-off immediately from the system's Hamiltonian. The corresponding dissipation rates are entirely determined by the disorder statistics $F^{(\alpha)}_{l_\alpha,k_\alpha}(t,t')$, defined in Eq. (5.11), via Eq. (5.18). Similarly, while each realisation preserves the purity of the initial state, the Hermitian jump operators of the master equation generate ensemble dynamics that are purity decreasing [276, 277], and thus drive the ensemble from a pure to a mixed state. In particular, for the SYK model with large enough N, the ensemble equilibrates to the infinite-temperature state $\hat{\rho}_\infty$ given in Eq. (5.7) [277, 278]. Note, however, that whilst the Hermitian jump operators of Eq. (5.16) and (5.17) ensure that $\hat{\rho}_\infty$ is a steady state of the Liouvillian dynamics, for an arbitrary Hamiltonian as given by Eq. (5.9), the steady-state of $\mathcal{L}(t)$ need not be unique in general [279, 280].

5.3.2 Application to the SYK Hamiltonian

To apply the formalism of Sec. 5.3.1 to the SYK model, one simply needs to rewrite its Hamiltonian $\hat{H}_{\mathrm{SYK}}$, as defined in Eq. (2.1), in the generic form of Eq. (5.9), and then read off the jump operators $\hat{h}^{(\alpha)}_{l_\alpha}$ and disorder functions $\xi^{(\alpha)}_{l_\alpha}$ that govern the dissipation rates.

Since $\hat{H}_{\mathrm{SYK}}$ is a purely disordered Hamiltonian, we have $\hat{H}_0 = 0$, and so the Liouvillian in Eq. (5.16) generates purely dissipative dynamics $\mathcal{L}(t) = \mathcal{D}(t)$. To rewrite $\hat{H}_{\mathrm{SYK}}$ in the form of the remaining term $\sum_\alpha \hat{H}_\alpha(t)$ of Eq. (5.9), we partially order the indices in the summation of Eq. (2.1) as $i_1 > i_2, j_1 > j_2$, and use the anti-symmetry of the SYK interactions, as defined by Eq. (2.3). Through this rewriting, one can identify three Hamiltonian terms $\hat{H}_\alpha$ with multi-indices

$$l_\alpha = \begin{cases} i_1 i_2; i_1 i_2, \text{ with } i_1 > i_2, & \alpha = 1 \\ i_1 i_2; j_1 j_2, \text{ with } i_1 > i_2, j_1 > j_2 \text{ and } (i_1, i_2) \neq (j_1, j_2), & \alpha = 2, 3 \end{cases} \tag{5.19}$$

and jump operators

$$\hat{h}^{(\alpha)}_{l_\alpha} = \begin{cases} \hat{c}^\dagger_{i_1} \hat{c}^\dagger_{i_2} \hat{c}_{i_1} \hat{c}_{i_2}, & \alpha = 1 \\ \hat{c}^\dagger_{i_1} \hat{c}^\dagger_{i_2} \hat{c}_{j_1} \hat{c}_{j_2} + \text{H.c.}, & \alpha = 2 \\ i\hat{c}^\dagger_{i_1} \hat{c}^\dagger_{i_2} \hat{c}_{j_1} \hat{c}_{j_2} + \text{H.c.}, & \alpha = 3\,. \end{cases} \tag{5.20}$$

The corresponding time-independent disorder coefficients are

$$\xi^{(\alpha)}_{l_\alpha} = \begin{cases} 4J_{i_1 i_2; i_1 i_2}/(2N)^{3/2}, & \alpha = 1 \\ 2\text{Re}J_{i_1 i_2; j_1 j_2}/(2N)^{3/2}, & \alpha = 2 \\ 2\text{Im}J_{i_1 i_2; j_1 j_2}/(2N)^{3/2}, & \alpha = 3 \end{cases} \tag{5.21}$$

Using the above expressions, we can determine the dissipation rates of Eqs. (5.17), (5.18) which correspond to the disorder averaged unitary evolution of $\hat{H}_{\text{SYK}}$. The relevant time integral is trivial in this case, and the rates are given by

$$2f^{(\alpha)}_{l_\alpha, k_\alpha}(t) = 2t\mathbb{E}\left[\xi^{(\alpha)}_{l_\alpha} \xi^{(\alpha)}_{k_\alpha}\right] = \begin{cases} 2t\dfrac{16J^2}{(2N)^3}\delta_{l_\alpha, k_\alpha}, & \alpha = 1 \\ 2t\dfrac{4(J^2/2)}{(2N)^3}(\delta_{l_\alpha, k_\alpha} + \delta_{l_\alpha, \overline{k_\alpha}}), & \alpha = 2, 3 \end{cases} \tag{5.22}$$

where $\overline{k_\alpha} = j_1 j_2; i_1 i_2$ when if $k_\alpha = i_1 i_2; j_1 j_2$. These additional correlations exist for $l_\alpha = \overline{k_\alpha}$ when $\alpha = 2, 3$ because $\text{Re}[J_{i_1 i_2; j_1 j_2}] = \text{Re}[J_{j_1 j_2; i_1 i_2}]$ and similarly $\text{Im}[J_{i_1 i_2; j_1 j_2}] = -\text{Im}[J_{j_1 j_2; i_1 i_2}]$, due to Eq. (2.3).

The main point is that the time-independent disorder correlations of $\hat{H}_{\text{SYK}}$ [or indeed any SYK-q model of Eq. (2.5)], given by Eq. (5.22), yield dissipation rates in the Liouvillian superoperator that grow linearly in time. Consequently, one can factor the Liouvillian as

$$\mathcal{L}(t) = 2t\mathcal{D}, \tag{5.23}$$

which naturally yields the super-exponential time-evolution

$$\tilde{\rho}(t) = \mathcal{T}e^{\int_0^t \mathrm{d}t' 2t' \mathcal{D}} \hat{\rho}(0) = e^{t^2 \mathcal{D}} \hat{\rho}(0), \tag{5.24}$$

where $\mathcal{T}$ denotes time-ordering.

We thus see that, in addition to clarifying the nature of the steady-state (as was discussed at the end of Sec. 5.3.1), the Liouvillian dynamics formally reproduce the Gaussian equilibration observed in Sec. 5.2 for the numerically simulated quench dynamics of the SYK model.

5.3.3 Comparison to exact numerics

In general, the ME as developed above may not be used to study the ensemble average of the QFI, due to the term $\langle\psi(t)|\hat{O}|\psi(t)\rangle^2$ in Eq. (5.5) that is non-linear in the density matrix. However, for the initial zero magnetisation states considered in Sec. 5.2, exact numerics show that the first moment fluctuates around zero (see also the footnote of Sec. 5.2.2, for a summary of the formal arguments given in the thesis [83]), such that in this case one may use the ME to approximate the dynamics of the QFI.

Figure 5.5(a) shows simulations of the QFI evolution generated by the master equation of Eq. (5.16) for $\hat{H}_{\mathrm{SYK}}$, constructed from Eqs. (5.19)–(5.22). The agreement with the ensemble averaged ED results is very good. The Liouvillian dynamics also reproduce the universality of the QFI with respect to different initial states, as shown in Fig. 5.5(b). A discrepancy at intermediate times can be attributed to the decorrelation and Markov approximations of the master equation. Improvements will be discussed in Sec. 5.5.

Figure 5.5(c,d) shows a comparison of ME and ED simulations for moment M_2 of the operator $\hat{R}$ defined in Eq. (5.6). As for the QFI, the super-exponential approach to equilibrium is captured, as well as the early and late time dynamics. In line with the above discussion, we again observe a discrepancy between ED and ME simulations at intermediate times. Recalling that hermitian jump operators guarantee the infinite temperature ensemble to be a (not necessarily unique) steady state of the general Liouvillian in Eq. (5.16), we determine the infinite temperature steady-state value of M_2 within the half-filling sector $N = 2Q$ to be

$$\operatorname{tr}\left(\hat{R}^2(t)\hat{\rho}_\infty\right) = \left(\frac{N}{2\sqrt{N-1}}\right)^2. \tag{5.25}$$

As Fig. 5.5(c) shows, this value agrees well with the steady-state plateaus of the exact unitary dynamics averaged over disorder realisations.

The fact that disorder induces dephasing between members of an ensemble—and thus leads to effective open-system evolution equations even in the absence of a heat bath—is long known; in particular for special single-body cases such as classical disordered dipoles and harmonic oscillators [268], or single

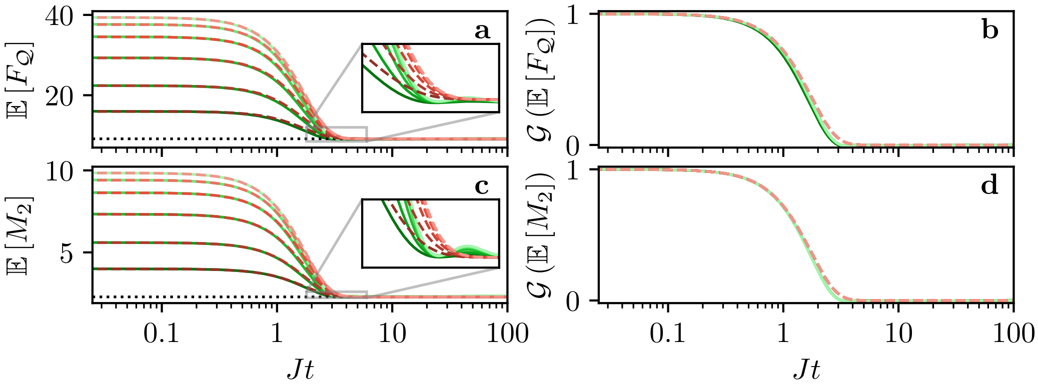

Figure 5.5: Comparison of ED and ME results. SYK dynamics of the QFI (a–b) and M_2 (c–d) of the staggered magnetisation $\hat{R}$, for $N = 8$. ED curves are averaged over 90 000 disorder realisations. For both ME (red, dashed) and ED (green, solid) curves, dark to light shading corresponds to the different initial states of Fig. 5.2. The black-dotted line (a,c) shows the analytically predicted steady-state value of Eq. (5.25) for the half-filling sector. (a,c) For each initial state, the ME simulation reproduces the dynamics of the exact numerics very well. There is a discrepancy at intermediate times due to non-Markovian effects and higher-order correlations, not captured by the approximate ME (inset). (b,d) The ME reproduces the collapse to a universal curve under the rescaling defined in Eq. (5.3). The slight spread in the rescaled ED curves is due to statistical fluctuations, which are suppressed for larger system sizes, as can be seen from a comparison with Figs. 5.2(b), 5.3(d–f).

atoms coupled to a photon field [281]. Here, our aim was the derivation of a general framework for quantum many-body systems. Such a platform for the evolution of disorder-averaged density operators has been developed previously [252], based on a matrix formalism [250, 251]. Our derivation based on the Novikov–Furutsu theorem provides an alternative, simpler, but nevertheless general approach, as the assumptions we made are not fundamental, but rather of practical nature: The Novikov–Furutsu formalism can be extended to non-Gaussian stochastic processes [263, 282], the decorrelation assumption may be lifted in favor of an infinite series of terms in Eq. (5.14) [268, 270], and the Markov approximation is—at least on a formal level—not necessary in the derivation of the evolution equations. The present framework has the additional feature that disorder and noise processes can be treated on equal footing, within the same master equation, without any further complications of the formalism.

To summarise, the Novikov–Furutsu theorem enables us to derive a master equation, for the ensemble average, that provides a general framework for disorder-averaged quantum many-body systems. For the case of the SYK model, it yields analytic insights into the out-of-equilibrium dynamics, such as the steady state reached at late times, and the approximately Gaussian decay. Even more, the Liouvillian formalism allows us to study the origin of the universal dynamics: In Sec. 5.4 below, we will analyse how different states and observables decompose over the eigenspaces of $\mathcal{L}(t)$, showing how these distributions conspire in the above dynamics to select a single time-scale, universal across different initial states.

5.4 Analyses of universality in master equation formalism

Having used the ME framework of Sec. 5.3.1 to formally demonstrate the Gaussian decay via Eq. (5.24), and having seen in Fig. 5.5 that the ME reproduces the universal (initial-state independent) decay of the QFI and operator moments M_2 for observable $\hat{R}$, we now study the origins of the observed universality within this formalism. We do so by decomposing the evolution equation (5.24) over the eigenspaces of $\mathcal{L}(t)$. As we will see, the population of various initial states and observables in the corresponding eigenspaces conspires to produce a universal curve under the rescaling $\mathcal{G}$ defined in Eq. (5.3).

5.4.1 Formal decomposition into Liouvillian eigenspaces

In general, a superoperator $\mathcal{L}$ is not normal, and thus has distinct left and right eigenmodes [283, 284]. However, as a result of $\hat{H}_0 = 0$, $\left(\hat{h}^{(\alpha)}_{l_\alpha}\right)^\dagger = \hat{h}^{(\alpha)}_{l_\alpha}$, and $F^{(\alpha)}_{l_\alpha,k_\alpha} = F^{(\alpha)}_{k_\alpha,l_\alpha} \in \mathbb{R}$, the Liouvillian of the SYK model $\mathcal{L}(t) = 2t\mathcal{D}$ is Hermitian and thus normal This will be made explicit by the matrix representation given in Eq. (5.30) below. Therefore, the left and right eigenmodes of $\mathcal{D}$ coincide, and one can always form a Hermitian basis for each eigenspace. We use the index $i \geq 0$ to label these eigenspaces, which in general have a d_i-fold degeneracy. The d_i Hermitian eigenmodes within the ith eigenspace are denoted as $\hat{\rho}_{i,\alpha_i}$, where $\alpha_i = 1, \dots, d_i$. The eigenmodes are orthogonal with respect to the Hilbert–Schmidt norm $\mathrm{tr}(\hat{\rho}^\dagger_{i,\alpha_i}\hat{\rho}_{j,\alpha_j}) = \delta_{i,j}\delta_{\alpha_i,\alpha_j}$ and thus form a basis of $\mathcal{B}(\mathcal{H})$, the space of linear operators acting on $\mathcal{H}$. For all (in our case typically degenerate) eigenspaces i, the corresponding eigenvalue λ_i is real and negative. So, we order the eigenspaces according to the magnitude of their respective eigenvalues as $|\lambda_0| < |\lambda_1| < \dots$.

Now, we can decompose any initial state and observable in $\mathcal{B}(\mathcal{H})$, respectively, as

$$\hat{\rho}(0) = \sum_{i\geq 0} \sum_{\alpha_i=1}^{d_i} c_{i,\alpha_i} \hat{\rho}_{i,\alpha_i} \quad \text{and} \quad \hat{O} = \sum_{i\geq 0} \sum_{\alpha_i=1}^{d_i} o_{i,\alpha_i} \hat{\rho}_{i,\alpha_i}, \tag{5.26}$$

with real coefficients $c_{i,\alpha_i} = \mathrm{tr}(\hat{\rho}(0)\hat{\rho}_{i,\alpha_i})$ and $o_{i,\alpha_i} = \mathrm{tr}(\hat{O}\hat{\rho}_{i,\alpha_i})$. It then follows that any state, time-evolved under the SYK dissipator according to Eq. (5.23)–(5.24), is given by

$$\tilde{\rho}(t) = \mathrm{e}^{t^2\mathcal{D}} \hat{\rho}(0) = \sum_{i\geq 0} \mathrm{e}^{-t^2|\lambda_i|} \sum_{\alpha_i=1}^{d_i} c_{i,\alpha_i} \hat{\rho}_{i,\alpha_i}. \tag{5.27}$$

Since Liouvillian dynamics are trace preserving, we have $\lambda_0 = 0$. Consequently, $\lim_{t\to\infty} \tilde{\rho}(t)$ is given in terms of the eigenmodes corresponding to λ_0 [279]. The Liouvillian spectrum $\{\lambda_i\}$ sets the time-scales of the dynamics of any observable quantity.

For sufficiently large Jt_0 [see Eq. (5.4)], the long-time average in $\mathcal{G}$ is simply the contribution due to the steady-state eigenmode $\hat{\rho}_0$. With the above eigen-decompositions in hand, we can thus express any rescaled operator expectation value as

$$\mathcal{G}\big(\mathrm{tr}\big(\hat{O}\tilde{\rho}(t)\big)\big) = \frac{\sum_{i\geq 1} \mathrm{e}^{-t^2|\lambda_i|} A_i}{\sum_{i\geq 1} A_i}, \tag{5.28}$$

where $A_i = \sum_{\alpha_i=1}^{d_i} c_{i,\alpha_i} o_{i,\alpha_i}$ is the effective amplitude within the ith eigenspace. Universality across different initial states can then occur if:

(i) The observable and initial state decompositions of Eq. (5.26) intersect in only one and the same eigenspace $i^* > 0$ for all initial states.

(ii) The decompositions intersect in multiple degenerate eigenspaces, but the $c_{i,\alpha_i} o_{i,\alpha_i}$ are distributed symmetrically about 0 in all but one eigenspace $i^* > 0$.

In both cases, there exists only one non-zero amplitude A_{i^*}, and $A_i = 0\ \forall i \neq i^*$, such that Eq. (5.28) reduces to the same Gaussian curve

$$\mathcal{G}\big(\langle \hat{O}(t) \rangle\big) = \mathrm{e}^{-t^2|\lambda_{i^*}|}, \tag{5.29}$$

for all initial states.

5.4.2 Numeric results

We now apply the above criteria to the SYK dynamics of the first four moments M_k of the staggered magnetisation $\hat{R}$ [Eq. (5.6)]. To this end, we numerically obtain the spectrum $\{\lambda_i\}$ and eigenmodes $\{\hat{\rho}_{i,\alpha_i}\}$ of the SYK Liouvillian superoperator $\mathcal{L}$ via a matrix representation $\bar{\bar{\mathcal{L}}}$ thereof. The latter acts on the duplicated Hilbert space $\mathcal{H}\otimes\mathcal{H}$ (see, e.g., Refs. [279, 283, 284] for detailed descriptions of such a procedure and for spectral properties of Liouvillian superoperators), and the density matrices $\hat{\rho}$ of Eq. (5.26) become vectors $|\vec{\rho}\rangle \in \mathcal{H}\otimes\mathcal{H}$ obtained by stacking the columns of the matrix representation of $\hat{\rho}$ (similarly for the observables $\hat{O}$). Left and right multiplication with operators transform as $\hat{A}\hat{\rho}\hat{B} \to \hat{B}^{\intercal}\otimes\hat{A}|\vec{\rho}\rangle$, where $\hat{B}^{\intercal}$ denotes the transpose of $\hat{B}$. For the general Liouvillian of Eq. (5.16), we then have the matrix representation

$$\bar{\bar{\mathcal{L}}}(t) = -\,i[\mathbb{1}\otimes\hat{H}_0(t) - (\hat{H}_0(t))^{\intercal}\otimes\mathbb{1}] + \bar{\bar{\mathcal{D}}},\ \text{with}$$
$$\bar{\bar{\mathcal{D}}} = \sum_{\alpha}\sum_{l_\alpha,k_\alpha} 2f^{(\alpha)}_{l_\alpha,k_\alpha}(t)\left[\left(\hat{h}^{(\alpha)}_{k_\alpha}\right)^{\intercal}\otimes\hat{h}^{(\alpha)}_{l_\alpha} - \frac{1}{2}\mathbb{1}\otimes\hat{h}^{(\alpha)}_{k_\alpha}\hat{h}^{(\alpha)}_{l_\alpha} - \frac{1}{2}\left(\hat{h}^{(\alpha)}_{k_\alpha}\hat{h}^{(\alpha)}_{l_\alpha}\right)^{\intercal}\otimes\mathbb{1}\right]. \tag{5.30}$$

We obtain the matrix representation of the SYK Liouvillian $\bar{\bar{\mathcal{L}}}(t) = 2t\bar{\bar{\mathcal{D}}}$ [factoring out $2t$ as in Eq. (5.23)] by setting $\hat{H}_0 = 0$ and inserting Eqs. (5.20)–(5.22) into Eq. (5.30).

Table 5.1 lists the spectrum of $\mathcal{D}$, obtained by numerically diagonalising the above matrix representation, for an SYK system of $N = 8$ modes at half filling. We find that λ_0 is non-degenerate, implying a unique steady-state in the present case of study, in agreement with rather general conditions [285]. The numerically obtained distributions of $c_{i,\alpha_i}o_{i,\alpha_i}$ and A_i for M_2 are shown in Fig. 5.6(a–d) for different initial FH ground states. For $i > 0$, $c_{i,\alpha_i}o_{i,\alpha_i} \neq 0$ only for $i = 2$, so that universality of type (i) for M_2 follows immediately with $i^* = 2$. The reason why this occurs lies in the decomposition of the observable: We observe $o_{i,\alpha_i} = 0$ for $i > 0$ and $i \neq 2$. This demonstrates why the choice of the initial state is irrelevant—regardless of the values of c_{i,α_i}, there can be only a single $A_i \neq 0$ for $i > 0$.

In Fig. 5.6(e–h), we display the behaviour of moments M_1, M_2, M_3, M_4 for the FH ground state at $U/\mathcal{J} = 10$. For odd moments, we find $A_i = 0\ \forall i$, making them trivially universal: For M_1, only $c_{1,\alpha_1}o_{1,\alpha_1} \neq 0$, whilst for M_3 additionally $c_{3,\alpha_3}o_{3,\alpha_3} \neq 0$. In either case, these terms are distributed near symmetrically about 0, such that the effective amplitudes vanish, reproducing the observation from exact numerics that odd moments of $\hat{R}$ average to zero (see discussion and footnote of Sec. 5.2.2). In contrast, even moments have

Table 5.1: Spectrum of SYK Liouvillian. Obtained by exact diagonalisation of the matrix representation given in Eq. (5.30), for $N = 8$ fermionic modes at half filling.

Eigenspace index i	Eigenvalue λ_i	Degeneracy d_i
0	0.000000	1
1	-0.234375	63
2	-0.328125	720
3	-0.351562	4116

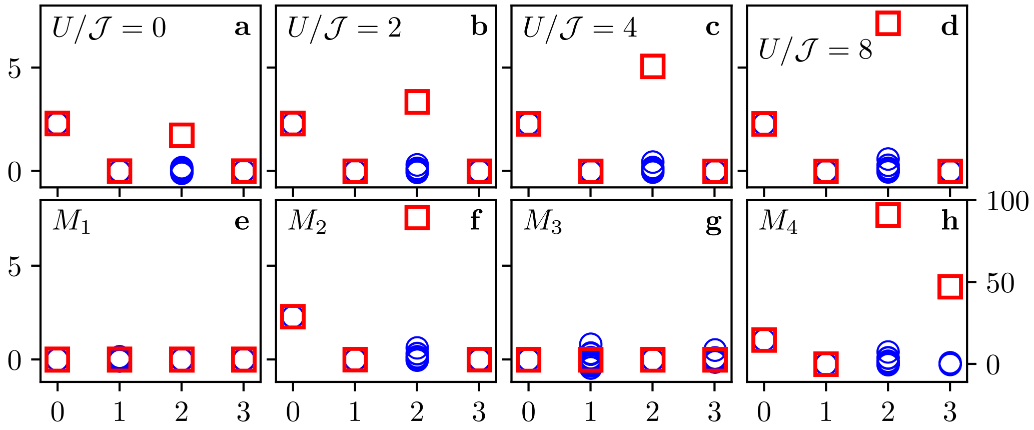

Figure 5.6: Distribution of effective amplitudes over Liouvillian eigenspaces. (a–d) Distributions of $c_{i,\alpha_i} o_{i,\alpha_i}$ (blue circles) and A_i (red squares) of Eq. (5.28) for M_2 of $\hat{R}$, for different initial FH ground states with $U/\mathcal{J} = 0, 2, 4$ and 8. Horizontal axes indicate the eigenspace index of Table 5.1. For all initial states, only one eigenspace $i^* = 2$ has non-zero effective amplitude A_2, yielding the universal evolution $\mathcal{G}[M_2(t)] = \mathrm{e}^{-t^2|\lambda_2|}$. (e–h) Similar top top row, but for moments M_1, M_2, M_3, M_4 of $\hat{R}$, for the initial FH ground state at $U/\mathcal{J} = 10$. For the highest moment, occupation of two eigenspaces can be observed, indicating that universality deteriorates in many-body operators. Note that panels e–g share the same vertical axis, whilst that of panel h is distinct and shown on its right border.

non-zero effective amplitudes in at least one eigenspace besides that of the steady state (the same holds for other initial states, such as the Néel state, see Fig. C.7). Concretely, for $k \geq 4$, we find the same two non-zero effective amplitudes A_2, A_3, yielding an approximately universal super-exponential decay $\mathcal{G}[M_k(t)] = (A_2 \mathrm{e}^{-t^2|\lambda_2|} + A_3 \mathrm{e}^{-t^2|\lambda_3|})/(A_2 + A_3)$ for even integers $k \geq 4$. The ratio A_3/A_2 is plotted in the upper-right inset of Fig. 5.4, from which a monotonic increase, and a saturation with respect to k, is evident. Together with the fact that $|\lambda_3| > |\lambda_2|$ (see Table 5.1), this explains—in accordance with Eq. (5.28)—the shift of the rescaled curve to earlier times, as well as its convergence, with moment order k.

In summary, we find (i) odd moments vanish for all t, (ii) the second moment exhibits truly universal super-exponential decay as is shown in Fig. 5.6(a–d), and (iii) higher-order even moments display approximate universality. As this analysis shows, the Bourret–Markov ME reproduces the universal features observed in our exact numerics.

Note that the aim of the ME framework developed in the previous sections is not to provide an efficient way of simulating the disorder-averaged dynamics. Indeed, the enlarged Hilbert-space, inherent to the process of mapping $\mathcal{D}$ to the matrix form of Eq. (5.30), reduces the size of numerically accessible systems. Rather, the aim is to gain additional insights by establishing a theoretical mapping to an open quantum system. For example, our present study reveals a non-trivial highly-degenerate eigenspace structure of the effective Liouvillian superoperator, through which we can explain the observed universality. The origin of this eigenspace structure is studied in-depth in our follow-up work Ref. [82], of which we provide a brief summary in the next section.

5.5 Cumulant expansion method for disorder averaged dynamics

The comparison of Sec. 5.3.3 verified that the Gaussian form of the average SYK dynamics, predicted by the master equation formalism in Eq. (5.24), agrees well with the exact numeric results. However, it also highlighted discrepancies at intermediate times (see Fig. 5.5) which, as discussed previously, are not surprising, considering that we made Markov and decorrelation assumptions during the derivation of the effective master equation given in Eq. (5.16). In particular, the decorrelation assumption came about by truncating the series expansion for the functional derivative arising from the Novikov–Furutsu theorem to lowest order [compare Eqs. (5.13)–(5.14) and (C.6)].

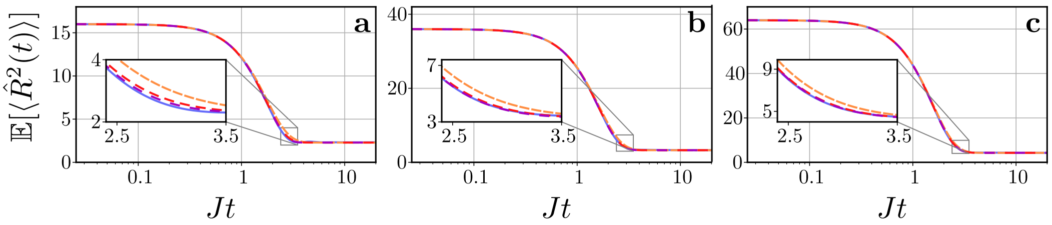

Figure 5.7: Disorder averaged dynamics via the cumulant expansion. Exact dynamics (solid-blue curve) of the second moment of the staggered magnetisation $\hat{R}$, averaged over multiple realisations of the $q = 4$ SYK Hamiltonian $\hat{H}_{\text{SYK}}$, compared to the cumulant expansion of Eq. (5.33) truncated at $k = 1$ (dashed-orange curve), $k = 2$ (dashed-red curve), and $k = 3$ (dashed-purple curve). Panels (a–c) show the dynamics at half-filling for increasing system sizes $N = 8, 12$ and 16, for which the exact numerics were averaged over 100 000, 3000, and 500 independent realisations, respectively. The initial state was taken as the Néel state for these simulations. As the insets show, the inclusion of higher cumulants improves the approximation of the exact dynamics over the simulated time-scales. Divergences at later times, arising from truncation to only a few cumulants, are studied further in Ref. [82].

This suggests that corrections to the framework of Sec. 5.3 can be obtained through the inclusion of higher order terms. A systematic approach was developed in our follow-up work Ref. [82], where we express the disorder-averaged time-evolution operator $\mathbb{E}\left[\mathrm{e}^{-\mathcal{L}t}\right]$—where now $\mathcal{L}\bullet \equiv -i[\hat{H}, \bullet]$ denotes the Liouvillian superoperator for a given disordered Hamiltonian $\hat{H}$ such that $\hat{\rho}(t) = \mathrm{e}^{-\mathcal{L}t}\hat{\rho}(0)$—as an expansion over cumulant superoperators

$$\mathbb{E}\left[\mathrm{e}^{-\mathcal{L}t}\right] = \mathrm{e}^{\mathcal{C}(t)} = \exp\left(\sum_{k=1}^{\infty} \frac{(Jt)^k}{k!}\mathcal{C}_k\right). \tag{5.31}$$

We will refer to $\mathcal{C}(t)$ as the cumulant generating superoperator, and similarly to the superoperators $\mathcal{C}_k$ as cumulants.

A convenient way to determine the cumulants is to expand both sides of Eq. (5.31), and then match equal powers of t. In particular, for any SYK-q model $\hat{H} = \hat{H}_q$, we immediately see that all superoperators $\mathcal{C}_k$ with odd k vanish, due to the Gaussian statistics of the interaction amplitudes [see Eqs. (2.5), (C.1)]. For the remaining even cumulants, calculating a given $\mathcal{C}_k$ requires the previous determination of all $\mathcal{C}_l$ with $l < k$, and thus the procedure is iterative. As an example, let us consider the first two non-vanishing cumulants for $\hat{H}_q$. Introducing the notation $\ell_\alpha\bullet = -i[\hat{h}_\alpha, \bullet]$, where $\alpha = \{i_1, \ldots, i_{q/2}; j_1, \ldots, j_{q/2}\}$ is a multi-index, and $\hat{h}_\alpha = \hat{c}^\dagger_{i_1}\ldots\hat{c}^\dagger_{i_{q/2}}\hat{c}_{j_1}\ldots\hat{c}_{j_{q/2}}$ are the $q/2$-body operators of

$\hat{H}_q$, we have

$$\mathcal{C}_2 = \mathcal{K}_q^2 \sum_{\alpha} \ell_\alpha^2, \tag{5.32a}$$

$$\mathcal{C}_4 = \mathcal{K}_q^4 \sum_{\alpha,\beta} \left(\ell_\alpha \ell_\beta^2 \ell_\alpha + \ell_\alpha \ell_\beta \ell_\alpha \ell_\beta - 2\ell_\alpha^2 \ell_\beta^2 \right), \tag{5.32b}$$

where the prefactors $\mathcal{K}_q$ are given by the numerator of the prefactor of $\hat{H}_q$ in Eq. (2.5).

Leading order truncation of the cumulant expansion, and setting $q = 4$, thus yields precisely the time-evolution of Eq. (5.24), whilst higher-order cumulants provide corrections to the ensemble-average dynamics of $\hat{H}_q$ as

$$\frac{\mathrm{d}}{\mathrm{d}t}\mathbb{E}\left[\hat{\rho}(t)\right] = \frac{\mathrm{d}}{\mathrm{d}t}\mathrm{e}^{\mathcal{C}(t)}\hat{\rho}_0 = \left(J \sum_{k=1}^{\infty} \frac{(Jt)^{2k-1}}{(2k-1)!}\mathcal{C}_{2k} \right) \mathbb{E}\left[\hat{\rho}(t)\right]. \tag{5.33}$$

For practical purposes, we can only evaluate this cumulant expansion up to some given finite order, which is as expensive as computing a short-time expansion up to that same order. Nevertheless, while the latter is limited to early times, the former is potentially able to reasonably reproduce the evolution at arbitrary times, due to the exponential form of the cumulant expansion: Even when $\mathcal{C}(t)$ is truncated, Eq. (5.31) still involves an infinite series of powers of t, and thus it can represent non-polynomial time-dependence. Further, the form of Eq. (5.33) shows that higher-order cumulants are relevant only on longer timescales, as they are suppressed by a factor $(2k)!$. For a system that thermalises quickly then, such as $\hat{H}_{\mathrm{SYK}}$, a finite number of cumulants is sufficient to obtain a valid approximation of the exact dynamics. Figure 5.7 shows the numerically simulated SYK dynamics of the second moment of the staggered magnetisation $\hat{R}$ [Eq. (5.6)], generated according to the cumulant expansion of Eq. (5.33) for up to $2k = 6$. Especially in the intermediate time domain, where the master equation of Sec. 5.3 showed deviations, the inclusion of higher cumulants yields a better approximation of the exact dynamics.

Finally, we note that the above cumulant expansion also allows one to analytically calculate the spectrum of the effective Liouvillian superoperator studied in Sec. 5.4. The key idea is that the disorder averaged dynamics of $\hat{H}_{\mathrm{SYK}}$ conserve operator-size, which allows one to define an operator bases with respect to which the cumulants $\mathcal{C}_k$ can be decomposed. Further details can be found in Ref. [82].

5.6 Discussion

In summary, we have theoretically investigated the post quench equilibration dynamics of the SYK model. By numerically studying the disorder-averaged exact evolution of a set of local observables and their higher-order moments, we find that the equilibration process is universal: The curves illustrating the equilibration of different initial states overlap throughout the dynamics under a straightforward rescaling, revealing the independence of the dynamics on chosen initial states. The equilibrated steady state, which is the Gibbs infinite temperature state in the present study, is reached in fast time-scales of leading-order processes determined by the variance of the disordered interaction. In addition, the universal equilibration curve can be well approximated by a Gaussian, yielding fast super-exponential equilibration dynamics.

In order to achieve an analytical understanding of the numerical findings, we have formulated a theoretical framework based on the Novikov–Furutsu theorem. This framework describes how a disordered quantum many-body system undergoes an effective dissipative dynamics due to phase mixing in the ensemble averaged evolution rather than to interactions with a heat bath [252, 268]. Having formulated the derivation for general disordered Hamiltonians, its scope for applications extends beyond the present investigation of the SYK model. Employing Bourret and Markov approximations, we obtain a Lindblad master equation that successfully describes the key features of the observed super-exponential equilibration dynamics under the SYK model. Furthermore, a spectral analysis of the corresponding Liouvillian superoperator illuminates the exact universality of low-order moments, representing few-body observables, as well as an approximate universality of higher-order moments representing many-body observables.

The Novikov–Furutsu theorem has been used extensively in the literature for the study of systems with noise of short correlation time [253–255], and equations equivalent to those derived in Sec. 5.3 have been obtained to second order in perturbative noise strength [256–258, 266, 267]. In the present scenario, where noise correlation times are formally infinite and where the disordered interactions provide the dominant (because only) energy scale, there is at first sight no reason for such perturbative approaches to hold. Yet, the strong chaoticity of the SYK model seems to yield a fast decorrelation, making the Bourret–Markov approximation a good description of the exact dynamics.

The salient features of the universal curve occur on sizable absolute scales and very fast time scales, on the order of the mean interaction strength J, and they can be extracted from the observation of local observables following a simple global quench. Thus, the discussed effects should be readily observable in laboratory implementations of the SYK model.

An interesting topic for future investigation is, for example, in how far the universality survives in disordered models without all-to-all connectivity, and to apply the effective master equation approach to these. Whilst time-independent Gaussian disorder will always yield a Gaussian decay according to our formalism, the universality (initial state independence) would depend on details of the Hamiltonian. For example, in models with a clean contribution $\hat{H}_0 \neq 0$ one can expect a complex interplay between disorder and clean dynamics, such as the many-body localisation transition [38, 286–288]. Various mathematical extensions of the presented master equation framework are also possible, e.g., to treat non-Gaussian disorder [263, 282]. Finally, as this framework can naturally include dephasing noise with arbitrary correlation spectrum, another interesting line of study would be to estimate the interplay between dissipation due to an external environment and dephasing due to disorder averaging, which is central, e.g., to environment-assisted quantum transport [188, 289–291].

6 Conclusion

We have studied the dynamics and quantum simulation of strongly-correlated systems with long-range interactions and quenched disorder, with a particular focus on the Sachdev–Ye–Kitaev (SYK) model and the cavity quantum electrodynamics (cQED) platform. Starting from the microscopic many-body Hamiltonian for a quasi two-dimensional fermionic quantum gas trapped in a multi-mode cavity, we have shown analytically that when driven in the dispersive regime and subjected to a spatially-disordered AC-Stark shift, the system is able to synthesise an effective model $\hat{H}_{\mathrm{eff}}$ with long-range, random interaction amplitudes, as required by the target SYK model $\hat{H}_{\mathrm{SYK}}$. Importantly, we have identified two key physical parameters that allow for the dynamics of $\hat{H}_{\mathrm{eff}}$ to replicate those of $\hat{H}_{\mathrm{SYK}}$, and which can be tuned experimentally: (i) The effective number of modes participating in the light–matter interactions, parameterised by $\widetilde{\delta\omega}$, and (ii) the transverse size ζ of the atomic cloud, controlling the mechanical coupling between atoms and cavity photons. Numeric simulations of the dynamics generated by $\hat{H}_{\mathrm{eff}}$, over an experimentally feasible range of $\widetilde{\delta\omega}$ and ζ, show that the quantum chaotic, fast-scrambling dynamics of $\hat{H}_{\mathrm{SYK}}$ should be achievable in current state-of-the-art multimode cQED experiments with fermionic atoms.

In particular the capability to introduce quenched disorder into the cQED system in a controlled manner, as recently demonstrated by Ref. [77], marks an important milestone in the above pursuit. This experiment demonstrated the feasibility of the disordered light-shift technique, employing it to synthesise random spin models in the single-mode regime with fermionic ^{6}Li atoms. We have shown analytically that in the far off-resonant regime, this generates a disordered Lipkin–Meshkov–Glick (LMG) model. By modelling the preparation and interrogation phases of the experiment through a Lindblad master equation, we have shown that the frequency-resolved transmission spectroscopy measurements of the atoms' dark-state manifold allowed for the extraction of the absorptive part of the dynamic susceptibility. This allowed us to analytically describe saturation effects, depending on the probe power and frequency, of the measured signal, and further guided our numeric simulations in reproducing the measured data by providing the correct relation between the susceptibility's linewidth and the atomic decay rate. An intriguing feature of the above experiment is that whilst disorder induces localisation of spin excitations over fewer-and-fewer atoms, the cavity-mediated global interaction nevertheless permits energetic resonances over arbitrary distances. We have demonstrated that, despite the lack of spatially-resolved information, the spectroscopic signal can nevertheless probe the localisation properties of the disorderd LMG system. Specifically, we have shown that the dynamic susceptibility's amplitude bounds the participation ratio (evaluated with respect to the single-excitation basis) of certain excited states, thereby allowing the experiment to observe the fragmentation of the zero-disorder collective spin state into ever-more localised spin excitations as a function of disorder strength.

Once synthesised, a typical protocol to probe the far-from-equilibrium dynamics of quantum many-body systems is a quench experiment. Focussing on operator moments of local observables, we have identified, through exact diagonalisation simulations, that after a global quench into the SYK model, the disorder averaged dynamics exhibit a rapid, super-exponential equilibration. For low operator moments, we further identified a dynamical universality in the sense that the functional form of the average evolution curve is independent of the initial state, as revealed by an appropriate rescaling. We have developed an analytic framework, mapping the unitary dynamics generated by an ensemble of disordered Hamiltonians to an effective dissipative evolution described by a Lindblad master equation. Under a decorrelation and Markov assumption, the clean and disordered parts of generic Hamiltonians map, respectively, to the coherent and dissipative parts of the Liouvillian superoperator governing the master equation, whose dissipation rates are controlled by the Hamiltonian disorder statistics. Applied to the SYK model, this framework yields a purely dissipative evolution, with dissipation rates growing linearly in time, thereby capturing the super-exponential equilibration, and providing further understanding of the initial-state independence on a formal level, via a spectral decomposition of the Liouvillian superoperator. Discrepancies with the exact evolution at intermediate times are addressed through a cumulant expansion, which formally allows one to go beyond the approximations made in deriving the above master equation.

Future directions of our work—addressed in more detail in the concluding remarks of the respective chapters—include the extension of the cQED proposal to variations of the SYK model, such as with Brownian noise, or coupled SYK systems; investigating the possibility to incorporate spin-orbit coupling or twisted cavities [292] in order to break time-reversal symmetry; or adapting the proposal to the formally similar platform of circuit-QED. The realisation of the disordered LMG model offers the prospect of studying the effects of disorder on superconductivity, due to its relation to the pairing Hamiltonian of

BCS theory and more broadly to Richardson–Gaudin models. To study the many-body physics of such systems it is necessary to go beyond the single-excitation regime realised here. This could be achieved via atomic species with long-lived excitations [180], or by encoding the spins in the ground state manifold and coupling them via Raman transitions [293]. Interesting future applications of the effective master equation framework could be to investigate the presence of universal far-from-equilibrium dynamics in models without all-to-all connectivity or with non-Gaussian disorder; as well as to study model Hamiltonians with competing clean and disordered contributions which may exhibit localisation transitions; or, in the case of disordered open quantum systems, to study the interplay of intrinsic dissipation with the effective loss processes arising from disorder averaging.

References

[1] V. Zelevinsky, B. A. Brown, N. Frazier and M. Horoi, "The nuclear shell model as a testing ground for many-body quantum chaos", Phys. Rep. **276**, 85–176 (1996).

[2] P. M. Chaikin and T. C. Lubensky, *Principles of Condensed Matter Physics* (Cambridge University Press, 1995).

[3] M. Boninsegni and N. V. Prokof'ev, "Colloquium: Supersolids: What and where are they?", Rev. Mod. Phys. **84**, 759–776 (2012).

[4] S. A. Hartnoll, A. Lucas and S. Sachdev, *Holographic Quantum Matter* (MIT Press, 2018).

[5] P. Nozières and D. Pines, *The Theory of Quantum Liquids* (CRC Press, 2018).

[6] J. B. Ketterson, *The Physics of Solids* (Oxford University Press, 2016).

[7] I. M. Georgescu, S. Ashhab and F. Nori, "Quantum simulation", Rev. Mod. Phys. **86**, 153–185 (2014).

[8] M. Troyer and U.-J. Wiese, "Computational Complexity and Fundamental Limitations to Fermionic Quantum Monte Carlo Simulations", Phys. Rev. Lett. **94**, 170201 (2005).

[9] P. Silvi, F. Tschirsich, M. Gerster, J. Jünemann, D. Jaschke, M. Rizzi and S. Montangero, "The Tensor Networks Anthology: Simulation techniques for many-body quantum lattice systems", SciPost Phys. Lect. Notes, 8 (2019).

[10] R. Orús, "Tensor networks for complex quantum systems", Nat. Rev. Phys. **1**, 538–550 (2019).

[11] I. Bloch, J. Dalibard and W. Zwerger, "Many-body physics with ultracold gases", Rev. Mod. Phys. **80**, 885–964 (2008).

[12] I. Bloch, J. Dalibard and S. Nascimbène, "Quantum simulations with ultracold quantum gases", Nat. Phys. **8**, 267–276 (2012).

[13] M. Lewenstein, A. Sanpera and V. Ahufinger, *Ultracold Atoms in Optical Lattices: Simulating quantum many-body systems* (Oxford University Press, 2012).

[14] E. Altman, K. R. Brown, G. Carleo, L. D. Carr, E. Demler, C. Chin, B. DeMarco, S. E. Economou, M. A. Eriksson, K.-M. C. Fu, M. Greiner, K. R. Hazzard, R. G. Hulet, A. J. Kollár, B. L. Lev, M. D. Lukin, R. Ma, X. Mi, S. Misra, C. Monroe, K. Murch, Z. Nazario, K.-K. Ni, A. C. Potter, P. Roushan, M. Saffman, M. Schleier-Smith, I. Siddiqi, R. Simmonds, M. Singh, I. Spielman, K. Temme, D. S. Weiss, J. Vučković, V. Vuletić, J. Ye and M. Zwierlein, "Quantum Simulators: Architectures and Opportunities", PRX Quantum **2**, 017003 (2021).

[15] R. Blatt and C. F. Roos, "Quantum simulations with trapped ions", Nat. Phys. **8**, 277–284 (2012).

[16] C. Monroe, W. C. Campbell, L.-M. Duan, Z.-X. Gong, A. V. Gorshkov, P. W. Hess, R. Islam, K. Kim, N. M. Linke, G. Pagano, P. Richerme, C. Senko and N. Y. Yao, "Programmable quantum simulations of spin systems with trapped ions", Rev. Mod. Phys. **93**, 025001 (2021).

[17] M. Lewenstein, A. Sanpera, V. Ahufinger, B. Damski, A. Sen(De) and U. Sen, "Ultracold atomic gases in optical lattices: mimicking condensed matter physics and beyond", Adv. Phys. **56**, 243–379 (2007).

[18] C. Gross and I. Bloch, "Quantum simulations with ultracold atoms in optical lattices", Science **357**, 995–1001 (2017).

[19] A. Browaeys and T. Lahaye, "Many-body physics with individually controlled Rydberg atoms", Nat. Phys. **16**, 132–142 (2020).

[20] I. Cong, H. Levine, A. Keesling, D. Bluvstein, S.-T. Wang and M. D. Lukin, "Hardware-Efficient, Fault-Tolerant Quantum Computation with Rydberg Atoms", Phys. Rev. X **12**, 021049 (2022).

[21] H. Ritsch, P. Domokos, F. Brennecke and T. Esslinger, "Cold atoms in cavity-generated dynamical optical potentials", Rev. Mod. Phys. **85**, 553–601 (2013).

[22] F. Mivehvar, F. Piazza, T. Donner and H. Ritsch, "Cavity QED with quantum gases: new paradigms in many-body physics", Adv. Phys. **70**, 1–153 (2021).

[23] M. Kjaergaard, M. E. Schwartz, J. Braumüller, P. Krantz, J. I.-J. Wang, S. Gustavsson and W. D. Oliver, "Superconducting Qubits: Current State of Play", Annu. Rev. Condens. Matter Phys. **11**, 369–395 (2020).

[24] A. Blais, A. L. Grimsmo, S. M. Girvin and A. Wallraff, “Circuit quantum electrodynamics”, Rev. Mod. Phys. **93**, 025005 (2021).

[25] M. Greiner, O. Mandel, T. Esslinger, T. W. Hänsch and I. Bloch, “Quantum phase transition from a superfluid to a Mott insulator in a gas of ultracold atoms”, Nature **415**, 39–44 (2002).

[26] S. Sachdev, *Quantum Phase Transitions*, 2nd ed. (Cambridge University Press, 2011).

[27] L. D’Alessio, Y. Kafri, A. Polkovnikov and M. Rigol, “From quantum chaos and eigenstate thermalization to statistical mechanics and thermodynamics”, Adv. Phys. **65**, 239–362 (2016).

[28] J. M. Deutsch, “Eigenstate thermalization hypothesis”, Rep. Prog. Phys. **81**, 082001 (2018).

[29] I. Rotter and J. P. Bird, “A review of progress in the physics of open quantum systems: theory and experiment”, Rep. Prog. Phys. **78**, 114001 (2015).

[30] H. Weimer, A. Kshetrimayum and R. Orús, “Simulation methods for open quantum many-body systems”, Rev. Mod. Phys. **93**, 015008 (2021).

[31] H. M. Wiseman and G. J. Milburn, *Quantum Measurement and Control* (Cambridge University Press, 2009).

[32] T. Kinoshita, T. Wenger and D. S. Weiss, “A quantum Newton’s cradle”, Nature **440**, 900–903 (2006).

[33] T. Langen, S. Erne, R. Geiger, B. Rauer, T. Schweigler, M. Kuhnert, W. Rohringer, I. E. Mazets, T. Gasenzer and J. Schmiedmayer, “Experimental observation of a generalized Gibbs ensemble”, Science **348**, 207–211 (2015).

[34] A. M. Kaufman, M. E. Tai, A. Lukin, M. Rispoli, R. Schittko, P. M. Preiss and M. Greiner, “Quantum thermalization through entanglement in an isolated many-body system”, Science **353**, 794–800 (2016).

[35] R. Horodecki, P. Horodecki, M. Horodecki and K. Horodecki, “Quantum entanglement”, Rev. Mod. Phys. **81**, 865–942 (2009).

[36] T. Brydges, A. Elben, P. Jurcevic, B. Vermersch, C. Maier, B. P. Lanyon, P. Zoller, R. Blatt and C. F. Roos, “Probing Rényi entanglement entropy via randomized measurements”, Science **364**, 260–263 (2019).

[37] P. W. Anderson, “Absence of Diffusion in Certain Random Lattices”, Phys. Rev. **109**, 1492–1505 (1958).

[38] R. Nandkishore and D. A. Huse, “Many-Body Localization and Thermalization in Quantum Statistical Mechanics”, Annu. Rev. Condens. Matter Phys. **6**, 15–38 (2015).

[39] M. Schreiber, S. S. Hodgman, P. Bordia, H. P. Lüschen, M. H. Fischer, R. Vosk, E. Altman, U. Schneider and I. Bloch, “Observation of many-body localization of interacting fermions in a quasirandom optical lattice”, Science **349**, 842–845 (2015).

[40] J.-Y. Choi, S. Hild, J. Zeiher, P. Schauß, A. Rubio-Abadal, T. Yefsah, V. Khemani, D. A. Huse, I. Bloch and C. Gross, “Exploring the many-body localization transition in two dimensions”, Science **352**, 1547–1552 (2016).

[41] A. Lukin, M. Rispoli, R. Schittko, M. E. Tai, A. M. Kaufman, S. Choi, V. Khemani, J. Léonard and M. Greiner, “Probing entanglement in a many-body–localized system”, Science **364**, 256–260 (2019).

[42] N. Lashkari, D. Stanford, M. Hastings, T. Osborne and P. Hayden, “Towards the fast scrambling conjecture”, J. High Energ. Phys. **2013**, 22 (2013).

[43] S. Xu and B. Swingle, “Scrambling Dynamics and Out-of-Time Ordered Correlators in Quantum Many-Body Systems: a Tutorial”, arXiv:2202.07060 [quant-ph] (2022).

[44] E. H. Lieb and D. W. Robinson, “The finite group velocity of quantum spin systems”, Commun. Math. Phys. **28**, 251–257 (1972).

[45] M. B. Hastings and T. Koma, “Spectral gap and exponential decay of correlations”, Commun. Math. Phys. **265**, 781–804 (2006).

[46] M. Foss-Feig, Z.-X. Gong, C. W. Clark and A. V. Gorshkov, “Nearly Linear Light Cones in Long-Range Interacting Quantum Systems”, Phys. Rev. Lett. **114**, 157201 (2015).

[47] Y. Sekino and L. Susskind, “Fast scramblers”, J. High Energ. Phys. **2008**, 065 (2008).

[48] P. Hayden and J. Preskill, “Black holes as mirrors: quantum information in random subsystems”, J. High Energ. Phys. **2007**, 120–120 (2007).

[49] S. H. Shenker and D. Stanford, “Black holes and the butterfly effect”, J. High Energ. Phys. **2014**, 67 (2014).

[50] D. A. Roberts, D. Stanford and L. Susskind, “Localized shocks”, J. High Energ. Phys. **2015**, 51 (2015).

[51] J. Maldacena, S. H. Shenker and D. Stanford, “A bound on chaos”, J. High Energ. Phys. **2016**, 106 (2016).

[52] S. Sachdev and J. Ye, “Gapless spin-fluid ground state in a random quantum Heisenberg magnet”, Phys. Rev. Lett. **70**, 3339–3342 (1993).

[53] A. Kitaev, “A simple model of quantum holography”, Talks given at “Entanglement in Strongly-Correlated Quantum Matter,” (Part 1, Part 2), KITP (2015).

[54] D. Chowdhury, A. Georges, O. Parcollet and S. Sachdev, “Sachdev-Ye-Kitaev models and beyond: Window into non-Fermi liquids”, Rev. Mod. Phys. **94**, 035004 (2022).

[55] S. Sachdev, “Bekenstein-Hawking Entropy and Strange Metals”, Phys. Rev. X **5**, 041025 (2015).

[56] O. Parcollet and A. Georges, “Non-Fermi-liquid regime of a doped Mott insulator”, Phys. Rev. B **59**, 5341–5360 (1999).

[57] J. Maldacena and D. Stanford, “Remarks on the Sachdev-Ye-Kitaev model”, Phys. Rev. D **94**, 106002 (2016).

[58] K. Jensen, “Chaos in AdS_2 Holography”, Phys. Rev. Lett. **117**, 111601 (2016).

[59] C. Teitelboim, “Gravitation and hamiltonian structure in two spacetime dimensions”, Phys. Lett. B **126**, 41–45 (1983).

[60] R. Jackiw, “Lower dimensional gravity”, Nucl. Phys. B **252**, 343–356 (1985).

[61] D. I. Pikulin and M. Franz, “Black Hole on a Chip: Proposal for a Physical Realization of the Sachdev-Ye-Kitaev model in a Solid-State System”, Phys. Rev. X **7**, 031006 (2017).

[62] A. Chew, A. Essin and J. Alicea, “Approximating the Sachdev-Ye-Kitaev model with Majorana wires”, Phys. Rev. B **96**, 121119 (2017).

[63] A. Chen, R. Ilan, F. de Juan, D. I. Pikulin and M. Franz, “Quantum Holography in a Graphene Flake with an Irregular Boundary”, Phys. Rev. Lett. **121**, 036403 (2018).

[64] I. Danshita, M. Hanada and M. Tezuka, “Creating and probing the Sachdev–Ye–Kitaev model with ultracold gases: Towards experimental studies of quantum gravity”, Prog. Theor. Exp. Phys. **2017**, 083I01 (2017).

[65] C. Wei and T. A. Sedrakyan, “Optical lattice platform for the Sachdev-Ye-Kitaev model”, Phys. Rev. A **103**, 013323 (2021).

[66] L. García-Álvarez, I. L. Egusquiza, L. Lamata, A. del Campo, J. Sonner and E. Solano, “Digital Quantum Simulation of Minimal AdS/CFT”, Phys. Rev. Lett. **119**, 040501 (2017).

[67] R. Babbush, D. W. Berry and H. Neven, “Quantum simulation of the Sachdev-Ye-Kitaev model by asymmetric qubitization”, Phys. Rev. A **99**, 040301 (2019).

[68] Z. Luo, Y.-Z. You, J. Li, C.-M. Jian, D. Lu, C. Xu, B. Zeng and R. Laflamme, “Quantum simulation of the non-fermi-liquid state of Sachdev-Ye-Kitaev model”, npj Quantum Inf. **5**, 53 (2019).

[69] D. L. Jafferis, A. Zlokapa, J. D. Lykken, D. K. Kolchmeyer, S. I. Davis, N. Lauk, H. Neven and M. Spiropulu, “Traversable wormhole dynamics on a quantum processor”, Nature **612**, 51–55 (2022).

[70] B. Kobrin, T. Schuster and N. Y. Yao, “Comment on “Traversable wormhole dynamics on a quantum processor””, arXiv:2302.07897 [quant-ph] (2023).

[71] D. L. Jafferis, A. Zlokapa, J. D. Lykken, D. K. Kolchmeyer, S. I. Davis, N. Lauk, H. Neven and M. Spiropulu, “Comment on “Comment on “Traversable wormhole dynamics on a quantum processor” ””, arXiv:2303.15423 [quant-ph] (2023).

[72] K. Roux, H. Konishi, V. Helson and J.-P. Brantut, “Strongly correlated Fermions strongly coupled to light”, Nat. Commun. **11**, 2974 (2020).

[73] X. Zhang, Y. Chen, Z. Wu, J. Wang, J. Fan, S. Deng and H. Wu, “Observation of a superradiant quantum phase transition in an intracavity degenerate Fermi gas”, Science **373**, 1359–1362 (2021).

[74] É. Lantagne-Hurtubise, C. Li and M. Franz, “Family of Sachdev-Ye-Kitaev models motivated by experimental considerations”, Phys. Rev. B **97**, 235124 (2018).

[75] J. Kim, X. Cao and E. Altman, “Low-rank Sachdev-Ye-Kitaev models”, Phys. Rev. B **101**, 125112 (2020).

[76] A. J. Kollár, A. T. Papageorge, B. K., M. A. Armen and B. L. Lev, “An adjustable-length cavity and Bose–Einstein condensate apparatus for multimode cavity QED”, New J. Phys. **17**, 043012 (2015).

[77] N. Sauerwein, F. Orsi, P. Uhrich, S. Bandyopadhyay, F. Mattiotti, T. Cantat-Moltrecht, G. Pupillo, P. Hauke and J.-P. Brantut, “Engineering random spin models with atoms in a high-finesse cavity”, Nat. Phys. (2023).

[78] G. Tóth, “Multipartite entanglement and high-precision metrology”, Phys. Rev. A **85**, 022322 (2012).

[79] P. Hyllus, W. Laskowski, R. Krischek, C. Schwemmer, W. Wieczorek, H. Weinfurter, L. Pezzé and A. Smerzi, “Fisher information and multiparticle entanglement”, Phys. Rev. A **85**, 022321 (2012).

[80] P. Uhrich, S. Bandyopadhyay, N. Sauerwein, J. Sonner, J.-P. Brantut and P. Hauke, “A cavity quantum electrodynamics implementation of the Sachdev–Ye–Kitaev model”, arXiv:2303.11343 [quant-ph] (2023).

[81] S. Bandyopadhyay, P. Uhrich, A. Paviglianiti and P. Hauke, “Universal equilibration dynamics of the Sachdev-Ye-Kitaev model”, Quantum **7**, 1022 (2023).

[82] A. Paviglianiti, S. Bandyopadhyay, P. Uhrich and P. Hauke, “Absence of operator growth for average equal-time observables in charge-conserved sectors of the Sachdev-Ye-Kitaev model”, J. High Energ. Phys. **2023**, 126 (2023).

[83] A. Paviglianiti, “Universality in the Quench Dynamics of the Sachdev-Ye-Kitaev Model: Master Equation and Cumulant Expansion Approaches”, MSc Thesis (Università di Trento, 2021).

[84] C. Dağ, Y. Wang, P. Uhrich, X. Na and J. Halimeh, “Critical slowing down in sudden quench dynamics”, Phys. Rev. B **107**, L121113 (2023).

[85] C. Dağ, P. Uhrich, Y. Wang, I. McCulloch and J. Halimeh, “Detecting quantum phase transitions in the quasistationary regime of Ising chains”, Phys. Rev. B **107**, 094432 (2023).

[86] Y. J. Joshi, N. Sauerwein, A. Youssefi, P. Uhrich and T. J. Kippenberg, “Automated wide-ranged finely tunable microwave cavity for narrowband phase noise filtering”, Rev. Sci. Instrum. **92**, 034710 (2021).

[87] A. Youssefi, I. Shomroni, Y. J. Joshi, N. R. Bernier, A. Lukashchuk, P. Uhrich, L. Qiu and T. J. Kippenberg, “A cryogenic electro-optic interconnect for superconducting devices”, Nat. Electron. **4**, 326–332 (2021).

[88] P. Uhrich, N. Defenu, R. Jafari and J. C. Halimeh, "Out-of-equilibrium phase diagram of long-range superconductors", Phys. Rev. B **101**, 245148 (2020).

[89] M. Endres, M. Cheneau, T. Fukuhara, C. Weitenberg, P. Schauß, C. Gross, L. Mazza, M. C. Bañuls, L. Pollet, I. Bloch and S. Kuhr, "Observation of Correlated Particle-Hole Pairs and String Order in Low-Dimensional Mott Insulators", Science **334**, 200–203 (2011).

[90] T. A. Hilker, G. Salomon, F. Grusdt, A. Omran, M. Boll, E. Demler, I. Bloch and C. Gross, "Revealing hidden antiferromagnetic correlations in doped Hubbard chains via string correlators", Science **357**, 484–487 (2017).

[91] J. Polchinski and V. Rosenhaus, "The spectrum in the Sachdev-Ye-Kitaev model", J. High Energ. Phys. **2016**, 1–25 (2016).

[92] D. A. Trunin, "Pedagogical introduction to the Sachdev–Ye–Kitaev model and two-dimensional dilaton gravity", Phys.-Usp. **64**, 219–252 (2021).

[93] C. M. Varma, P. B. Littlewood, S. Schmitt-Rink, E. Abrahams and A. E. Ruckenstein, "Phenomenology of the normal state of Cu-O high-temperature superconductors", Phys. Rev. Lett. **63**, 1996–1999 (1989).

[94] H. Liu and J. Sonner, "Holographic systems far from equilibrium: a review", Rep. Prog. Phys. **83**, 016001 (2019).

[95] H. Liu and J. Julian Sonner, "Quantum many-body physics from a gravitational lens", Nat. Rev. Phys. **2**, 615–633 (2020).

[96] W. Fu and S. Sachdev, "Numerical study of fermion and boson models with infinite-range random interactions", Phys. Rev. B **94**, 035135 (2016).

[97] Y.-Z. You, A. W. W. Ludwig and C. Xu, "Sachdev-Ye-Kitaev model and thermalization on the boundary of many-body localized fermionic symmetry-protected topological states", Phys. Rev. B **95**, 115150 (2017).

[98] J. S. Cotler, G. Gur-Ari, M. Hanada, J. Polchinski, P. Saad, S. H. Shenker, D. Stanford, A. Streicher and M. Tezuka, "Black holes and random matrices", J. High Energ. Phys. **2017**, 118 (2017).

[99] T. A. Brody, J. Flores, J. B. French, P. A. Mello, A. Pandey and S. S. M. Wong, "Random-matrix physics: spectrum and strength fluctuations", Rev. Mod. Phys. **53**, 385–479 (1981).

[100] C. Sünderhauf, L. Piroli, X.-L. Qi, N. Schuch and J. I. Cirac, "Quantum chaos in the Brownian SYK model with large finite N: OTOCs and tripartite information", J. High Energ. Phys. **2019**, 38 (2019).

[101] Y. Gu, A. Kitaev, S. Sachdev and G. Tarnopolsky, "Notes on the complex Sachdev-Ye-Kitaev model", J. High Energ. Phys. **2020**, 157 (2020).

[102] A. M. García-García, B. Loureiro, A. Romero-Bermúdez and M. Tezuka, "Chaotic-Integrable Transition in the Sachdev-Ye-Kitaev Model", Phys. Rev. Lett. **120**, 241603 (2018).

[103] S. Xu, L. Susskind, Y. Su and B. Swingle, "A Sparse Model of Quantum Holography", arXiv:2008.02303 [cond-mat.str-el] (2020).

[104] Y. Cao, Y. N. Zhou, T. T. Shi and W. Zhang, "Towards quantum simulation of Sachdev-Ye-Kitaev model", Sci. Bull. **65**, 1170–1176 (2020).

[105] A. M. García-García, Y. Jia, D. Rosa and J. J. M. Verbaarschot, "Sparse Sachdev-Ye-Kitaev model, quantum chaos, and gravity duals", Phys. Rev. D **103**, 106002 (2021).

[106] M. Tezuka, O. Oktay, E. Rinaldi, M. Hanada and F. Nori, "Binary-coupling sparse Sachdev-Ye-Kitaev model: An improved model of quantum chaos and holography", Phys. Rev. B **107**, L081103 (2023).

[107] D. Chowdhury, Y. Werman, E. Berg and T. Senthil, "Translationally Invariant Non-Fermi-Liquid Metals with Critical Fermi Surfaces: Solvable Models", Phys. Rev. X **8**, 031024 (2018).

[108] J. Maldacena and X.-L. Qi, "Eternal traversable wormhole", arXiv:1804.00491 [hep-th] (2018).

[109] P. Gao and D. L. Jafferis, "A traversable wormhole teleportation protocol in the SYK model", J. High Energ. Phys. **2021**, 97 (2021).

[110] O. Bohigas, M. J. Giannoni and C. Schmit, "Characterization of Chaotic Quantum Spectra and Universality of Level Fluctuation Laws", Phys. Rev. Lett. **52**, 1–4 (1984).

[111] F. Haake, *Quantum Signatures of Chaos* (Springer Berlin Heidelberg, 2010).

[112] J. Cotler, N. Hunter-Jones, J. Liu and B. Yoshida, "Chaos, complexity, and random matrices", J. High Energ. Phys. **2017**, 48 (2017).

[113] M. V. Berry and M. Tabor, "Level clustering in the regular spectrum", Proc. R. Soc. Lond. A. **356**, 375–394 (1977).

[114] J. Sonner and M. Vielma, “Eigenstate thermalization in the Sachdev-Ye-Kitaev model”, J. High Energ. Phys. **2017**, `10.1007/jhep11(2017)149` (2017).

[115] H. Gharibyan, M. Hanada, S. H. Shenker and M. Tezuka, “Onset of random matrix behavior in scrambling systems”, J. High Energ. Phys. **2018**, 124 (2018).

[116] L. K. Joshi, A. Elben, A. Vikram, B. Vermersch, V. Galitski and P. Zoller, “Probing Many-Body Quantum Chaos with Quantum Simulators”, Phys. Rev. X **12**, 011018 (2022).

[117] A. del Campo, J. Molina-Vilaplana and J. Sonner, “Scrambling the spectral form factor: Unitarity constraints and exact results”, Phys. Rev. D **95**, 126008 (2017).

[118] A. Altland and D. Bagrets, “Quantum ergodicity in the SYK model”, Nucl. Phys. B **930**, 45–68 (2018).

[119] A. del Campo, J. Molina-Vilaplana, L. F. Santos and J. Sonner, “Decay of a thermofield-double state in chaotic quantum systems”, Eur. Phys. J. Spec. Top. **227**, 247–258 (2018).

[120] A. Altland, D. Bagrets, P. Nayak, J. Sonner and M. Vielma, “From operator statistics to wormholes”, Phys. Rev. Res. **3**, 033259 (2021).

[121] R. A. Davison, W. Fu, A. Georges, Y. Gu, K. Jensen and S. Sachdev, “Thermoelectric transport in disordered metals without quasiparticles: The Sachdev-Ye-Kitaev models and holography”, Phys. Rev. B **95**, 155131 (2017).

[122] A. M. García-García and J. J. M. Verbaarschot, “Analytical spectral density of the Sachdev-Ye-Kitaev model at finite N”, Phys. Rev. D **96**, 066012 (2017).

[123] P. Hosur, X.-L. Qi, D. A. Roberts and B. Yoshida, “Chaos in quantum channels”, J. High Energ. Phys. **2016**, 4 (2016).

[124] D. N. Page, “Average entropy of a subsystem”, Phys. Rev. Lett. **71**, 1291–1294 (1993).

[125] Y. Liao and V. Galitski, “Nonlinear sigma model approach to many-body quantum chaos: Regularized and unregularized out-of-time-ordered correlators”, Phys. Rev. B **98**, 205124 (2018).

[126] A. Romero-Bermúdez, K. Schalm and V. Scopelliti, “Regularization dependence of the OTOC. Which Lyapunov spectrum is the physical one?”, J. High Energ. Phys. **2019**, 107 (2019).

[127] D. A. Roberts and B. Yoshida, “Chaos and complexity by design”, J. High Energ. Phys. **2017**, 121 (2017).

[128] M. C. Gutzwiller, *Chaos in Classical and Quantum Mechanics* (Springer New York, 1990).

[129] T. Xu, T. Scaffidi and X. Cao, “Does Scrambling Equal Chaos?”, Phys. Rev. Lett. **124**, 140602 (2020).

[130] K. Hashimoto, K. Murata and R. Yoshii, “Out-of-time-order correlators in quantum mechanics”, J. High Energ. Phys. **2017**, 138 (2017).

[131] R. H. Dicke, “Coherence in Spontaneous Radiation Processes”, Phys. Rev. **93**, 99–110 (1954).

[132] K. Baumann, C. Guerlin, F. Brennecke and T. Esslinger, “Dicke quantum phase transition with a superfluid gas in an optical cavity”, Nature **464**, 1301–1306 (2010).

[133] R. Landig, L. Hruby, N. Dogra, M. Landini, R. Mottl, T. Donner and T. Esslinger, “Quantum phases from competing short- and long-range interactions in an optical lattice”, Nature **532**, 476–479 (2016).

[134] J. Léonard, A. Morales, P. Zupancic, T. Esslinger and T. Donner, “Supersolid formation in a quantum gas breaking a continuous translational symmetry”, Nature **543**, 87–90 (2017).

[135] P. Sierant, K. Biedroń, G. Morigi and J. Zakrzewski, “Many-body localization in presence of cavity mediated long-range interactions”, SciPost Phys. **7**, 008 (2019).

[136] M. Müller, P. Strack and S. Sachdev, “Quantum charge glasses of itinerant fermions with cavity-mediated long-range interactions”, Phys. Rev. A **86**, 023604 (2012).

[137] V. D. Vaidya, Y. Guo, R. M. Kroeze, K. E. Ballantine, A. J. Kollár, J. Keeling and B. L. Lev, “Tunable-Range, Photon-Mediated Atomic Interactions in Multimode Cavity QED”, Phys. Rev. X **8**, 011002 (2018).

[138] Y. Guo, R. M. Kroeze, B. P. Marsh, S. Gopalakrishnan, J. Keeling and B. L. Lev, “An optical lattice with sound”, Nature **599**, 211–215 (2021).

[139] B. P. Marsh, Y. Guo, R. M. Kroeze, S. Gopalakrishnan, S. Ganguli, J. Keeling and B. L. Lev, “Enhancing Associative Memory Recall and Storage Capacity Using Confocal Cavity QED”, Phys. Rev. X **11**, 021048 (2021).

[140] F. Schlawin, D. M. Kennes and M. A. Sentef, “Cavity quantum materials”, Appl. Phys. Rev. **9**, 011312 (2022).

[141] M. O. Scully and M. S. Zubairy, *Quantum Optics* (Cambridge University Press, 1997).

[142] I. I. Rabi, “Space Quantization in a Gyrating Magnetic Field”, Phys. Rev. **51**, 652–654 (1937).

[143] A. F. Kockum, A. Miranowicz, S. De Liberato, S. Savasta and F. Nori, “Ultrastrong coupling between light and matter”, Nat. Rev. Phys. **1**, 19–40 (2019).

[144] C. Cohen-Tannoudji, J. Dupont-Roc and G. Grynberg, *Atom-Photon Interactions* (John Wiley & Sons, 1998).

[145] C. Gerry and P. Knight, *Introductory Quantum Optics* (Cambridge University Press, 2004).

[146] E. T. Jaynes and F. W. Cummings, “Comparison of quantum and semiclassical radiation theories with application to the beam maser”, Proc. IEEE **51**, 89–109 (1963).

[147] B. W. Shore and P. L. Knight, “The Jaynes-Cummings Model”, J. Mod. Opt. **40**, 1195–1238 (1993).

[148] M. Tavis and F. W. Cummings, “Exact Solution for an N-Molecule—Radiation-Field Hamiltonian”, Phys. Rev. **170**, 379–384 (1968).

[149] R. Mottl, “Roton-type mode softening in a dissipative quantum many-body system with cavity-mediated long-range interactions”, PhD Thesis (ETH Zürich, 2014).

[150] H. J. Metcalf and P. van der Straten, *Laser Cooling and Trapping* (Springer, 2002).

[151] C. Maschler, I. B. Mekhov and H. Ritsch, “Ultracold atoms in optical lattices generated by quantized light fields”, Eur. Phys. J. D **46**, 545–560 (2008).

[152] E. S. Mananga and T. Charpentier, “Introduction of the Floquet-Magnus expansion in solid-state nuclear magnetic resonance spectroscopy”, J. Chem. Phys. **135**, 044109 (2011).

[153] N. Goldman and J. Dalibard, “Periodically Driven Quantum Systems: Effective Hamiltonians and Engineered Gauge Fields”, Phys. Rev. X **4**, 031027 (2014).

[154] J. M. Luttinger and W. Kohn, “Motion of Electrons and Holes in Perturbed Periodic Fields”, Phys. Rev. **97**, 869–883 (1955).

[155] J. R. Schrieffer and P. A. Wolff, “Relation between the Anderson and Kondo Hamiltonians”, Phys. Rev. **149**, 491–492 (1966).

[156] P. Strack and S. Sachdev, “Dicke Quantum Spin Glass of Atoms and Photons”, Phys. Rev. Lett. **107**, 277202 (2011).

[157] M. Buchhold, P. Strack, S. Sachdev and S. Diehl, “Dicke-model quantum spin and photon glass in optical cavities: Nonequilibrium theory and experimental signatures”, Phys. Rev. A **87**, 063622 (2013).

[158] A. Periwal, E. S. Cooper, P. Kunkel, J. F. Wienand, E. J. Davis and M. Schleier-Smith, “Programmable interactions and emergent geometry in an array of atom clouds”, Nature **600**, 630–635 (2021).

[159] M. Baghdad, P.-A. Bourdel, S. Schwartz, F. Ferri, J. Reichel and R. Long, “Spectral engineering of cavity-protected polaritons in an atomic ensemble”, Nat. Phys. (2023).

[160] M. Franz and M. Rozali, “Mimicking black hole event horizons in atomic and solid-state systems”, Nat. Rev. Mater. **3**, 491–501 (2018).

[161] S. Xu, L. Susskind, Y. Su and B. Swingle, “A Sparse Model of Quantum Holography”, arXiv:2008.02303 [cond-mat.str-el] (2020).

[162] J. W. Goodman, *Speckle Phenomena in Optics: Theory and Applications* (SPIE, 2006).

[163] F. Jendrzejewski, “Quantum transport of ultracold atoms in disordered potentials”, PhD Thesis (Université Paris Sud - Paris XI, 2012).

[164] B. M. Scott (https://math.stackexchange.com/users/12042/brian-m-scott), *Inverting the Cantor pairing function*, Mathematics Stack Exchange, URL:https://math.stackexchange.com/q/222835 (version: 2020-06-12).

[165] S. Giorgini, L. P. Pitaevskii and S. Stringari, “Theory of ultracold atomic Fermi gases”, Rev. Mod. Phys. **80**, 1215–1274 (2008).

[166] K. Roux, V. Helson, H. Konishi and J.-P. Brantut, “Cavity-assisted preparation and detection of a unitary Fermi gas”, New J. Phys. **23**, 043029 (2021).

[167] J. L. van Hemmen, “A Note on the Diagonalization of Quadratic Boson and Fermion Hamiltonians”, Z. Physik B - Condensed Matter **38**, 271–277 (1980).

[168] F. Monteiro, M. Tezuka, A. Altland, D. A. Huse and T. Micklitz, “Quantum Ergodicity in the Many-Body Localization Problem”, Phys. Rev. Lett. **127**, 030601 (2021).

[169] O. Roy and M. Vetterli, "The effective rank: A measure of effective dimensionality", in 2007 15th European Signal Processing Conference (2007), pp. 606–610.

[170] K. Swanepoel, *The rank lemma*, Geometry and Combinatorics, URL:https://konradswanepoel.wordpress.com/2014/03/04/the-rank-lemma/.

[171] G. K. Wertheim, M. A. Butler, K. W. West and D. N. E. Buchanan, "Determination of the Gaussian and Lorentzian content of experimental line shapes", Rev. Sci. Instrum. **45**, 1369–1371 (1974).

[172] T. Krajewski, M. Laudonio, R. Pascalie and A. Tanasa, "Non-Gaussian disorder average in the Sachdev-Ye-Kitaev model", Phys. Rev. D **99**, 126014 (2019).

[173] B. Kobrin, Z. Yang, G. D. Kahanamoku-Meyer, C. T. Olund, J. E. Moore, D. Stanford and N. Y. Yao, "Many-Body Chaos in the Sachdev-Ye-Kitaev Model", Phys. Rev. Lett. **126**, 030602 (2021).

[174] F. Serwane, G. Zürn, T. Lompe, T. B. Ottenstein, A. N. Wenz and S. Jochim, "Deterministic Preparation of a Tunable Few-Fermion System", Science **332**, 336–338 (2011).

[175] C. H. Nguyen, A. N. Utama, N. Lewty and C. Kurtsiefer, "Operating a near-concentric cavity at the last stable resonance", Phys. Rev. A **98**, 063833 (2018).

[176] C. H. Johansen, J. Lang, A. Morales, A. Baumgärtner, T. Donner and F. Piazza, "Multimode-polariton superradiance via Floquet engineering", SciPost Phys. **12**, 094 (2022).

[177] L. Sá, P. Ribeiro and T. Prosen, "Lindbladian dissipation of strongly-correlated quantum matter", Phys. Rev. Res. **4**, L022068 (2022).

[178] M. Fremling, M. Haque and L. Fritz, "Bipartite Sachdev-Ye-Kitaev model: Conformal limit and level statistics", Phys. Rev. D **105**, 066017 (2022).

[179] J. Dalibard, F. Gerbier, G. Juzeliūnas and P. Öhberg, "Colloquium: Artificial gauge potentials for neutral atoms", Rev. Mod. Phys. **83**, 1523–1543 (2011).

[180] J. A. Muniz, D. Barberena, R. J. Lewis-Swan, D. J. Young, J. R. K. Cline, A. M. Rey and J. K. Thompson, "Exploring Dynamical Phase Transitions with Cold Atoms in an Optical Cavity", Nature **580**, 602–607 (2020).

[181] C. Lippe, T. Klas, J. Bender, P. Mischke, T. Niederprüm and H. Ott, "Experimental realization of a 3D random hopping model", Nat. Commun. **12**, 6976 (2021).

[182] A. Signoles, T. Franz, R. Ferracini Alves, M. Gärttner, S. Whitlock, G. Zürn and M. Weidemüller, "Glassy Dynamics in a Disordered Heisenberg Quantum Spin System", Phys. Rev. X **11**, 011011 (2021).

[183] M. Marcuzzi, Minář, D. Barredo, S. de Léséleuc, H. Labuhn, T. Lahaye, A. Browaeys, E. Levi and I. Lesanovsky, "Facilitation Dynamics and Localization Phenomena in Rydberg Lattice Gases with Position Disorder", Phys. Rev. Lett. **118**, 063606 (2017).

[184] G. Roati, C. D'Errico, L. Fallani, M. Fattori, C. Fort, M. Zaccanti, G. Modugno, M. Modugno and M. Inguscio, "Anderson localization of a non-interacting Bose–Einstein condensate", Nature **453**, 895–898 (2008).

[185] J. Billy, V. Josse, Z. Zuo, A. Bernard, B. Hambrecht, P. Lugan, D. Clément, L. Sanchez-Palencia, P. Bouyer and A. Aspect, "Direct observation of Anderson localization of matter waves in a controlled disorder", Nature **453**, 891–894 (2008).

[186] F. Jendrzejewski, A. Bernard, K. Müller, P. Cheinet, V. Josse, M. Piraud, L. Pezzé, L. Sanchez-Palencia, A. Aspect and P. Bouyer, "Three-Dimensional Localization of Ultracold Atoms in an Optical Disordered Potential", Nat. Phys. **8**, 398–403 (2012).

[187] S. S. Kondov, W. R. McGehee, J. J. Zirbel and B. DeMarco, "Three-Dimensional Anderson Localization of Ultracold Matter", Science **334**, 66–68 (2011).

[188] C. Maier, T. Brydges, P. Jurcevic, N. Trautmann, C. Hempel, B. P. Lanyon, P. Hauke, R. Blatt and C. F. Roos, "Environment-Assisted Quantum Transport in a 10-qubit Network", Phys. Rev. Lett. **122**, 050501 (2019).

[189] J. Smith, A. Lee, P. Richerme, B. Neyenhuis, P. W. Hess, P. Hauke, M. Heyl, D. A. Huse and C. Monroe, "Many-Body Localization in a Quantum Simulator with Programmable Random Disorder", Nat. Phys. **12**, 907–911 (2016).

[190] M. A. Zeb, "Analytical solution of the disordered Tavis-Cummings model and its Fano resonances", Phys. Rev. A **106**, 063720 (2022).

[191] E. Orgiu, J. George, J. A. Hutchison, E. Devaux, J. F. Dayen, B. Doudin, F. Stellacci, C. Genet, J. Schachenmayer, C. Genes, G. Pupillo, P. Samorì and T. W. Ebbesen, "Conductivity in organic semiconductors hybridized with the vacuum field", Nat. Mater. **14**, 1123–1129 (2015).

[192] T. Botzung, D. Hagenmüller, S. Schütz, J. Dubail, G. Pupillo and J. Schachenmayer, "Dark State Semilocalization of Quantum Emitters in a Cavity", Phys. Rev. B **102**, 144202 (2020).

[193] G. D. Scholes, "Polaritons and excitons: Hamiltonian design for enhanced coherence", Proc. R. Soc. A **476**, 20200278 (2020).

[194] J. Dubail, T. Botzung, J. Schachenmayer, G. Pupillo and D. Hagenmüller, "Large Random Arrowhead Matrices: Multifractality, Semilocalization, and Protected Transport in Disordered Quantum Spins Coupled to a Cavity", Phys. Rev. A **105**, 023714 (2022).

[195] H. Tanji-Suzuki, I. D. Leroux, M. H. Schleier-Smith, M. Cetina, A. T. Grier, J. Simon and V. Vuletić, "Interaction between Atomic Ensembles and Optical Resonators", in *Advances in atomic, molecular, and optical physics* (Elsevier, 2011), pp. 201–237.

[196] J. Jensen and A. R. Mackintosch, *Rare Earth Magnetism: Structures and Excitations*, The International Series of Monographs on Physics (Clarendon Press Oxford, 1991).

[197] H. J. Lipkin, N. Meshkov and A. J. Glick, "Validity of Many-Body Approximation Methods for a Solvable Model: (I). Exact Solutions and Perturbation Theory", Nucl. Phys. **62**, 188–198 (1965).

[198] V. Makhalov, T. Satoor, A. Evrard, T. Chalopin, R. Lopes and S. Nascimbene, "Probing Quantum Criticality and Symmetry Breaking at the Microscopic Level", Phys. Rev. Lett. **123**, 120601 (2019).

[199] H. P. Breuer and F. Petruccione, *The Theory of Open Quantum Systems* (Oxford University Press, Great Clarendon Street, 2002).

[200] M. C. Cambiaggio, A. M. F. Rivas and M. Saraceno, "Integrability of the pairing hamiltonian", Nucl. Phys. A **624**, 157–167 (1997).

[201] P. Kulish, A. Stolin and L. H. Johannesson, "Deformed Richardson-Gaudin model", Journal of Physics: Conference Series **532**, 012012 (2014).

[202] J. Bardeen, L. N. Cooper and J. R. Schrieffer, "Theory of Superconductivity", Phys. Rev. **108**, 1175–1204 (1957).

[203] R. W. Richardson, “A restricted class of exact eigenstates of the pairing-force Hamiltonian”, Phys. Lett. **3**, 277–279 (1963).

[204] M. Gaudin, “Diagonalisation d’une classe d’hamiltoniens de spin”, Journal de Physique **37**, 1087–1098 (1976).

[205] J. Dukelsky, S. Pittel and G. Sierra, “Colloquium: Exactly solvable Richardson-Gaudin models for many-body quantum systems”, Rev. Mod. Phys. **76**, 643–662 (2004).

[206] N. Wiener, “Generalized harmonic analysis”, Acta Math. **55**, 117–258 (1930).

[207] A. Khintchine, “Korrelationstheorie der stationären stochastischen Prozesse”, Math. Ann. **109**, 604–615 (1934).

[208] C. Beck and F. Schögl, *Thermodynamics of Chaotic Systems: An Introduction*, Cambridge Nonlinear Science Series (Cambridge University Press, Cambridge, 1993).

[209] C. D. Meyer, *Matrix Analysis and Applied Linear Algebra* (Society for Industrial and Applied Mathematics, USA, 2000).

[210] F. Evers and A. D. Mirlin, “Anderson transitions”, Rev. Mod. Phys. **80**, 1355–1417 (2008).

[211] F. Buccheri, A. De Luca and A. Scardicchio, “Structure of typical states of a disordered richardson model and many-body localization”, Phys. Rev. B **84**, 094203 (2011).

[212] R. J. Lewis-Swan, D. Barberena, J. R. K. Cline, D. J. Young, J. K. Thompson and A. M. Rey, “Cavity-QED Quantum Simulator of Dynamical Phases of a Bardeen-Cooper-Schrieffer Superconductor”, Phys. Rev. Lett. **126**, 173601 (2021).

[213] S. P. Kelly, J. K. Thompson, A. M. Rey and J. Marino, “Resonant light enhances phase coherence in a cavity QED simulator of fermionic superfluidity”, Phys. Rev. Research **4**, L042032 (2022).

[214] S. Gopalakrishnan, B. L. Lev and P. M. Goldbart, “Frustration and Glassiness in Spin Models with Cavity-Mediated Interactions”, Phys. Rev. Lett. **107**, 277201 (2011).

[215] H. Nishimori and G. Ortiz, *Elements of Phase Transitions and Critical Phenomena* (Oxford University Press, 2010).

[216] M. Marcuzzi, E. Levi, S. Diehl, J. P. Garrahan and I. Lesanovsky, “Universal Nonequilibrium Properties of Dissipative Rydberg Gases”, Phys. Rev. Lett. **113**, 210401 (2014).

[217] M. Marcuzzi, E. Levi, W. Li, J. P. Garrahan, B. Olmos and I. Lesanovsky, "Non-equilibrium universality in the dynamics of dissipative cold atomic gases", New J. Phys. **17**, 072003 (2015).

[218] D. Trapin and M. Heyl, "Constructing effective free energies for dynamical quantum phase transitions in the transverse-field Ising chain", Phys. Rev. B **97**, 174303 (2018).

[219] M. Heyl, "Dynamical quantum phase transitions: a review", Rep. Prog. Phys. **81**, 054001 (2018).

[220] Erne, S. and Bücker, R. and Gasenzer, T. and Berges, J. and Schmiedmayer, J., "Universal dynamics in an isolated one-dimensional Bose gas far from equilibrium", Nature **563**, 225–229 (2018).

[221] J. Surace, L. Tagliacozzo and E. Tonni, "Operator content of entanglement spectra in the transverse field Ising chain after global quenches", Phys. Rev. B **101**, 241107 (2020).

[222] R. Prakash and A. Lakshminarayan, "Scrambling in strongly chaotic weakly coupled bipartite systems: Universality beyond the Ehrenfest timescale", Phys. Rev. B **101**, 121108 (2020).

[223] W. V. Berdanier, "Universality in Non-Equilibrium Quantum Systems", PhD thesis (University of California, Berkeley, UC Berkeley, 2020).

[224] T. W. B. Kibble, "Topology of cosmic domains and strings", J. Phys. A **9**, 1387–1398 (1976).

[225] W. H. Zurek, "Cosmological experiments in superfluid helium?", Nature **317**, 505–508 (1985).

[226] A. del Campo and W. H. Zurek, "Universality of phase transition dynamics: Topological defects from symmetry breaking", Int. J. Mod. Phys. A **29**, 1430018 (2014).

[227] J. Berges, A. Rothkopf and J. Schmidt, "Nonthermal Fixed Points: Effective Weak Coupling for Strongly Correlated Systems Far from Equilibrium", Phys. Rev. Lett. **101**, 041603 (2008).

[228] A. Piñeiro Orioli, K. Boguslavski and J. Berges, "Universal self-similar dynamics of relativistic and nonrelativistic field theories near nonthermal fixed points", Phys. Rev. D **92**, 025041 (2015).

[229] J. Berges, K. Boguslavski, S. Schlichting and R. Venugopalan, "Universality Far from Equilibrium: From Superfluid Bose Gases to Heavy-Ion Collisions", Phys. Rev. Lett. **114**, 061601 (2015).

[230] M. Karl and T. Gasenzer, “Strongly anomalous non-thermal fixed point in a quenched two-dimensional Bose gas”, New J. Phys. **19**, 093014 (2017).

[231] M. Prüfer, P. Kunkel, H. Strobel, S. Lannig, D. Linnemann, C.-M. Schmied, J. Berges, T. Gasenzer and M. K. Oberthaler, “Observation of universal dynamics in a spinor Bose gas far from equilibrium”, Nature **563**, 217–220 (2018).

[232] A. Chatrchyan, K. T. Geier, M. K. Oberthaler, J. Berges and P. Hauke, “Analog cosmological reheating in an ultracold Bose gas”, Phys. Rev. A **104**, 023302 (2021).

[233] L. Gresista, T. V. Zache and J. Berges, “Dimensional crossover for universal scaling far from equilibrium”, Phys. Rev. A **105**, 013320 (2022).

[234] J. Hubbard, “Electron correlations in narrow energy bands”, Proc. R. Soc. Lond. A **276**, 238–257 (1963).

[235] E. Fradkin, “The Hubbard model”, in *Field Theories of Condensed Matter Physics*, 2nd ed. (Cambridge University Press, 2013), pp. 8–26.

[236] L. Pezzè and A. Smerzi, “Quantum theory of phase estimation”, Proceedings of the International School of Physics “Enrico Fermi” **188**, 691–741 (2014).

[237] C. L. Degen, F. Reinhard and P. Cappellaro, “Quantum sensing”, Rev. Mod. Phys. **89**, 035002 (2017).

[238] L. Pezzé, A. Smerzi, M. K. Oberthaler, R. Schmied and P. Treutlein, “Quantum metrology with nonclassical states of atomic ensembles”, Rev. Mod. Phys. **90**, 035005 (2018).

[239] P. Hauke, M. Heyl, L. Tagliacozzo and P. Zoller, “Measuring multipartite entanglement through dynamic susceptibilities”, Nat. Phys. **12**, 778–782 (2016).

[240] M. Gabbrielli, A. Smerzi and L. Pezzè, “Multipartite Entanglement at Finite Temperature”, Sci. Rep. **8**, 15663 (2018).

[241] R. Costa de Almeida and P. Hauke, “From entanglement certification with quench dynamics to multipartite entanglement of interacting fermions”, Phys. Rev. Res. **3**, L032051 (2021).

[242] L. Foini and J. Kurchan, “Eigenstate thermalization hypothesis and out of time order correlators”, Phys. Rev. E **99**, 042139 (2019).

[243] A. Chan, A. De Luca and J. T. Chalker, "Eigenstate Correlations, Thermalization, and the Butterfly Effect", Phys. Rev. Lett. **122**, 220601 (2019).

[244] M. Brenes, S. Pappalardi, J. Goold and A. Silva, "Multipartite Entanglement Structure in the Eigenstate Thermalization Hypothesis", Phys. Rev. Lett. **124**, 040605 (2020).

[245] P. Reimann, "Typical fast thermalization processes in closed many-body systems", Nat. Commun. **7**, 10821 (2016).

[246] V. V. Flambaum and F. M. Izrailev, "Unconventional decay law for excited states in closed many-body systems", Phys. Rev. E **64**, 026124 (2001).

[247] F. Borgonovi, F. M. Izrailev, L. F. Santos and V. G. Zelevinsky, "Quantum chaos and thermalization in isolated systems of interacting particles", Phys. Rep. **626**, 1–58 (2016).

[248] M. Vyas, "Non-equilibrium many-body dynamics following a quantum quench", AIP Conf. Proc. **1912**, 020020 (2017).

[249] M. Távora, E. J. Torres-Herrera and L. F. Santos, "Inevitable power-law behavior of isolated many-body quantum systems and how it anticipates thermalization", Phys. Rev. A **94**, 041603 (2016).

[250] E. Andersson, J. D. Cresser and M. J. W. Hall, "Finding the Kraus decomposition from a master equation and vice versa", J. Mod. Opt. **54**, 1695–1716 (2007).

[251] M. J. W. Hall, J. D. Cresser, L. Li and E. Andersson, "Canonical form of master equations and characterization of non-Markovianity", Phys. Rev. A **89**, 042120 (2014).

[252] C. M. Kropf, C. Gneiting and A. Buchleitner, "Effective Dynamics of Disordered Quantum Systems", Phys. Rev. X **6**, 031023 (2016).

[253] R. d. J. León-Montiel, V. Méndez, M. A. Quiroz-Juárez, A. Ortega, L. Benet, A. Perez-Leija and K. Busch, "Two-particle quantum correlations in stochastically-coupled networks", New J. Phys. **21**, 053041 (2019).

[254] R. Román-Ancheyta, B. Çakmak, R. d. J. León-Montiel and A. Perez-Leija, "Quantum transport in non-Markovian dynamically disordered photonic lattices", Phys. Rev. A **103**, 033520 (2021).

[255] F. Benatti, R. Floreanini and S. Olivares, "Non-divisibility and non-Markovianity in a Gaussian dissipative dynamics", Phys. Lett. A **376**, 2951–2954 (2012).

[256] A. Chenu, M. Beau, J. Cao and A. del Campo, "Quantum Simulation of Generic Many-Body Open System Dynamics Using Classical Noise", Phys. Rev. Lett. **118**, 140403 (2017).

[257] A. A. Budini, "Non-Markovian Gaussian dissipative stochastic wave vector", Phys. Rev. A **63**, 012106 (2000).

[258] A. A. Budini, "Quantum systems subject to the action of classical stochastic fields", Phys. Rev. A **64**, 052110 (2001).

[259] J. Mildenberger, "Trapped-ion quantum simulations of spin systems at non-vanishing temperature", MA thesis (Kirchhoff-Institut für Physik, Universität Heidelberg, Heidelberg, Germany, 2019).

[260] E. A. Novikov, "Functionals and the random-force method in turbulence theory", Sov. Phys. - JETP **20**, 1290 (1965).

[261] K. Furutsu, "On the Statistical Theory of Electromagnetic Waves in a Fluctuating Medium (I)", J. Res. Natl. Bur. Stand. **D-67**, 303–323 (1963).

[262] K. Furutsu, "Statistical Theory of Wave Propagation in a Random Medium and the Irradiance Distribution Function", J. Opt. Soc. Am. **62**, 240–254 (1972).

[263] V. I. Klyatskin and V. I. Tatarskii, "Statistical averages in dynamical systems", Theor. Math. Phys. **17**, 1143–1149 (1973).

[264] C. Gardiner and P. Zoller, *The Quantum World of Ultra-Cold Atoms and Light I: Foundations of Quantum Optics* (Imperial College Press, 2014).

[265] N. G. van Kampen, *Stochastic Processes in Physics and Chemistry*, 1st ed. (Elsevier, 1992).

[266] R. C. Bourret, "Propagation of Randomly Perturbed Fields", Can. J. Phys. **40**, 782–790 (1962).

[267] A. Dubkov and O. Muzychuk, "Analysis of higher approximations of Dyson's equation for the mean value of the Green function", Radiophys. Quantum Electron. **20**, 623–627 (1977).

[268] N. G. van Kampen, "A cumulant expansion for stochastic linear differential equations. I and II", Physica **74**, 215–238 and 239–247 (1974).

[269] W. M. Visscher, "Transport processes in solids and linear-response theory", Phys. Rev. A **10**, 2461–2472 (1974).

[270] A. Schekochihin and R. Kulsrud, "Finite-correlation-time effects in the kinematic dynamo problem", Phys. Plasmas **8**, 4937 (2001).

[271] R. Kubo, "Statistical-Mechanical Theory of Irreversible Processes. I. General Theory and Simple Applications to Magnetic and Conduction Problems", J. Phys. Soc. Jpn. **12**, 570–586 (1957).

[272] J. F. C. van Velsen, "On linear response theory and area preserving mappings", Phys. Rep. **41**, 135–190 (1978).

[273] R. Kubo, M. Toda and N. Hashitsume, *Statistical Physics II, Nonequilibrium Statistical Mechanics*, 1st ed., Vol. 31, Springer Series in Solid-State Sciences (Springer-Verlag Berlin Heidelberg, 1985).

[274] C. M. van Vliet, "On van Kampen's objections against linear response theory", J. Stat. Phys. **53**, 49–60 (1988).

[275] D. Goderis, A. Verbeure and P. Vets, "About the Exactness of the Linear Response Theory", Commun. Math. Phys. **136**, 265–283 (1991).

[276] D. Manzano, "A short introduction to the Lindblad master equation", AIP Adv. **10**, 025106 (2020).

[277] D. A. Lidar, A. Shabani and R. Alicki, "Conditions for strictly purity-decreasing quantum Markovian dynamics", Chem. Phys. **322**, 82–86 (2020).

[278] B. Kraus, H. P. Büchler, S. Diehl, A. Kantian, A. Micheli and P. Zoller, "Preparation of entangled states by quantum Markov processes", Phys. Rev. A **78**, 042307 (2008).

[279] F. Minganti, A. Biella, N. Bartolo and C. Ciuti, "Spectral theory of Liouvillians for dissipative phase transitions", Phys. Rev. A **98**, 042118 (2018).

[280] J. Tindall, B. Buča, J. R. Coulthard and D. Jaksch, "Heating-Induced Long-Range η Pairing in the Hubbard Model", Phys. Rev. Lett. **123**, 030603 (2019).

[281] A. Ghoshal, S. Das, A. Sen(De) and U. Sen, "Population inversion and entanglement in single and double glassy Jaynes–Cummings models", Phys. Rev. A **101**, 053805 (2020).

[282] P. Hänggi, "Correlation functions and masterequations of generalized (non-Markovian) Langevin equations", Z. Physik B **31**, 407–416 (1978).

[283] D. A. Lidar, "Lecture notes on the theory of open quantum systems", arXiv:1902.00967 [quant-ph] (2020).

[284] Á. Rivas and S. F. Huelga, *Open Quantum Systems: An Introdution*, SpringerBriefs in Physics (Springer Berlin Heidelberg, 2012).

[285] D. Nigro, "On the uniqueness of the steady-state solution of the Lindblad–Gorini–Kossakowski–Sudarshan equation", J. Stat. Mech. **2019**, 043202 (2019).

[286] P. Sierant, D. Delande and J. Zakrzewski, "Many-body localization due to random interactions", Phys. Rev. A **95**, 021601 (2017).

[287] D. A. Abanin, E. Altman, I. Bloch and M. Serbyn, "Colloquium: Many-body localization, thermalization, and entanglement", Rev. Mod. Phys. **91**, 021001 (2019).

[288] P. Sierant and J. Zakrzewski, "Challenges to observation of many-body localization", Phys. Rev. B **105**, 224203 (2022).

[289] M. B. Plenio and S. F. Huelga, "Dephasing-assisted transport: quantum networks and biomolecules", New J. Phys. **10**, 113019 (2008).

[290] P. Rebentrost, M. Mohseni, I. Kassal, S. Lloyd and A. Aspuru-Guzik, "Environment-assisted quantum transport", New J. Phys. **11**, 033003 (2009).

[291] R. de J. León-Montiel, M. A. Quiroz-Juárez, R. Quintero-Torres, J. L. Domínguez-Juárez, H. M. Moya-Cessa, J. P. Torres and J. L. Aragón, "Noise-assisted energy transport in electrical oscillator networks with off-diagonal dynamical disorder", Sci. Rep. **5**, 17339 (2015).

[292] L. W. Clark, N. Schine, C. Baum, N. Jia and J. Simon, "Observation of Laughlin states made of light", Nature **582**, 41–45 (2020).

[293] E. J. Davis, G. Bentsen, L. Homeier, T. Li and M. H. Schleier-Smith, "Photon-Mediated Spin-Exchange Dynamics of Spin-1 Atoms", Phys. Rev. Lett. **122**, 010405 (2019).

[294] S. H. Autler and C. H. Townes, "Stark Effect in Rapidly Varying Fields", Phys. Rev. **100**, 703–722 (1955).

[295] D. D. Duncan and S. J. Kirkpatrick, "Algorithms for simulation of speckle (laser and otherwise)", in Complex dynamics and fluctuations in biomedical photonics v, Vol. 6855, edited by V. V. Tuchin and L. V. Wang (International Society for Optics and Photonics, 2008), p. 685505.

[296] C. Gardiner and P. Zoller, *The Quantum World of Ultra-Cold Atoms and Light Book II: The Physics of Quantum-Optical Devices* (Imperial College Press, 2014).

[297] P. Domokos, P. Horak and H. Ritsch, “Semiclassical theory of cavity-assisted atom cooling”, J. Phys. B: At. Mol. Opt. Phys. **34**, 187 (2001).

[298] H. J. Metcalf and P. van der Straten, *Laser Cooling and Trapping* (Springer, 2002).

[299] T. Giamarchi, A. Iucci and C. Berthod, *Introduction to Many Body physics*, lecture notes, 2008.

[300] G. L. Celardo, R. Kaiser and F. Borgonovi, “Shielding and localization in the presence of long-range hopping”, Phys. Rev. B **94**, 144206 (2016).

[301] R. Abou-Chacra, D. J. Thouless and P. W. Anderson, “A selfconsistent theory of localization”, J. Phys. C: Solid State Phys. **6**, 1734–1752 (1973).

[302] A. D. Mirlin and Y. V. Fyodorov, “Distribution of local densities of states, order parameter function, and critical behavior near the Anderson transition”, Phys. Rev. Lett. **72**, 526–529 (1994).

[303] E. Tarquini, G. Biroli and M. Tarzia, “Critical properties of the Anderson localization transition and the high-dimensional limit”, Phys. Rev. B **95**, 094204 (2017).

[304] S. Roy and D. E. Logan, “Localization on Certain Graphs with Strongly Correlated Disorder”, Phys. Rev. Lett. **125**, 250402 (2020).

[305] J. S. Liu, “Siegel’s formula via Stein’s identities”, Stat. Probabil. Lett. **21**, 247–251 (1994).

[306] E. Anderson, Z. Bai, C. Bischof, S. Blackford, J. Demmel, J. Dongarra, J. Du Croz, A. Greenbaum, S. Hammarling, A. McKenney, and D. Sorensen, *LAPACK Users’ Guide*, 3rd ed. (Society for Industrial and Applied Mathematics, 1999).

[307] Message Passing Interface Forum, *MPI: A Message-Passing Interface Standard Version 4.0* (2021).

[308] E. J. Torres-Herrera and L. F. Santos, “Signatures of chaos and thermalization in the dynamics of many-body quantum systems”, Eur. Phys. J. Spec. Top. **227**, 1897–1910 (2019).

[309] M. Schiulaz, E. J. Torres-Herrera, F. Pérez-Bernal and L. F. Santos, “Self-averaging in many-body quantum systems out of equilibrium: Chaotic systems”, Phys. Rev. B **101**, 174312 (2020).

[310] E. J. Torres-Herrera, I. Vallejo-Fabila, A. J. Martínez-Mendoza and L. F. Santos, "Self-averaging in many-body quantum systems out of equilibrium: Time dependence of distributions", Phys. Rev. E **102**, 062126 (2020).

[311] A. Chenu, J. Molina-Vilaplana and A. del Campo, "Work Statistics, Loschmidt Echo and Information Scrambling in Chaotic Quantum Systems", Quantum **3**, 127 (2019).

Appendix A

Additional details for Chapter 3

In this appendix, we provide supplementary derivations and discussions for our proposed cQED implementation of the SYK model of Chap. 3.

A.1 Disordered AC-Stark shift from microscopic Hamiltonian

Consider the scenario where, in addition to the drive beam addressing the ground-to-excited-state transition, a light-shifting beam of angular(Rabi) frequency $\omega_{\mathrm{b}}(\Omega_{\mathrm{b}}(\boldsymbol{r}))$ is detuned from the excited-to-auxiliary-state transition, as sketched in Fig. 3.1(c). This adds the following terms to $\hat{H}_{\mathrm{mb}}(t)$ in Eq. (3.6),

$$\int \mathrm{d}\boldsymbol{r}\omega_{\mathrm{aux}}\hat{\psi}^{\dagger}_{\mathrm{aux}}(\boldsymbol{r})\hat{\psi}_{\mathrm{aux}}(\boldsymbol{r}) + \int \mathrm{d}\boldsymbol{r}\left(\Omega_{\mathrm{b}}(\boldsymbol{r})\mathrm{e}^{-i\omega_{\mathrm{b}}t}\hat{\psi}^{\dagger}_{\mathrm{aux}}(\boldsymbol{r})\hat{\psi}_{\mathrm{e}}(\boldsymbol{r}) + \mathrm{H.c.}\right), \tag{A.1}$$

where $\hat{\psi}_{\mathrm{aux}}(\boldsymbol{r})$ are the field operators for the auxiliary electronic state $|a\rangle$. Here we have assumed that the light-shifting beam is far off-resonant from the ground-to-auxiliary transition, and that the cavity is far off-resonant with transitions to $|a\rangle$, such that the above terms are the relevant processes.

Eliminating the time-dependence by going into a rotating frame generated by

$$\hat{H}'_{\mathrm{RF}} = \omega_{\mathrm{d}}\left(\int \mathrm{d}\boldsymbol{r}\hat{\psi}^{\dagger}_{\mathrm{e}}(\boldsymbol{r})\hat{\psi}_{\mathrm{e}}(\boldsymbol{r}) + \sum_{m}\hat{a}^{\dagger}_{m}\hat{a}_{m}\right) + (\omega_{\mathrm{d}}+\omega_{\mathrm{b}})\int \mathrm{d}\boldsymbol{r}\hat{\psi}^{\dagger}_{\mathrm{aux}}(\boldsymbol{r})\hat{\psi}_{\mathrm{aux}}(\boldsymbol{r}), \tag{A.2}$$

we obtain

$$\begin{aligned}\hat{H}_{\mathrm{mb}} = &\sum_m \Delta_m \hat{a}_m^\dagger \hat{a}_m - \int \mathrm{d}\boldsymbol{r} \left(\Delta_{\mathrm{da}} \hat{\psi}_{\mathrm{e}}^\dagger(\boldsymbol{r}) \hat{\psi}_{\mathrm{e}}(\boldsymbol{r}) + \Delta_{\mathrm{baux}} \hat{\psi}_{\mathrm{aux}}^\dagger(\boldsymbol{r}) \hat{\psi}_{\mathrm{aux}}(\boldsymbol{r})\right) \\ &+ \frac{1}{2} \sum_m \int \mathrm{d}\boldsymbol{r} \left(\Omega_m g_m(\boldsymbol{r}) \hat{a}_m \hat{\psi}_{\mathrm{e}}^\dagger(\boldsymbol{r}) \hat{\psi}_{\mathrm{g}}(\boldsymbol{r}) + \mathrm{H.c.}\right) \\ &+ \int \mathrm{d}\boldsymbol{r} \left(\Omega_{\mathrm{d}} g_{\mathrm{d}}(\boldsymbol{r}) \hat{\psi}_{\mathrm{e}}^\dagger(\boldsymbol{r}) \hat{\psi}_{\mathrm{g}}(\boldsymbol{r}) + \Omega_{\mathrm{b}}(\boldsymbol{r}) \hat{\psi}_{\mathrm{aux}}^\dagger(\boldsymbol{r}) \hat{\psi}_{\mathrm{e}}(\boldsymbol{r}) + \mathrm{H.c.}\right),\end{aligned} \tag{A.3}$$

where $\Delta_{\mathrm{baux}} \equiv \omega_{\mathrm{d}} + \omega_{\mathrm{b}} - \omega_{\mathrm{aux}}$.

Similar to the procedure of Sec. 3.3.2, by assuming the detuning $|\Delta_{\mathrm{baux}}|$ to be sufficiently large, the auxiliary state field operators $\hat{\psi}_{\mathrm{aux}}(\boldsymbol{r})$ adiabatically follow those of the excited state,

$$\hat{\psi}_{\mathrm{aux}}(\boldsymbol{r}) = \frac{\Omega_{\mathrm{b}}(\boldsymbol{r})}{\Delta_{\mathrm{baux}}} \hat{\psi}_{\mathrm{e}}(\boldsymbol{r}). \tag{A.4}$$

Substituting this into the Heisenberg equations of motion for $\hat{\psi}_{\mathrm{e}}(\boldsymbol{r})$, we find

$$i\partial_t \hat{\psi}_{\mathrm{e}}(\boldsymbol{r}) = -\Delta_{\mathrm{da}}(\boldsymbol{r}) \hat{\psi}_{\mathrm{e}}(\boldsymbol{r}) + \hat{\Phi}(\boldsymbol{r}) \hat{\psi}_{\mathrm{g}}(\boldsymbol{r}) \tag{A.5}$$

where $\hat{\Phi}(\boldsymbol{r})$ is as in Eq. (3.13), and now $\tilde{\Delta}_{\mathrm{da}}(\boldsymbol{r})$ is given by

$$\Delta_{\mathrm{da}}(\boldsymbol{r}) = \Delta_{\mathrm{da}} - \frac{|\Omega_{\mathrm{b}}(\boldsymbol{r})|^2}{\Delta_{\mathrm{baux}}} = \omega_{\mathrm{d}} - \left(\omega_{\mathrm{a}} + \frac{|\Omega_{\mathrm{b}}(\boldsymbol{r})|^2}{\Delta_{\mathrm{baux}}}\right). \tag{A.6}$$

The term in parenthesis yields a spatially dependent atomic resonance $\omega_{\mathrm{a}}(\boldsymbol{r})$, similar to that introduced in Sec. 3.2.1.

A.2 Compensating the disordered dipole potential

We have seen in the derivation of $\hat{H}_{\mathrm{eff}}$ [Eq. (3.23)], that the one-body term [Eq. (3.22)] contains an effective disordered dipole potential

$$\int \mathrm{d}\boldsymbol{r} \frac{|\Omega_{\mathrm{d}} g_{\mathrm{d}}(\boldsymbol{r})|^2}{\Delta_{\mathrm{da}}(\boldsymbol{r})} \hat{\psi}^\dagger(\boldsymbol{r}) \hat{\psi}(\boldsymbol{r}), \tag{A.7}$$

which appears after adiabatic elimination of the excited state [see Eqs. (3.15)–(3.17)]. Here we briefly discuss how this term could be compensated by introducing an additional drive.

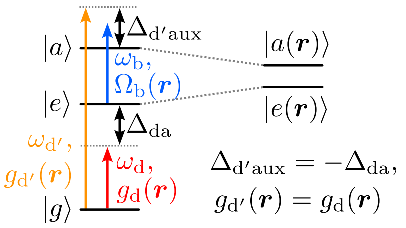

Figure A.1: Additional drive for compensation of dipole potential. Level scheme of Fig. 3.1(c), but with an an additional drive, tailored so as to compensate the disordered dipole potential of the original drive.

The light-shift technique described in Sec. 3.2.1 produces in the dressed-state picture two energetically shifted states (Autler–Townes doublet [294]). The energy shifts of these dressed states, relative to the bare states, are perfectly anti-correlated. In the microscopic Hamiltonian of Eq. (3.6), it is the energetically lower state of this doublet which is designated as the excited state, at frequency $\omega_{\mathrm{a}}(\boldsymbol{r})$, and thus yields the spatially-dependent detuning $\Delta_{\mathrm{da}}(\boldsymbol{r})$ [see also the level scheme of Fig. 3.1(c)]. Let the transition frequency from the ground state to the higher lying dressed state be $\omega_{\mathrm{aux}}(\boldsymbol{r})$, and consider an additional drive beam, at angular(Rabi) frequency $\omega_{\mathrm{d'}}(\Omega_{\mathrm{d'}})$, detuned by $\Delta_{\mathrm{d'aux}}$ from this transition, as sketched in Fig. A.1. The microscopic model of Eqs. (3.6)–(3.10) is then modified by the additional terms

$$\int \mathrm{d}\boldsymbol{r}\omega_{\mathrm{aux}}(\boldsymbol{r})\hat{\psi}^{\dagger}_{\mathrm{aux}}(\boldsymbol{r})\hat{\psi}_{\mathrm{aux}}(\boldsymbol{r}) + \Omega_{\mathrm{d'}}\int \mathrm{d}\boldsymbol{r}\left(g_{\mathrm{d'}}(\boldsymbol{r})\mathrm{e}^{-i\omega_{\mathrm{d'}}t}\hat{\psi}^{\dagger}_{\mathrm{aux}}(\boldsymbol{r})\hat{\psi}_{\mathrm{g}}(\boldsymbol{r}) + \mathrm{H.c.}\right). \tag{A.8}$$

Going into the rotating frame generated by $\hat{H}_{\mathrm{RF}} = \omega_{\mathrm{d}}\int \mathrm{d}\boldsymbol{r}\hat{\psi}^{\dagger}_{\mathrm{e}}(\boldsymbol{r})\hat{\psi}_{\mathrm{e}}(\boldsymbol{r}) + \omega_{\mathrm{d}}\sum_m \hat{a}^{\dagger}_m\hat{a}_m + \omega_{\mathrm{d'}}\int \mathrm{d}\boldsymbol{r}\hat{\psi}^{\dagger}_{\mathrm{aux}}(\boldsymbol{r})\hat{\psi}_{\mathrm{aux}}(\boldsymbol{r})$, and adiabatically eliminating $\hat{\psi}_{\mathrm{e}}(\boldsymbol{r})$ and $\hat{\psi}_{\mathrm{aux}}(\boldsymbol{r})$ (following the procedure outlined in Sec. 2.2.4), then yields the expression of Eq. (3.17), but with an additional term

$$\int \mathrm{d}\boldsymbol{r}\frac{|\Omega_{\mathrm{d'}}g_{\mathrm{d'}}(\boldsymbol{r})|^2}{\Delta_{\mathrm{d'aux}}(\boldsymbol{r})}\hat{\psi}^{\dagger}(\boldsymbol{r})\hat{\psi}(\boldsymbol{r}), \tag{A.9}$$

where we have let $\hat{\psi}_{\mathrm{g}}(\boldsymbol{r}) = \hat{\psi}(\boldsymbol{r})$, as in Eq. (3.17).

By tailoring the two drives such that they have matching intensity $\Omega_{\mathrm{d}} = \Omega_{\mathrm{d'}}$ and profiles $g_{\mathrm{d}}(\boldsymbol{r}) = g_{\mathrm{d'}}(\boldsymbol{r})$, the two dipole terms of Eqs. (A.7) and (A.9) can be made to cancel by choosing their angular frequencies such that $\Delta_{\mathrm{da}}(\boldsymbol{r}) = -\Delta_{\mathrm{d'aux}}(\boldsymbol{r})$. This can be achieved by choosing the detunings from the bare states to have equal magnitude, but opposite sign $\Delta_{\mathrm{da}} = -\Delta_{\mathrm{d'aux}}$, since at any given position $\boldsymbol{r}$ the dressed states' energy shifts are perfectly anti-correlated.

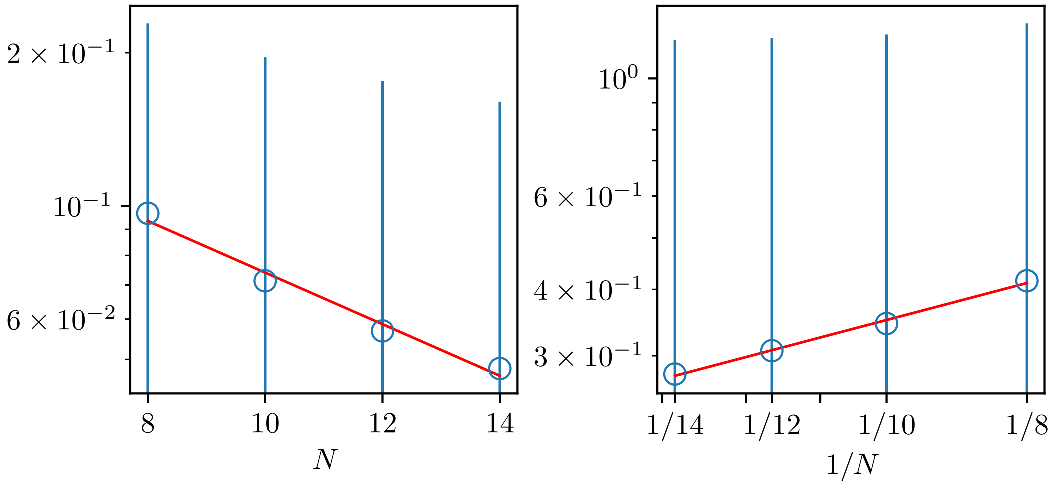

Figure A.2: Comparison of lowest energy gap of $\hat{H}_{\mathrm{SYK}}$ and $\hat{H}_{q=2}$. Scaling of mean lowest energy gap $\mathbb{E}\left[\epsilon_1-\epsilon_0\right]$ (circles) with system sizes $N=8,10,12,14$ (at half filling), for $\hat{H}_{\mathrm{SYK}}$ (left) and $\hat{H}_{q=2}$ (right). For $\hat{H}_{\mathrm{SYK}}$, the average is performed over $10^4, 5\times10^3, 10^3, 10^3$ disorder realisations, for the respective system sizes listed above. For $\hat{H}_{q=2}$, the average is performed over $10^4, 10^4, 10^4, 10^3$ disorder realisations, respectively. The exponential scaling e^{-aN} for $\hat{H}_{\mathrm{SYK}}$ is evident, in contrast to the N^{-p} scaling for $\hat{H}_{q=2}$. Red lines represent the best (least-squares) fit, from which we extract exponents $a=0.12\pm0.01$ and $p=0.72\pm0.03$. Deviations from the expected large-N scalings $p=1$ and $a\simeq0.232$ (for the Majorana variant of $\hat{H}_{\mathrm{SYK}}$), are likely due to numeric limitation to small system sizes, as well as finite sample sizes over which we average. Error bars indicate the standard deviation of the mean value obtained for the above sample sizes, and would be reduced further by increasing the number of disorder realisations over which one averages.

A.3 Numeric implementation

Here we provide details on the numeric simulation of $\hat{H}_{\mathrm{eff}}$, as implemented for the data presented in Secs. 3.4 and 3.5. In short, for a given realization of the speckle [see Fig. A.4], we solve for the eigenmodes $\phi_i(\boldsymbol{r})$ of $\hat{H}_0$, and use these to approximate the interaction integrals $I_{i_1 j_1,m}$ of Eq. (3.24) via Riemann sums. From these, we construct the antisymmetric interactions $\tilde{\mathcal{J}}_{i_1 i_2;j_1 j_2}=\mathcal{J}_{i_1 i_2;j_1 j_2}/\mathcal{E}$ as given by Eq. (3.32), and finally diagonalise the normal-ordered two body part of $\hat{H}_{\mathrm{eff}}$ in Eqs. (3.26)–(3.28), $\hat{H}_{\mathrm{eff}}^{(4)}/\mathcal{E}=\sum_{i_1,i_2,j_1,j_2}\tilde{\mathcal{J}}_{i_1 i_2;j_1 j_2}\hat{c}_{i_1}^{\dagger}\hat{c}_{i_2}^{\dagger}\hat{c}_{j_1}\hat{c}_{j_2}$. The thus obtained spectrum is then used to simulate the dynamics of $\hat{H}_{\mathrm{eff}}^{(4)}$ presented in Sec. 3.5.

As motivated in App. A.2, we drop the dipole term of $\hat{H}_0$ in Eq. (3.22), such that

$$\hat{H}_0 = \hat{H}_{\mathrm{kt}} = \int \mathrm{d}\boldsymbol{r} \hat{\psi}^\dagger(\boldsymbol{r}) \left(\frac{-\boldsymbol{\nabla}^2}{2m_{\mathrm{at}}} + V_{\mathrm{t}}(\boldsymbol{r}) \right) \hat{\psi}(\boldsymbol{r}), \tag{A.10}$$

which is simply a quantum harmonic oscillator (QHO) Hamiltonian for the harmonic trapping potential $V_{\mathrm{t}}(\boldsymbol{r}) = (m_{\mathrm{at}}\omega_{\mathrm{t}}^2/2)\boldsymbol{r}^2$ (we assume the trap to be isotropic in the plane transverse to the cavity axis). Introducing dimensionless coordinates $\boldsymbol{r}' \equiv \boldsymbol{r}/x_0$, where $x_0 = \sqrt{1/(m_{\mathrm{at}}\omega_{\mathrm{t}})}$ is the zero-point fluctuation of the ground state of $\hat{H}_{\mathrm{kt}}$, we obtain

$$\hat{H}_0 = \frac{\omega_{\mathrm{t}}}{2} \int \mathrm{d}\boldsymbol{r}' \hat{\psi}^\dagger(\boldsymbol{r}') \left(-\boldsymbol{\nabla}'^2 + \boldsymbol{r}'^2 \right) \hat{\psi}(\boldsymbol{r}'). \tag{A.11}$$

The eigenmodes $\phi_i(\boldsymbol{r}')$ of the above QHO Hamiltonian are products of Hermite–Gauss modes $\phi_i(\boldsymbol{r}') = \psi_{n_x^{(i)}}(x')\psi_{n_y^{(i)}}(y')$ [given by Eq. (A.13) with $w_0/\sqrt{2}$ replaced by x_0]. Nevertheless, we calculate the eigenmodes via exact diagonalisation, to maintain flexibility of our numeric calculations for possible future extensions.

We construct the matrix representation of the Hamiltonian of Eq. (A.11) in the position basis over a square grid of $N_x \times N_x$ coordinates $\boldsymbol{r}'$, centred at $\boldsymbol{r}' = (0,0)$, and set $\omega_{\mathrm{t}} = 1$. For the remainder of this section, we drop the prime notation, and all length scales are to be understood as expressed in units of x_0.

Using exact diagonalisation, we obtain the N energetically lowest eigenmodes $\{\phi_i(\boldsymbol{r})\}_{i=0}^{N-1}$, where N is the desired system size. To prevent distortions of the eigenmodes, the grid diameter L must be chosen sufficiently large: The spatial variance of a given mode $\phi_i(\boldsymbol{r}) = \psi_{n_x^{(i)}}(x)\psi_{n_y^{(i)}}(y)$ is (in units of x_0) given by $(n^{(i)}+1)$, where $n^{(i)} = \max(n_x^{(i)}, n_y^{(i)})$. In the main text, we consider systems of $N \leq 14$, for which the largest variance is $(4+1)$, and we thus set $L = 10 \approx 5 \times \sqrt{4+1}$. We set the number of grid-points as $N_x = 200$, for which the relative error in the energy of the highest utilised mode is less than 0.1%.

Next, we use the set $\{\phi_i(\boldsymbol{r})\}_{i=0}^{N-1}$ to calculate the $[N(N-1)/2]^2$ antisymmetrised, two-body interaction amplitudes $\mathcal{J}_{i_1 i_2; j_1 j_2}/\mathcal{E}$ as defined by Eq. (3.32), for a given input value of $\tilde{\delta\omega} = \delta\omega/\Delta_{\mathrm{cd}}$. The spatial integrals are approximated as Riemann sums over the above coordinate grid. As motivated in the main text, we work in a long-wavelength approximation such that $g_{\mathrm{d}}(\boldsymbol{r}) = 1$. Assuming the pancake to be placed at the centre of the cavity-axis ($z = 0$), the cavity modes $g_m(\boldsymbol{r})$ are Hermite–Gauss modes $g_m(\boldsymbol{r}) = \psi_{n_x}(x)\psi_{n_y}(y)$, where m is obtained from integers $n_x, n_y \geq 0$ via Cantor's pairing function

$$m = \mathrm{CP}(n_x, n_y) \equiv (n_x + n_y)(n_x + n_y + 1)/2 + n_y, \tag{A.12}$$

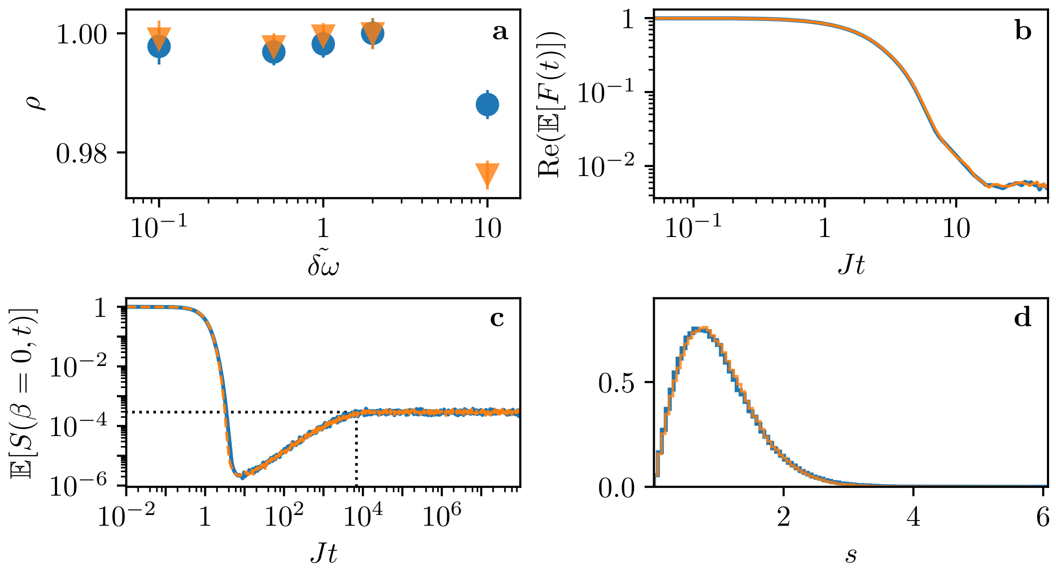

Figure A.3: Convergence with respect to mode-cut-off. Comparison of data for mode-cut-off $M = 240$ (blue) versus $M = 500$ (orange). (a) The interpolation parameter ρ [see Eq. (3.33)], quantifying the shape of the probability distribution of $\tilde{\mathcal{J}}_{i_1 i_2; j_1 j_2}$ for $\tilde{\delta\omega} = 1/10, 1/2, 1, 2, 10$. Each marker and its error-bars, respectively, represent the mean and standard deviation of ρ for an ensemble of 100 disorder realizations. (b OTOC (operator choice as in main text) and (c) SFF for $N = 10(N = 14)$ fermionic modes at half-filling, with $\zeta = 1$, and $\tilde{\delta\omega} = 1/10(\tilde{\delta\omega} = 1/1000)$, averaged over 250(100) disorder realizations. (d) Convergence of $p(s)$, with respect to mode-cut-off M, of $\hat{H}^{(4)}_{\text{eff}}$ for $N = 14$ fermionic modes at half-filling, $\zeta = 1$, and $\tilde{\delta\omega} = 1/1000$.

and

$$\psi_{n_x}(x) = \sqrt{\frac{\sqrt{2}/w_0}{\sqrt{\pi}2^{n_x}n_x!}} \exp\left(\frac{-x^2}{2(w_0/\sqrt{2})^2}\right) H_{n_x}\left(\frac{x}{w_0/\sqrt{2}}\right). \tag{A.13}$$

Note that since we consider a planar atomic cloud, here we have neglected the longitudinal profile of the cavity modes, the frequency of which is governed by the Guoy phase [22]. Depending on the type of cavity used, and the clouds position along the cavity axis, this will have to be included in future works. The parameter w_0 is the cavity waist at centre, and $\zeta = x_0/(w_0/\sqrt{2})$ (introduced in Sec. 3.2) quantifies the spatial extent of the fermionic modes $\phi_i(\boldsymbol{r})$ relative to this waist.

In Figs. 3.6–3.7, we present data for a range of sizes $\zeta \in [0.1, 1]$, which is implemented in our numerics by keeping $x_0 = 1$ fixed, and varying the cavity

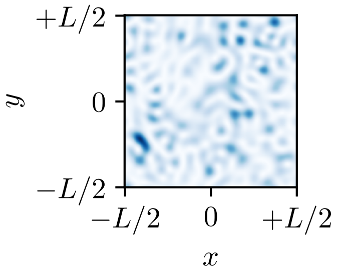

Figure A.4: Example of a speckle realisation. A realization of the speckled intensity distribution used to numerically define the disordered drive–atom detuning $\Delta_{\mathrm{da}}(\boldsymbol{r})$.

waist as $w_0 = \sqrt{2}\zeta$. We set a mode-cut-off $m = 0, 1, \ldots, M$ in Eq. (3.32) as $M = 240$, and ensure that N_x is large enough such that the spatial frequencies of all modes entering Eq. (3.32) are sampled above the Nyquist rate. For a test of convergence with respect to M, see Fig. A.3.

Finally, to produce the disordered detuning $\Delta_{\mathrm{da}}(\boldsymbol{r})$ of Eq. (3.2), we numerically generate speckle patterns according to the method of Ref. [295]. We assume the blue-detuned scenario $\Delta_{\mathrm{b}} > 0$ of Eq. (3.2), and set the spatial average of $\frac{|\Omega_{\mathrm{b}}(\boldsymbol{r})|^2/(4|\Delta_{\mathrm{b}}|)}{|\Delta_{\mathrm{da}}|}$ to unity. The mean number of speckle grains per linear dimension of the grid is a tunable parameter in the numerics. Physically, this number is determined by the speckle correlation length ξ. As an example, the light-shifting beam and numerical aperture of the setup of Chap. 4 (Ref. [77]) would yield $(w_0/\sqrt{2})/\xi \approx 17$. We thus set the average number of speckle grains per linear dimension of the pancake to 17. An example realisation is shown in Fig. A.4.

Having obtained the set of amplitudes $\mathcal{J}_{i_1 i_2; j_1 j_2}/\mathcal{E}$, we use them to construct the Fock-space representation of $\hat{H}^{(4)}_{\mathrm{eff}}/\mathcal{E} = \sum_{i_1, i_2, j_1, j_2} (\mathcal{J}_{i_1 i_2; j_1 j_2}/\mathcal{E}) \hat{c}^{\dagger}_{i_1} \hat{c}^{\dagger}_{i_2} \hat{c}_{j_1} \hat{c}_{j_2}$ within the half-filling sector $\langle \hat{Q} \rangle = 1/2$. The dynamics are then solved, using the exact diagonalisation code which was also utilised for the numerics of Chap. 5.

The above procedure is repeated multiple times, with independent speckle realizations, to obtain the ensemble-averaged data ($\mathbb{E}[\ldots]$) presented in Chap. 3. From this, we can also determine the covariance of a given amplitude $\mathcal{J}_{i_1 i_2; j_1 j_2}$ for a given choice of indices, with all of the $(N(N-1)/2)^2$ amplitudes in the set of antisymmetrised amplitudes $\{\mathcal{J}_{i_1 i_2; j_1 j_2}\}$. An example is show in Fig. A.5 for an ensemble of 100 disorder realisations, which signifies the presence of correlations within $\{\mathcal{J}_{i_1 i_2; j_1 j_2}\}$.

From our simulations of the spectral form factor (SFF), we extract the ramp, respectively, Heisenberg time via the procedure used in Ref. [115]. In short, we fit a linear function to the ramp, respectively, plateau of a given

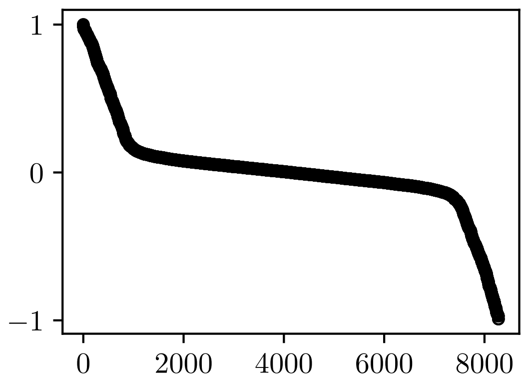

Figure A.5: Covariance of effective interaction amplitude. Example of covariances of an effective interaction amplitude $\mathcal{J}_{i_1 i_2; j_1 j_2}$, for an arbitrary choice of indices, with all other amplitudes. Data points represent mean values for 100 independent realisations of $\hat{H}^{(4)}_{\text{eff}}$ with $N = 14$, $\zeta = 1$ and $\tilde{\delta\omega} = 1/10$, and have been a arranged from largest to smallest value, for the $(N(N-1)/2)^2 = 8281$ amplitudes.

ensemble-averaged SFF, and then determine the earliest time at which the relative deviation of the SFF from this fit is below 1%. An example is shown in Fig. A.6.

All numerics presented in Secs. 3.4–3.5, are done under the long-wavelength approximation for the amplitude of the transverse drive beam $g_{\text{d}}(\boldsymbol{r}) = 1$ which is motivated by the assumption of being within the Lamb–Dicke regime $k_{\text{d}} x_0 \ll 1$, where $k_{\text{d}} = 2\pi/\lambda_{\text{d}}$, and λ_{d} is the wavelength of the transverse drive. The case of an *oscillating* drive amplitude $g_{\text{d}}(\boldsymbol{r}) = \exp(i k_{\text{d}} x)$, propagating along the (transverse) x direction, is shown in Fig. A.7, which shows realizations of out-of-time-order correlators (OTOCs) for the same operators considered in Sec. 3.5, and the SFF, for small ($\zeta = 0.1$) and large ($\zeta = 1.0$) transverse sizes of the atomic cloud and $\tilde{\delta\omega} = 1/1000, 100$, with the latter interpolating between many and few modes contributing to $\mathcal{J}_{i_1 i_2; j_1 j_2}/\mathcal{E}$. We observe drastic deviations from the desired SYK behaviour. The long-wavelength approximation is thus an important ingredient, fulfilled either by a drive impinging on the atomic cloud at an angle, or via an on-axis drive, as in Sec. 3.6.3.

For the rank data presented in Fig. 3.5, we use the interaction integrals $I_{i_1 j_1, m}$ to construct the matrix M as defined in Eq. (3.30), whose matrix elements are the unsymmetrised interaction amplitudes as given in the two body term of Eq. (3.23). The row indices are assigned as $i_1 j_1 \rightarrow N j_1 + i_1$, and similarly the column indices as $j_2 i_2 \rightarrow N i_2 + j_2$. Determining the matrix rank, defined as the number of non-zero eigenvalues, typically requires one to define a cut-off below which the numerically determined eigenvalues are treated as vanishing. To avoid this, we use the two alternative measures of the matrix rank defined in Eq. (3.31) of the main text.

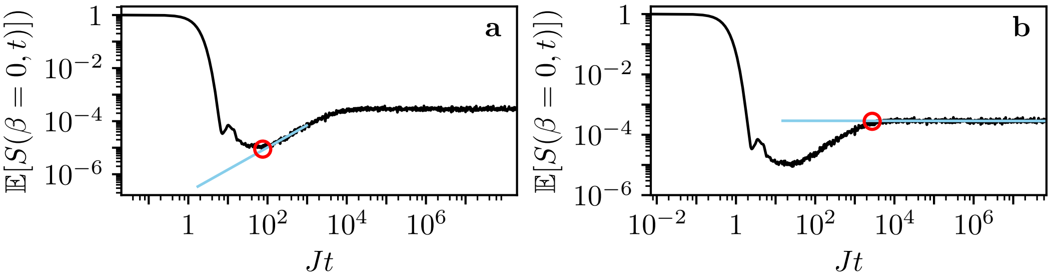

Figure A.6: Extraction of ramp and Heisenberg time. Examples of the relative error technique of Ref. [115], used here to extract (a) the ramp time t_r, and (b) the Heisenberg time t_H of the SFF (black curve) of Fig. 3.7(a,b) for $\widetilde{\delta\omega} = 1.0$. A linear fit (sky-blue line) to the ramp, respectively plateau, is used to determine the earliest time at which the relative deviation $\varepsilon \equiv |S(t) - f(t)| \,/\, |f(t)|$ of the SFF $S(t)$ from the linear fit $f(t)$ falls below an error threshold. This time is designated as the ramp, respectively, Heisenberg time. Here, and for the data of the main text, we set the threshold to 0.01, and the red circle markers are centred on $S(t = t_\mathrm{r})$, respectively, $S(t = t_\mathrm{H})$. For illustrative purposes, the linear fits have been plotted beyond their domain of validity, which is chosen by inspection for each data set.

A.4 Role of $\hat{H}_\mathrm{kt}$ in the derivation of $\hat{H}_\mathrm{eff}$

Here, we consider explicitly the role of the atoms' motional (external) degrees of freedom in the derivation of $\hat{H}_\mathrm{eff}$ [Eqs. (3.11)–(3.23)], presented in Sec. 3.3.

Specifically, we will show that

$$\hat{H}_\mathrm{kt} = \sum_{\mathrm{s=e,g}} \int \mathrm{d}\boldsymbol{r} \hat{\psi}_\mathrm{s}^\dagger(\boldsymbol{r}) \left(\frac{-\boldsymbol{\nabla}^2}{2m_\mathrm{at}} + V_\mathrm{t}(\boldsymbol{r}) \right) \hat{\psi}_\mathrm{s}(\boldsymbol{r}) \tag{A.14}$$

passes through the various transformations of Sec. 3.3, starting with the many-body Hamiltonian of Eqs. (3.6)–(3.10), so that it simply modifies the one-body Hamiltonian of Eq. (3.22).

A.4.1 Rotating frame

$\hat{H}_\mathrm{kt}$ is unaltered by the rotating frame transformation generated by $\hat{H}_\mathrm{RF}$ defined in Eq. (3.11), since $[\hat{H}_\mathrm{kt}, \hat{H}_\mathrm{RF}] = 0$, as we now show. We decompose the field operators $\hat{\psi}_\mathrm{g}(\boldsymbol{r})$, $\hat{\psi}_\mathrm{e}(\boldsymbol{r})$, respectively, into an arbitrary basis of mode-functions

$$\hat{\psi}_\mathrm{s}(\boldsymbol{r}) = \sum_i \phi_{\mathrm{s}i}(\boldsymbol{r}) \hat{c}_{\mathrm{s}i}. \tag{A.15}$$

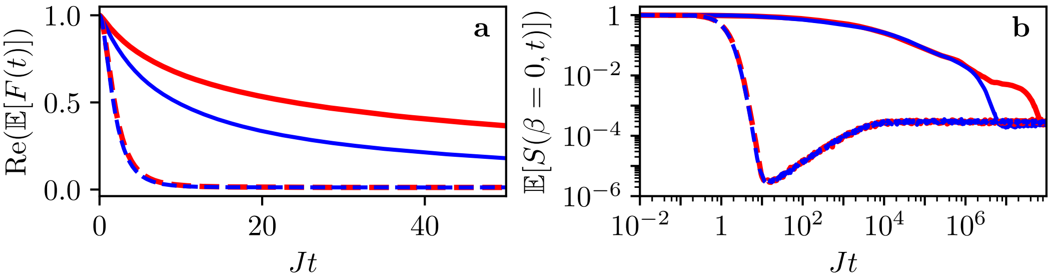

Figure A.7: OTOC and SFF for drive amplitudes with non-uniform phases. The OTOCs (a) and SFFs (b) are generated by $\hat{H}_{\mathrm{eff}}^{(4)}$ with interactions $\tilde{\mathcal{J}}_{i_1 i_2; j_1 j_2}$ in which the amplitude of the transverse drive has an oscillating phase $g_{\mathrm{d}}(\boldsymbol{r}) = \exp(ik_{\mathrm{d}}x)$. OTOC(SFF) data are for a system of $N = 10(N = 14)$ fermionic modes at half-filling, averaged over 500(200) disorder realizations. Both panels compare dynamics for different transverse atomic cloud sizes $\zeta = 1(\zeta = 0.1)$, indicated by solid(dashed) curves, and different $\tilde{\delta\omega} = 100(\tilde{\delta\omega} = 1/1000)$ shown in red(blue). Contrary to the case of homogeneous drive (main text), the dynamics in the smaller cloud ($\zeta = 0.1$) are faster than in the larger cloud ($\zeta = 1$). However, the data for different $\tilde{\delta\omega}$ collapse on top of one-another, so that no speed up is apparent as $\tilde{\delta\omega}$ is tuned. This indicates that the homogeneous drive utilised in the main text is an important ingredient for the proposal.

In terms of this decomposition, $\hat{H}_{\mathrm{kt}}$ is given by

$$\hat{H}_{\mathrm{kt}} = \sum_{\mathrm{s=e,g}} \sum_{i,j} \left(\int \mathrm{d}\boldsymbol{r} \phi_{\mathrm{s}i}^{*}(\boldsymbol{r}) \left(\frac{-\boldsymbol{\nabla}^2}{2m_{\mathrm{at}}} + V_{\mathrm{t}}(\boldsymbol{r}) \right) \phi_{\mathrm{s}j}(\boldsymbol{r}) \right) \hat{c}_{\mathrm{s}i}^{\dagger} \hat{c}_{\mathrm{s}j}. \tag{A.16}$$

This decomposition allows us to decouple the Laplacian $\boldsymbol{\nabla}^2$ from the field operators, which simplifies the calculation of commutators here and below. For the present case, we find

$$\left[\hat{H}_{\mathrm{kt}}, \hat{H}_{\mathrm{RF}}\right] \propto \left[\hat{c}_{\mathrm{s}i}^{\dagger} \hat{c}_{\mathrm{s}j}, \sum_{k} \hat{c}_{\mathrm{e}k}^{\dagger} \hat{c}_{\mathrm{e}k}\right], \tag{A.17}$$

where we have used that the fermionic part of $\hat{H}_{\mathrm{RF}}$ is proportional to $\sum_k \hat{c}_{\mathrm{e}k}^{\dagger} \hat{c}_{\mathrm{e}k}$. The commutator on the right-hand-side vanishes since the operator on its left conserves the total (excited-state) particle number symmetry encoded by the operator on its right. So we see that $\hat{H}_{\mathrm{kt}}$ propagates unaltered into the rotating-frame Hamiltonian given by Eq. (3.12), i.e., Eq. (3.12) changes to $\hat{H}_{\mathrm{mb}} + \hat{H}_{\mathrm{kt}}$.

A.4.2 Adiabatic elimination of $\hat{\psi}_{\mathrm{e}}(\boldsymbol{r})$

The inclusion of $\hat{H}_{\mathrm{kt}}$ in Eq. (3.12) modifies the Heisenberg equation of motion for $\hat{\psi}_{\mathrm{e}}(\boldsymbol{r})$ due to the additional commutator

$$\left[\hat{\psi}_{\mathrm{e}}(\boldsymbol{r}), \hat{H}_{\mathrm{kt}}\right] = \left(\frac{-\boldsymbol{\nabla}^2}{2m_{\mathrm{at}}} + V_{\mathrm{t}}(\boldsymbol{r})\right) \hat{\psi}_{\mathrm{e}}(\boldsymbol{r}), \tag{A.18}$$

which can be calculated using the decomposition of Eq. (A.16). The Heisenberg equation of motion for $\hat{\psi}_{\mathrm{e}}(\boldsymbol{r})$ is thus,

$$i\partial_t \hat{\psi}_{\mathrm{e}}(\boldsymbol{r}) = -\Delta_{\mathrm{da}}(\boldsymbol{r})\hat{\psi}_{\mathrm{e}}(\boldsymbol{r}) + \hat{\Phi}(\boldsymbol{r})\hat{\psi}_{\mathrm{g}}(\boldsymbol{r}) + \left(\frac{-\boldsymbol{\nabla}^2}{2m_{\mathrm{at}}} + V_{\mathrm{t}}(\boldsymbol{r})\right) \hat{\psi}_{\mathrm{e}}(\boldsymbol{r}). \tag{A.19}$$

We drop the term in parenthesis, which is motivated by a separation of energy scales [151] [see also the discussion following Eq. (2.28)]; Having already assumed $\Delta_{\mathrm{da}}(\boldsymbol{r})$ to be the dominant energy scale in the system at all $\boldsymbol{r}$, the comparatively slow dynamics of the atoms' external degrees of freedom (typically on the order of tens of kHz [166]) may be safely neglected. Formally setting the time-derivative to zero, then yields the expression for the field operator of Eq. (3.15).

Inserting this into the Heisenberg equations of motion for $\hat{\psi}_{\mathrm{g}}(\boldsymbol{r})$ and $\hat{a}_m$, and deducing the corresponding effective Hamiltonian, then yields the same Hamiltonian as Eq. (3.16), with the additional ground-state contribution of the kinetic energy.

So, taking $\hat{H}_{\mathrm{kt}}$ into account during the adiabatic elimination of $\hat{\psi}_{\mathrm{e}}(\boldsymbol{r})$, simply adds to Eq. (3.16) the dynamics of the external degrees of freedom of the ground state species $\hat{H}_{\mathrm{kt}} = \int \mathrm{d}\boldsymbol{r} \hat{\psi}^\dagger(\boldsymbol{r}) \left(-\boldsymbol{\nabla}^2/(2m_{\mathrm{at}}) + V_{\mathrm{t}}(\boldsymbol{r})\right) \hat{\psi}(\boldsymbol{r})$, where we have denoted $\hat{\psi}_{\mathrm{g}}(\boldsymbol{r})$ as $\hat{\psi}(\boldsymbol{r}) = \sum_i \phi_i(\boldsymbol{r})\hat{c}_i$ and redefined $\hat{H}_{\mathrm{kt}}$ accordingly as

$$\hat{H}_{\mathrm{kt}} = \sum_{i,j} \left(\int \mathrm{d}\boldsymbol{r} \phi_i^*(\boldsymbol{r}) \left(\frac{-\boldsymbol{\nabla}^2}{2m_{\mathrm{at}}} + V_{\mathrm{t}}(\boldsymbol{r})\right) \phi_j(\boldsymbol{r})\right) \hat{c}_i^\dagger \hat{c}_j. \tag{A.20}$$

A.4.3 Schrieffer–Wolff transformation

The presence of $\hat{H}_{\mathrm{kt}}$, as given by Eq. (A.20) above, in the Hamiltonian obtained after adiabatic elimination merely modifies $\hat{H}_0$ of Eq. (3.17) to $\hat{H}_0 + \hat{H}_{\mathrm{kt}}$, i.e., it does not couple photonic and atomic degrees of freedom. We may therefore continue to use the generator $\hat{S}$ of Eq. (3.20) to eliminate the coupling term $\hat{V}$ given by Eq. (3.18). All that remains to do, is to take into account the additional contributions to the commutator $[\hat{S}, \hat{H}_0]$, which is modified to $[\hat{S}, \hat{H}_0] + [\hat{S}, \hat{H}_{\mathrm{kt}}]$.

We now show that this additional term vanishes, thereby proving that the effective Hamiltonian of Eq. (3.21) only changes from $\hat{H}_{\text{eff}}$ to $\hat{H}_{\text{eff}} + \hat{H}_{\text{kt}}$.

To simplify the notation, we start by summarising the term in parenthesis of Eq. (A.20) as $K(i,j)$, i.e., $\hat{H}_{\text{kt}} = \sum_{i,j} K(i,j)\hat{c}_i^\dagger \hat{c}_j$. Similarly, we group all scalar terms in Eq. (3.20) such that $\hat{S} = \sum_m \sum_{k,l} s(m,k,l)\hat{a}_m \hat{c}_k^\dagger \hat{c}_l - \text{H.c.}$. With this in hand, we have

$$[\hat{S}, \hat{H}_{\text{kt}}] = \sum_m \hat{a}_m \sum_{j,k} \left[\sum_i \left(K(i,j)s(m,k,i) - K(i,k)^* s(m,i,j) \right) \right] \hat{c}_k^\dagger \hat{c}_j + \text{H.c.}\,. \tag{A.21}$$

Now, since the various $\phi_i(\boldsymbol{r})$ form a basis [see Eq. (A.15)], the sum over i is $\sum_i \phi_i(\boldsymbol{r})^* \phi_i(\boldsymbol{r}') = \delta(\boldsymbol{r} - \boldsymbol{r}')$ Thus, the term in square-brackets above is proportional to (expanding $K(i,j)$ and $s(m,k,i)$ back into their microscopic expressions),

$$\begin{aligned} &\int \mathrm{d}\boldsymbol{r} \frac{g_{\mathrm{d}}^*(\boldsymbol{r}) g_m(\boldsymbol{r})}{\Delta_{\mathrm{da}}(\boldsymbol{r})} \left\{ \phi_k^*(\boldsymbol{r}) \left(\frac{-\boldsymbol{\nabla}^2}{2m_{\text{at}}} + V_{\mathrm{t}}(\boldsymbol{r}) \right) \phi_j(\boldsymbol{r}) \right. \\ &\left. - \left[\left(\frac{-\boldsymbol{\nabla}^2}{2m_{\text{at}}} + V_{\mathrm{t}}(\boldsymbol{r}) \right) \phi_k(\boldsymbol{r}) \right]^* \phi_j(\boldsymbol{r}) \right\}. \end{aligned} \tag{A.22}$$

Multiplying this by $\hat{c}_k^\dagger \hat{c}_j$ and summing over k, j reduces the term in curly braces above to

$$\hat{\psi}^\dagger(\boldsymbol{r}) \left(\frac{-\boldsymbol{\nabla}^2}{2m_{\text{at}}} + V_{\mathrm{t}}(\boldsymbol{r}) \right) \hat{\psi}(\boldsymbol{r}) - \text{H.c.}\,. \tag{A.23}$$

This is zero, by hermiticity of $\hat{H}_{\text{kt}}$, and so $[\hat{S}, \hat{H}_{\text{kt}}] = 0$. Therefore, the effective Hamiltonian of Eq. (3.21) is simply modified to $\hat{H}_{\text{eff}} = \hat{H}_0 + \hat{H}_{\text{kt}} - \sum_m \frac{\hat{\Theta}_m^\dagger \hat{\Theta}_m}{\Delta_m}$.

In summary, we have shown that in the derivation of the effective model given by Eq. (3.21), one may disregard $\hat{H}_{\text{kt}}$ when performing all necessary transformations, and simply add it back into the final one-body contribution in Eq. (3.22).

A.5 A note on dissipation

Here, we consider the role of losses in the effective model derived in Sec. 3.3. They arise due to spontaneous emission, at rate Γ, of the atomic excited state, and from out-coupling of the cavity modes, at rates κ_m. For this open quantum system, we model the equation of motion of a given Heisenberg operator $\hat{O}(t)$ via the adjoint master equation, which (for time-independent Lindblad generators) is [199],

$$\begin{aligned}\partial_t \hat{O}(t) =& i\left[\hat{H}_{\mathrm{mb}}, \hat{O}(t)\right] + \int \mathrm{d}\boldsymbol{r} \left(\hat{L}^\dagger(\boldsymbol{r})\hat{O}(t)\hat{L}(\boldsymbol{r}) - \frac{1}{2}\left\{\hat{L}^\dagger(\boldsymbol{r})\hat{L}(\boldsymbol{r}), \hat{O}(t)\right\}\right) \\ &+ \sum_m \left(\hat{L}_m^\dagger \hat{O}(t)\hat{L}_m - \frac{1}{2}\left\{\hat{L}_m^\dagger \hat{L}_m, \hat{O}(t)\right\}\right),\end{aligned} \tag{A.24}$$

where spontaneous emission of the atoms, and photon loss are, respectively, described by the jump operators $\hat{L}(\boldsymbol{r}) = \sqrt{\Gamma}\hat{\psi}_{\mathrm{g}}^\dagger(\boldsymbol{r})\hat{\psi}_{\mathrm{e}}(\boldsymbol{r})$ and $\hat{L}_m = \sqrt{\kappa_m}\hat{a}_m$. Here we have neglected the effect of atomic recoil due to spontaneous emission, which is equivalent to working at zeroth order in the Lamb–Dicke parameter η [296]. The first correction is of order η^2, and describes diffusion of the atoms due to spontaneous emission. Here, we focus on the dynamics of the atoms' internal degrees-of-freedom.

The equation of motion for $\hat{\psi}_{\mathrm{g}}^\dagger(\boldsymbol{r})\hat{\psi}_{\mathrm{e}}(\boldsymbol{r})$ under the dynamics described by Eq. (A.24), with $\hat{H}_{\mathrm{mb}}$ and $\hat{\Phi}(\boldsymbol{r})$ given by Eqs. (3.12), (3.13), is

$$\begin{aligned}\partial_t \left(\hat{\psi}_{\mathrm{g}}^\dagger(\boldsymbol{r})\hat{\psi}_{\mathrm{e}}(\boldsymbol{r})\right) =& i\left(\Delta_{\mathrm{da}}(\boldsymbol{r}) + i\Gamma/2\right)\hat{\psi}_{\mathrm{g}}^\dagger(\boldsymbol{r})\hat{\psi}_{\mathrm{e}}(\boldsymbol{r}) \\ &- i\hat{\Phi}(\boldsymbol{r})\hat{\psi}_{\mathrm{g}}^\dagger(\boldsymbol{r})\hat{\psi}_{\mathrm{g}}(\boldsymbol{r}) - i\hat{\Phi}(\boldsymbol{r})\hat{\psi}_{\mathrm{e}}^\dagger(\boldsymbol{r})\hat{\psi}_{\mathrm{e}}(\boldsymbol{r}).\end{aligned} \tag{A.25}$$

Adiabatically eliminating $\hat{\psi}_{\mathrm{g}}^\dagger(\boldsymbol{r})\hat{\psi}_{\mathrm{e}}(\boldsymbol{r})$, we obtain, similar to Ref. [297],

$$\hat{\psi}_{\mathrm{g}}^\dagger(\boldsymbol{r})\hat{\psi}_{\mathrm{e}}(\boldsymbol{r}) = \frac{\hat{\Phi}(\boldsymbol{r})\hat{\psi}_{\mathrm{g}}^\dagger(\boldsymbol{r})\hat{\psi}_{\mathrm{g}}(\boldsymbol{r})}{\Delta_{\mathrm{da}}(\boldsymbol{r}) + i\Gamma/2}, \tag{A.26}$$

where we have assumed the contribution from the $\hat{\psi}_{\mathrm{e}}^\dagger(\boldsymbol{r})\hat{\psi}_{\mathrm{e}}(\boldsymbol{r})$ term to be subleading, since in the dispersive regime $|\Omega_{\mathrm{d}}/\Delta_{\mathrm{da}}| \ll 1$, the low-saturation limit is satisfied [298].

Similarly, adiabatic elimination of the photonic operator $\hat{a}_m$ yields

$$\hat{a}_m \approx \frac{-\Omega_{\mathrm{d}}\Omega_m^*}{2(\Delta_m - i\kappa_m/2)} \int \mathrm{d}\boldsymbol{r} \frac{g_{\mathrm{d}}(\boldsymbol{r})g_m^*(\boldsymbol{r})}{\Delta_{\mathrm{da}}(\boldsymbol{r}) + i\Gamma/2}\hat{\psi}_{\mathrm{g}}^\dagger(\boldsymbol{r})\hat{\psi}_{\mathrm{g}}(\boldsymbol{r}), \tag{A.27}$$

where we dropped terms of order $\Omega_m/\Omega_{\mathrm{d}}$, motivated by the discussion of Sec. 3.3.1.

Inserting the operators of Eq. (A.26) and (A.27) into Eq. (A.24) then yields an effective dissipator superoperator

$$\begin{aligned}\mathcal{D}_{\text{eff}}\bullet = &\int \mathrm{d}\boldsymbol{r} \left(\hat{L}_{\text{eff}}(\boldsymbol{r}) \bullet \hat{L}^{\dagger}_{\text{eff}}(\boldsymbol{r}) - \frac{1}{2}\left\{ \hat{L}^{\dagger}_{\text{eff}}(\boldsymbol{r}) \hat{L}_{\text{eff}}(\boldsymbol{r}), \bullet \right\} \right) \\ &+ \sum_{m} \left(\hat{L}_{m,\text{eff}} \bullet \hat{L}^{\dagger}_{m,\text{eff}} - \frac{1}{2}\left\{ \hat{L}^{\dagger}_{m,\text{eff}} \hat{L}_{m,\text{eff}}, \bullet \right\} \right),\end{aligned} \tag{A.28}$$

describing dephasing of the remaining internal atomic degree-of-freedom (up to order $1/\Delta^2_{\text{da}}$ included), via the effective jump operators

$$\hat{L}_{\text{eff}}(\boldsymbol{r}) = \frac{\sqrt{\Gamma}}{\Delta_{\text{da}}(\boldsymbol{r}) + i\Gamma/2} \Omega_{\text{d}} g_{\text{d}}(\boldsymbol{r}) \hat{\psi}^{\dagger}_{\text{g}}(\boldsymbol{r}) \hat{\psi}_{\text{g}}(\boldsymbol{r}), \tag{A.29}$$

and

$$\hat{L}_{m,\text{eff}} = \sqrt{\kappa_m} \frac{\Omega_{\text{d}} \Omega^{*}_{m}}{2(\Delta_m - i\kappa_m/2)} \int \mathrm{d}\boldsymbol{r} \frac{g_{\text{d}}(\boldsymbol{r}) g^{*}_{m}(\boldsymbol{r})}{\Delta_{\text{da}}(\boldsymbol{r}) + i\Gamma/2} \hat{\psi}^{\dagger}_{\text{g}}(\boldsymbol{r}) \hat{\psi}_{\text{g}}(\boldsymbol{r}). \tag{A.30}$$

The integral over the atomic cloud's volume in $\hat{L}^{(\text{eff})}_{m}$ reflects a "global dephasing" arising from the fact that a photon emitted via the cavity mirrors leaves the observer ignorant as to the position $\boldsymbol{r}$ at which the photon was scattered by an atom.

The effective jump operators are randomised via the disordered detuning $\Delta_{\text{da}}(\boldsymbol{r})$, thus yielding random, quadratic jump operators. This is similar to the dissipative SYK model studied in Ref. [177].

A.6 SYK model with Cauchy distribution

Here, we numerically compare the spectral properties of a variation of the SYK Hamiltonian, with the interaction amplitudes drawn from the Cauchy distribution, and compare them to that of the target model $\hat{H}_{\text{SYK}}$ in Eq. (3.1).

The normalised Cauchy distribution $P(x)$, defined over the domain $x \in (-\infty, \infty)$, and centred at $x = 0$ is given by

$$P(x) = \frac{1}{\pi} \frac{\gamma}{\gamma^2 + x^2}, \tag{A.31}$$

where γ is the half-width at half-maximum of the distribution. Since the moments of this distribution are not defined, in our numerics we truncate the domain to $x \in [-a, a]$, for some real number $a \geq 0$, which in turn results in a

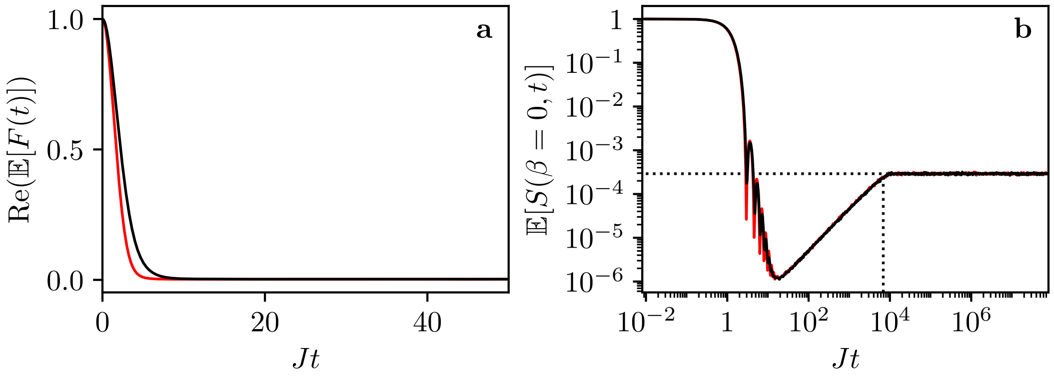

Figure A.8: SYK model with Cauchy-distributed interactions. Comparison of OTOC (a) and SFF (b) dynamics, generated by the target Hamiltonian $\hat{H}_{\mathrm{SYK}}$ with complex Gaussian(truncated Cauchy) distributed $J_{i_1i_2;j_1j_2}$, as indicated by the red-solid(black-dashed) curves. The OTOC(SFF) data are for a system of $N = 10(N = 14)$ fermionic modes at half-filling, and averaged over 1000 realizations. For the OTOCs, the choice of operators is the same as for the OTOCs shown in Fig. 3.7(a) of Chap. 3. The time axes of the SFF curves were rescaled so as to match their respective Heisenberg times. Dotted black curves are as in Fig. 3.7(a).

domain-dependent variance of the distribution $P_a(x)$. We choose the value of a such that we cover a desired fraction $f \equiv \int_{-a}^{a} \mathrm{d}x P(x) = 0.975$ of the probability mass of Eq. (A.31). With this rationale, one has the relation $a = \gamma \tan(f\pi/2)$, and the normalised truncated Cauchy distribution function is then given by

$$P_a(x) = \frac{1}{2\arctan(a/\gamma)} \frac{\gamma}{\gamma^2 + x^2}, \tag{A.32}$$

which can be tuned by changing the width γ for a fixed f.

We draw interaction amplitudes $J_{i_1i_2;j_1j_2}$ from the distribution $P_a(x)$, and construct the matrix representation of the SYK model in the same way as for the usual Gaussian definition in Eq. (3.1). In Fig. A.8 we compare the OTOCs and the SFF generated by the target SYK model of Eq. (3.1), with complex Gaussian-distributed interactions (red curves), to the variation of the model with Cauchy-distributed interactions drawn from $P_a(x)$ for $\gamma = 0.2$ (black curves), averaged over 1000 disorder realizations. The OTOCs of the variant with Cauchy-distributed interactions decay slower than those of the model with Gaussian-distributed interactions. For the SFF, the qualitative features (early-time power-law decaying oscillations, followed by a linear-in-t ramp, and a plateau) agree well. We note that in plotting the SFF, a slight difference in the Heisenberg times has been corrected for by rescaling the time axes. Since the Heisenberg time is set by the mean level-spacing, this amounts to having done a spectral unfolding—which normalises the mean level-spacing—for the ensembles of either model.

Appendix B

Additional details for Chapter 4

B.1 Distribution of energy shifts

The pseudo-random energy shifts described in Sec. 4.1.2 are implemented via a light-shifting lattice, whose wavelength is incommensurate with that of the atomic lattice. Let the intensity profile of the light-shifting lattice (with some wave-number k) be

$$I(x) = \frac{W}{2}(1 + \sin(kx)), \tag{B.1}$$

such that for a given position x, we have the energy shift $\epsilon = I(x) \in (0, W)$.

Unique values of ϵ are then obtained over an interval $x \in [x_0, x_0 + \pi/k]$ for an arbitrary $x_0 \in \mathbb{R}$. Let us assume that the position x is sampled uniformly within this interval, such that the probability to sample $I(x)$ at a given location $x \in [x_0, x_0 + \pi/k]$ is $p(x) = k/\pi$.

We now wish to determine the resultant distribution of energy shifts $\rho_{\mathrm{a}}(\epsilon)$. To this end note that the cumulative distribution functions of ϵ and x are related as

$$\int_a^{\epsilon} \mathrm{d}\epsilon' \rho_{\mathrm{a}}(\epsilon') = \int_{I^{-1}(a)}^{I^{-1}(\epsilon)} \mathrm{d}x p(x), \tag{B.2}$$

where a is an arbitrary value in the range of $I(x)$, and $I^{-1}(x) = \arcsin(2\epsilon/W - 1)/k$ is the inverse of Eq. (B.1).

By differentiating the above equation with respect to ϵ, it then follows that

$$\rho_{\mathrm{a}}(\epsilon) = \frac{k}{\pi}\frac{\mathrm{d}I^{-1}(\epsilon)}{\mathrm{d}\epsilon} = \frac{1}{\pi\sqrt{\epsilon(W - \epsilon)}}, \tag{B.3}$$

which is the distribution of energy shifts reported in Eq. (4.2).

B.2 Modelling the measurement protocol through a Lindblad master equation

Here, we provide further details for the derivation sketched in Sec. 4.2.3.

As motivated in Chap. 4, we work in the single excitation regime, valid for a probe beam whose strength is weak compared to the decay rate of the atomic excited state $|e\rangle$, $|\Omega_\mathrm{p}| \ll \Gamma$. This excitation can exist either in the single-excitation manifold (SEM) $\{|m\rangle \equiv \sum_{i=1}^{N} c_{mi}\hat{\sigma}_i^{+}|G\rangle\}_{m=1}^{N}$ of $\hat{H}_\mathrm{LMG}$, after coherent excitation from the ground state $|G\rangle$ by the probe, or it can exist in the manifold formed by the auxiliary states $|a_i\rangle \equiv |a_i\rangle\langle G||G\rangle$, after an incoherent decay from the SEM. In analogy to the SEM, we denote a general basis for the auxiliary-single-excitation manifold (AEM) as $|\alpha\rangle \equiv \sum_{i=1}^{N} c_{\alpha i}|a_i\rangle$.

Including the energy $\hat{H}_A = \sum_{i=1}^{N} \epsilon_\mathrm{aux}|a_i\rangle\langle a_i|$ of the auxiliary states in the Hamiltonian $\hat{H}(t)$ of Eq. (4.6), and going into the rotating frame generated by $N\Delta_\mathrm{pa}\hat{S}^z$, the coherent evolution of our system is generated by

$$\hat{H} = \hat{H}_\mathrm{LMG} + \hat{H}_A - N\Delta_\mathrm{pa}\hat{S}^z + \hat{\mathcal{V}}, \tag{B.4}$$

where $\hat{\mathcal{V}} = \hat{\mathcal{V}}(t=0)$.

An atom in the excited state $|e\rangle$ can decay into the ground state $|g\rangle$ at a rate Γ_g, or into the auxiliary state $|a\rangle$ at a rate Γ_a. The total decay rate Γ of the excited state is thus $\Gamma = \Gamma_\mathrm{a} + \Gamma_\mathrm{g}$. For generality, we include also a decay channel from $|a\rangle$ to $|g\rangle$, at a rate Γ_ag (although for the experiment of Chap. 4 spontaneous emission from $|a\rangle$ to $|g\rangle$ is prohibited by selection rules). The jump operators for these three processes are, respectively, $\hat{\sigma}_i^- = |g\rangle\langle e|_i$, $|a\rangle\langle e|_i$, and $|g\rangle\langle a|_i$.

Our goal is to derive an equation for the total atomic population $P_\mathrm{A}(t) \equiv \sum_{i=1}^{N}\langle a_i|\hat{\rho}(t)|a_i\rangle$ in the auxiliary state at a time t. We do so by modelling the above scenario through a Lindblad master equation

$$\partial_t\hat{\rho}(t) = -i\left[\hat{H}, \hat{\rho}(t)\right] + \left(\mathcal{D}[\Gamma_\mathrm{g}; \{\hat{\sigma}_i^-\}] + \mathcal{D}[\Gamma_\mathrm{a}; \{|a\rangle\langle e|_i\}] + +\mathcal{D}[\Gamma_\mathrm{ag}; \{|g\rangle\langle a|_i\}]\right)\hat{\rho}(t), \tag{B.5}$$

where the superoperators $\mathcal{D}[\gamma'; \{\hat{L}_i\}]$ are defined in Eq. (4.16).

Projecting Eq. (B.5) onto the state space spanned by $\{|G\rangle, \{|m\rangle\}, \{|\alpha\rangle\}\}$ (i.e. the state space containing at most one excitation), we obtain the following evolution equations

$$\partial_t\rho_{mn}(t) = -\, i\big[(H_{mG}\rho_{Gn}(t) - \rho_{mG}(t)H_{Gn}) + E_{mn}\rho_{mn}(t)\big] - (\Gamma_{\rm g} + \Gamma_{\rm a})\rho_{mn}(t), \tag{B.6}$$

$$\partial_t\rho_{mG}(t) = -\, i\left[E'_{mG}\rho_{mG}(t) + H_{mG}p_G(t) - \sum_{n\in\rm SEM}\rho_{mn}(t)H_{nG}\right] - \frac{(\Gamma_{\rm g} + \Gamma_{\rm a})}{2}\rho_{mG}(t), \tag{B.7}$$

$$\partial_t p_G(t) = \sum_{m\in\rm SEM}\left[-i\left(H_{Gm}\rho_{mG}(t) - \text{c.c.}\right) + \Gamma_{\rm g}\rho_{mm}(t)\right] + \Gamma_{\rm ag}\sum_{\alpha\in\rm AEM}\rho_{\alpha\alpha}(t), \tag{B.8}$$

$$\partial_t\rho_{\alpha G}(t) = -\, i\left((H_{\alpha\alpha} - H_{GG})\rho_{\alpha G}(t) - \sum_{m\in\rm SEM}\rho_{\alpha m}(t)H_{mG}\right) - \frac{\Gamma_{\rm ag}}{2}\rho_{\alpha G}(t), \tag{B.9}$$

$$\begin{aligned}\partial_t\rho_{\alpha m}(t) = &-\, i\left(H_{\alpha\alpha}\rho_{\alpha m}(t) - \rho_{\alpha G}(t)H_{Gm} - \sum_{n\in\rm SEM}\rho_{\alpha n}(t)H_{nm}\right)\\ &- \frac{\Gamma_{\rm a} + \Gamma_{\rm g} + \Gamma_{\rm ag}}{2}\rho_{\alpha m}(t), \end{aligned}\tag{B.10}$$

$$\begin{aligned}\partial_t\rho_{\alpha\beta}(t) = &-\, i\left(H_{\alpha\alpha} - H_{\beta\beta}\right)\rho_{\alpha\beta}(t) - \Gamma_{\rm ag}\rho_{\alpha\beta}(t)\\ &+ \Gamma_{\rm a}\sum_{i=1}^{N} c^*_{\alpha i}c_{\beta i}\sum_{m,n\in\rm SEM} c^*_{mi}c_{ni}\rho_{mn}(t), \end{aligned}\tag{B.11}$$

where $E_{mn} \equiv \mathcal{E}_m - \mathcal{E}_n$, $E'_{mG} \equiv \mathcal{E}_m - \mathcal{E}_G - \Delta_{\rm pa} = -E'_{Gm}$, and $\rho_{mn}(t) = \langle m|\hat{\rho}(t)|n\rangle$ denote coherences within the SEM. Similarly, $\rho_{mG}(t) = \langle m|\hat{\rho}(t)|G\rangle$, $p_G(t) = \langle G|\hat{\rho}(t)|G\rangle$, $\rho_{\alpha G}(t) = \langle \alpha|\hat{\rho}(t)|G\rangle$, $\rho_{\alpha m}(t) = \langle \alpha|\hat{\rho}(t)|m\rangle$, and $\rho_{\alpha\beta}(t) = \langle \alpha|\hat{\rho}(t)|\beta\rangle$, where $|m\rangle, |n\rangle \in$ SEM and $|\alpha\rangle, |\beta\rangle \in$ AEM. The matrix elements of $\hat{H}$ [Eq. (B.4)] are defined similarly, e.g., $H_{mG} = \langle m|\hat{H}|G\rangle$.

The rate equation for our target population $P_A(t)$, can obtained from

Eq. (B.11) since

$$\begin{aligned}
P_A(t) &\equiv \sum_{i=1}^{N} \langle a_i|\hat{\rho}(t)|a_i\rangle \\
&= \sum_{i=1}^{N} \sum_{\alpha,\beta\in\text{AEM}} \langle a_i||\alpha\rangle\langle\alpha|\hat{\rho}(t)|\beta\rangle\langle\beta||a_i\rangle \\
&= \sum_{\alpha,\beta\in\text{AEM}} \rho_{\alpha\beta}(t) \underbrace{\sum_{i=1}^{N} c_{\alpha i} c^*_{\beta i}}_{\delta_{\alpha\beta}} .
\end{aligned} \tag{B.12}$$

We thus have

$$\partial_t P_A(t) = \sum_{\alpha\in\text{AEM}} \partial_t \rho_{\alpha\alpha}(t) = -\Gamma_{\text{ag}} P_A(t) + \Gamma_{\text{a}} \sum_{m\in\text{SEM}} p_m(t), \tag{B.13}$$

where $p_m(t) \equiv \rho_{mm}(t)$.

Solving Eq. (B.13) is synonymous with solving the complete set of coupled differential equations given by Eqs. (B.6)–(B.11). We will instead make use of a separation of time-scales to obtain a solution valid for times $t \gg (\Gamma/2)^{-1}$. To do so, we take the Laplace transform $\mathcal{L}$ of Eq. (B.13), defining functions in the conjugate space as $f(s) \equiv \mathcal{L}[f(t)] = \int_0^\infty \mathrm{d}t \exp(-st) f(t)$. Using that $\mathcal{L}[\partial_t f(t)] = sf(s) - f(t=0)$, this yields

$$P_A(s) = \frac{P_A(t=0) + \Gamma_{\text{a}} \sum_{m\in\text{SEM}} p_m(s)}{s + \Gamma_{\text{ag}}}. \tag{B.14}$$

Inspection of the dependencies in Eq. (B.6)–(B.11), (B.14), shows that to solve the above equation we need to substitute expressions for $p_m(s)$, $\rho_{Gm}(s)$, $\rho_{nm}(s)$, and $p_G(s)$. These are given by

$$p_m(s) = \frac{p_m(t=0) + 2\text{Im}\left[H_{mG}\rho_{Gm}(s)\right]}{s + \Gamma_{\text{a}} + \Gamma_{\text{g}}}, \tag{B.15}$$

$$\rho_{Gm}(s) = \frac{\rho_{Gm}(t=0) + i\left(H_{Gm} p_G(s) - \sum_{n\in\text{SEM}} \rho_{nm}(s) H_{Gn}\right)}{s + (\Gamma_{\text{a}} + \Gamma_{\text{g}})/2 - iE'_{mG}}, \tag{B.16}$$

$$\rho_{nm}(s) = \frac{\rho_{nm}(t=0) + i\left(H_{Gm}\rho_{nG}(s) - \rho_{Gm}(s) H_{nG}\right)}{s + \Gamma_{\text{a}} + \Gamma_{\text{g}} - iE_{mn}}, \tag{B.17}$$

$$p_G(s) = \frac{1}{s}\left(p_G(t=0) + \Gamma_{\text{ag}} P_A(s) + \Gamma_{\text{g}} \sum_{m\in\text{SEM}} p_m(s) + 2 \sum_{m\in\text{SEM}} \text{Im}\left[H_{Gm}\rho_{mG}(s)\right]\right). \tag{B.18}$$

For the initial conditions, we will impose

$$p_G(t=0)=1, \tag{B.19}$$

with all other initial populations and coherences vanishing. This is motivated from the experimental protocol of Sec. 4.1.3, in which the atoms are initialised in $|g\rangle$.

We now impose that $s \ll (\Gamma_{\mathrm{a}}+\Gamma_{\mathrm{g}})/2 = \Gamma/2$, which is motivated by the large spontaneous emission rate of ^{6}Li (see Table 4.1). We use this to expand Eqs. (B.15)–(B.17) to zeroth order in $s/(\Gamma_{\mathrm{a}}+\Gamma_{\mathrm{g}})$, so that, after taking the inverse Laplace transform, we obtain

$$\begin{aligned}
p_m(t) =& \frac{2\mathrm{Im}\left[H_{mG}\rho_{Gm}(t)\right]}{\Gamma_{\mathrm{a}}+\Gamma_{\mathrm{g}}}, && \text{(B.20)}\\
\rho_{Gm}(t) =& \frac{i\left(H_{Gm}p_G(t)-\sum_{n\in\mathrm{SEM}}\rho_{nm}(t)H_{Gn}\right)}{(\Gamma_{\mathrm{a}}+\Gamma_{\mathrm{g}})/2-iE'_{mG}}, && \text{(B.21)}\\
\rho_{nm}(t) =& \frac{i\left(H_{Gm}\rho_{nG}(t)-\rho_{Gm}(t)H_{nG}\right)}{\Gamma_{\mathrm{a}}+\Gamma_{\mathrm{g}}-iE_{mn}}. && \text{(B.22)}
\end{aligned}$$

These expressions are valid for times $t \gg (\Gamma/2)^{-1}$. Substituting Eqs. (B.20)–(B.22) into $\partial_t p_G(t)$ and $\partial_t P_A(t)$ [as given by Eqs. (B.8) and (B.13)], and keeping only terms up to linear order in Γ_{a}^{-1} and Γ_{g}^{-1}, then yields $\partial_t p_G(t) = -\partial_t P_A(t)$, with

$$\begin{aligned}
\partial_t p_G(t) =& \Gamma_{\mathrm{ag}}P_A(t) - \Gamma_{\mathrm{a}}\sum_{m\in\mathrm{SEM}}\frac{|\mathcal{V}_{mG}|^2}{(\Gamma/2)^2+(E_{mG}-\Delta_{\mathrm{pa}})^2}p_G(t)\\
=& \Gamma_{\mathrm{ag}}P_A(t) - \frac{\Gamma_{\mathrm{a}}}{(\Gamma/2)^2}\left|\frac{g\Omega_{\mathrm{p}}}{\Delta_{\mathrm{ca}}}\right|^2\chi_{\mathrm{a}}(\Delta_{\mathrm{pa}})p_G(t),
\end{aligned} \tag{B.23}$$

where in the first line we have used $E'_{mG} = E_{mG}-\Delta_{\mathrm{pa}}$ and $H_{mG} = \mathcal{V}_{mG}$ [see Eq. (B.4)].

These two coupled differential equations are solved by (using the initial conditions stated above, namely $p_G(t=0)=1$ and $P_A(t=0)=0$),

$$p_G(t) = \frac{\Gamma_{\mathrm{ag}} + \frac{\Gamma_{\mathrm{a}}}{(\Gamma/2)^2}\left|\frac{g\Omega_{\mathrm{p}}}{\Delta_{\mathrm{ca}}}\right|^2\chi_{\mathrm{a}}(\Delta_{\mathrm{pa}})\exp\!\left(-\Gamma_{\mathrm{ag}}t-\frac{\Gamma_{\mathrm{a}}}{(\Gamma/2)^2}\left|\frac{g\Omega_{\mathrm{p}}}{\Delta_{\mathrm{ca}}}\right|^2\chi_{\mathrm{a}}(\Delta_{\mathrm{pa}})t\right)}{\Gamma_{\mathrm{ag}}+\frac{\Gamma_{\mathrm{a}}}{(\Gamma/2)^2}\left|\frac{g\Omega_{\mathrm{p}}}{\Delta_{\mathrm{ca}}}\right|^2\chi_{\mathrm{a}}(\Delta_{\mathrm{pa}})}, \tag{B.24}$$

$$P_A(t) = 1 - p_G(t). \tag{B.25}$$

In the limit where the auxiliary state acts as a dark state, i.e., $\Gamma_{\mathrm{ag}} \to 0$, the above reduces to the expressions summarised in Eqs. (4.17)–(4.19) of the main text.

B.3 Linear response derivation of dynamic susceptibility

We are interested in the average amount of energy deposited by the probe beam into the system, over a duration of time T,

$$\bar{\mathcal{E}} \equiv \frac{1}{T}\int_0^T \mathrm{d}t \frac{\mathrm{d}\mathcal{E}(t)}{\mathrm{d}t}, \tag{B.26}$$

where $\mathcal{E}(t) \equiv \mathrm{tr}(\hat{\rho}(t)\hat{H}(t))$ denotes the energy expectation value of the system, in state $\hat{\rho}(t)$, at a given time $t \geq 0$. The Hamiltonian $\hat{H}(t)$ is given by Eq. (4.6), which consists of the time-independent term $\hat{H}_{\mathrm{LMG}}$, and the time-dependent perturbation $\hat{H}_{\mathrm{pert}} = -\mathcal{V}(t)$.

Using the definition of $\mathcal{E}(t)$, as well as the von Neumann equation, it follows that

$$\frac{\mathrm{d}\mathcal{E}(t)}{\mathrm{d}t} = \mathrm{tr}\left(\hat{\rho}(t)\frac{\mathrm{d}\hat{H}_{\mathrm{pert}}(t)}{\mathrm{d}t}\right). \tag{B.27}$$

From the definition of $\mathcal{V}(t)$ in Eq. (4.8), we have

$$\hat{H}_{\mathrm{pert}}(t) = h\mathrm{e}^{i\Delta_{\mathrm{pa}}t}\hat{O} + \mathrm{H.c.}, \tag{B.28}$$

where $h = -g\sqrt{N}\Omega_{\mathrm{p}}^*/\Delta_{\mathrm{ca}}$ and $\hat{O} = \hat{S}^-$. Then, we have that

$$\frac{\mathrm{d}\mathcal{E}(t)}{\mathrm{d}t} = ih\Delta_{\mathrm{pa}}\mathrm{e}^{i\Delta_{\mathrm{pa}}t}\langle\hat{O}\rangle_{\rho(t)} + \mathrm{c.c.}, \tag{B.29}$$

where $\langle\hat{O}\rangle_{\rho(t)} = \mathrm{tr}(\hat{\rho}(t)\hat{O})$.

Within linear-response [196, 299], this operator expectation value is given by

$$\langle\hat{O}\rangle_{\rho(t)} = \langle\hat{O}\rangle_0 - i\int_{-\infty}^t \mathrm{d}t' \left\langle\left[\hat{O}(t), \hat{H}_{\mathrm{pert}}(t')\right]\right\rangle_{\rho(0)}. \tag{B.30}$$

Inserting Eq. (B.28) into Eq. (B.30), we have

$$\langle\hat{O}\rangle_{\rho(t)} =\langle\hat{O}\rangle_0 + \int_{-\infty}^{\infty} \mathrm{d}t' \left(\chi_{\hat{O}\hat{O}}(t-t')h\mathrm{e}^{i\Delta_{\mathrm{pa}}t'} + \chi_{\hat{O}\hat{O}^\dagger}(t-t')h^*\mathrm{e}^{-i\Delta_{\mathrm{pa}}t'}\right), \tag{B.31}$$

where we have introduced $\chi_{\hat{A}\hat{B}}(t-t') \equiv -i\Theta(t-t')\left\langle\left[\hat{A}(t),\hat{B}(t')\right]\right\rangle_{\rho(0)}$, of which we have used the Heaviside function $\Theta(t-t')$ to extend the upper integration bound. Identifying the resultant integrals as Fourier transforms $\chi_{\hat{A}\hat{B}}(\omega) = \int_{-\infty}^{\infty} \mathrm{d}t \chi_{\hat{A}\hat{B}}(t)\mathrm{e}^{i\omega t}$, we obtain

$$\begin{aligned}\frac{\mathrm{d}\mathcal{E}(t)}{\mathrm{d}t} =& ih\Delta_{\mathrm{pa}}\mathrm{e}^{i\Delta_{\mathrm{pa}}t}\left(\langle\hat{O}\rangle_{\rho(0)} + h\chi_{\hat{O}\hat{O}}(-\Delta_{\mathrm{pa}})\mathrm{e}^{i\Delta_{\mathrm{pa}}t} + h^*\chi_{\hat{O}\hat{O}^\dagger}(\Delta_{\mathrm{pa}})\mathrm{e}^{-i\Delta_{\mathrm{pa}}t}\right)\\ &-ih^*\Delta_{\mathrm{pa}}\mathrm{e}^{-i\Delta_{\mathrm{pa}}t}\left(\langle\hat{O}^\dagger\rangle_{\rho(0)} + h\chi_{\hat{O}^\dagger\hat{O}}(-\Delta_{\mathrm{pa}})\mathrm{e}^{i\Delta_{\mathrm{pa}}t} + h^*\chi_{\hat{O}^\dagger\hat{O}^\dagger}(\Delta_{\mathrm{pa}})\mathrm{e}^{-i\Delta_{\mathrm{pa}}t}\right).\end{aligned} \tag{B.32}$$

Inserting this into Eq. (B.26), and using $\int_0^T \mathrm{d}t \exp(\pm i2\Delta_{\mathrm{pa}}t) = 0$ for $T = 2\pi/\Delta_{\mathrm{pa}}$ (alternatively, let $T \to \infty$), we obtain

$$\bar{\mathcal{E}} = i\Delta_{\mathrm{pa}}hh^*\left(\chi_{\hat{O}\hat{O}^\dagger}(\Delta_{\mathrm{pa}}) - \chi_{\hat{O}^\dagger\hat{O}}(-\Delta_{\mathrm{pa}})\right) = -2\Delta_{\mathrm{pa}}\left|h\right|^2\mathrm{Im}[\chi_{\hat{O}\hat{O}^\dagger}(\Delta_{\mathrm{pa}})], \tag{B.33}$$

in which the last equality follows from $\chi_{\hat{O}\hat{O}^\dagger}(\Delta_{\mathrm{pa}})^* = \chi_{\hat{O}^\dagger\hat{O}}(-\Delta_{\mathrm{pa}})$, which is easily verified from the definition. Equation (B.33) is a standard linear response result, namely that the time-averaged energy transferred by the probe to the systems is given by the imaginary part of the (frequency-space) dynamic susceptibility. For this reason, the latter is referred to as the *absorptive* part of the dynamic susceptibility, and typically denoted as $\chi''_{\hat{O}\hat{O}^\dagger}(\Delta_{\mathrm{pa}}) = \mathrm{Im}[\chi_{\hat{O}\hat{O}^\dagger}(\Delta_{\mathrm{pa}})]$ [196, 299].

For the present case, the derivation elucidates for which choice of operators one should evaluate χ'': Inserting the expressions for $h = -g\sqrt{N}\Omega_{\mathrm{p}}^*/\Delta_{\mathrm{ca}}$ and $\hat{O} = \hat{S}^-$, it remains to determine the spectral representation for

$$\mathrm{Im}[\chi_{\hat{S}^-\hat{S}^+}(\Delta_{\mathrm{pa}})] = \mathrm{Im}\left[\int_{-\infty}^{\infty}\mathrm{d}t(-i)\Theta(t)\left\langle\left[\hat{S}^-(t),\hat{S}^+(0)\right]\right\rangle\mathrm{e}^{i\Delta_{\mathrm{pa}}t}\right]. \tag{B.34}$$

To do so, we recall that the dynamics of $\hat{H}_{\mathrm{LMG}}$ can safely be assumed to be restricted to the set of states with at most one excitation $\mathcal{S} = \{|G\rangle, \{|m\rangle\}_{m=1}^N\}$, which is physically motivated by the fact that the system is initialised in the zero-excitation (global ground) state $|G\rangle$ and that the atomic dissipation rate is dominant over the probe strength $\Gamma \gg |\Omega_{\mathrm{p}}|$ such that excitations rapidly decay. We write the corresponding initial state as $\hat{\rho}(0) = \sum_{\mu\in\mathcal{S}} p_\mu|\mu\rangle\langle\mu|$ with $p_\mu = \delta_{\mu G}$, in order to facilitate our calculation of the spectral representation of $\chi''(\Delta_{\mathrm{pa}})$. Inserting this, and the identity $\mathbb{1} = \sum_{\nu\in\mathcal{S}}|\nu\rangle\langle\nu|$ between the operator products in Eq. (B.34), we find

$$\begin{aligned}\mathrm{Im}[\chi_{\hat{S}^-\hat{S}^+}(\Delta_{\mathrm{pa}})] =&\mathrm{Im}\left[\int_0^\infty \mathrm{d}t(-i)\sum_{\mu,\nu\in\mathcal{S}}(p_\mu-p_\nu)\mathrm{e}^{i(\mathcal{E}_\mu-\mathcal{E}_\nu)t}\langle\mu|\hat{S}^-|\nu\rangle\langle\nu|\hat{S}^+|\mu\rangle\mathrm{e}^{i\Delta_{\mathrm{pa}}t}\right]\\ =&\mathrm{Im}\left[\lim_{\delta\to0^+}\int_0^\infty \mathrm{d}t(-i)\sum_{\mu,\nu\in\mathcal{S}}(p_\mu-p_\nu)\mathrm{e}^{i(\mathcal{E}_\mu-\mathcal{E}_\nu)t}\left|\langle\nu|\hat{S}^+|\mu\rangle\right|^2\mathrm{e}^{i(\Delta_{\mathrm{pa}}+i\delta)t}\right]\\ =&\mathrm{Im}\left[\lim_{\delta\to0^+}\sum_{\mu,\nu\in\mathcal{S}}\left|\langle\nu|\hat{S}^+|\mu\rangle\right|^2\frac{(p_\mu-p_\nu)}{\Delta_{\mathrm{pa}}+E_{\mu\nu}+i\delta}\right], \qquad \text{(B.35)}\end{aligned}$$

where $E_{\mu\nu}=\mathcal{E}_\mu-\mathcal{E}_\nu$. Using that $\lim_{\delta\to0^+}\frac{1}{x+i\delta}=\mathcal{P}\frac{1}{x}-i\pi\delta(x)$, where $\mathcal{P}$ denotes the principle part and $\delta(x)$ is the Dirac delta function, we find

$$\mathrm{Im}[\chi_{\hat{S}^-\hat{S}^+}(\Delta_{\mathrm{pa}})]=-\pi\sum_{\mu,\nu\in\mathcal{S}}\left|\langle\nu|\hat{S}^+|\mu\rangle\right|^2(p_\mu-p_\nu)\delta(\Delta_{\mathrm{pa}}-E_{\nu\mu}). \qquad \text{(B.36)}$$

Inserting the initial state distribution $p_\mu=\delta_{\mu G}$ then finally yields

$$\bar{\mathcal{E}}=2\pi\Delta_{\mathrm{pa}}\left|\frac{g\sqrt{N}\Omega_{\mathrm{p}}}{\Delta_{\mathrm{ca}}}\right|^2\sum_{m\in\mathrm{SEM}}\left|\langle m|\hat{S}^+|G\rangle\right|^2\delta(\Delta_{\mathrm{pa}}-E_{mG})=2\Delta_{\mathrm{pa}}\chi''(\Delta_{\mathrm{pa}}), \qquad \text{(B.37)}$$

with $\chi''(\Delta_{\mathrm{pa}})$ defined in Eq. (4.10).

B.4 Proof that the lowest SEM eigenstate is non-negative

Here we prove that, for any disorder strength $W\geq0$, the $|m=1\rangle=\sum_{i=1}^N c_{mi}\hat{\sigma}_i|G\rangle$ state of $\hat{H}_{\mathrm{LMG}}$, as defined in Eqs. (4.9) and (4.7), respectively, is real and non-negative, i.e., that $c_{mi}\geq0$ for all $i=1,\ldots,N$ and $m=1$. The $W=0$ case was already treated in Eq. (4.13), so here we focus on non-zero disorder $W>0$.

Our strategy is to relate the matrix representation of $\hat{H}_{\mathrm{LMG}}$ within the single-excitation manifold (SEM) to a real, non-negative, irreducible matrix M, to which we can apply the Perron–Frobenius theorem [209]. To this end, let us introduce the following notation: Let $\sigma(M)$ represent the set of unique eigenvalues λ of an arbitrary real matrix M, and let $\rho(M)=\max_{\lambda\in\sigma(M)}|\lambda|$ denote the spectral radius of M. The Perron–Frobenius theorem then states that if M is a non-negative, irreducible matrix, then:

(i) $r \equiv \rho(M) \in \sigma(M)$,

(ii) $r > 0$,

(iii) r is non-degenerate,

(iv) there exists a unique positive eigenvector $\boldsymbol{p}$ such that $M\boldsymbol{p} = r\boldsymbol{p}$ and $\sum_{i=1}^{N} p_i = 1$.

To start, recall that in $\hat{H}_{\mathrm{LMG}}$ the random energy shifts satisfy $\epsilon_i \in (0, W)$, and the spin-exchange interaction is given by $J = g^2/\Delta_{\mathrm{ca}}$. Further, recall that $J > 0$, since the cavity was blue detuned with respect to the clean atomic resonance. Now, let $\hat{M} \equiv -\hat{H}_{\mathrm{LMG}}$. Within the SEM, the matrix representation M of $\hat{M}$, when expressed with respect to the single-excitation basis $\{|i\rangle = \hat{\sigma}_i|G\rangle\}_{i=1}^{N}$, is given by

$$M_{ij} = \begin{cases} J - \epsilon_i/2, & i = j \\ J, & i \neq j \end{cases} . \tag{B.38}$$

It is clear that the minimum matrix element lies on the diagonal, and that this may even be negative when $W > J$. So M is not necessarily non-negative. To remedy this, let $\alpha \equiv \min_k M_{kk} = J - \max_k \epsilon_k/2$, where $k = 1, \ldots, N$. Then the matrix $M' \equiv M - \alpha\mathbb{1}$ (where $\mathbb{1}$ is the identity matrix) is non-negative. To see that M' is also irreducible, we consider its graph $\mathcal{G}(M)$, composed of vertices $\{v_i | i = 1, \ldots, N\}$ and directed edges $\{e_{ij} | M_{ij} \neq 0\}$ (i.e. vertices v_i and v_j are joined by a directed edge e_{ij} if and only if $M_{ij} \neq 0$). A directed graph $\mathcal{G}$ is said to be strongly connected if there is a directed path between any pair of vertices (v_i, v_j). It is known that M' is irreducible if and only if $\mathcal{G}(M)$ is strongly connected [209]. The latter property follows trivially in our case, since all off-diagonal entries $M'_{ij} = \max_k \epsilon_k/2$ are positive.

So, we can apply the Perron–Frobenius theorem to M', i.e., there exists a unique positive eigenvector $\boldsymbol{p}$ satisfying $M'\boldsymbol{p} = r'\boldsymbol{p}$, with $r' > 0$ non-degenerate and also the algebraically largest eigenvalue of M', since $r' = \rho(M')$. It then follows that $M\boldsymbol{p} = r\boldsymbol{p}$, with $r = r' + \alpha > 0$ being the algebraically largest eigenvalue of M, by definition of r'. Finally then, the algebraically *smallest* eigenvalue of $\hat{H}_{\mathrm{LMG}} = -\hat{M}$ within the SEM is $\mathcal{E}_{m=1} = -r$ and the corresponding eigenstate is $|m = 1\rangle = \sum_{i=1}^{N} \sqrt{p_i}|i\rangle$.

B.5 Numeric simulation of the large-detuning regime

We numerically compute χ_a and the participation ratios by diagonalising the random LMG Hamiltonian of Eq. (4.7) for system sizes $N = 303$ and 610. These system sizes correspond to the mean atom numbers realised in the experiment, which were determined from the dispersive shift $JN = g^2N/\Delta_\mathrm{ca}$ measured at zero disorder ($W = 0$), for each iteration of the measurement sequence. The effect of the atoms' thermal motion on the value of g, quoted as $\bar{g}$ in Table. 4.1, was taken into account for the conversion of the dispersive shifts into atom numbers, as well as for the matrix elements of the Hamiltonian. Taking the mean atom number across all experimental runs, yields the system sizes quoted above.

We choose the random energy shifts ϵ_i in two different ways: (i) By directly simulating the incommensurate light shift potential of Sec. 4.1.2 by sampling

$$\epsilon_i = \frac{W}{2}\cos(2\pi Q i) \tag{B.39}$$

in an incommensurate way by setting $Q = (\sqrt{5} - 1)/2$. This generates correlated quasi-random disorder. (ii) We sample ϵ_i independent and identically distributed (i.i.d.) according to $\rho_\mathrm{a}(\epsilon)$ of Eq. (4.2). For both cases, we find quantitative agreement of χ_a, and similarly of the partition ratio (PR), within numerical accuracy.

The Hamiltonian matrix is constructed with respect to the basis states $|i\rangle = \hat{\sigma}_i^+|G\rangle$ of the SEM, and diagonalised exactly. In the absence of disorder, i.e., $\epsilon_i = 0\,\forall i$, the diagonalisation is analytically tractable, and the eigenstates and eigenenergies are as given by Eqs. (4.13)–(4.14), from which follows the zero-disorder ferromagnetic gap $\Delta_\mathrm{FM} \equiv \mathcal{E}_{m>1} - \mathcal{E}_{m=1} = JN$, as mentioned in Sec. 4.2.4. However, the presence of disorder mixes the Hamiltonian's zero-disorder eigenstates, necessitating the analysis through numerical diagonalisation. Using the numerically determined eigenenergies and eigenstates, we compute the atomic susceptibility and PR from Eqs. (4.12) and (4.20), respectively. We average these quantities with respect to 2000 disorder realisations of the Hamiltonian, the results of which are illustrated in Figs. 4.6 and 4.7. The corresponding variances are strongly suppressed, falling within the linewidths of the simulated data.

B.6 Finite-size scaling of the minimal ferromagnetic gap in the large-detuning regime

Here, we analyse the finite-size scaling of the minimal ferromagnetic gap Δ_{FM} of the disordered LMG model. For this, we first Kac normalise the all-to-all spin-exchange interaction term in the Hamiltonian [Eq. (4.7)] by N^{-1}, which renders the model extensive. In contrast to the experimental scenario, Kac normalisation is necessary to theoretically analyse any critical behaviour stemming from the competition between different terms in the Hamiltonian. Under this rescaling, the zero-disorder gap is $\Delta_{\mathrm{FM}}/J = 1$, which decreases to a minimal value $\Delta^{\star}_{\mathrm{FM}}/J$ as the disorder strength W/J is increased. We denote the disorder strength at which this minimum is realised as $W^{\star}/J$. The minimal gap is indicative of significant changes in the ground-state properties in a finite-size system [26]. We perform a finite-size scaling of $\Delta^{\star}_{\mathrm{FM}}/J$ and $W^{\star}/J$ for the system with (i) quasi-random disorder sampled from the correlated energy potential of Eq. (B.39), and compare it with (ii) uncorrelated disorder with distribution $\rho_{\mathrm{a}}(\epsilon)$ of Eq. (4.2), and (iii) uniform distributions, see Fig. B.1(b–d).

The dependence of Δ_{FM}/J on W/J is shown in Fig. B.1(a) for the correlated disorder, which (adapting for different scalings, see below) is representative also of the two other studied cases. The minimal gap $\Delta^{\star}_{FM}/J$, and its location $W^{\star}/J$, are determined by fitting a parabola to the minimum of the curves. For all three disorder distributions, the gap $\Delta^{\star}_{\mathrm{FM}}/J$ decreases as $N^{-\beta}$ [see Fig. B.1(e)], indicating that the gap disappears in the thermodynamic limit. The gap location $W^{\star}/J$, however, scales linearly with system-size ($\propto N^{\alpha}$ with $\alpha \approx 1$) for the uncorrelated and correlated ρ_{a} [see Fig. B.1(f)]. In contrast, $W^{\star}/J \propto \log N$ for the uncorrelated uniform disorder [inset of Fig. B.1(f)], which is consistent with the vanishing Richardson's superconducting gap, which was estimated for uniform disorder from the mean level spacing [300]. These findings are in agreement with the generic behaviour of the critical disorder strength W_{c} for the Anderson localisation transition in models with a high connectivity, which increases with the number of connections [301–304]. For example, in a d-dimensional hypercube with coordination number $z \sim 2^{d}$, one finds $W_{c} \propto d \log d$ [303]. By visualising the all-to-all connectivity realised in the large-detuning regime as a hypercube with dimension $d \sim N$, we can expect $W_{\mathrm{c}} \propto \log N$ to leading order. This similarity indicates the significant change in localisation properties that a finite system experiences around $W^{\star}/J$, which is also supported by the decreasing trend in the PR (similar to Fig. 4.7). Correlations in the disorder tend to delocalise the system more, consistent

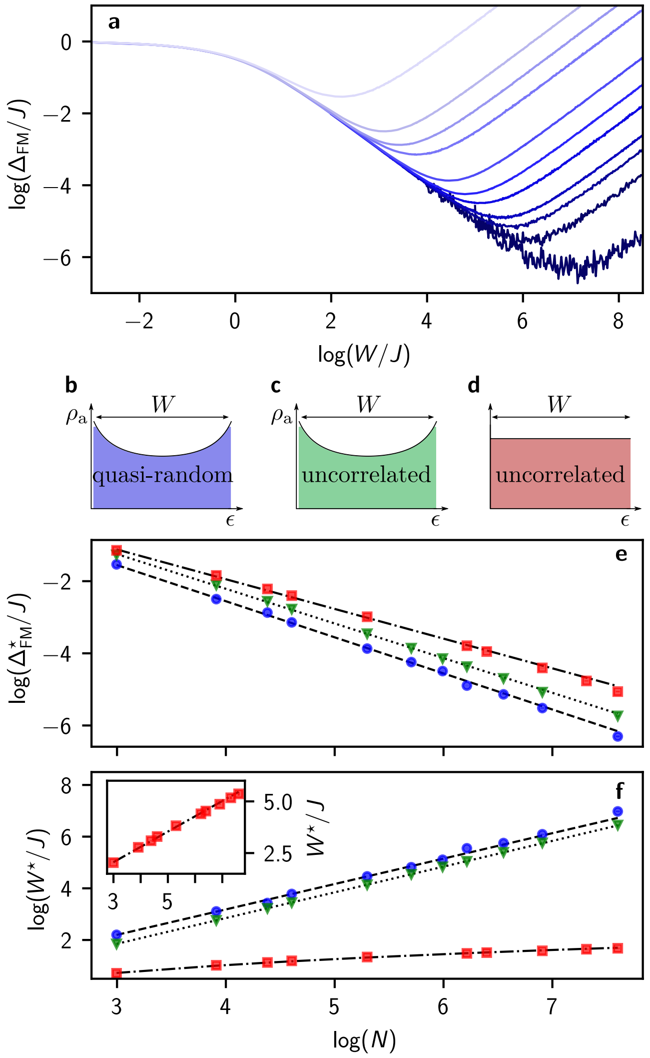

Figure B.1: Finite-size scaling of the minimal ferromagnetic gap of the random LMG model. (a) Disorder averaged ferromagnetic gap $\Delta_{\mathrm{F}M}/J$ of the Kac-normalised random LMG Hamiltonian, as a function of disorder strength W/J. Only data for the quasi-disordered case is shown as a representative. Lighter to darker shades of blue correspond to increasing N from 20 to 2000. For each N, the minimal gap $\Delta^{\star}_{\mathrm{F}M}/J$ and its location $W^{\star}/J$ are determined from a parabolic fit to the corresponding curve. (b–d) Sketches of the considered disorder distributions: quasi-random (b) and i.i.d. (c) ϵ_i from ρ_{a}, and i.i.d. ϵ_i from uniform distribution (d). (e,f) $\log(\Delta^{\star}_{\mathrm{F}M}/J)$ and $\log(W^{\star}/J)$ versus $\log(N)$, respectively, for the quasi-random ρ_{a} (blue circles), uncorrelated ρ_{a} (green triangles), and uniform (red squares) disorder distributions. The errors in the parabolic fits are smaller than the size of the markers. From linear fits to the data points for the quasi-random (dashed) and the uncorrelated (dotted) ρ_{a}, we find $W^{\star}/J \propto N^{\alpha}$ with $\alpha \approx 0.98$ and 0.99, respectively, indicating linear dependence. For the uniform disorder distribution, we fit a logarithmic curve (dot-dashed), which suggests that $W^{\star}/J \propto \log(N)$. This is verified by the linear fit (dot-dashed) in the inset of (e), where the y-axis depicts $W^{\star}/J$ instead of $\log(W^{\star}/J)$. In contrast, the minimal ferromagnetic gap $\Delta^{\star}_{\mathrm{F}M}/J$ scales as $N^{-\beta}$ with $\beta \approx 1.00$, 0.96, and 0.82 for the considered disorders, respectively.

with our finding in Fig. B.1(f). In the thermodynamic limit, however, the infinitely-connected system does not support a localisation transition.

Appendix C

Additional details for Chapter 5

C.1 Details of SYK-q model

Here, we present further details for the SYK-q Hamiltonian $\hat{H}_q$ of Eq. (2.5), of which Eq. (2.1) represents the $q = 4$ case.

The interaction amplitudes $J_{i_1 \ldots i_{q/2}; j_1 \ldots j_{q/2}}$ in Eq. (2.5) are complex Gaussian random variables, whose real and imaginary parts are independently distributed, with zero mean and variances parameterised by $J \in \mathbb{R}_{>0}$ as

$$\mathbb{E}\left[\left(\mathrm{Re}[J_{i_1 \ldots i_{q/2}; j_1 \ldots j_{q/2}}]\right)^2\right] = \begin{cases} J^2, & \text{if } i_l = j_l, \forall\, l = 1, \ldots, q/2 \\ J^2/2, & \text{otherwise,} \end{cases} \tag{C.1}$$

$$\mathbb{E}\left[\left(\mathrm{Im}[J_{i_1 \ldots i_{q/2}; j_1 \ldots j_{q/2}}]\right)^2\right] = \begin{cases} 0, & \text{if } i_l = j_l, \forall\, l = 1, \ldots, q/2 \\ J^2/2, & \text{otherwise.} \end{cases} \tag{C.2}$$

Furthermore, the amplitudes satisfy

$$\begin{aligned} J_{i_1 \ldots i_{q/2}; j_1 \ldots j_{q/2}} &= J^*_{j_1 \ldots j_{q/2}; i_1 \ldots i_{q/2}}, \\ J_{i_1 \ldots i_{q/2}; j_1 \ldots j_{q/2}} &= \mathrm{sgn}(\mathcal{P})\mathrm{sgn}(\mathcal{P}') J_{\mathcal{P}\{i_1 \ldots i_{q/2}\}; \mathcal{P}'\{j_1 \ldots j_{q/2}\}}, \end{aligned} \tag{C.3}$$

where $\mathcal{P}$ and $\mathcal{P}'$ perform permutations of the indices, and $\mathrm{sgn}(\mathcal{P}), \mathrm{sgn}(\mathcal{P}') = \pm 1$ denote the sign of the permutations. The first equality ensures Hermiticity of $\hat{H}_q$, whereas the second is due to the fermionic anticommutation relations of the creation and annihilation operators.

C.2 Details of master equation derivation

Here, we provide further details on the derivation of the Lindblad master equation (ME) presented in Sec. 5.3.

C.2.1 Functional derivative

The functional derivative presented in Eq. (5.14) is obtained from the integrated von Neumann equation of a single Hamiltonian realization,

$$\hat{\rho}(t) = \hat{\rho}(0) - i \int_0^t \mathrm{d}t_1 \left[\hat{H}(t_1), \hat{\rho}(t_1)\right], \tag{C.4}$$

as

$$\frac{\delta\hat{\rho}[\xi,t]}{\delta\xi^{(\alpha)}_{k_\alpha}(t')} = -i\left[\hat{h}^{(\alpha)}_{k_\alpha}, \hat{\rho}(t')\right]\Theta(t-t') - i\int_0^t \mathrm{d}t_1 \left[\hat{H}(t_1), \frac{\delta\hat{\rho}[\xi,t_1]}{\delta\xi^{(\alpha)}_{k_\alpha}(t')}\right]\Theta(t-t'), \tag{C.5}$$

in which the Heaviside step-function Θ arises from causality. This recursive expression for the functional derivative yields a series of nested commutators,

$$\begin{aligned}\frac{\delta\hat{\rho}[\xi,t]}{\delta\xi^{(\alpha)}_{k_\alpha}(t')} &= \sum_{n=1}^{\infty}\frac{(-i)^n}{n!}\int_0^t \mathrm{d}t_1\mathrm{d}t_2\ldots\mathrm{d}t_{n-1} \\ &\times \mathcal{T}\left[\hat{H}(t_1),\left[\hat{H}(t_2),\ldots\left[\hat{H}(t_{n-1}),\left[\hat{h}^{(\alpha)}_{k_\alpha},\hat{\rho}(t')\right]\right]\right]\right]\Theta(t_{n-1}-t')\ldots\Theta(t-t'),\end{aligned} \tag{C.6}$$

where we have introduced the time-ordering operator $\mathcal{T}$ such that the integration bounds decouple. Truncating Eq. (C.6) at $n=1$ then yields the term quoted in Eq. (5.14) of the main text.

As mentioned there, truncation to this lowest order is motivated by the fact that the resulting evolution equation of Eq. (5.15) is formally equivalent to that obtained when making the decorrelation assumption in the study of stochastic evolution equations [264, 265]. This is readily seen in the interaction picture generated by $\hat{H}_0$ [for simplicity of the notation, we assume below that the clean part of $\hat{H}(t)$ as given by Eq. (5.9) is time-independent)]: Let $\hat{\rho}_{\mathrm{I}}(t) \equiv \exp(i\hat{H}_0 t)\hat{\rho}(t)\exp(-i\hat{H}_0 t)$ and $\hat{H}_{\mathrm{I}}(t) = \sum_{\alpha,l_\alpha}\xi^{(\alpha)}_{l_\alpha}(t)\hat{h}^{(\alpha)}_{\mathrm{I},l_\alpha}(t)$, where $\hat{h}^{(\alpha)}_{\mathrm{I},l_\alpha}(t) \equiv \exp(i\hat{H}_0 t)\hat{h}^{(\alpha)}_{l_\alpha}\exp(-i\hat{H}_0 t)$. The dynamics of an individual Hamiltonian realization are then

$$\partial_t\hat{\rho}_{\mathrm{I}}(t) = -i\left[\hat{H}_{\mathrm{I}}(t), \hat{\rho}_{\mathrm{I}}(t)\right] = -i\sum_{\alpha,l_\alpha}\left[\xi^{(\alpha)}_{l_\alpha}(t)\hat{h}^{(\alpha)}_{\mathrm{I},l_\alpha}(t), \hat{\rho}_{\mathrm{I}}(t)\right]. \tag{C.7}$$

Integrating this von Neumann equation, one obtains a self-consistent integral equation for $\hat{\rho}_{\mathrm{I}}(t)$. Inserting this back into itself once, and taking the disorder average, with $\tilde{\rho}_{\mathrm{I}}(t) \equiv \mathbb{E}\left[\hat{\rho}_{\mathrm{I}}(t)\right]$, one obtains, after differentiating with respect to time,

$$\partial_t\tilde{\rho}_{\mathrm{I}}(t) = -\sum_{\alpha,\beta,l_\alpha,k_\beta}\int_0^t \mathrm{d}t'\left[\hat{h}^{(\beta)}_{\mathrm{I},k_\beta}(t),\left[\hat{h}^{(\alpha)}_{\mathrm{I},l_\alpha}(t'),\mathbb{E}\left[\xi^{(\beta)}_{k_\beta}(t)\xi^{(\alpha)}_{l_\alpha}(t')\hat{\rho}_{\mathrm{I}}(t')\right]\right]\right]. \tag{C.8}$$

Here we have made use of $\mathbb{E}\left[\xi_{l_\alpha}^{(\alpha)}(t)\right] = 0$ to eliminate terms which are linear in the disorder. Performing the decorrelation approximation

$$\mathbb{E}\left[\xi_{k_\beta}^{(\beta)}(t)\xi_{l_\alpha}^{(\alpha)}(t')\hat{\rho}(t')\right] \simeq \mathbb{E}\left[\xi_{k_\beta}^{(\beta)}(t)\xi_{l_\alpha}^{(\alpha)}(t')\right]\tilde{\rho}(t'), \tag{C.9}$$

and assuming, as in the main text, independent processes for $\alpha \neq \beta$, one obtains

$$\partial_t \tilde{\rho}_{\mathrm{I}}(t) = -\sum_{\alpha,l_\alpha,k_\alpha} \int_0^t \mathrm{d}t' F_{k_\alpha,l_\alpha}^{(\alpha)}(t,t')\left[\hat{h}_{\mathrm{I},k_\alpha}^{(\alpha)}(t), \left[\hat{h}_{\mathrm{I},l_\alpha}^{(\alpha)}(t'), \tilde{\rho}_{\mathrm{I}}(t')\right]\right]. \tag{C.10}$$

This is simply the interaction picture version of Eq. (5.15), which was obtained via the Novikov–Furutsu theorem.

C.2.2 Lindblad form

The final Lindblad master equation of Eq. (5.16) is obtained from Eq. (5.15) by first making the Markov approximation $\tilde{\rho}(t') \simeq \tilde{\rho}(t)$ and then expanding the double commutator. Simplifying our notation, this expansion is

$$\sum_{l,k} f_{l,k}(t)(\hat{h}_l\hat{h}_k\tilde{\rho} - \hat{h}_l\tilde{\rho}\hat{h}_k - \hat{h}_k\tilde{\rho}\hat{h}_l + \tilde{\rho}\hat{h}_k\hat{h}_l), \tag{C.11}$$

which is already reminiscent of a master equation in standard form. The latter is obtained in a final step in which we require the correlations to be symmetric under an exchange of the indices, i.e., $f_{l,k}(t) = f_{k,l}(t)$. This is trivially fulfilled for static processes such as those of the SYK model. For continuous processes, our requirement is equivalent to symmetry in time, i.e., $\mathbb{E}\left[\xi_l(t)\xi_k(t')\right] = \mathbb{E}\left[\xi_l(t')\xi_k(t)\right]$. We can then regroup the terms of Eq. (C.11) as

$$\begin{aligned} &\frac{1}{2}\sum_{l,k}\left[f_{l,k}(t)(\hat{h}_l\hat{h}_k\tilde{\rho} - \hat{h}_l\tilde{\rho}\hat{h}_k - \hat{h}_k\tilde{\rho}\hat{h}_l + \tilde{\rho}\hat{h}_k\hat{h}_l) + l \leftrightarrow k\right] \\ &= \sum_{k,l} 2f_{k,l}(t)\left(\frac{1}{2}\left\{\hat{h}_k\hat{h}_l, \tilde{\rho}\right\} - \hat{h}_l\tilde{\rho}\hat{h}_k\right). \end{aligned} \tag{C.12}$$

We thus finally obtain the Lindblad master equation in non-diagonal form, given in the main text by Eqs. (5.16)–(5.17).

C.2.3 Limit of time-independent processes

Here we explicitly show that the Lindblad ME of Eqs. (5.16)–(5.18), formally derived for Gaussian processes with arbitrary time-dependence, is valid in the limit of time-independent (static) processes $\xi_{k_\alpha}^{(\alpha)}(t) \to \xi_{k_\alpha}^{(\alpha)}$.

In this limit, the generic Hamiltonian defined in Eq. (5.9) and the corresponding ensemble averaged von Neumann equation given by Eq. (5.12) formally remain the same, but with time-independent disorder contributions

$$\partial_t \tilde{\rho}(t) = -i \left[\hat{H}_0(t), \tilde{\rho}(t)\right] - i \sum_{\alpha, l_\alpha} \left[\hat{h}^{(\alpha)}_{l_\alpha}, \mathbb{E}\left[\xi^{(\alpha)}_{l_\alpha} \hat{\rho}(t)\right]\right]. \tag{C.13}$$

We now have modified correlations $\mathbb{E}\left[\xi^{(\alpha)}_{l_\alpha} \hat{\rho}(t)\right]$, in which $\hat{\rho}(t)$ is a function (as opposed to a functional) of the Gaussian distributed random numbers $\xi^{(\alpha)}_{l_\alpha}$ (as opposed to random functions). These correlations may, however, still be treated via the Novikov–Furutsu theorem, which simplifies accordingly to [263]

$$\mathbb{E}\left[\xi^{(\alpha)}_{l_\alpha} \hat{\rho}(\xi, t)\right] = \sum_{k_\alpha} F^{(\alpha)}_{l_\alpha, k_\alpha} \mathbb{E}\left[\frac{\mathrm{d}\hat{\rho}(\xi, t)}{\mathrm{d}\xi^{(\alpha)}_{k_\alpha}}\right], \tag{C.14}$$

where now we have disorder correlations $F^{(\alpha)}_{l_\alpha, k_\alpha} = \mathbb{E}\left[\xi^{(\alpha)}_{l_\alpha} \xi^{(\alpha)}_{k_\alpha}\right]$ with infinite correlation time. This static version of the Novikov–Furutsu theorem is also known as Stein's lemma [305].

The right-hand-side of Eq. (C.14) now contains an ordinary total derivative (as opposed to a functional derivative), which we again obtain to lowest order from the integrated von Neumann equation as

$$\frac{\mathrm{d}\hat{\rho}(\xi, t)}{\mathrm{d}\xi^{(\alpha)}_{k_\alpha}} \simeq -i \int_0^t \mathrm{d}t' \left[\hat{h}^{(\alpha)}_{k_\alpha}, \hat{\rho}(t')\right]. \tag{C.15}$$

Substituting Eqs. (C.15) and (C.14) into Eq. (C.13) then yields

$$\partial_t \tilde{\rho}(t) = -i \left[\hat{H}_0(t), \tilde{\rho}(t)\right] - \sum_{\alpha, l_\alpha, k_\alpha} F^{(\alpha)}_{l_\alpha, k_\alpha} \left[\hat{h}^{(\alpha)}_{l_\alpha}, \left[\hat{h}^{(\alpha)}_{k_\alpha}, \int_0^t \mathrm{d}t' \tilde{\rho}(t')\right]\right]. \tag{C.16}$$

This is exactly the evolution equation that one obtains by taking the limit of time-independent processes, i.e., of infinite correlation times in Eq. (5.15). Taking the Markov approximation in Eq. (C.16) thus yields the Lindblad master equation of Eqs. (5.16)–(5.18) for time-independent correlations $F^{(\alpha)}_{l_\alpha, k_\alpha}$. This shows that starting from time-dependent noise and then taking the limit of infinite correlation time is equivalent to working with static noise all the way. The advantage of the time-dependent formulation used in the main text is that it naturally incorporates static disorder and temporally fluctuating noise on the same footing.

C.3 Further numeric results

C.3.1 Details on numeric simulation of exact dynamics

Here, we provide a brief description of the algorithm implemented to solve the exact dynamics of $\hat{H}_{\mathrm{SYK}}$. We exploit particle number conservation by restricting our simulations to a given particle number sector Q [Eq. (2.4)] of the Hilbert space. In particular, all simulations are performed within the half-filling sector $Q = 1/2$, whose Hilbert space dimension is $D = N!/((N/2)!)^2$.

The matrix representation of $\hat{H}_{\mathrm{SYK}}$ is constructed with respect to the fermion mode occupation number Fock basis: Each Fock state $|s_a\rangle$, where $a = 1, \dots, D$, is represented by one of the N-bit strings s_a of which NQ bits are 1 (representing the occupied fermion modes). The Hamiltonian's matrix elements $H_{ab} \equiv \langle s_a|\hat{H}_{\mathrm{SYK}}|s_b\rangle$ are non-zero only for those pairs of states whose bit string representation have a Hamming distance $d(s_a, s_b) = 0, 2, 4$. This follows from the quartic operators $\hat{c}^\dagger_{i_1}\hat{c}^\dagger_{i_2}\hat{c}_{j_1}\hat{c}_{j_2}$ appearing in $\hat{H}_{\mathrm{SYK}}$, where $d(s_a, s_b) = 0$ corresponds to $(i_1, i_2) = (j_1, j_2)$, $d(s_a, s_b) = 2$ to $i_k = j_l\,, i_{k'} \neq j_{l'}$ for $k, k', l, l' = 1, 2$, and $d(s_a, s_b) = 4$ to $i_1 \neq i_2 \neq j_1 \neq j_2$. These non-zero elements are populated by independent random complex Gaussian variables $J_{i_1 i_2; j_1 j_2}$, in accordance with Eqs. (2.2) and (2.3) to ensure Hermiticity of the Hamiltonian and antisymmetry of the interaction amplitudes under permutation of the indices. In this way, a single realization of the random SYK$_4$ Hamiltonian is constructed.

For system sizes $N \leq 14$, D is sufficiently small such that the full eigensystem (energy basis) of the above matrix representation can be solved exactly. For this we employ diagonalization routines from `LAPACK` [306]. Time evolution of a given initial state $|\psi(0)\rangle$ is then solved by rotating the corresponding vector representation into the SYK energy basis and calculating the time-dependent phases $\exp(-i\epsilon_n t)$ for any time $t \in \mathbb{R}$, where ϵ_n for $n = 1, \dots, D$ are the eigenenergies of $\hat{H}_{\mathrm{SYK}}$.

For system sizes $N > 14$, D is so large as to prohibit the above exact numeric solution of the entire eigensystem. Instead, we utilize a Runge–Kutta 4 (RK4) method to solve the Schrödinger equation for $\hat{H}_{\mathrm{SYK}}$. The matrix-vector multiplication employed within the RK4 method makes use of a sparse matrix representation of $\hat{H}_{\mathrm{SYK}}$ in order to exploit the large amount of zero matrix elements, and thus enhance the speed of the algorithm. Further reduction of computation time is achieved by parallelizing this matrix-vector multiplication via `MPI` methods [307], allowing us to exactly solve (within numeric precision) the dynamics for system sizes up to $N = 20$ at $Q = N/2$. To ensure accuracy of this RK4 based algorithm, we benchmark its dynamics against those of the above exact diagonalization scheme for $N \leq 14$, verifying that they agree.

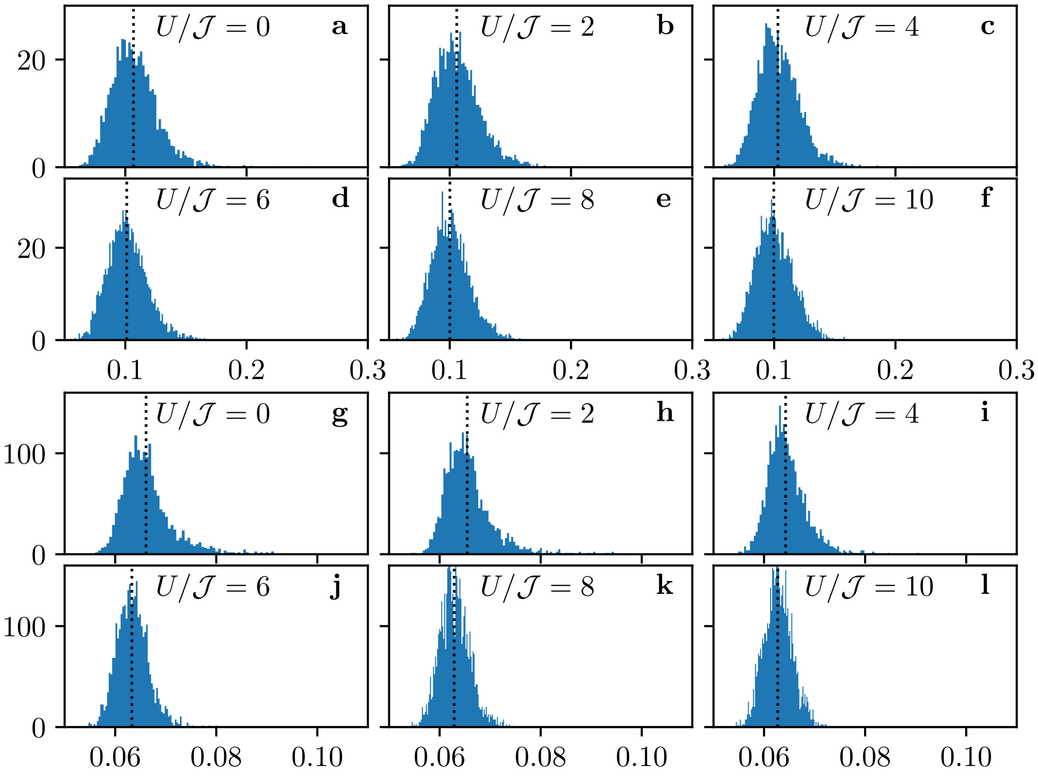

Figure C.1: Kullback–Leibler divergence. Distribution of $D_{\mathrm{KL}}(P(E)\|Q(E))$ for initial states taken as ground-states of the FH model with $U/\mathcal{J} = 0, 2, 4, 6, 8, 10$, as indicated on the panels, for 4000(2000) independent realisations of $\hat{H}_{\mathrm{SYK}}$ for $N = 8 (N = 12)$ in panels (a–f)[(g–l)]. The states' amplitude distribution over the energy eigenbasis of $\hat{H}_{\mathrm{SYK}}$, $P(E) = |\langle\psi(0)|E\rangle|^2$, is near-uniform $Q(E) = 1/D$.

Finally, we average over the dynamics of multiple disorder realizations of $\hat{H}_{\mathrm{SYK}}$. To this end, we again utilize `MPI` methods to solve the dynamics of multiple disorder realizations in parallel.

C.3.2 Distribution of initial states over eigenbasis of $\hat{H}_{\mathrm{SYK}}$

Figure C.1 shows the distribution of various initial states, taken as ground-states of the FH model, over the eigenbasis of $\hat{H}_{\mathrm{SYK}}$. In particular, we study the Kullback–Leibler divergence $D_{\mathrm{KL}}(P(E)\|Q(E))$, between the uniform distribution $Q(E) = 1/D$ and the initial states' amplitude distribution $P(E) = |\langle\psi(0)|E\rangle|^2$ with respect to the energy basis $\{|E\rangle\}$. Since $\hat{H}_{\mathrm{SYK}}$ has random matrix elements, we compute D_{KL} for an ensemble of disorder realisations, and plot the histogram of D_{KL} over this ensemble.

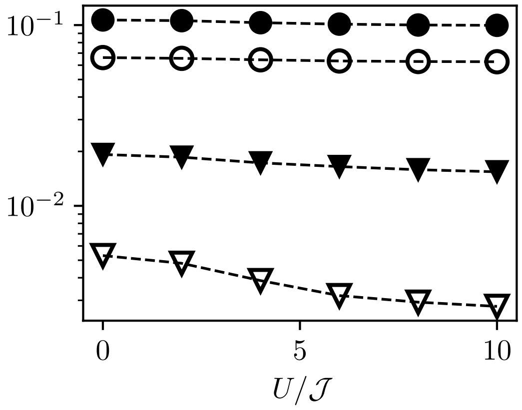

Figure C.2: Mean and standard-deviation of Kullback–Leibler divergence. Mean $\mathbb{E}[D_{\mathrm{KL}}]$ (circles), and standard deviation $\sqrt{\mathrm{var}[D_{\mathrm{KL}}]}$ (triangles) extracted from the distributions in Fig. C.1, for $N = 8$ (solid markers) versus $N = 12$ (empty markers). Both mean and standard-deviation decrease with N, suggesting that $D_{\mathrm{KL}}(P(E)\|Q(E)) \to 0$ as $N \to \infty$. Dashed lines included to guide the eye.

The figure shows that, on average, the initial states are near-uniformly distributed over the energy basis of $\hat{H}_{\mathrm{SYK}}$. Comparison of the data for $N = 8$ (panels a–f) versus $N = 12$ (panels g–l), shows that both the mean, and the variance of D_{KL} reduce with N. This is shown quantitatively in Fig. C.2, which shows the mean and standard-deviation of D_{KL} over 4000 realisations for $N = 8$ and over 2000 realisations for $N = 12$. This data suggests that in the thermodynamic limit, the initial states become uniformly distributed over the energy eigenbasis of $\hat{H}_{\mathrm{SYK}}$.

C.3.3 Higher-order moments

In figure C.3, we present additional results for the quench dynamics of moments $k = 8, 10, 12$ of the staggered magnetization $\hat{R}$ defined in Eq. (5.6). The original and rescaled dynamics show the same qualitative behaviour as moments $2 < k < 8$ studied in Sec. 5.2.2.

The kth moment of $\hat{R}$ contains interactions of up to k fermionic modes, and thus probes increasingly non-local physics for larger values of k. As a limiting case of a truly global many-body quantity, we show in Fig. C.4 the disorder-averaged survival probability (or fidelity) $\mathbb{E}\left[|\langle\psi(0)|\psi(t)\rangle|^2\right]$. For this quantity, the curves corresponding to different initial states do not collapse. Whilst this suggests that universality is absent for (superpositions of) highly non-local observables, we do not exclude the possibility that one may be able to specifically construct such an observable which does exhibit universality.

C.3.4 Additional observables

Here, we extend the investigations of Chap. 5 to other observables.

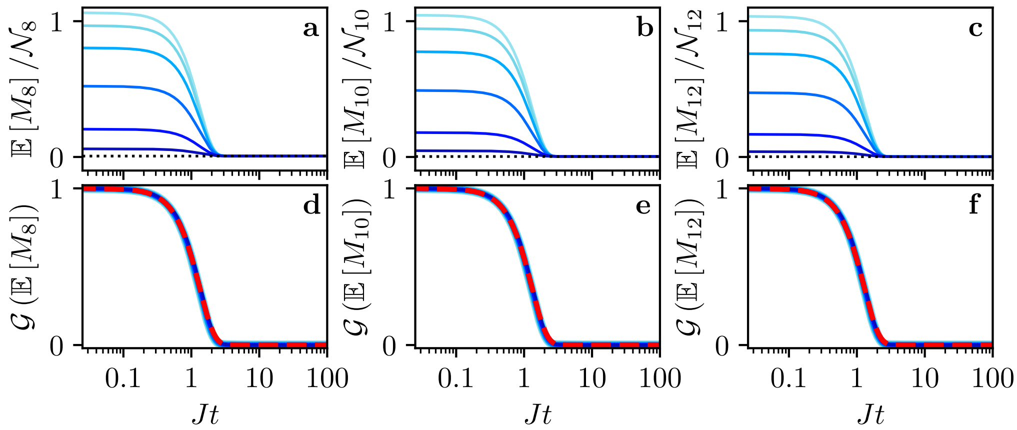

Figure C.3: Equilibration dynamics of operator moments M_k, under $\hat{H}_{\mathrm{SYK}}$. (a–c) Dynamics of moments $k = 8, 10$, and 12 of the operator $\hat{R}$, averaged over 400 realisations of $\hat{H}_{\mathrm{SYK}}$ for $Q = 8$ fermions occupying $N = 16$ modes. (d–f) Corresponding dynamics rescaled by the function $\mathcal{G}$ given in Eq. (5.3). Dark to light shading of the curves represents initial FH ground states for $U/\mathcal{J} = 0, 2, 4, 6, 8$, and 10, respectively. The dotted black lines mark the values of the operator moments calculated with respect to the Gibbs infinite temperature state. The rescaled curves are well approximated by Gaussian fits, $\exp\left[-(Jt/\tau)^2\right]$, with $\tau = 1.32, 1.3, 1.28$ for increasing k, respectively (dashed red curves).

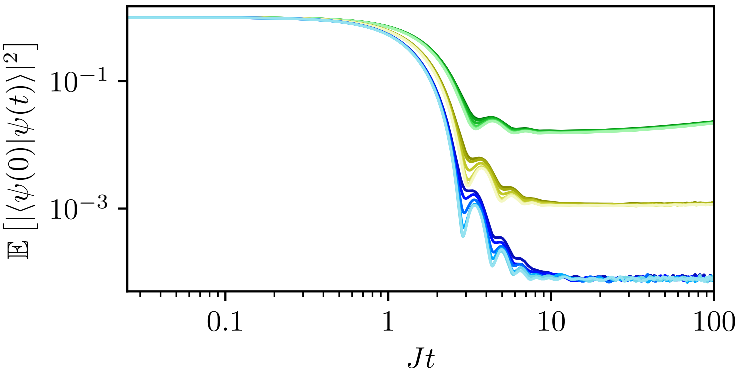

Figure C.4: Ensemble averaged survival probability of $\hat{H}_{\mathrm{SYK}}$. System sizes $N = 8$ (green), 12 (yellow), 16 (blue), and sample sizes 90000, 10000, 400, respectively. Shadings of a given colour represent different initial states, as in Fig. C.3. There is a clear lack of universality with respect to different initial states from early to late times. The early-time Gaussian decay followed by oscillations at intermediate times are expected from random matrix theory (RMT) [249, 308]. In contrast to RMT where universality is expected for the survival probability, here we observe an initial state *dependence*, which can be attributed to the structure of the SYK Hamiltonian, imposed by the fermionic statistics.

For this, we first consider the following 4-local operators defined in terms of the $\hat{\kappa}_i$ operators introduced in Eq. (5.6),

$$\hat{S}_j = -\hat{\kappa}_{2j-1}\hat{\kappa}_{2j} = (\hat{n}_{4j-2} - \hat{n}_{4j-3})(\hat{n}_{4j-1} - \hat{n}_{4j}). \tag{C.17}$$

The system average of these operators is defined as $\hat{S} = \frac{1}{(N/4)} \sum_j \hat{S}_j$, where $j \in \{1, 2, ..., N/4\}$. For an $N = 16$ system, we can construct four such 4-local operators, i.e., $\hat{S}_1$, $\hat{S}_2$, $\hat{S}_3$, and $\hat{S}_4$. In Fig. C.5(a–d), we show the representative evolution of $S_1(t) = \langle\psi(t)|\hat{S}_1|\psi(t)\rangle$ as well as of $S(t) = \langle\psi(t)|\hat{S}|\psi(t)\rangle$. As in the cases of the QFI and moments of the staggered magnetization, we recover the super-exponential universal equilibration dynamics of these 4-local operators.

All the operators considered so far are diagonal with respect to the Fock-space spanned by the occupation number basis vectors $\{|n_1, n_2, ..., n_N\rangle\}$. We thus additionally investigate the dynamics of a non-diagonal operator,

$$\hat{T} = \sum_{i=1}^{N/2} (\hat{c}^\dagger_{2i}\hat{c}_{2i-1} + \mathrm{H.c.}). \tag{C.18}$$

The dynamics of the QFI, F'_Q, computed with respect to this operator are

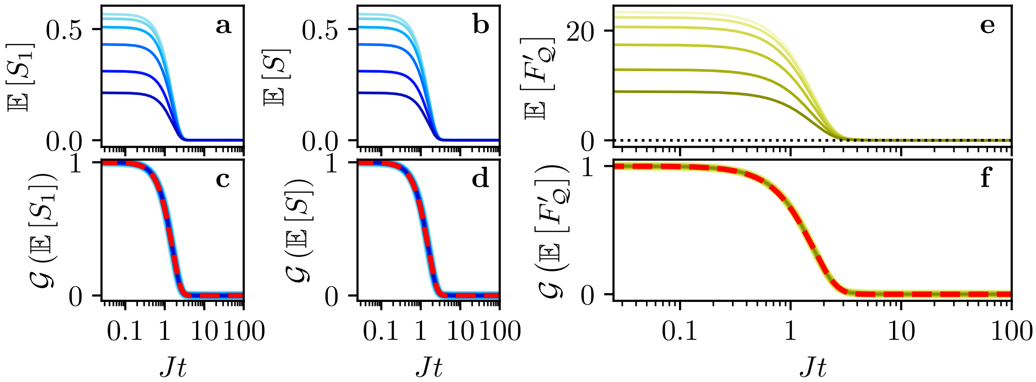

Figure C.5: Universal equilibration dynamics of further obervables. (a–d) Dynamics of the 4-local operators of Eq. (C.17), averaged over 400 disorder realizations of $\hat{H}_{\mathrm{SYK}}$ for $Q = 8$ fermions occupying $N = 16$ fermionic modes. (e,f) Dynamics of the QFI, $F'_{\mathcal{Q}}$ with respect to the operator $\hat{T}$ of Eq. (C.18), averaged over 2000 realisations of $\hat{H}_{\mathrm{SYK}}$ for $Q = 6$ fermions occupying $N = 12$ fermionic modes. The dotted black line in (e) marks the QFI calculated with respect to the Gibbs infinite temperature state. The rescaled data of the operator moments (c,d), and of the QFI (f) are well fitted by a Gaussian, $\exp\left[-(Jt/\tau)^2\right]$, with $\tau = 1.52$, respectively, $\tau = 1.58$ (dashed red curves). Dark to light shading represents different initial states, as in Fig. C.3.

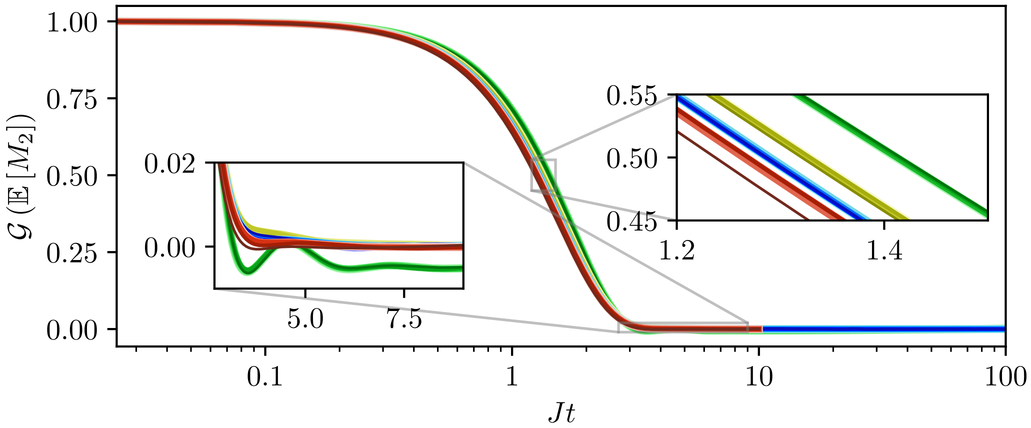

Figure C.6: System-size dependence. Rescaled equilibration dynamics of the disorder-averaged second moment $\mathcal{G}\left(\mathbb{E}\left[M_2\right]\right)$ of the operator $\hat{R}$, averaged over 90000, 2700, 400, and 50 disorder realisations of $\hat{H}_{\text{SYK}}$ for $N = 8, 12, 16,$ and 20 (green, yellow, blue, and red curves, respectively). Dark to light shadings of a given colour correspond to the different initial states of Fig. 5.2. Initial state independence is observed for all N, and the universal curves equilibrate faster, with an indication of convergence with increasing N to a fastest decay curve (right inset). The small spread of the curves for a given N at intermediate times (left inset) is of statistical nature due to finite sample sizes.

shown in Fig. C.5(e–f). Similar to all the previous cases, we again obtain the super-exponential universal equilibration dynamics of this observable.

C.3.5 Finite-size analysis of universal decay

To study the finite-size dependency of the rescaled universal curves, we consider in Fig. C.6 the representative case $k = 2$ of the operator moments [defined in Eq. (5.8)].

We consider the (exact diagonalisation) evolution for systems consisting of $N = 8, 12, 16,$ and 20 complex fermionic modes. For the largest accessible system size $N = 20$, the Hamiltonian matrix dimension is $D = N!/[(N/2)!(N/2)!] = 184\,756$. Due to the disorder, no symmetries other than particle number conservation can be used, and due to all-to-all connectivity the matrix is denser than for models with finite-range interactions. However, thanks to the self-averaging nature of the model [114], with increasing N smaller numbers of disorder realisations suffice for satisfactory convergence [309] (we consider $90\,000, 2700, 400,$ and 50 ensemble members for the above values of

N).

With increasing N, faster equilibration as well as an approach to convergence is observed, as shown by the right inset of Fig. C.6, which highlights the dynamics in the transient time domain. A similar feature has been seen in the initial dynamics of other quantities for time evolution under the SYK [98] and other disordered, chaotic Hamiltonians [308, 310], as well as random matrices [311]. For smaller N, the curves show oscillations before equilibrating to the steady state value. In addition, for $N = 8$, at large times the equilibrated curves slowly drift from the steady state value, with a rate that depends on the considered initial states. As a consequence, the rescaled curves cross zero and become negative at intermediate time, which is in accordance with Eq. (5.3) (see the left inset in Fig. C.6, which highlights the approach of the curves to the steady state value). Further finite-size analyses can be found in Ref. [81].

C.3.6 Liouvillian spectrum

As mentioned in Sec. 5.4.2, we find also for other states, which are not ground-states of the FH model, that for a given even moment, any non-zero amplitudes A_i always occupy the same eigenspaces. This is shown in Fig. C.7 for the symmetrised Néel state $|\psi(0)\rangle = (|010101\ldots\rangle + |101010\ldots\rangle)/\sqrt{2}$.

To conclude this section, we comment on the system-size dependence of the Liouvillian spectrum (see for instance, Table 5.1). We find numerically that all non-zero eigenvalues decrease as N is increased from 6 to 8. In particular, for λ_2—the only timescale entering M_2 [see Fig. 5.6(a–d)]—we find, respectively, the values -0.28 and -0.33. This explains the shift to a faster equilibration time of M_2 with increasing N, as observed previously in Fig. C.6. As seen there, this shift of M_2 exhibits a convergence, i.e., decreases as N is increased. We thus expect the eigenvalues λ_i to not decrease indefinitely with N, but to individually approach some asymptotic value. However, the enlarged Hilbert-space, inherent to the process of mapping $\mathcal{D}$ to the matrix form of Eq. (5.30), limits our study of the Liouvillian spectrum to $N \leq 8$, thus preventing us from probing this convergence.

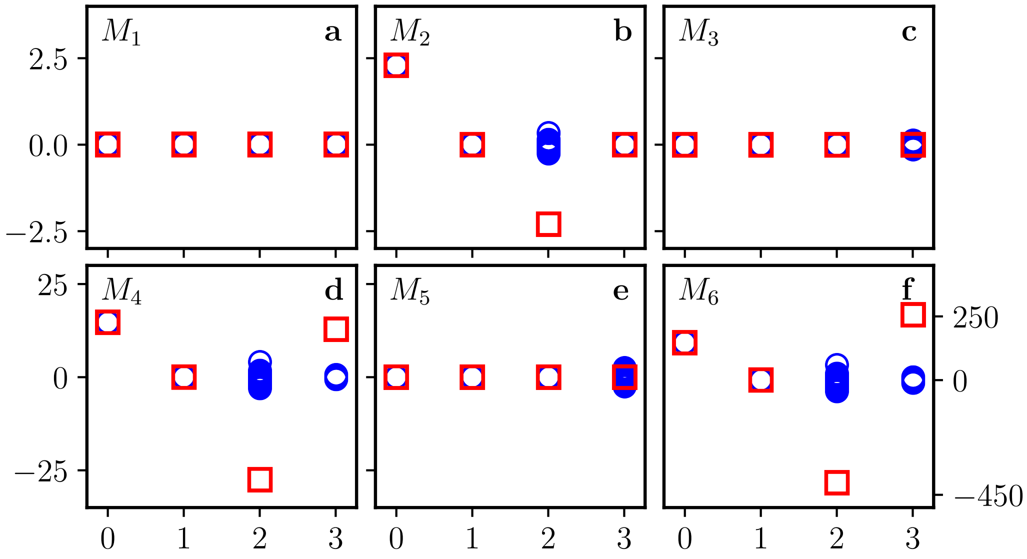

Figure C.7: Distribution of effective amplitudes over Liouvillian eigenspaces for Néel state. Distributions of $c_{i,\alpha_i} o_{i,\alpha_i}$ (blue circles) and A_i (red squares) of Eq. (5.28) for moments M_k of $\hat{R}$, with initial state given by the Néel state. Horizontal axes indicate the eigenspace index of Table 5.1. All amplitudes A_i vanish for odd moments. For M_2, only $A_2 \neq 0$ (besides the steady-state amplitude A_0), in line with the universality observed for initial FH states in Chap. 5. For even moments with $k \geq 4$, the non-zero amplitudes occupy the same two eigenspaces (besides the steady-state amplitude A_0), yielding an approximate universality, see discussion of Sec. 5.4.2.